UNIVERSIDADE DE SÃO PAULO

INSTITUTO DE ASTRONOMIA, GEOFÍSICA E CIÊNCIAS ATMOSFÉRICAS

MARCO ANTONIO COUTO JUNIOR

Gold Deposits Investigation in Quadrilátero Ferrífero, MG, Brazil by The Analysis of HTEM Data

São Paulo

2021

MARCO ANTONIO COUTO JUNIOR

Gold Deposits Investigation in Quadrilátero Ferrífero, MG, Brazil by The Analysis of HTEM Data

Tese apresentada ao Instituto de Astronomia, Geofísica e Ciências Atmosféricas da Universidade de São Paulo como requisito parcial para obtenção do título de Doutor em Ciências.

Orientador: Prof. Jorge Luís Porsani

Co-orientador: Prof. Neils Esben Auken

Versão corrigida. O original encontra-se disponível na Unidade.

São Paulo

2021

“The first principle is that you must not fool yourself and you are the easiest person to fool.” - **Richard P. Feynman**

Agradecimentos / Acknowledgements

Em primeiro lugar, agradeço à minha família, meu pai Marco Antonio Couto, minha mãe Vera Lúcia Costa Milliatti Couto e minha noiva Mayara Laís Oliveira Cunha, que sempre me apoiaram em todas as minhas iniciativas e esta é mais uma delas. Sobretudo naqueles momentos de sacrifício pessoal necessários para atingirmos nossos objetivos.

Agradeço enormemente ao meu orientador Prof. Jorge Luís Porsani por acreditar no meu potencial e incentivar meu embarque no doutorado, além de sempre ter uma palavra amiga, mas realista, quando necessária.

Agradeço ao Instituto de Astronomia, Geofísica e Ciências Atmosféricas, seus corpos docente e discente, além do competente quadro de funcionários, por todo o apoio que recebi ao longo da minha trajetória acadêmica que me trouxe até aqui.

Agradeço ao Serviço Geológico do Brasil - CPRM por me disponibilizar um período de 2 anos de licença para que pudesse me dedicar integralmente ao meu projeto de doutorado. Um agradecimento especial aos amigos Paulo Henrique Amorim Dias e Joanna Chaves Souto Araújo, por sempre me resgatarem na geologia do Quadrilátero Ferrífero, e a Raphael Ribeiro Severino, pela discussão sobre o MVI. Agradeço ao meu chefe direto, diretor do Centro de Geociências Aplicadas do SGB-CPRM, Noevaldo Araújo Teixeira, por me incentivar e ceder o espaço e tempo necessário para o término da tese.

I would like to strongly thank my co-advisor, Esben Auken, for accepting me in the Hydrogeophysics Group for the period of one year in Aarhus during 2018. I am also very thankful to Professors Gianluca Fiandaca and Anders Vest Christiansen, for the great insights about IP effect and TEM method, and for the interest to collaborate in this research. I also thank my colleagues in Aarhus, especially my friends Pradip Maurya, for helping me with Workbench and Lichao Liu, for sharing the office during my period in Aarhus. Also, off course, for grabbing some beers and eat something together at late in the night after a hard day of work.

Agradeço à CAPES, pela bolsa de 6 meses para o período sanduíche em Aarhus (processo 88881.188567/2018-01). Agradeço a todos que de forma direta ou indireta me ajudaram no desenvolvimento desta tese. Muito obrigado!

Resumo

O efeito de IP aéreo (AIP) tem sido tema de grande interesse na comunidade geocientífica internacional, com evidências cada vez maiores sobre sua importância para definir melhor os modelos de resistividade elétrica em levantamentos eletromagnéticos aéreos no domínio do tempo. Suas implicações são significativas no mapeamento geológico e na exploração mineral, em particular, mineralizações em sulfetos metálicos. No entanto, no Brasil, estudos sobre este tema são escassos ou praticamente inexistentes. Nesta pesquisa, abordou-se a aplicação do AIP em dados eletromagnéticos no domínio do tempo voados por helicóptero (*Helicopter Transient Electromagnetic* - HTEM) sob o *Greenstone Belt* Rio das Velhas, na região do Quadrilátero Ferrífero (QF), MG. O trabalho focou na modelagem dos dados HTEM considerando-se o efeito AIP e sua potencialidade em identificar zonas favoráveis às mineralizações auríferas. Para isso, utilizou-se um método inovador de reparametrização do modelo de Cole-Cole, denominado ângulo de fase máxima, combinado com um esquema de inversão robusta adaptado para um algoritmo 1D com vínculos laterais. Os resultados foram apresentados tanto para modelos sintéticos, quanto para dados reais, visando a validação da metodologia. Para verificar a aplicabilidade nos dados do QF, adquiridos com um sistema AeroTEM^{HD}, um estudo de caso na região da Mina de Lamego foi conduzido, indicando a aplicabilidade de AIP nestes dados. Os resultados mostraram que um horizonte de filitos carbonosos foi identificado, ainda que num ambiente 3D complexo, servindo como guia estrutural e litológico para mineralização de ouro. A metodologia foi estendida para averiguar sua aplicabilidade em escala regional/distrito, na região de Roça Grande, arredores do município de Caeté. Os resultados foram integrados a dados aeromagnéticos e indicaram que uma cobertura de alteração de unidades máficas pode afetar significativamente os dados nos *early-times*. Ainda assim, corpos polarizáveis mais profundos foram identificados em zonas de formações ferríferas bandadas, estruturalmente condicionadas em áreas de potencial aurífero, mostrando que o AIP pode ser também aplicável em escala regional ou de distrito.

Palavras-chave: HTEM, IP, AIP, Exploração Mineral, Mineralização de ouro, Quadrilátero Ferrífero, Minas Gerais.

Abstract

In this research, the approach to process the electromagnetic data was developed to study the Airborne Induced Polarization (AIP) effect to identify polarizable anomalies associated with metallic sulfides or polarizable lithologies related to gold mineralization. This thesis was focused on the modeling of Helicopter Transient Electromagnetic (HTEM) data under the AIP paradigm. The research was conducted in the region of Quadrilátero Ferrífero (QF), MG, Brazil. To address to this problem, the recent developed Maximum Phase Angle reparameterization of the Cole-Cole model was applied and a robust inversion scheme study to invert the electromagnetic data and recover the underground distribution of the IP parameters using a 1D Lateral Constrained Inversion was conducted. These results are presented for both synthetic and real data strongly affected by the IP effect. To validate the use of this methodology in QF region, a case study in Lamego Mine was conducted, seeking to understand the behavior of the induced polarization response in the AeroTEM^{HD} survey, the system used in the area. The polarization response in Lamego Mine was able to characterize the carbonaceous units associated with the gold mineralization, therefore validating the possibility to identify AIP response in the AeroTEM^{HD} data and its use in a complex structural environment in the study area, even using a 1D laterally constrained inversion scheme. Then, the approach was extended to other areas in QF area, seeking to characterize potential gold mineralized zones associated with strongly magnetic iron formations, in which magnetic data was integrated as ancillary information. The results for Roça Grande area (Caeté municipality) are presented. In this area, the induced polarization anomalies suggested that a thick polarizable cover with mafic origin may affect the data in the very early-times, although deeper polarization bodies could be identified associated with linear magnetic anomalies related to banded iron formation layers structurally controlled by the regional deformation in known potential zones. These results demonstrated that AIP approach can be used to map potential zones in a regional/district scale as well.

Keywords: HTEM, IP Effect, AIP, Mineral exploration, Gold mineralization, Quadrilátero Ferrífero, Minas Gerais

Summary

Figure Index

Table Index

Chapter 1: Introduction and Objectives

1.1. Introduction

The Transient Electromagnetic Method (TEM) has been successfully applied in geophysical investigations focused on massive and disseminated metallic sulfides zones. In particular, the Airborne Electromagnetic Methods (AEM) has been used for mineral exploration with good results for over 60 years. The Helicopter TEM (HTEM) systems have been gone to the spotlight in mineral exploration during the 2000's due to their high quality lateral resolution of the conductors bodies, detailed fast coverage of large areas of interest, low maintenance cost in relation to the fixed-wings AEM systems and deeper depth of investigation compared to the Helicopter Frequency Domain Electromagnetic (HFEM) systems. In fact, Allard (2007) points out that the success of HTEM is related to their higher adaption capacity to the demands coming from the mineral exploration industry, in a sense of a Darwinian Natural Selection process within the AEM methods.

In addition to the AEM methods, the Induced Polarization (IP) method also became an efficient geophysical application in mineral exploration, with good results to identify mineralized zones associated with metallic disseminated sulfides (Thomson, 2007). Conventionally, the IP systems are based on galvanic injection of electrical currents in the underground, which measurements of the associated secundary electrical potential through grounded electrodes (Oldenburg and Li, 1994; Kratzer and Macnae, 2012).

Since the 1960's, negative sign values in the transient fields in TEM systems have been observed (Walker, 2008). Generally, these negatives are associated with IP effects caused by the transient electromagnetic field in the TEM method. During the 1980's and 1990's, much effort was devoted to understand the causes of negatives transients related to the IP effect and how to model it (Spies, 1980, Lee, 1981, Weidelt, 1982, Smith et al. 1988, Smith and West, 1988a, 1988b, 1988c, 1988d, 1989, Flis et al. 1989, Smith and Klein, 1996). During the last 15 years, this topic has come to attention again due the increase in number of HTEM surveys for mineral exploration, which was followed by technological improvements that allowed to identify negative transients more often (Walker, 2008, Flores and Peralta-Ortega, 2009, Kratzer and Macnae, 2012, Marchant et

al., 2012, Chuan-Tao et al. 2013, Marchant et al. 2013, Viezzoli et al., 2013, Marchant et al. 2014, Viezzoli et al. 2015, Kwan et al. 2015, Kang et al., 2015; Macnae, 2016; Kaminski and Viezzoli et al., 2017; Viezzoli and Manca, 2018).

The possible causes of IP negative values were intensely debated in the literature. Weidelt (1982) demonstrated that the negative values in the late times domain in coincident loop TEM systems cannot be generated in non-polarizable environments, regardless their electrical conductivity spatial distribution. Smith and West (1988a, 1988b, 1988c, 1988d, 1989) presented an extensive synthetic modeling and field examples of these IP negatives in coincident-loop configuration TEM systems. Smith and Klein (1996) presented results from a GEOTEM survey in Canadá in which they identified the necessary conditions for the occurrence of the IP effect, like lower soil conductivity, predominancy of the IP effect over the transient fields generated by the TEM method in the late times domain and good signal-to-noise ratio in this interval. Nevertheless, negative IP values can also be generated and modeled in non-coincident loops surveys, as long (Marchandt, 2012; Macnae, 2016; Kaminski and Viezzoli et al., 2017; Viezzoli and Manca, 2018).

However, the absence of negative values not necessarily implies in the absence of IP effect, once it is needed a finite time interval for its set up, which could not be noticeable at the late times of TEM decays in comparison to the magnitudes of the transient fields (Kratzer e Macnae, 2012). Moreover, electrically conductive soils can mask the IP effect as well (Smith and Klein, 1996).

Despite the intense debate related to the causes of IP effect in TEM data, this technique is already used in AEM mineral exploration surveys, which became known as Airborne Induced Polarization (AIP) - (Kratzer e Macnae, 2012; Kwan et al, 2015a, 2015b; Viezzoli and Kaminski, 2016; Kang et al., 2017; Kwan and Müller, 2019; Viezzoli et al. 2019). The interest in AIP surveys is related to their reduced costs and faster surveys to cover big areas with prospective interest, in comparison with the ordinary galvanic ground surveys. Therefore, there is an important effort to develop new computational techniques to model the AIP data. Kratzer e Macnae (2012) developed a method to least-square fit both ground and airborne TEM data, using an exponential decays functions basis. Marchant et al. (2014) developed a 3D forward modeling scheme directly calculated in the time domains and able to work with a generalized waveform. Kang and

Oldenburg (2015, 2017) developed techniques to separate the IP response from the pure non-polarizable response of the subsurface. Viezzoli et al. (2017) applied a modification of a inversion scheme developed by Fiandaca et al. (2012), originally developed for galvanic IP, to model AIP data in Cu-Au porphyry deposits in Canadá and orogenic Au mineralizations in Australia.

This thesis aims to present an adaptation and application for Au exploration of a robust inversion scheme for IP influenced HTEM data in Quadrilátero Ferrífero (QF) area, using the Maximum Phase Angle (MPA) parameterization, originally developed by Fiandaca et al. (2018) for IP galvanic methodology. The methodology was fully developed in Li et al. (2019) as partial results of this thesis, in which we tested for both synthetic and real data strongly influenced by IP effect. The achievements in this preliminary work allowed to improve the IP effect modeling in Lamego Mine, QF region, and test its applicability to the HTEM survey over QF region, which was presented in Couto et al. (2020). Finally, the approach developed in the second paper was generalized to other QF areas, like Roça Grande area, integrating it with airborne magnetic data for a more complete interpretation of the anomalies related to Au mineralizations associated with banded iron formations (BIFs). These results are quite promising to characterize Au mineralization associated with magnetic BIFs and are presented as a paper and should be sent for publication soon.

The thesis text is structured as follows: Chapters 1 describes the overview and objectives; Chapter 2 describes the geological environment of QF region; Chapter 3 covers the theoretical aspects about the IP effect in TEM method; Chapter 4 goes through the methodologies used to model both the AIP data and the magnetic data, which was integrated in the last part of this work (Section 6.3); Chapter 5 presents the HTEM dataset and its preparation for AIP modeling; Chapter 6 presents the achieved results mentioned in the last paragraph, which are detailed presented as two papers in Appendixes 1 and 2 and Section 6.3, which describes the results with HTEM and airborne magnetics in Roça Grande area; Chapters 7 presents the conclusions and future work direction of this thesis.

1.2. Objectives

This research features the forward and inverse modeling of the IP (Induced Polarization) effect in HTEM data applied in the region of Quadrilátero Ferrifero (QF), and its integration to the associated airborne magnetic data, seeking to identify prospective Au mineralized zones. The QF region is a world metallogenic province, with world class orogenic gold deposits. The geological environment is associated with the Greenstone Belt Rio das Velhas terrain, and gold mineralization are presented in disseminated sulfides structures.

To achieve this objective, this research was composed by three steps: 1) a robust inversion using the MPA parameterization (Fiandaca et al., 2018) scheme was developed and tested for both synthetic and real data; 2) this approach was tested for an AeroTEM^{HD} survey over Lamego Mine, QF region, seeking to validate the modeling algorithm for the QF 3D geological environment and the AeroTEM^{HD} system, as the structural and lithological controls of this area were well known through borehole information; and 3) the generalization of this approach for further areas in QF region, incorporating other geophysical methods (magnetics) to identify prospective Au mineralized zones, for a regional study in the Roça Grande area. The first two parts of this research was conducted during my visiting period (one year) at Aarhus University, Denmark, in collaboration with the Hydrogeophysics Group (HGG), which resulted in the publication of two papers, Lin et al. (2019) and Couto et al. (2020), presented in Appendixes A and B, respectively. The third part was conducted after my coming back to Brazil. All results are commented and referenced in Chapter 6.

This research aims to collaborate for the advancement of AEM techniques applied for mineral exploration, providing new insights that can be used by the mineral industry and governments (geological surveys) as well.

Chapter 2: Study Area

2.1. Regional Geology

The Quadrilátero Ferrífero (QF) area is characterized by an Archean Greesntone Belt terrain, localized at the south border of the São Francisco Craton (central-southern portion of Minas Gerais State, Brazil) – Figure 2. 1, covered by volcano-sedimentary rocks and Proterozoic sediments.

The name denomination of the QF area is originated by the geometry in map of the iron deposits, which presents a quadrangular geometry for the mountains in this region, whose edges are formed by the Curral, Moeda, Ouro Branco and Salto hills (Figure 2. 2).

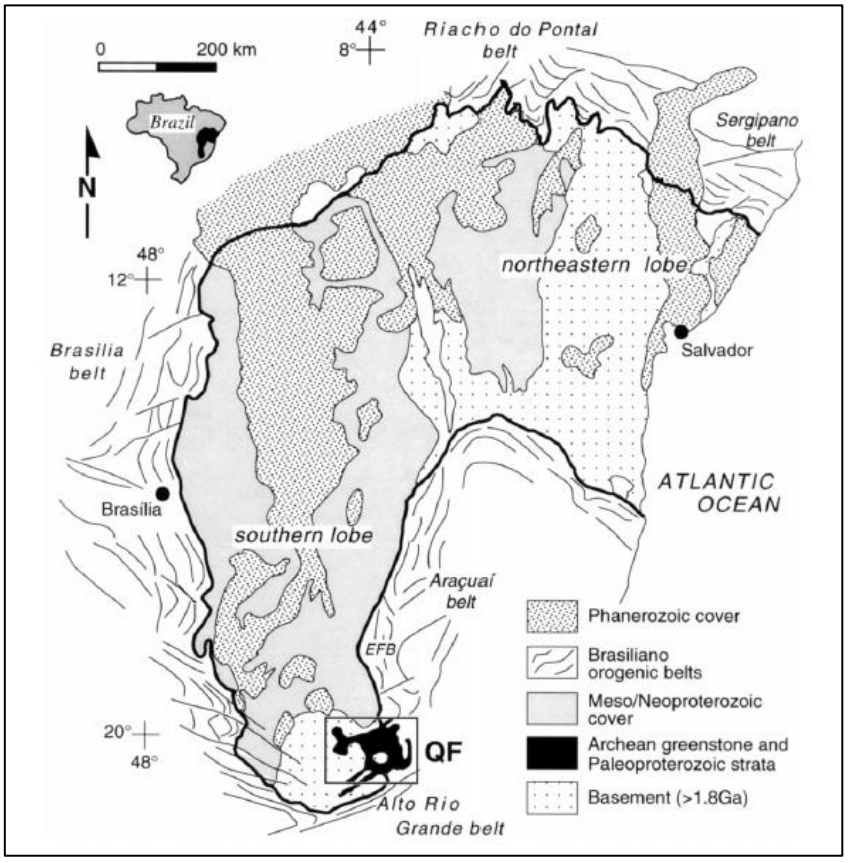

Figure 2. 1: Geological map of São Francisco Craton with the location of Quadrilátero Ferrífero (QF) in the Southern area (adapted from Alkmim and Marshak, 1998).

Although the region presents large and important iron deposits, it is one of the most important gold production areas in Brazil, characterized as a world class province

(Lobato et al., 2001). For this reason, this area is also one of the most geologically investigated. There are individual gold occurrences, small gold deposits – like the Raposos, Engenho D'água and Juca Vieira mines – and world class gold deposits – like Morro Velho and Cuibá mines (Lobato et al., 2001).

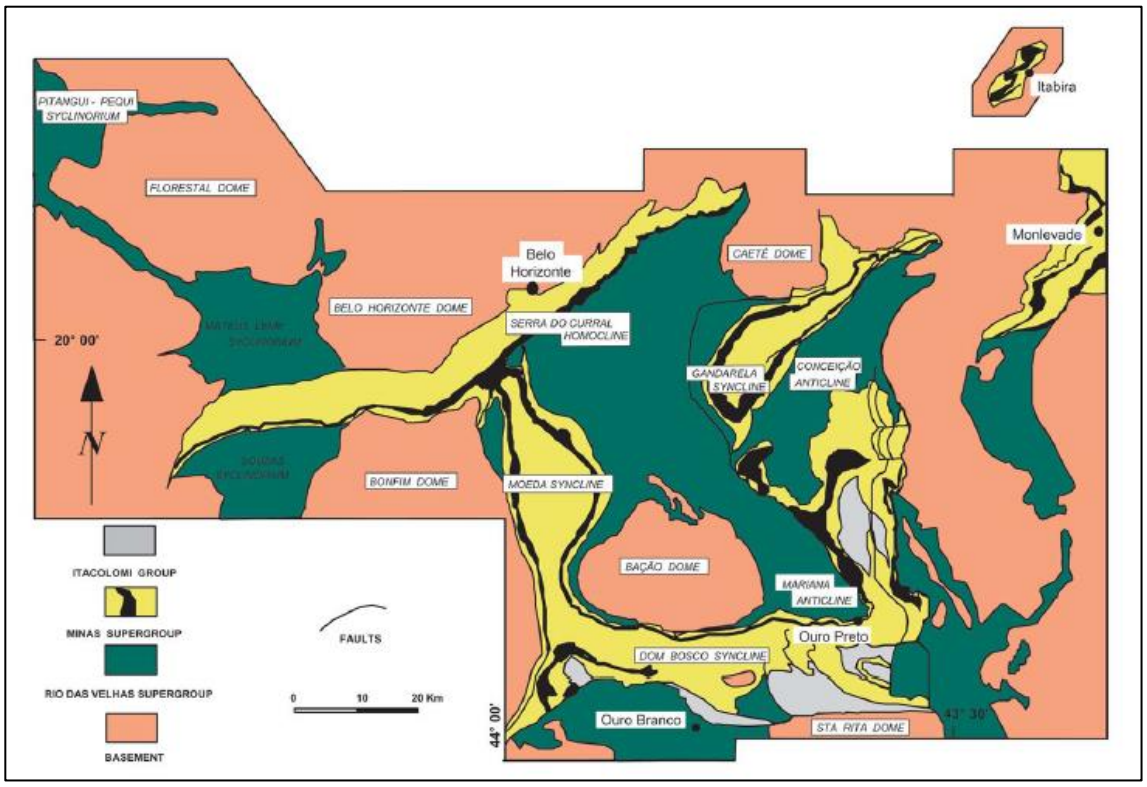

Figure 2. 2: Simplified geological map of Quadrilátero Ferrífero área with the main structural and stratigraphic. (adapted from Alkmim and Noce, 2006).

2.2. Local Geology

According to Baltazar and Zucchetti (2007) and Alkmim and Noce (2006), the QF structural/stratigraphic framework is divided in four main domains (Figure 2. 2and Figure 2. 3):

- Archean granite-gnaissic terrains in the basal portion;
- Rio das Velhas Supergroup (RVSG) constituted by Archean greenstone belt sequences;
- Minas Supergroup Minas (MSG) and;
- Itacolomi Group (IG).

The granite-gnaissic terrains constitute the basal sequence of the stratigraphy, which comprises tonalite–trondhjemite–granodiorite (TTG) gneisses, granites intercalated with anfibolites and metasssedimentary rocks associated with dome structural framework, surrounded by supracrustal sequences. According to Almeida (1967), Ladeira (1980), Baltazar and Zuchetti (2007), Lana et al. (2013) and Soares et al. (2020), this is the most ancient Archean unity occurrence in the area, which age lies between 3.2 and 2.9 Ga. This unity is divided between the Caeté, Belo Horizonte, Bonfim, Santa Bárbara and Bação Complexes (Figure 2. 3). The first one presents a granodiorite composition, the second is composed by gneisses predominantly with tonalitic composition, the third presents trondhjemite composition and the last two present tonalite and trondhjemite composition.

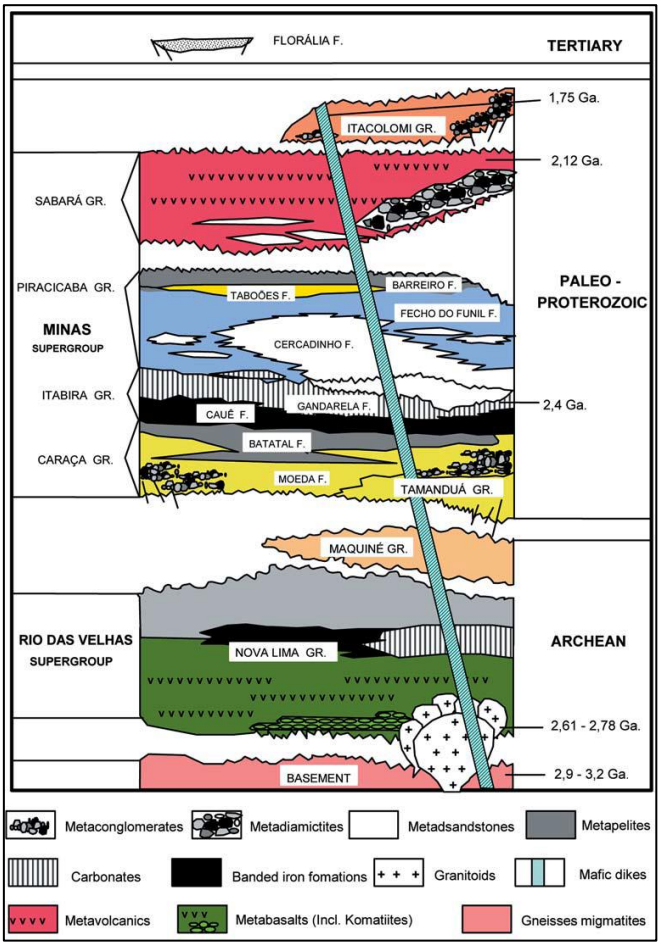

Figure 2. 3: Stratigraphic sequence of Quadrilátero Ferrífero. (from Alkmim and Noce, 2006).

The RVSG is characterized by a Neoarchean greenstone belt sequence known as the Greenstone Belt Rio das Velhas (GBRV) – Schorscher (1978), which comprises the

main domain of the gold mineralization in QF area (Lobato et al., 2001) and it is composed by the Nova Lima and Maquiné Groups.

According to Baltazar and Zucchetti (2007), the structural evolution o QF is characterized by three main deformation events related to the RVSG orogeny, which resulted in the generation of four structural domains in the area: D1, D2, D3 and D4. The first deformation event occurred during the Archean Eon (2.8 – 2.67 Ga), intrinsically related to GBRV evolution, which is related to D1 and D2 domains and it is characterized by a NNE-SSW tectonic transport, structural vergence of faults and folds to NNE (Martins et al., 2016). The D1 domain (2749 – 2670 Ma) presents tectonic transport from North to South, while the D2 domain (~ 2700 Ma) is related to a NE to SW tectonic transport.

The second deformation event occurred in the Transamazonian crustal extension event (2100 – 1900 Ma) in the Proterozoic Eon, with which is related to the D3 domain, characterized by two types of structures: i) the first is represented by regional synclines that defines the QF quadrangle shape (Serra do Curral, Moeda, Dom Bosco and Santa Rita synclines) related to the deposition of the sediments of Minas Supergroup in a intracratonic environment during the extensional event and; ii) diapiric uprising of the granite-gnaisse basement defining the domelike shapes, that are represented by the Bação, Caeté, Santa Rita, Belo Horizonte and Santa Bárbara complexes.

The third and final deformation event occurred during the Brasiliano orogenic cycle (700 – 500 Ma), as a compressional deformation oriented from East to West, defining the D4 domain.

Stratigraphically, the Nova Lima Group is part of the basal sequence of RVSG, composed by rocks originated from mafic-ultramafic volcanism in the bottom part of stratigraphy (toleitics-komatiitics unities) and chemical sedimentary rocks associated. In the intermediary portion of the stratigraphic sequence, it is composed by a volcanoclastic unit associated with felsic volcanism and clastic sedimentation in the upper part (Baltazar and Zuchetti, 2007). This group presents the higher economic importance in the area, since it hosts the main gold deposits and it is regionally related to the D2 structural group (thrust shear zones), characterized by epigenetic deposits related to sulfide enrichment mostly frequent in banded iron formations (BIFs) and “lapa seca” lithological type, as

discussed in Subsection 2.3. The Maquiné Group is composed mainly by quartzites, conglomerates and phyllites, which cover the Nova Lima Group. The contact in the bottom part with the Nova Lima Group could be concordant or discordant with gradational contact (Baltazar and Zuchetti, 2007).

2.3. Orogenic Gold Mineralizations

The orogenic Au mineralizations in QF area are hosted in the SRV and correspond to the most economically important gold mineralization in the region (Lobato et al., 2001). The QF area was considered the most important gold production area in Brazil until the 1970's and represent a world class gold province. The biggest and more important gold deposits in QF area are located in the North portion, which the Cuiabá, Morro Velho, Raposos, São Bento, Córrego do Sítio, Faria, Bicalho and Bela Fama mines are the most important.

The Au deposits in QF area were originated from the metamorphism and deformation events of the GBRV during the Archean Eon, which affected mainly the Nova Lima Group in the mafic-ultramafic basal sequence (Lobato et al., 2001 and Noce et al., 2007). These mineralizations present strong structural control associated with NE-SW and E-W lineaments and shear zones.

Lobato et al. (2001) discussed that the main mineralization types are: (1) sulfide zones in banded iron formation (BIF) bodies; (2) sulfides and Au dissemination in hydrothermal altered rocks along shear zones; and (3) quartz-carbonate-sulfides veins with Au content inside mafic, ultramafic, volcanic felsic and clastic sedimentary rocks.

The majority of these mineralized bodies in the deposits are hosted in high grade hydrothermal altered rocks known as "lapa seca" (an informal denomination) and also in BIFs bodies of carbonaceous facies. The rest of the mineralization is subordinately hosted in mafic-ultramafic and metasedimentary rocks (Figure 2. 4). The second case describes the lithological type of important deposits in QF like Cuiabá (Kresse et al., 2020, Senna et al., 2021), Lamego (Martins et al., 2016) and Roça Grande (Pressaco and Sepp, 2018, Araújo and Lobato, 2019), in which the first is currently the most important gold deposit in the area. In this work, only Lamego is analysed in detail, while a regional/district scale study was conducted in the Roça Grande deposit region.

The geological features of these deposits could imply in ambiguity responses for the Transient Electromagnetic Method (TEM) method, once the electrical conductivity contrast in the mineralized sulfides zones could not be enough expressively to map these bodies, like the deposits associated with carbonaceous facies BIFs bodies and the "lapa seca" rocks. One way to try to eliminate these ambiguities is analyze the possible IP response in the HTEM data and the galvanic IP effect in these deposits, seeking to associate the response with the mineralized sulfides zones.

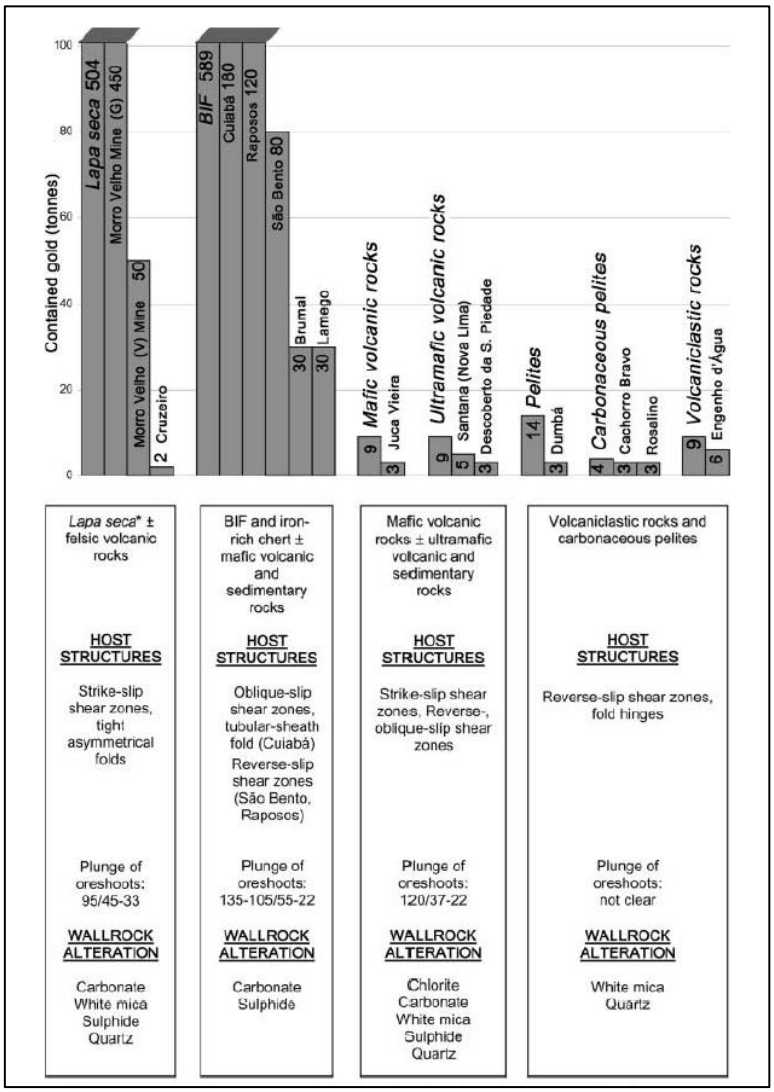

Figure 2. 4: Relative importance associated with the type of host rock and structural framework of the main orogenic gold deposits of Rio das Velhas Supergroup in the Quadrilátero Ferrífero area (from Lobato et al., 2001).

Chapter 3: Geophysical Methodology

In this chapter, the TEM method and its associated IP effect are discussed. It is also. Presented a brief description about the magnetic method.

3.1. Transient Electromagnetic Method (TEM)

The TEM method or Time Domain Electromagnetic (TDEM) method is an inductive electromagnetic (EM) method used to map the electrical conductivity (or resistivity) contrast in subsurface. The method is quite versatile and finds applications in the mineral exploration (Oliveira, 2014; Couto et al, 2016; Viezzoli et al, 2016; Couto et al., 2017b; Kang et al, 2017; Oliveira, 2020), hydrogeology investigation (Danielsen, et al., 2002; Porsani et al., 2012a, 2012b; Bortolozo et al., 2014; Bortolozo et al, 2015; Almeida, et al., 2017; Campaña, et al., 2017; Hamada, et al., 2018; Leite, et al, 2018; Rangel, et al., 2018).The TEM methodology was developed in face of the difficulties in the applications of the Frequency Domain Electromagnetic (FDEM) method, which the induction of the EM field in subsurface (secondary field) is generated through an alternate current (AC) within a transmitter loop (Tx) on surface and the secondary field is measured through a receiver coil (Rx) still in the presence of the primary field generated by the current in Tx (Figure 3. 1-a). In general, the intensity of the secondary field is many orders of magnitude smaller than the primary field and even though the primary field is known, there are many difficulties to remove it from Earth's response, i.e., the secondary field (Nabighian and Macnae, 1991, Dentith and Mudge 2014).

In the TEM method, differently from the FDEM, the induction of the secondary EM field is created turning off the direct steady current in the Tx (Figure 3. 1-b and Figure 3. 1-c), which causes a time-decay of the primary magnetic field (B) and, according to Faraday's Law from the Classical Electrodynamics, the electromotive force (e.m.f) induces secondary electrical currents (or eddy currents) in the subsurface. Due to ohmic energy losses, these eddy currents diffuse in subsurface following the shape of the transmitter loop, but increasing in area, in a geometry known as smoke rings (Figure 3. 2-a), which concept was introduced by Nabighian (1979). Initially, in the very early times, it is concentrated just beneath the transmitter loop, with similar size and goes down in

depth, increasing the area and being attenuated in amplitude. The receiver coil is used to measure the time decay of the secondary magnetic field amplitude (dB/dt).

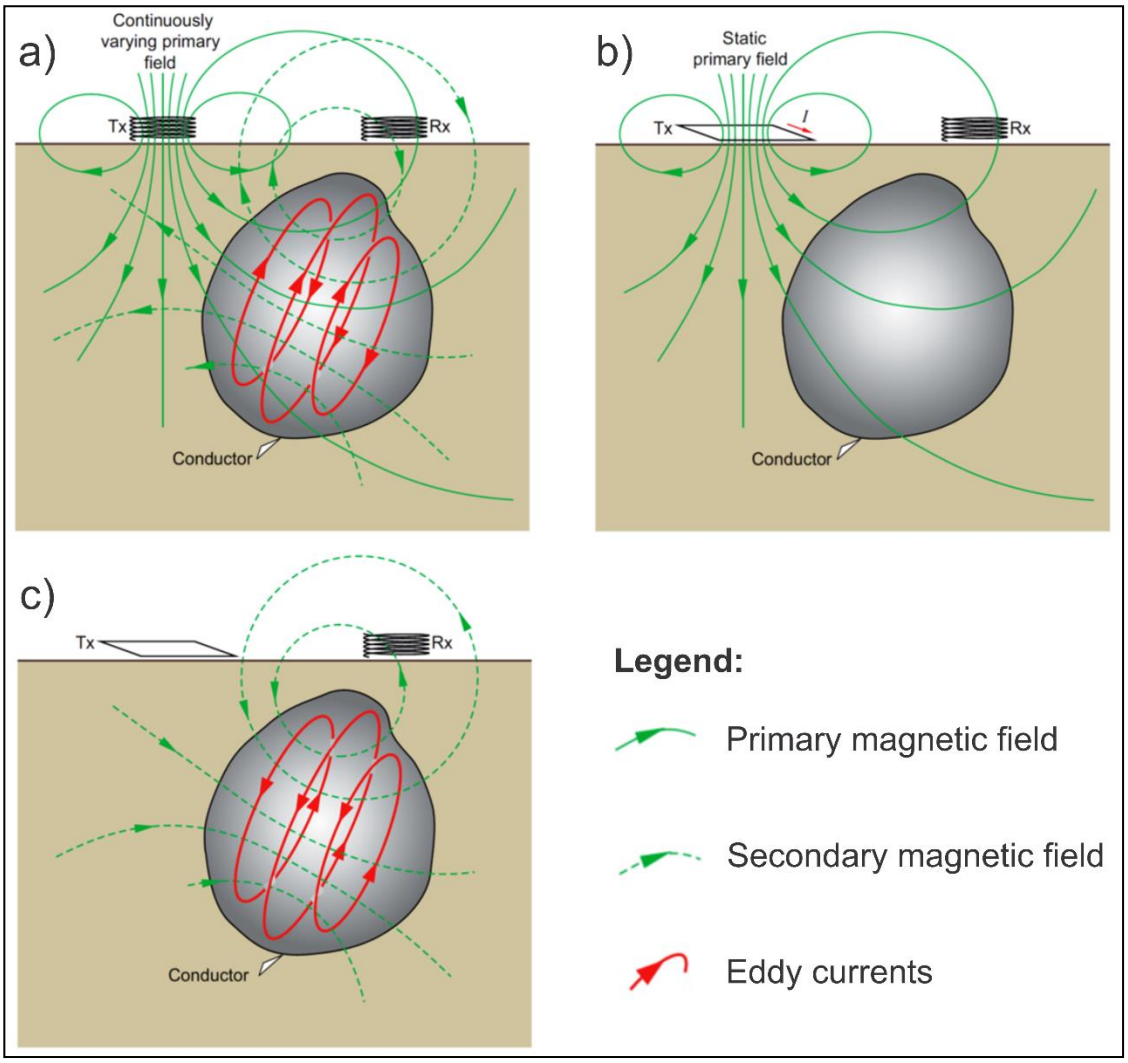

Figure 3. 1: Difusion process of electromagnetic fields for both FDEM and TEM methods. a) Electromagnetic difusion process and associated eddy currents (in red) for the FDEM case, note the superposition of the primary and induced fields b) Static primary magnetic field (before turning-off) for the TEM case. c) Difusion process of the secundary electromagnetic field (after the turning-off) and associated eddy currents for the TEM case (adapted from Dentith and Mudge, 2014).

This dB/dt decay is sampled through specified time intervals (or time gates), characteristic for each TEM system. The measurement is made over the decay of the e.m.f. induced in the receiver Rx (Figure 3. 2-b). The measured time interval is divided by early, intermediate and late times.

Considering a homogeneous semi-space model for the Earth and a conductive body within it, the early times interval is characterized by the first gates measurements in the receiver. The eddy currents will be initially confined on the surface of the conductor and the subsurface induced magnetic field preserves the geometric features and amplitude

of the primary field in the conductor. In another words, in the very beginning of the diffusion processes (at time $t = 0$), the magnetic field remains unchanged and there is no current flow inside the conductor (Nabighian and Macnae, 1991). During the intermediate times interval, the diffusion process within the conductor actually starts due the ohmic losses on its surface, which generates an internal decaying magnetic field and, finally, the induction of the eddy currents within it. In the late times interval, for the deep diffusion, the eddy currents are too far away from the transmitter loop, the area of the extension reaches the maximum values (limited by the characteristics of the TEM system) and the speed of the diffusion process is strongly decreased. In this part, the secondary magnetic field is mainly vertical and with constant amplitude over the whole extension of the field array, including a large area outside the transmitter loop. In this interval, the time variation of the secondary magnetic field amplitude (dB/dt) decreases quickly to zero, following an exponential decay in time $t^{-\gamma}$, where γ is the power-law constant (Dentith and Mudge, 2014).

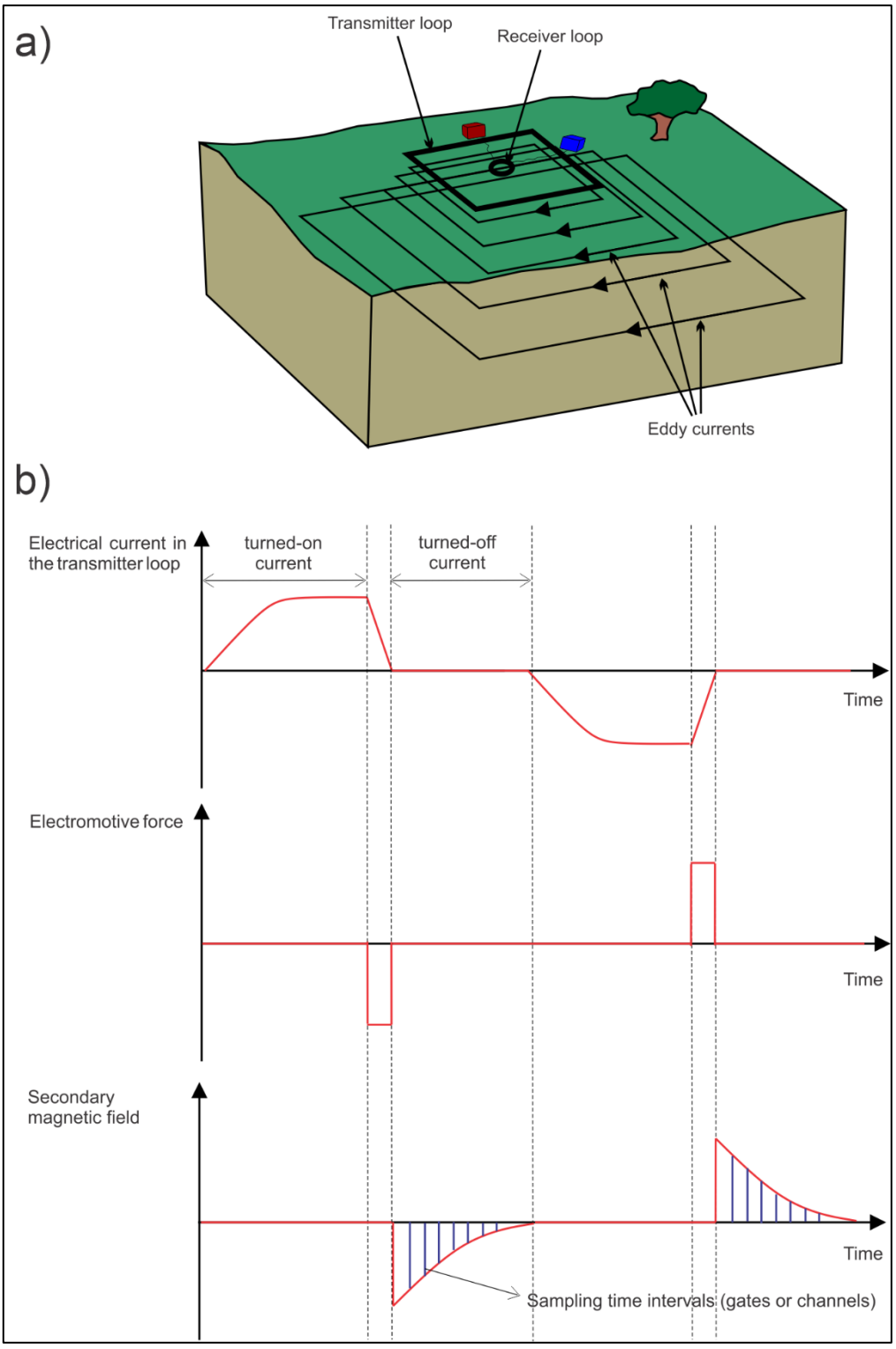

Figure 3. 2: a) TEM survey array example presenting the transmitter loop, the receiver coil and the diffusion process of the eddy currents (adapted from McNeill, 1994 and inspired by the Zoge website explanation about the TEM method: http://zonge.com/geophysical-methods/electrical-em/tem/). b) Schematic diagram representation of the TEM method, with a hypothetical current waveform in the transmitter loop, the e.m.f waveform in the receiver coild and the dB/dt measurements through the time gates – (adapted from McNeill, 1994).

Using the dB/dt transient decay measurements in the receiver coil and a homogeneous halfspace, the electrical resistivity can be calculated by (Kauffman and Keller, 1983 e McNeill, 1994):

$$\rho_a = k\left(\frac{M}{V(t)}\right)^{2/3} t^{-5/2} \tag{3.1.1}$$

where M is the transmitter loop magnetic dipole moment, $V(t)$ is the e.m.f. measured in the receiver coil and k is a constant related with the geometric parameters of the receiver coil:

$$k = -\frac{\mu}{\pi}\left(\frac{a_{ef} n}{20}\right)^{2/3} \tag{3.1.2}$$

where a_{ef} is the effective area and n is the number of turns of the receiver coil. $V(t)$ is given by:

$$V(t) = -a_{ef} n \frac{\partial B_z}{\partial t} \tag{3.1.3}$$

3.2. The IP Effect in TEM Data and the Negative Transient Values

The negative transient values associated with IP in TEM soundings are an intense subject of study in the applied geophysics field since the 1960`s (Walker, 2008). In fact, there are many works in the literature that point the relevance of the IP effect in TEM data associated with negatives decays or, at least, distortions in the TEM response, and how to identify and model it, as can be found in Lee (1975), Spies (1980), Lee (1981), Weidelt, (1982), Smith et al. (1988), Smith and West (1988a, 1988b, 1988c, 1988d, 1989), Flis et al. (1989), Smith and Klein, (1996); Walker, (2008), Flores and Peralta-Ortega, (2009), Kratzer and Macnae, (2012), Marchant et al., (2012), Yu et al. (2013), Marchant et al. (2012), Viezzoli et al. (2013), Marchant et al. (2014), Viezzoli et al. (2015), Kwan et al. (2015), Kang et al. (2015); Macnae, 2016; Kang and Oldeburg (2016,

2017); Kang (2017); Viezzoli et al. (2017); Kwan and Müller (2019), Viezzoli et al. (2019), Viezzoli and Manca (2020).

Lee (1975, 1981) and Spies (1980) already reported negative transients and pointed out that the IP effect was the possible cause. In particular, Spies (1980) suggested three possible physical mechanisms to explain the negative values:

1. **Magnetic effects:** caused by the magnetic permeability effect over a step function response for conductors with simple geometry (like spherical or cylindrical) within homogeneous background. Even though it was known in Spies (1980) publication period that these configurations would not cause negative values, this author pointed out that could happen for more complex geometries.
2. **Reflection phenomena:** the reflection of electromagnetic (EM) fields in layered geolectrical models with conductive bodies during field surveys suggested that negative values could be generated in the dataset. However, it can be experimentally demonstrated that this signals are automatically cancelled or, numerically, their amplitudes are too low to be detected. Furthermore, Spies (1980) conclude that it is not possible confirm if the negatives were caused or not by the reflection effect.
3. **Complex electrical conductivity effect:** the geolectrical models that used a complex electrical conductivity distribution take into account the displacement currents existence, which could cause IP effect induced by the transient decay in the underground. In this assumption, the electrical conductivity is dispersive in a polarizable subsurface, i.e., it has dependency with the frequency. The variation of the displacement currents induces the negative transients that could be associated with the IP effect in the underground.

In fact, Gubatyenko and Tikshayev (1979) demonstrated that the negative transients cannot be caused by the first two mechanisms, showing that at any non-frequency dependent subsurface, only positive transients can be generated. Weidelt (1980) also demonstrated that for a coincident-loop array and frequency-independent conductivity and magnetic permeability subsurface distribution, the TEM sounding can

generates signals with only one sign, which leads the IP effect to the best explanation of the sign reversal.

As discussed above, the negative transients are generated by the IP effect in the geological subsurface due the dependency of the electrical resistivity (or its inverse, the conductivity) with the frequency of the electromagnetic induction, which means that the resistivity is dispersive in the underground (Kratzer and Macnae, 2012). When this dependency occurs, the subsurface is defined as a polarizable environment and, in general, the electrical conductivity increases with the frequency (Smith *et al.*, 1988). This dependency with the frequency demands to consider a complex conductivity model. There are many complex conductivity models available for IP effect studies. However, the most accepted and used in literature is the Cole-Cole model (Cole and Cole, 1941), modified and introduced in the geophysical prospection literature by Pelton *et al.* (1978). In this model, the electrical resistivity is given by:

$$\tilde{\rho}(\omega) = \rho_0 \left[1 - m_0 \left(1 - \frac{1}{1 + \left(i\omega\tau_\rho \right)^C} \right) \right] \tag{3.2.1}$$

where $\rho_0 = \tilde{\rho}(\omega = 0)$ is the direct current resistivity, m_0 is the intrinsic chargeability as described in (Seigel 1959), τ_ρ is the relaxation time, C is the frequency dependency parameter, $\omega = 2\pi f$ is the angular frequency for the frequency *f*, and $i = \sqrt{-1}$ is the imaginary unit.

For the electrical conductivity, as presented by Smith *et al.* (1988), Marchandt *et al.* (2014) and Kang and Oldenburg (2016):

$$\tilde{\sigma}(s) = \sigma_\infty \left[1 - \frac{m_0}{1 + (1 - m_0)(s\tau_\sigma)^c} \right] \tag{3.2.2}$$

where $s = i\omega$ is the Laplace transform variable, τ_σ is the relaxation time associated with the conductivity and σ_∞ is the electrical conductivity in the limit of infinity frequency. In this research, the Cole-Cole model for the resistivity in equation (3.2.1) was used.

It is usual to consider positive the TEM signal in the off-times for non-polarizable subsurfaces. In the literature, there is an important discussion about the mechanism that

a polarizable geological environment generates negative transients. However, the usual mechanism is summarized by the follow steps (Flis et al., 1989; Walker, 2008):

- Considering an initial configuration in a polarizable substratum, with electrical charges in equilibrium, i.e., not polarized (Figure 3. 3-a). When the primary field is turned off in the transmitter loop and the underground diffusion starts, these charges are polarized in order to cancel the diffused EM field (Figure 3. 3-b);
- At some time, still in the presence of the eddy currents, the substratum reaches the maximum polarization (Figure 3. 3-c);
- During the dissipation of the eddy currents, the polarizable substratum will discharge and the charges will tend to come back to the equilibrium configuration. This discharge generates a transient EM field in the opposite direction in relation to the diffusion caused by the shutdown of the primary field in the transmitter loop (Figure 3. 3-d) and;
- This transient EM field caused by discharge is measured at the same time of the transient generated by shut down of the primary field, but with a negative sign due the opposite diffusion direction.

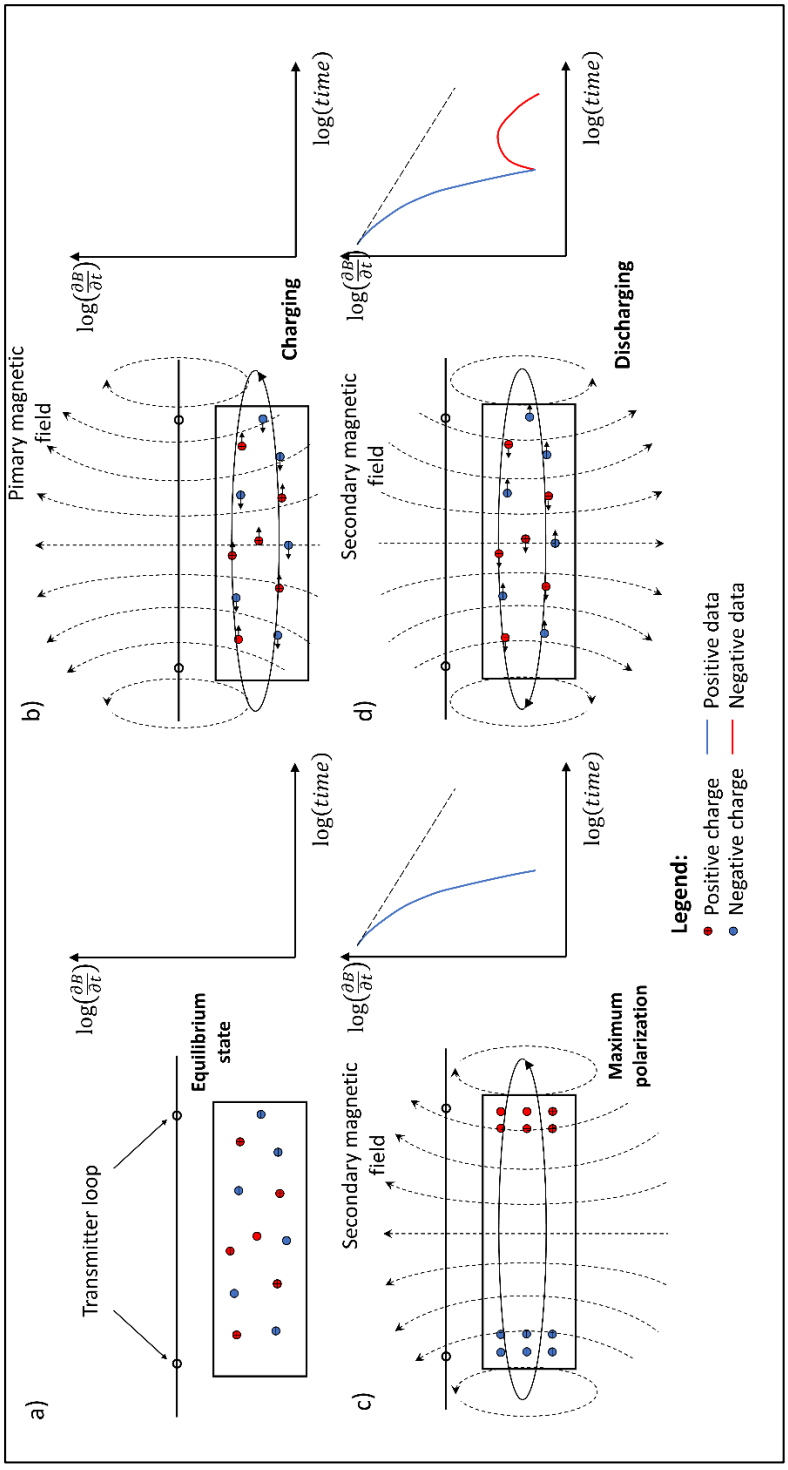

Figure 3. 3: Schematic representation of the IP effect process induced in the geological substratum in a TEM sounding. a) Polarizable substratum in equilibrium. b) Initial polarization process of the substratum due the turning on of the transmitter loop. c) Maximum polarization of the substratum, during the difusion of the secondary magnetic field. d) Discharging of the substratum and generation of the negative transient associated with the late-times IP effect (adapted from Flis et al. 1989).

According to Walker (2008), to detect the negatives transients due the IP effect, there are two criteria to be considered in a TEM survey:

1. The transient EM field generated by the current turning-off in the transmitter loop must be strong enough to polarize the geological substratum in the early times and;
2. The eddy currents generated by the turning-off in the transmitter loop must decay quickly enough, in order for the detectability of the transient generated by the IP effect. That way, the negative transients are usually better visualized in the intermediate and late times.

The negative transients generated by the IP effect are usually visualized or presented in the decay curve for $\partial B/\partial t$ (or for the e.m.f. $V(t)$). As commented above, in the early times (or the initial part of the decay curve), the data is mostly positive and there is the dominance of the transient generated when the transmitter is shuttled down (the situation in Figure 3. 3-b). In the intermediate and late times, the transient generated by the discharge process of the polarizable substratum could dominate the decay process and the negatives will be evidenced (the cases in Figure 3. 3-d and Figure 3. 4-a, for real data). These data are usually presented in a log-log plot and the initial negative data appears as an inverted spike in the decay curve, which continues to decay for later times (Figure 3. 4-a). When the plot is not in the log-log scale, the negatives data achieve a local minimum, which tends to come up to zero value again, due the energy dispersion process.

For TEM surveys with dense spatial coverage, like HTEM surveys or TEM profiles, the negative data can also be presented as a function of the sounding position. Figure 3. 4-b presents an example of how the negative transients appear in flight-line profile. The time gates are plotted all together (which can be the $\partial B/\partial t$, $V(t)$ or the B-field measurements) along the profile position and the negatives are presented as a local spatial minimum of the data in the vicinity of the polarizable area. Like the decay curve, they usually appear in the intermediate and late times. However, the IP effect can be strong enough to cause negative transients in earlier times as well.

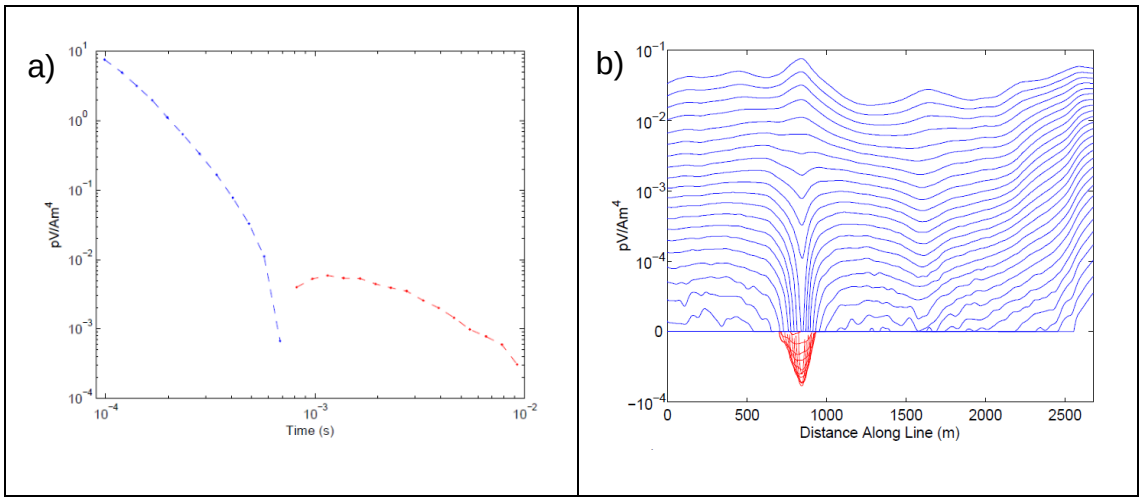

Figure 3. 4: Typical presentation of negative TEM data with IP effect. a) Negative transients in the $\partial B/\partial t$ decay curve (red curves) plotted together with the positive decay (blue curves). b) Negative transients (in red) along a flight-line profile showing the time gates, the blue curves are the positive data. These examples are from a VTEM (Versatile Time Domain Electromagnetic) system and were adapted from Marchant et al. (2013).

Walker (2008) identifies three types of negative transients caused by the IP effect. These types are presented in Figure 3. 5, which presents the second channel of a HTEM system in the column on the left, the time gates profiles in the central column and the transient decay curves in the column on the right. The first row (Figure 3. 5-a) presents the negative transients for IP effect of type 1, associated with compact, circular or oval polarizable bodies. The second row (Figure 3. 5-b) presents the type 2 IP effect response associated with linear structures, with the negative transients very concentrated, relatively to the non-polarizable or positive sign regions. Finally, the third row (Figure 3. 5-c) presents the type 3 IP effect response, which is characterized by a spatially diffuse response, with negative data present in all time gates. This last type of IP response is usually associated with permafrost regions.

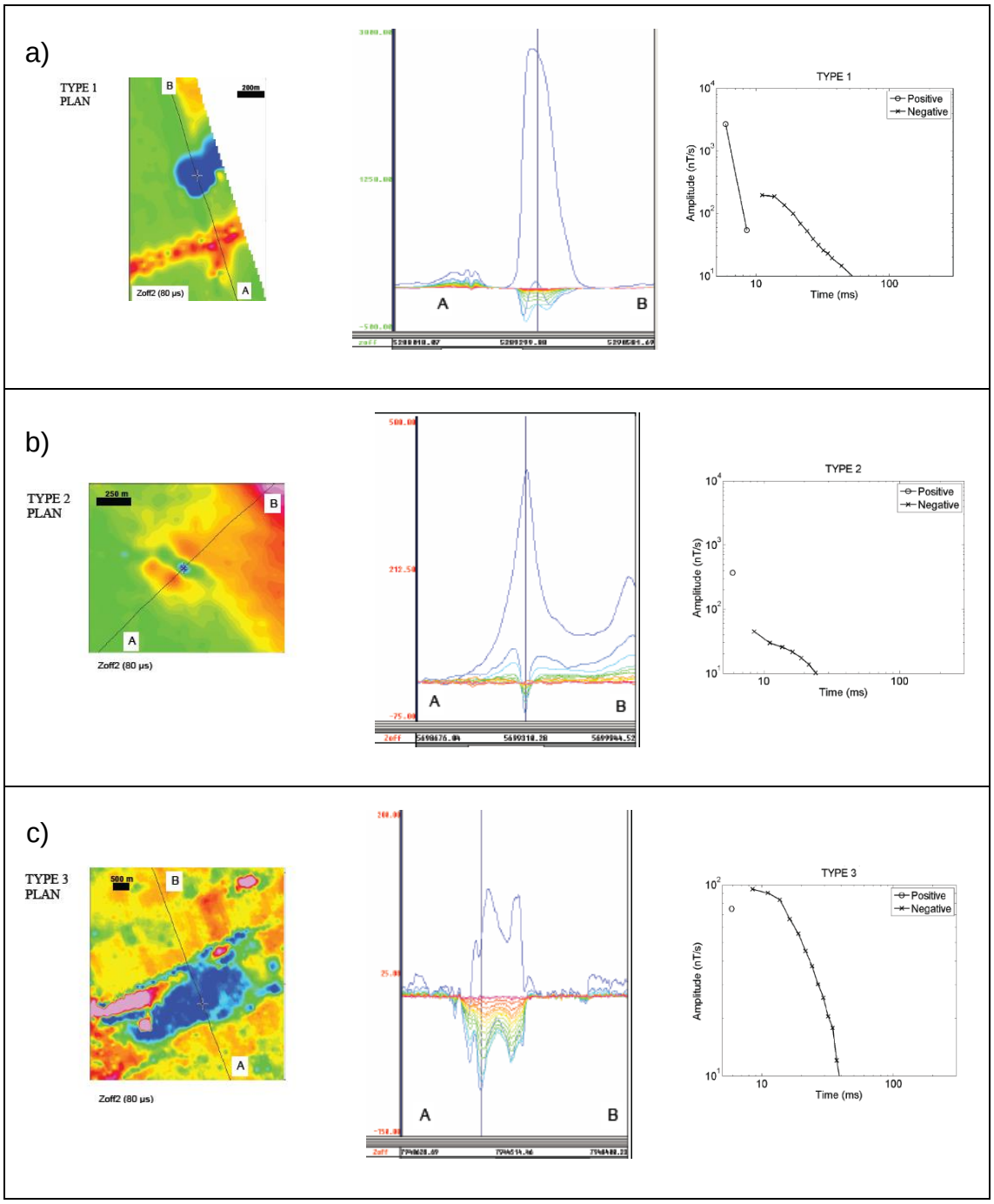

Figure 3. 5: Examples of negative transients generated by IP effect in HTEM data. The maps in the column on the left present the second channel of the HTEM system, the central column present the time gates profile (indicated in the maps) and the column on the right presents the transient decay curves for a) Type 1, b) Type 2 and c) Type 3 responses (Adapted from Walker, 2008).

The IP effect in TEM data still is a subject of intense debate in the EM methods field and, in the last decade, it gained even more interest due the technological advances, increase in the number of HTEM systems, mostly driven by the demands in mineral and groundwater exploration. For mineral exploration, especially for mineralization associated with disseminated sulfides, the study of the IP effect seems to be a promising

tool. However, even that the understanding about the mechanism of the IP effect had some advances in the last decades, as discussed in Smith et al. (1996) and Walker (2008), the conditions of the sulfation process are determinant to detect the IP effect. Macnae (2016) made a discussion about it, indicating that the fine-grained sulfides areas are more favorable to detect the negative data associated with IP, which indicates that the chargeability in the IP effect phenomena for TEM soundings is proportional to the size of the sulfide grains volume. In addition, lithologies enriched in clay material and rocks with high porosity filled typically by ice (permafrost areas) are also more likely to generate IP effect.

In the next chapter, the techniques used in the research to model HTEM data affected by IP effect are presented. As well as the magnetic data used in the Roça Grande area.

Chapter 4: Theoretical Outlook About the Forward and Inverse Problems: TEM and Magnetic Methods

In this research, the 1D forward problem for the TEM method in Aarhus Workbench (version 6.4.1.0) is based on the methodology of the AarhusInv (versions 8.X) code (Auken et al., 2015). This software provides the forward calculation for a varied geophysical methodologies, such as EM methods (frequency and time domains), IP (frequency and time domains) and electrorresistivity (ER) methods. The following subsections described the theoretical concepts implemented in the AarhusInv code for the forward calculations of the TEM method.

4.1. TEM Forward Problem

The geophysical forward problem is understood as the mathematical procedure to calculate theoretical values for a physical quantity (such as electrical potential, chargeability, magnetic field, gravitational potential, etc) related to a set of physical parameters in a geophysical model (such as electrical resistivity, magnetic susceptibility or mass density). In the TEM method, the physical quantities of interest are the magnetic field ($\boldsymbol{H}$) and the electrical field ($\boldsymbol{E}$) generated by the diffusion process. The physical parameters associated to geophysical model are the electrical resistivity (ρ) or conductivity (σ) and its geometrical features (depth values, lateral and vertical extensions– only vertical extension for the 1D case). The calculation of the forward response is the key procedure to solve the inverse problem in Geophysics. In this section, we present a general discussion of the forward calculation of the EM fields implemented in AarhusInv code (Auken et al., 2015), the software used in this research. For that, we followed the mathematical derivation presented in the Ward and Homman (1987) and Christensen (2013).

The Classical Electromagnetic Theory states the relation between the fields $\boldsymbol{H}$ and $\boldsymbol{E}$ through the Maxwell equations, which in the frequency domain is given by:

$$\boldsymbol{\nabla} \times \boldsymbol{E} = -i\omega \boldsymbol{B} \tag{4.1.1}$$

$$\boldsymbol{\nabla} \times \boldsymbol{H} = \boldsymbol{J}_f + i\omega \boldsymbol{D} \tag{4.1.2}$$

$$\boldsymbol{\nabla} \cdot \boldsymbol{D} = \rho_f \tag{4.1.3}$$

$$\boldsymbol{\nabla} \cdot \boldsymbol{B} = 0 \tag{4.1.4}$$

where $i = \sqrt{-1}$, $\omega = 2\pi f$ is the angular frequency related to the frequency f, ρ_f is the free charge density, $\boldsymbol{D}$ is the electrical displacement, $\boldsymbol{B}$ is the magnetic vector induction and $\boldsymbol{J}_f$ is the density of free electric currents, which are related to the fields $\boldsymbol{H}$ and $\boldsymbol{E}$ through the constituve relations:

$$\boldsymbol{D} = \varepsilon(\omega, \boldsymbol{E}, \boldsymbol{r}, t, T, P, \dots)\boldsymbol{E} \tag{4.1.5}$$

$$\boldsymbol{B} = \mu(\omega, \boldsymbol{H}, \boldsymbol{r}, t, T, P, \dots)\boldsymbol{H} \tag{4.1.6}$$

$$\boldsymbol{J}_f = \sigma(\omega, \boldsymbol{E}, \boldsymbol{r}, t, T, P, \dots)\boldsymbol{E} \tag{4.1.7}$$

where ε is the dielectric permittivity, μ is the magnetic permeability, σ is the electrical conductivity of the material in the substratum; $\boldsymbol{r}$ is the position in space, t is the time, T is the temperature and P is the pressure.

For most elementary applications of the electromagnetic methods in Geophysics, the substratum is considered a linear, isotropic, homogeneous and time, temperature and pressure independent media (Ward and Homman, 1987). Which is the case considered in this work. In this way,

$$\begin{gathered} \varepsilon = \varepsilon(\omega) \\ \mu = \mu_0, \\ \sigma = \sigma(\omega) \end{gathered} \tag{4.1.8}$$

where μ_0 is the magnetic permeability of the free space.

Using equations (4.1.5), (4.1.6) and (4.1.7) in equations (4.1.1) and (4.1.2), the Maxwell Equations are rewritten as:

$$\boldsymbol{\nabla} \times \boldsymbol{E} = -i\omega\mu\boldsymbol{H} \tag{4.1.9}$$

$$\boldsymbol{\nabla} \times \boldsymbol{H} = (\sigma + i\omega\varepsilon)\boldsymbol{E} \tag{4.1.10}$$

Relations (4.1.9) and (4.1.10) are the homogeneous Maxwell equations in frequency domains and only holds for source-free regions. In the TEM case, there are regions with electrical currents sources, which imply to rewrite them as the inhomogeneous Maxwell Equations:

$$\boldsymbol{\nabla} \times \boldsymbol{E} + \hat{z}\boldsymbol{H} = -\boldsymbol{J}_m^S \tag{4.1.11}$$

$$\boldsymbol{\nabla} \times \boldsymbol{H} - \hat{y}\boldsymbol{E} = \boldsymbol{J}_e^S \tag{4.1.12}$$

where $\boldsymbol{J_m^S}$ and $\boldsymbol{J_e^S}$ are the currents from magnetic and electrical sources, respectively, and:

$$\hat{z} \equiv i\omega\mu_0 \tag{4.1.13}$$

$$\hat{y} \equiv i\omega\varepsilon(\omega) + \sigma(\omega) \tag{4.1.14}$$

The electric and magnetic fields in equation (4.1.11)and (4.1.12) are described as a superposition of sources of electric and magnetic type in homogeneous regions, i.e.:

$$\boldsymbol{E} = \boldsymbol{E}_m + \boldsymbol{E}_e \tag{4.1.15}$$

$$\boldsymbol{H} = \boldsymbol{H}_m + \boldsymbol{H}_e \tag{4.1.16}$$

Using these equations into equations (4.1.13) and (4.1.14), the following relations are derived for the magnetic sources:

$$\boldsymbol{\nabla} \times \boldsymbol{E}_m + \hat{z}\boldsymbol{H}_m = -\boldsymbol{J}_m^S \tag{4.1.17}$$

$$\boldsymbol{\nabla} \times \boldsymbol{H}_m - \hat{y}\boldsymbol{E}_m = \boldsymbol{0} \tag{4.1.18}$$

And for the electric sources:

$$\boldsymbol{\nabla} \times \boldsymbol{E}_e + \hat{z}\boldsymbol{H}_e = 0 \tag{4.1.19}$$

$$\boldsymbol{\nabla} \times \boldsymbol{H}_e - \hat{y}\boldsymbol{E}_e = \boldsymbol{J}_e^S \tag{4.1.20}$$

Taking the divergent from equations (4.1.17), (4.1.18), (4.1.19) and (4.1.20), important relations are derived:

$$\boldsymbol{\nabla} \cdot \boldsymbol{H}_m = -\frac{\boldsymbol{\nabla} \cdot \boldsymbol{J}_m^S}{\hat{z}} \tag{4.1.21}$$

$$\boldsymbol{\nabla} \cdot \boldsymbol{E}_m = 0 \tag{4.1.22}$$

$$\boldsymbol{\nabla} \cdot \boldsymbol{E}_e = -\frac{\boldsymbol{\nabla} \cdot \boldsymbol{J}_e^S}{\hat{y}} \tag{4.1.23}$$

$$\boldsymbol{\nabla} \cdot \boldsymbol{H}_e = 0 \tag{4.1.24}$$

Equations (4.1.22) and (4.1.24) suggest that the $\boldsymbol{E}_m$ and $\boldsymbol{H}_e$ could be represented as curls of potential field vectors, i.e.:

$$\boldsymbol{E}_m \equiv -\boldsymbol{\nabla} \times \boldsymbol{F} \tag{4.1.25}$$

$$\boldsymbol{H}_e \equiv \boldsymbol{\nabla} \times \boldsymbol{A} \tag{4.1.26}$$

where $\boldsymbol{F}$ and $\boldsymbol{A}$ are the Schelkunoff Potentials. In Classical Electrodynamics, it is very common and a convenient way to wright the electric and magnetic fields as functions of potentials vector functions, seeking the best way to solve the differential equations related to the problem. In the next lines, it will be clear to understand.

Using equations (4.1.25) and (4.1.26) into (4.1.19) and (4.1.20), the equality between the curl operators yields:

$$\boldsymbol{H}_m = -\hat{y}\boldsymbol{F} - \boldsymbol{\nabla}U \tag{4.1.27}$$

$$\boldsymbol{E}_e = -\hat{z}\boldsymbol{A} - \boldsymbol{\nabla}V \tag{4.1.28}$$

where U and V are arbitrary scalar potentials which were introduced because the equality between two curl operator do not imply that the vector functions are equal.

Since U and V are arbitrary functions, it is convenient to use the Lorentz conditions for this problem, given by:

$$\boldsymbol{\nabla} \cdot \boldsymbol{F} = -\hat{z}U \tag{4.1.29}$$

$$\boldsymbol{\nabla} \cdot \boldsymbol{A} = -\hat{y}V \tag{4.1.30}$$

Using relations (4.1.25), (4.1.26), (4.1.27), (4.1.28), (4.1.29) and (4.1.30) in equations (4.1.17) and (4.1.20) yelds:

$$\boldsymbol{\nabla} \times (\boldsymbol{\nabla} \times \boldsymbol{F}) + \hat{y}\hat{z}\boldsymbol{F} + \hat{z}\boldsymbol{\nabla}U = \boldsymbol{J}_m^S \tag{4.1.31}$$

$$\boldsymbol{\nabla} \times (\boldsymbol{\nabla} \times \boldsymbol{A}) + \hat{y}\hat{z}\boldsymbol{A} + \hat{y}\boldsymbol{\nabla}V = \boldsymbol{J}_e^S \tag{4.1.32}$$

Using the Lorentz conditions in equations (30) and (31) and considering the vector identity $\boldsymbol{\nabla} \times (\boldsymbol{\nabla} \times \boldsymbol{F}) = \boldsymbol{\nabla}(\boldsymbol{\nabla} \cdot \boldsymbol{F}) - \boldsymbol{\nabla}^2\boldsymbol{F}$ for any vector function, yields:

$$\boldsymbol{\nabla}^2\boldsymbol{F} + k^2\boldsymbol{F} = -\boldsymbol{J}_m^S \tag{4.1.33}$$

$$\boldsymbol{\nabla}^2\boldsymbol{A} + k^2\boldsymbol{A} = -\boldsymbol{J}_e^S \tag{4.1.34}$$

where $k^2 = -\hat{y}\hat{z}$.

Equations (4.1.33) and (4.1.34) are the inhomogeneous Helmholtz equations for the $\boldsymbol{F}$ and $\boldsymbol{A}$ vector fields, for homogeneous regions with current sources $\boldsymbol{J}_m^S$ and $\boldsymbol{J}_e^S$. Here, it can be noticed the advantages to use the Schelkunoff potentials to solve the Maxwell differencial equations: the vector potentials have the same direction of the current sources, which makes the assumptions for the geometry of the problem much easier to deal with.

Many geophysical problems consider the vertical geometry for the the $\boldsymbol{F}$ and $\boldsymbol{A}$ vector fields, i.e. (in Cartesian coordinates):

$$\boldsymbol{F} = F(x, y, z)\hat{\boldsymbol{e}}_{\boldsymbol{z}} \tag{4.1.35}$$

$$\boldsymbol{A} = A(x, y, z)\hat{\boldsymbol{e}}_{\boldsymbol{z}} \tag{4.1.36}$$

where $\hat{\boldsymbol{e}}_{\boldsymbol{z}}$ is the unitary vector associated with the vertical direction.

Using relations (4.1.35) and (4.1.36) into equations (4.1.27) and (4.1.28), the electrical and magnetic fields spatial components can be rewritten as shown in Table 4. 1: Electrical and Magnetic field componentes por TE and TM modes.:

Table 4. 1: Electrical and Magnetic field componentes por TE and TM modes.

TM_z Mode	**TE_z Mode**
$E_x = \frac{1}{\hat{y}}\frac{\partial^2 A_z}{\partial x \partial z}$	$E_x = -\frac{\partial F_z}{\partial y}$
$E_y = \frac{1}{\hat{y}}\frac{\partial^2 A_z}{\partial y \partial x}$	$E_y = \frac{\partial F_z}{\partial x}$
$E_z = \frac{1}{\hat{y}}\left(\frac{\partial^2}{\partial z^2} + k^2\right)A_z$	$E_z = 0$
$H_x = \frac{\partial A_z}{\partial y}$	$H_x = \frac{1}{\hat{z}}\frac{\partial^2 F_z}{\partial x \partial z}$
$H_y = -\frac{\partial A_z}{\partial x}$	$H_y = \frac{1}{\hat{z}}\frac{\partial^2 F_z}{\partial y \partial x}$
$H_z = 0$	$H_z = \frac{1}{\hat{z}}\left(\frac{\partial^2}{\partial z^2} + k^2\right)F_z$

To not saturate the mathematical notation, the indexes "e" and "m" were dropped. The set of equations from the left side of the Table 4. 1concerns about the case which the vertical magnetic field is zero, i.e., the magnetic field is totally horizontal and is transversal to the $\hat{\boldsymbol{e}}_{\boldsymbol{z}}$ direction (Transversal Magnetic Mode – TM_z Mode). On the other hand, the right side presents the case which the vertical electrical field is zero, i.e., it is transversal to the $\hat{\boldsymbol{e}}_{\boldsymbol{z}}$ direction (Transversal Electric Mode – TE_z Mode). In other words, in TM_z mode, mathemathicaly only the $\boldsymbol{A}$ given in equation (35) matters to work with. While in the TE_z Mode, only $\boldsymbol{F}$ matters.

For the TEM modeling, the AarhusInv (versions 8.X) code (Auken et al., 2015) was used. This software uses the vertical magnetic dipole for a 1D layered model using

the TE_Z mode, i.e., using the parameterization only for the F potential for the numerical modeling, as discussed in the following subsections. To model the IP effect in the TEM data, the Cole-Cole model presented in equation (3.2.1) is considered for the calculation of the complex resistivity function.

4.1.1. A Finite Magnetic Source of Electrical Currents Over A Layered Earth Model

The TEM method works as a finite source of electrical currents over the earth. In this research, the earth is considered as a layered model (i.e. 1D earth).

The TEM method works in the TE_z mode, which implies to be in the case of a vertical magnetic dipole, i.e., using the transverse electric field. Physically, the TEM method does not have any type of current sources of electric nature, the transmitter loop just irradiates currents generated by magnetic sources, which demands $\boldsymbol{J_e^S = 0}$ and works with only the $\boldsymbol{F}$ Schelkunoff potential approach given in equation (34).

Because $\boldsymbol{F} = F(x, y, z)\hat{\boldsymbol{e}}_{\boldsymbol{z}}$, equation (32) can be rewritten as:

$$\boldsymbol{\nabla^2} F + k^2 F = 0 \tag{4.1.37}$$

It is convenient to convert equation (4.1.37) into a ordinary differential equation. One way to do this is to calculate the Fourier transform and make F as a function of the wave number in the x and y directions, k_x and k_y respectively. The Fourier transform definition used in this work is given by the following pair relation:

$$\tilde{F}(k_x, k_y, z) = \int_{-\infty}^{\infty}\int_{-\infty}^{\infty} F(x, y, z) e^{-i(k_x x + k_y y)} dx dy \tag{4.1.38}$$

$$F(x, y, z) = \frac{1}{4\pi^2}\int_{-\infty}^{\infty}\int_{-\infty}^{\infty} \tilde{F}(k_x, k_y, z) e^{i(k_x x + k_y y)} dk_x dk_y \tag{4.1.39}$$

Applying this definition of Fourier transform in the equation (4.1.37) yields:

$$\frac{d^2\tilde{F}}{dz^2} - u^2\tilde{F} = 0 \tag{4.1.40}$$

where:

$$u^2 = k_x^2 + k_y^2 - k^2 \tag{4.1.41}$$

The solution of differential equation (39) is:

$$\tilde{F}(k_x, k_y, z) = F^+(k_x, k_y)e^{-uz} + F^-(k_x, k_y)e^{uz} \tag{4.1.42}$$

Where F^+ and F^- represents the amplitudes of the downward and upward decaying solutions, respectively.

The F field from point EM source which generates a vertical magnetic dipole, just like the type used in the TEM, positioned at the air with a high $-h$ (considering $z > 0$ downwards and the origin at the surface) from the ground, is the described by (Ward):

$$F_S(z) = F_p(k_x, k_y)e^{-u_0|z+h|} \tag{4.1.43}$$

where F_p is the amplitude of the incident F potential field. From equation (4.1.44), the field at the surface, coming directly from the source, i.e., when $z = 0$, is given by:

$$F_S(z = 0) = F_p(k_x, k_y)e^{-u_0 h} \tag{4.1.44}$$

Considering a homogeneous and isotropic halfspace, the reflected potential field at the surface is given by (Christensen, 2013; Ward and Homman, 1987):

$$F_0^- = r\left[F_p(k_x, k_y)e^{-u_0 h}\right] \tag{4.1.45}$$

where, r is the reflection coefficient given by:

$$r = \frac{Y_0 - \hat{Y}_1}{Y_0 + \hat{Y}_1} \tag{4.1.46}$$

where Y_0 and $\hat{Y}_1$ are the intrinsic admittance of the free-space (air) the surface admittance at $z = 0$, respectively, given by:

$$Y_0 = \frac{u_0}{\hat{z}_0} \tag{4.1.48}$$

$$\hat{Y}_1 = \frac{H_y^{TE}}{E_x^{TE}}$$

Where H_y^{TE} and E_x^{TE} are the magnetic and electric fields in TE mode described in Table 4. 1, respectively.

The results above can be generalized for a N-layered Earth with each layer homogeneous, isotropic and nonmagnetic (Ward and Homman, 1987; Christensen, 2013). For the n-th layer, $n = 1,2, \dots, N$, the relations (4.1.13), (4.1.14) and (4.1.41) must be applied:

$$u_n^2 = k_x^2 + k_y^2 - k_n^2 \tag{4.1.49}$$

where $k_n^2 = -\hat{y}_n \hat{z}_n$, with:

$$\hat{z}_n \equiv i\omega\mu_0 \tag{4.1.50}$$

$$\hat{y}_n \equiv i\omega\varepsilon_n(\omega) + \sigma_n(\omega) \tag{4.1.51}$$

Also, a recursive relation between $\hat{Y}_n$ and Y_n can be derived from the bottom to the top , in which $\hat{Y}_n$ is given by:

$$Y_n = \frac{u_n}{\hat{z}_n} \tag{4.1.52}$$

where $\hat{z}_n$ and u_n are given by equations (4.1.50) and (4.1.51), respectively. $\hat{Y}_n$ is generalized by:

$$\hat{Y}_n = Y_n \frac{\hat{Y}_{n+1} + Y_n \tanh(u_n h_n)}{Y_n + \hat{Y}_{n+1} \tanh(u_n h_n)} \tag{4.1.53}$$

where $h_n$is the thicknes of the n-th layer. For the last layer, the following condition applies:

$$\hat{Y}_N = Y_N \tag{4.1.54}$$

From equations (4.1.53), (4.1.54) and (4.1.55), the reflection coefficient at the surface can still be recovered, which is also defined by the equation (4.146).

With this result, the reflected potential F_0^- is also defined in equation (4.1.45). Substituting it and equation(4.1.44) into equation (4.1.42), the $\tilde{F}$ field at the surface is given by:

$$\tilde{F}(k_x, k_y, z) = F_p(k_x, k_y)\left(e^{u_0(z+h)} + re^{u_0(z-h)}\right) \tag{4.1.55}$$

For the vertical magnetic dipole parameterization used in the TEM method, $F_p(k_x, k_y)$ is described by:

$$F_p(k_x, k_y) = \frac{\hat{z}_0 m}{2u_0} \tag{4.1.56}$$

Substituting equation (4.1.56) into (4.1.55) and taking its inverse Fourier transform in the x and y directions, yields to:

$$F(x, y, z) = \frac{\hat{z}_0 m}{8\pi^2}\int_{-\infty}^{\infty}\int_{-\infty}^{\infty}\frac{e^{i(k_x x + k_y y)}}{u_0}\left(e^{u_0(z+h)} + re^{u_0(z-h)}\right)dk_x dk_y \tag{4.1.57}$$

The integral in equation (4.1.57) can be converted in a Hankel transform, given by (Ward and Homman, 1987; Christensen, 2013):

$$F(\rho, z) = \frac{\hat{z}_0 m}{4\pi}\int_0^{\infty}\lambda\hat{F}(\lambda, z)J_0(\lambda\rho)\,d\lambda \tag{4.1.58}$$

where:

$$\hat{F}(\lambda, z) = \frac{1}{u_0}\left(e^{u_0(z+h)} + re^{u_0(z-h)}\right) \tag{4.1.59}$$

$$u_n = \sqrt{\lambda^2 - k_n^2}$$
$$\rho = \sqrt{x^2 + y^2} \tag{4.1.60}$$

From the relations (4.1.58), (4.1.59) and (4.1.60), the F field is defined for the TEM method at any point (x, y, z) for a vertical dipole source at the height h from the surface, considering a 1D layered earth, with homogeneous, isotropic and nonmagnetic

layers. In defining F, the magnetic $\boldsymbol{H}$ and electrical $\boldsymbol{E}$ fields components for the TE mode are also defined (Table 4. 1) at any point in the space, which are the fields of interest to be measured in a TEM survey. This is the formalism implemented in the AarhusInv code and the numerical implementation using it is discussed in the following subsection.

4.1.2. Numerical Implementation to Calculate *E* and *H* Fields in AarhusInv

The calculation of the Schelkunoff potential F field through the Hankel transform in the TEM case for the 1D Earth model is better evaluated numerically, due its definition as an improper integral and the difficulty of analytical mathematical solutions of its integrand. To solve it, the AarhusInv code uses linear digital filtering approach that follows the development in Johansen and Sørensen (1979) and Christensen (1990) – (Auken et al, 2015). In the description presented in this thesis, we followed the approach presented in Christensen (2013) and Johansen and Christensen (1978). It does not present the detailed filter coefficients values and approximations used in the numerical assumptions, as the AarhusInv code has been in development for more than 20 years and is not open source, as it is property of the Aarhus GeoSoftware. However, the numerical description given here provides a good idea about what are the main assumptions of the code.

The equation (4.1.58) can be rewritten in the general form:

$$g(r) = \int_0^\infty f(\lambda)\lambda J_\nu(\lambda r)\, d\lambda \tag{4.1.61}$$

where J_ν is the Bessel function defined for $\nu > -1$. Comparing to equation (4.1.58), $g(r) = F(\rho, z)$, $f(\lambda) = \frac{\hat{z}_0 m}{4\pi}\hat{F}(\lambda, z)$ e $\nu = 0$. However, to keep the same notation as presented in Christensen (2013) and Johansen and Christensen (1978), we define the following relations:

$$F(u) = e^{-u} f(e^{-u}) \tag{4.1.62}$$

$$H_\nu = e^{\nu} J_\nu(e^{\nu}) \tag{4.1.63}$$

$$G(v) = e^{v} g(e^{v}) \tag{4.1.64}$$

$$\lambda = e^{-u}; r = e^{v} \tag{4.1.65}$$

where $u, v \in \ ]-\infty, \infty[$. Note that the $F(.)$ function in relation (4.1.62) is not the same defined in (4.1.58), but, as previously mentioned, we use this notation to keep the pattern presented in Christensen (2013) and Johansen and Christensen (1978).

Using equations (4.1.62), (4.1.63) and (4.1.64) in (4.1.61), yields to:

$$G(v) = \int_{-\infty}^{\infty} F(u) H_v(v-u)\, du \tag{4.1.66}$$

As can be seen in equation (4.1.66), G(v) is defined as a convolution between F and H_v. For the numerical calculation, it is needed to define an approximation $G^*$for G, such that $|G^*(v) - G(v)| < \varepsilon$, for some maximum allowed error $\varepsilon > 0$. This construction depends on the discretization of F, named F^*, defined as:

$$F^*(u) = \sum_{n=-\infty}^{\infty} F(n\Delta) P\left(\frac{u}{\Delta} - n\right) \tag{4.1.67}$$

where Δ is the logarithmic sampling distance and $P(.)$ is an interpolation function that can be defined, for the convenience of further Fourier transform calculation, as:

$$P(u) = a \frac{\sin(\pi u)}{\sinh(\pi a u)} \tag{4.1.68}$$

where a is a smoothness factor that is usually chosen to be small (< 1 – Johansen and Christensen, 1978). Therefore, G^* is defined substituting equation (4.1.67) in (4.1.66):

$$G^*(v) = \sum_{n=-\infty}^{\infty} F(n\Delta) H_v^*(v - n\Delta) \tag{4.1.69}$$

where:

$$H_v^*(v) = \int_{-\infty}^{\infty} P\left(\frac{u}{\Delta}\right) H_v(v-u)\, du \tag{4.1.70}$$

Note that H_ν^* is defined as a convolution between P and H_ν, as presented in equation (4.1.70). In this way, we can calculate the Fourier transform, followed by the inverse Fourier transform of equation (4.1.70), which yields to:

$$H_\nu^*(v) = \int_{-\infty}^{\infty} \Delta\hat{P}(\Delta s)\hat{H}_\nu(s)\, e^{i2\pi\nu s} ds \tag{4.1.71}$$

where $\hat{H}_\nu$ and $\hat{P}$ is the Fourier transform of H_ν and P, respectively. $\hat{H}_\nu$ has an analytical expression given by:

$$\begin{aligned} \hat{H}_\nu(v) &= \int_{-\infty}^{\infty} J_\nu(t)\, t^{-2\pi i s} dt \\ &= 2^{-2\pi i s} \frac{\Gamma\left(\frac{\nu+1}{2} - i\pi s\right)}{\Gamma\left(\frac{\nu+1}{2} + i\pi s\right)} \end{aligned} \tag{4.1.72}$$

To recover a numerical expression for H_ν^* it is still needed to make a few assumptions for $\hat{P}$ and $\hat{H}_\nu$. Johansens and Christensen (1978) define $\hat{P}$ as a product of two Fermi distributions, which allow P to be a combination of sinusoidal and hyperbolic functions and define an attenuation factor such that:

$$\frac{\Delta}{a} = M\pi \tag{4.1.73}$$

where $M \in \mathbb{N}$. With a few considerations of the integration path in equation (4.1.71) (for detailed discussion, see page 880 of Johansen and Christensen, 1978) and considering the assumptions discussed above, H_ν^* can be written as:

$$H_\nu^*(v) = cH_\nu(v) + \mathrm{Im}\left\{A_\nu(v)e^{i\pi v/\Delta}\right\} \tag{4.1.74}$$

where c and A_ν are given by:

$$c = \left(1 - e^{-2M\pi^2/\Delta}\right) \sum_{l=0}^{\infty} \sum_{m=0}^{\infty} (-1)^{[l+m+(\nu+1)M(l-m)]} \tag{4.1.75}$$

$$A_v(v) = -M\pi \sum_{k=0}^{\infty} \widehat{H}_v \left(\frac{k+1/2}{iM\pi} + \frac{1}{2\Delta} \right) e^{v(k+1/2)/M} \tag{4.1.76}$$

To completely evaluate the numerical approximation of G^*in equation(4.1.69), it is needed to make some assumptions for the function F as well (Christensen, 2013). From equation (4.1.63), considering $f(\lambda)$ analytic at the origin ($\lambda = 0$), it can be expanded as a power series and considering the equidistant points $n\Delta$, yields:

$$f(\lambda) = \sum_{j=0}^{\infty} c_j \lambda^j \xrightarrow{\lambda = e^{-n\Delta}} F(n\Delta) = e^{-n\Delta} \sum_{j=0}^{\infty} c_j e^{-jn\Delta} \tag{4.1.77}$$

Usually, the first few coefficients are not usually complicated to be evaluated (Johansen and Christensen, 1978). However, as Christensen (2013) pointed out, it can become trickier for higher orders ($j \geq 2$). However, defining n in equation (4.1.69) large enough, these higher orders can be neglected (Christensen, 2013). Thus, denoting n^+ as this value for n, it is possible to divide G^* in equation (4.1.69) as the following combination at equidistant points $m\Delta$:

$$G^*(m\Delta) = S + S^+ \tag{4.1.78}$$

where:

$$S(m) = \sum_{n=-\infty}^{n^+-1} F(n\Delta) H_v^*\big((m-n)\Delta\big) \tag{4.1.79}$$

$$S^+(m) = \sum_{n=n^+}^{\infty} F(n\Delta) H_v^*\big((m-n)\Delta\big) \tag{4.1.80}$$

The limit n^+ is defined by (Christensen, 2013):

$$\left| \frac{c_2}{c_0} \right| e^{-2n^+\Delta} < \varepsilon_0 \tag{4.1.81}$$

where ε_0 is the numerical representation error in the computer.

Using the expansion for F presented in equation (4.1.77) in equation (4.1.80) and making the substitution $x = e^{-\Delta}$ yields:

$$S^{+}(m) = \sum_{n=n^{+}}^{\infty} \sum_{j=0}^{\infty} c_j \, x^{(j+1)n} H_v^*\big((m-n)\Delta\big)$$

Making the summation index change $l = n - n^{+}$ yields:

$$S^{+}(m) = \sum_{l=0}^{\infty} \sum_{j=0}^{\infty} c_j \, x^{(j+1)l} x^{(j+1)n^{+}} H_v^*\big((m-l-n^{+})\Delta\big) \tag{4.1.82}$$

Then, defining:

$$T_j(m) = \sum_{l=0}^{\infty} x^{jl} H_v^*\big((m-l)\Delta\big) \tag{4.1.83}$$

and substituting it in equation (4.1.82) yields:

$$S^{+}(m) = \sum_{j=0}^{\infty} c_j \, x^{(j+1)n^{+}} T_{j+1}(m-n^{+}) \tag{4.1.84}$$

T_j in equation (4.1.83) can be written as (pages 894 and 895 in Johansen and Christensen, 1978)):

$$T_j(m) = T_j^{(1)} + T_j^{(2)} \tag{4.1.84}$$

where:

$$T_j^{(1)}(m) = \sum_{k=0}^{\infty} h_k \frac{x^{-m(k+1/2)/M}}{1 - x^{[\nu+1+j+2k]}} \tag{4.1.85}$$

$$T_j^{(2)}(m) = \sum_{k=0}^{\infty} a_k \frac{x^{-m(k+1/2)/M}}{1 - x^{[j+(k+1/2)/M]}} \tag{4.1.86}$$

which indicates that S^+ can be calculated for all m values with an accuracy only limited by the computer error ε_0 (Johansen and Christensen, 1978).

As discussed in Johansen and Christensen (1978) and Christensen (2013), the discretization discussed above can be applied for the case of the vertical magnetic dipole (TEM case). As the response of the homogeneous halfspace can be derived analytically (page 231 from Ward and Homann, 1987), the $f(\lambda)$ function can be chosen to describe the difference between the layered earth and homogeneous halfspace responses (Johansen and Christensen, 1978). In this case, if $d_1 > 0$ is the thickness of the first layer, $f(\lambda) \propto e^{-2d_1\lambda}$, for $\lambda \to \infty$, i.e., $n \to -\infty$, where $\lambda = e^{-n\Delta}$, then:

$$F(n\Delta) \propto e^{-n\Delta} e^{-2d_1 e^{-n\Delta}} \tag{4.1.87}$$

Then, as can be noted in the relation (4.1.87), for $n < 0$, the contribution of the positive values of n is much greater than the negatives. Furthermore, the sum S defined in equation (4.1.79) does not contribute significantly to G^*, as written in equation (4.1.78). For the limit $n \to \infty$, F goes to zero, as can be noted in equation (4.1.77).

In this way, for higher values of $|n|$, G^* can be numerically evaluated, avoiding its divergences for $n < 0$ and for the limit $n \to \infty$. As $|G^*(v) - G(v)| < \varepsilon$, for $\varepsilon > 0$, $g(r)$ can be numerically estimated, defining the solution of the Hankel integral in equation (4.1.62). Comparing to equation (4.1.59), vertical component of the Schelkunoff $\boldsymbol{F} = F_z \hat{\boldsymbol{e}}_{\boldsymbol{z}}$ can be estimated and, consequently, the components of the $\boldsymbol{E}$ and $\boldsymbol{H}$ fields can be calculated for the TE_z mode (Table 4. 1).

The mathematical steps briefly discussed in this subsection describes the general form of the equations implemented in the AarhusInv code (Christensen, 2013). In this way, it can not be considered as the final form of the Hankel filter coefficients H_v^*, as this information is not public domain. However, the discussion made in this subsection intends to provide a general view about the methodology used in this thesis and provides enough information for future works related to AIP.

4.2. Inverse TEM Problem

In Geophysics, the inverse problem is the procedure to determine the geophysical model (geolectrical model in the case of this research) that best fit the physical quantities from a field or numerical dataset. Data misfit analysis techniques are applied in order to minimize the deviation between the data and the forward response calculated in the sense presented in the previous section.

The inverse problem in Geophysics is summarized by these three steps:

1. Formulation of the forward problem and definition of the most adequate geophysical model to the geological environment;
2. Calculation of the physical responses related to the defined geophysical model through the forward formulation and;
3. Analysis of the results, minimizing the objective function, i.e., a function that represents the deviation between the calculated response and field or synthetic data. This function may contain constrains that might be related to previous geological or a-priori physical information related to the investigated subsurface.

The inversion algorithm used in this research is implemented in the Aarhus Workbench and it is based on the AarhusInv code, which follows the approach presented in Auken et al. (2015), based in the inversion through processing modules (Figure 3. 6). The minimization process is based on the Gauss-Newton scheme, with the Marquadt modification, in order to minimize the objective function using the L_2 norm. The whole dataset is inverted simultaneously, through the minimization of a common objective function, given by:

$$Q = \left(\frac{[\delta \boldsymbol{d}^T \boldsymbol{C'^{-1}} \delta \boldsymbol{d}]}{N_d + N_m + N_R} \right)^{1/2} \tag{4.2.1}$$

where N_d is the number of observed data points, N_m is the number of model parameters, N_R is the quantity of spatial constraints, $\delta \boldsymbol{d} = \boldsymbol{d} - \boldsymbol{d}_{obs}$ is the difference between the forward response $\boldsymbol{d}$ and observed data $\boldsymbol{d}_{obs}$ and $\boldsymbol{C'}$ is the covariance matrix of the observed error.

In this way, the algorithm performs a reweighting process between the model constraints, the physics of the EM forward problem and the observed data. The reweighting step is fundamental to lateral and spatial constraints definition between the 1D soundings, which allows the transmission of geoloectrical/geological information between each point of investigation. In the HTEM case, these features are very useful and necessary for the interpretation between the flight lines. In the AarhusInv software, this link between the model parameters is made based on the variance of the difference between two parameters of the same type. This variance is free to be specified by the user, which allows that the parameters could be linked through 2D or 3D constraints, which results in quasi-2D and quasi-3D models. The 2D process is used for the LCI (Lateral Constrained Inversion - Auken et al., 2004, 2005) and the 3D is used for the SCI (Spatial Constrained Inversion – Viezzoli et al., 2008).

4.2.1. Detph of Investigation (DOI) Calculation

Non-Multiparametric Inversions

For non-multiparametric inversions, AarhusInv also allows the sensitivity analysis for the parameters of the resulting models (Figure 3.6), through the computation of its Jacobian matrix. With the results from the sensitivity analysis, the Depth of Investigation (DOI) is estimated. This approach is described in (Christiansen and Auken, 2012), but is briefly described here as well. To conduct the sensitivity calculations, the software initially inverts the data with a smooth (many layers) or few-layered 1D model, in which it is included the data uncertainty, estimated from the stacking process, and the regularization method for the chosen inversion algorithm. Then, in the case of the few-layered model, the resulting model is subdiscretized to increase the precision of the DOI estimation. For the smooth model, this step can be skipped due to the enough information for a good DOI estimation (Christiansen and Auken, 2012).

Then the Jacobian matrix for N to a 1D model with M layers is calculated by:

$$G_{ij} = \frac{\partial \log (d_i)}{\partial \log (m_j)} \tag{4.2.2}$$

where d_i is the i-th component of the data vector $\boldsymbol{d} = (d_1, d_2, \dots, d_N)$ and m_j is j-th component of the model vector in the logarithmic space $\boldsymbol{m} = (\log(\rho_1), \log(\rho_2), \dots, \log(\rho_M), \log(t_1), \log(t_2), \dots, \log(t_{M-1}))$. $\rho_{1\dots M}$ and $t_{1\dots M}$ are the resistivity and thicknesses of the 1D model, respectively.

Based on the calculation of G_{ij} in equation (4.2.2), the normalized sensitivity s_j^* for the j-th parameter in $\boldsymbol{m}$ is calculated by:

$$s_j^* = \frac{\sum_{i=1}^{N} \frac{G_{ij}}{\Delta d_i}}{t_j} \tag{4.2.3}$$

where Δd_i is the standard deviation for the i-th observation and t_j is the thickness for the j-th layer. Note that t_j is not defined for the last layer.

Then, a cumulated sensitivity S_j is defined for the j-th layer, starting from the bottom, i.e., the $(M-1)$-th layer, as:

$$S_j = \sum_{i=M-1}^{j} s_i^* \tag{4.2.4}$$

The DOI is then defined as the depth of the layer according to a chosen threshold value for S_j, that is defined purely empirically. In this thesis, this threshold was kept to the default one in AarhusInv code in the Aarhus Workbench, at the value of 0.75 for the standard DOI calculations (see the documentation at http://www.ags-cloud.dk/Wiki/WH_VisualizeDataOrInversion).

In this way, for the non-multiparametric inversion, the DOI is based on the actual model output from the inversion and recalculated sensitivity matrix, which does not consider the spatial constraints for the recalculation (Christiansen and Auken, 2012). The recovered information is mostly data-driven or it is strongly dependent from the input starting model or the regularization parameters.

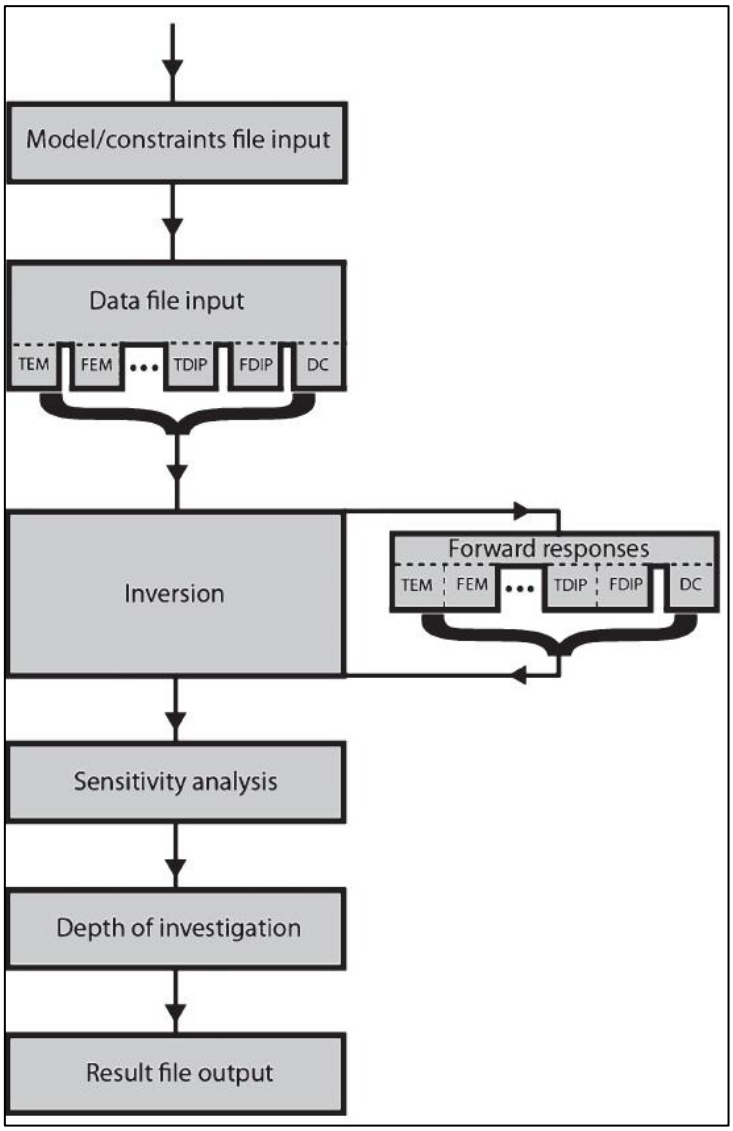

Figure 3. 6: Inverse process scheme in AarhusInv (from Auken et al., 2015). The software accepts data for the Transient Electromagnetic (TEM), Frequency Electromagnetic (FEM), Time-Domain Induced Polarization (TDIP), Frequency-Domain Induced Polarization (FDIP) and DC-Resistivity methods.

Multiparametric Inversions

For the multiparametric inversions, the case for the AIP, the AarhusInv calculates the DOI differently from the method presented in Christiansen and Auken (2012). It follows the method presented in Fiandaca et al. (2015), which considers the cross-correlation. The method is introduced as an evolution of the method from Christiansen and Auken (2012), which does not consider the correlation between the multiparemeters in the DOI calculation (in the AIP case, the Cole-Cole model parameters).

Let be the dataset with N_{data} points to be inverted with a multiparametric model with N_{par} parameters. The calculation starts dividing the model as a 2D section,

containing cells discretized in N_{layers} layers and $N_{columns}$ columns. Then, a sum of the Jacobian elements is conducted downwards from the n-th layer to the bottom. For each layer n and column l, the cumulated ($N_{data} \times N_{par}$) quasi-Jacobian matrix is defined as:

$$G_{cum}^{(n,l)}{}_{ik} = \sum_{j=j_{k,l^{(n)}}}^{j_{k,l^{(last)}}} G_{ij} \tag{4.2.5}$$

$\forall i \in [1, N_{data}]$, $\forall k \in [1, N_{par}]$, $\forall n \in [1, N_{layers}]$ and $\forall l \in [1, N_{columns}]$, where $j_{k,l^{(n)}}$ and $j_{k,l^{(last)}}$ are the indexes of the n-th and the last layer, for the l-th column and k-th parameter, respectively.

Then, a cumulated approximate analysis (CAA) with dimension ($N_{par} \times N_{par}$) for each column l and layer n is defined by:

$$\boldsymbol{CAA}^{n,l} = \left[\left(\boldsymbol{G}_{cum}^{(n,l)}\right)^{-1} \boldsymbol{C}_d^{-1} \left(\boldsymbol{G}_{cum}^{(n,l)}\right)\right]^{-1} \tag{4.2.6}$$

where $\boldsymbol{C}_d$ is the data covariance matrix. From equation (4.2.6), it is noted that the CAA analysis returns a cumulative information from all the layers below the n-th layer for each column l. Also, it neglects the correlation between model parameters from different the columns, but considers it for the parameters related to the same l-th column.

Based on the construction of the CAA analysis, the DOI is calculated for a given threshold for standard deviation factor ($STDF^{n,l}$), wich is defined by each para meter k as (as the inversions are conducted in the logarithmic space):

$$STDF^{(n,l)}(k) = e^{\sqrt{CAA^{n,l}(k,k)}} \tag{4.2.7}$$

In this way, the DOI can be calculated for each parameter k and each column l according to a threshold value. It will be considered the depth of top of the shallower layer with the $STDF$ smaller than this value. In this thesis, it was used the standard value in the AarhusInv code within the Aarhus Workbench, which is 5.0.

4.3. Modifications of the LCI Technique to Recover the IP Effect Parameters for AEM Data – The Robust Inversion Scheme

To invert the negative transients associated with the IP effect in HTEM data, in this research, we used the methodology presented in Lin et al. (2019), which is fully presented in Appendix 1. The method consists of a robust inversion scheme to invert TEM data using the LCI technique in the sense of Auken et al. (2004), with the Maximum Phase Angle (MPA) reparameterization (Fiandaca et al., 2018). The MPA reparameterization is described in the next section. The inverse problem for the IP effect in AEM data (in particular, for HTEM surveys) is significantly ill-posed, which could be very challenging to recovery the parameter vector $\boldsymbol{m} = (\rho_0, m_0, \tau_\rho, C)$ from equation (3.2.1). In this way, the modification presented in Lin et al. (2019) seeks to increase the stability of the LCI technique to recover a more reliable parameter vector for the IP effect in comparison with the geology of a priori information of the study area.

The robust inversion scheme uses a modification of the objective function presented in equation (4.2.1):

$$Q = \left(\frac{\delta \boldsymbol{d}^T \boldsymbol{C}_{obs}^{-1} \delta \boldsymbol{d} + \delta \boldsymbol{r}^T \boldsymbol{C}_R^{-1} \delta \boldsymbol{r}}{N_d + N_R} \right)^{1/2} \tag{4.3.1}$$

where $\boldsymbol{C}_{obs}$ and $\boldsymbol{C}_R$ are the data and constraints covariance matrices, respectively, $\delta \boldsymbol{r} = -\boldsymbol{R}\boldsymbol{m}$ is the roughness of the model parameter vector $\boldsymbol{m}$, calculated through the roughness matrix $\boldsymbol{R}$ and N_d and N_R are the number of observed data points and roughness constraints, respectively.

In this research, the modifications to the LCI approach can be summarized by these five steps:

1. Model re-parameterization using the Cole-Cole MPA approach, introduced by Fiandaca et al. (2018), which is discussed in detail in the Appendix 1;
2. Definition of a robust initial resistivity model based on a priori borehole data, through inversions of positive-only data using very tight spatial constraints. The

initial models for the other parameters were defined manually, based on values to similar lithologies in the literature. In this work, the initial values for ϕ_{max} varied between 200-300 mrad (the expected phase range of disseminated sulfides based on similar lithologies presented in Smith et al., (1983) and τ_ϕ and C started from 0.001 s and 0.5, respectively;

3. Locking of τ_ϕ and C for the first few (here five) iterations, to build structure in the resistivity and chargeability domains first. τ_ϕ is the relaxation time constant used in the MPA reparameterization, which is explained in the next subsection;
4. Increasing the data standard deviation around the sign change in the dB/dt decay curve. In this work, we used 2.5% for this increment for one time gate before and one after the first negative transient, depending on the flight line and;
5. Modification of the damping scheme allowing for individual damping of the different parameters, which improves the balance of the multi-parameter model space.

4.3.1. Reparameterization of the Classical Cole-Cole Resistivity Model: Maximum Phase Angle (MPA)

The reparameterization of the classical Cole-Cole resistivity model (RCC – Resistivity Cole-Cole) presented in equation (3.2.1) - which spectrum is presented in Figure 3. 7-a - used in this research is based in the MPA technique, introduced by Fiandaca et al. (2018). This reparameterization is based on the use of the model parameter vector $\boldsymbol{m}_{MPA} = (\rho_0, \varphi_{max}, \tau_\varphi, C)$, instead of $\boldsymbol{m}_{RCC} = (\rho_0, m_0, \tau_\rho, C)$ used in equation (3.2.1), where, ϕ_{max} is the maximum phase angle of the RCC complex conductivity (i.e. the minimum of the complex resistivity phase) and τ_ϕ is the relaxation time associated with the frequency ($f = 1/2\pi\tau_\phi$) where $\phi_{max}$is reached (Figure 3. 7-b). According to Fiandaca et al. (2018), $\tilde{\rho}(\omega)$ and $\varphi(\omega)$ reach their maximum values at different frequencies, which are related to the inverse of (τ_φ, τ_ρ) and are related by:

$$\tau_\varphi = \tau_\rho (1 - m_0)^{1/2C} \tag{4.3.1}$$

This relation explicit the dependency of the maximum points of $\tilde{\rho}(\omega)$ and $\varphi(\omega)$ with m_0 and C, which indicates the strong correlation between these parameters. The MPA reparameterization intends to uncouple these parameters, decrease this correlation and improve the reliability of the resistivity and chargeability models.

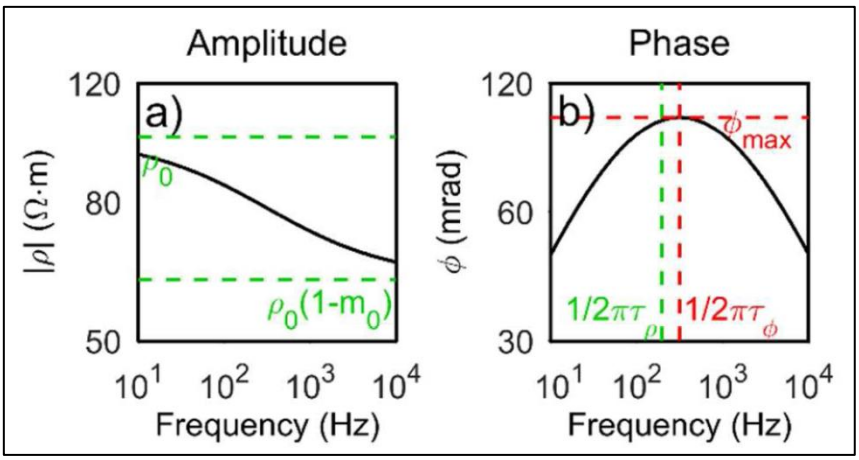

Figure 3. 7: Absolut value for the complex resistivity $\tilde{\rho}$ as function of the frequency. B) Phase of $\tilde{\rho}$ (φ) for the Cole-Cole model. The reference model is $\boldsymbol{m} = (\rho_0 = 100\ ohm.m, \varphi_{max} = 100\ mrad, \tau_\varphi = 5 \times 10^{-4}\ s, C = 0.5)$ – adapted from Lin *et al.* (2019).

In fact, Fiandaca et al. (2018) demonstrated that this reparameterization works in this direction for galvanic IP data and Lin et al. (2019) showed that this also works for AEM data (Section 6.1 and Appendix 1 for further details). Figure 3. 8 presents the comparison between the variation for the pairs of parameters m_0/C and φ_{max}/C for the RCC and MPA approaches, respectively. For this figure, the reference model used is $\boldsymbol{m}_{MPA} = (\rho_0 = 100\ ohm.m, \varphi_{max} = 100\ mrad, \tau_\varphi = 5 \times 10^{-4}\ s, C = 0.5)$. Figure 3. 8-a and Figure 3. 8-c present the curves for $\varphi(\omega)$ for the RCC and MPA parameterizations, respectively (the reference model is presented by the dark grey curve). In Figure 3. 8-a, the orange and green curves present the phase curve with an attenuation and increment factor of 20% applied for m_0 and C, respectively. It is noted that this attenuation in the RCC parameters presents a similar behavior in the neighborhood of the maximum value of the phase and the negatives transients are not distinguishable (bellow the noise level – Figure 3. 8-b), which means that it does not allow to differ which parameter m_0/C presents more influence in the resultating model, a consequence of their strong correlation. On the other hand, for the MPA reparameterization (Figure 3. 8-c), the attenuation and increment factors for φ_{max} and C present a clear difference between the curves in the maxmum phase neighborhood. The negatives transients differences (Figure

3. 8-d) are also better distinguishable between $\varphi_{max} - C$ parameters, when compared to the RCC results, which indicates the decrease in their correlation.

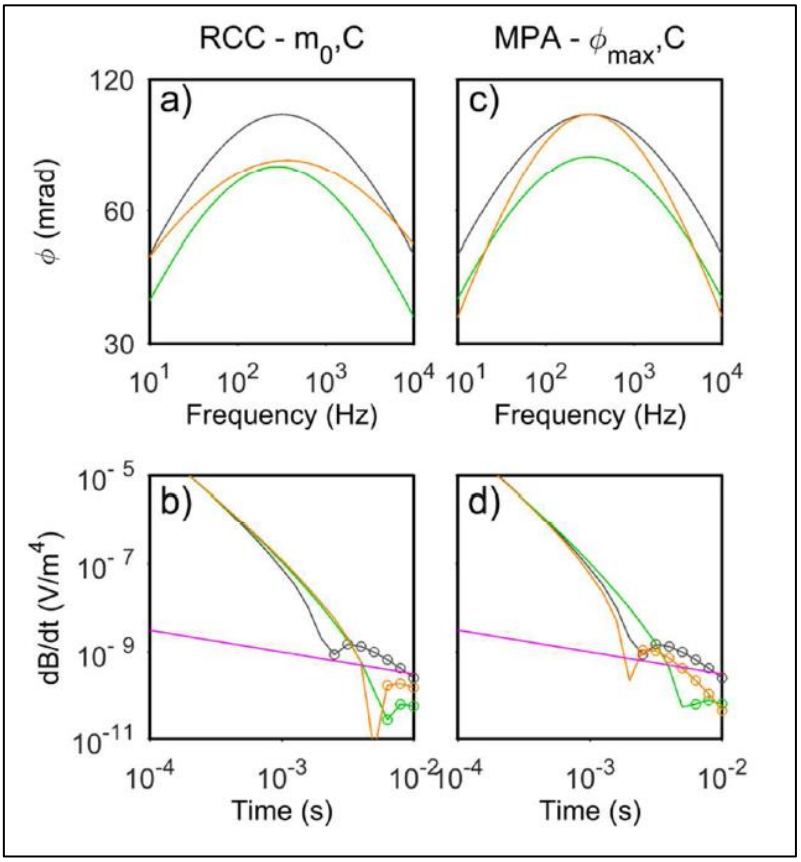

Figure 3. 8: Phase comparison (a) and (c) and transient responses (b) and (d) for the RCC and MPA parameterizations. The curves indicate the reponse for the reference model $m_{MPA} = (\rho_0 = 100\ ohm.m, \varphi_{max} = 100\ mrad, \tau_\varphi = 5 \times 10^{-4}\ s, C = 0.5)$. In (a) and (b) the green and orange curves represent the models with an attenuation and increase factors of 20% for m_0 and C, respectively. In (c) and (d), the curves represent the transient responses for these models, according to their colors. The magenta lines in (b) and (d) represent the noise level and the negative data is represented by the white circles – adapted from Lin et al. (2019).

4.4. Magnetic Forward and Inverse Problems

In this research, we also integrated airborne magnetic survey data (as discussed in Section 3). We do not discuss the magnetic method itself in this text, as there is very good literature about this, which we refer to Telford (1990), Blakely (1996) and Dentith and Mudge (2014). However, it is worthy to provide a brief explanation about the forward and inverse problems for the magnetic data inversion used in this thesis, namely the Magnetization Vector Inversion (MVI) method, as its interest has been growing in the

last 12 years (Lelièvre and Oldenburg, 2009; Ellis et al., 2012; Zhu et al., 2015; Liu et al., 2015; Liu et al., 2017; Fournier et al., 2020).

In the Quadrilátero Ferrífero area, remanent magnetization is an important issue to be considered in magnetic surveys (Oliveira, 2014; Couto et al., 2017a). Seeking to attenuate this issue, in this work, the magnetic data was modeled using the MVI algorithm available in the VOXI module in the software Seequent Oasis Montaj (version 9.9.1). This algorithm is introduced in Ellis et al. (2012). In this section, we provide a brief explanation about it, as it is not extensively developed in the original paper, which is an extended abstract. Also, we discuss a modification in the default approach to conduct the inversion process in the Oasis Montaj.

4.4.1. Magnetization Vector Inversion – Forward Problem

Considering a magnetic body with volume V and total magnetization $\boldsymbol{M}$, described in a reference frame (x, y, z). Discretizing the volume V into v_k ($k = 1,2, \dots, N$) volumes, each one with $\boldsymbol{m}_k$ constant magnetization (Figure 4. 1), from magnetostatics, the magnetic scalar potential $A^{(k)}(\boldsymbol{r_j})$ at a point P_j ($j = 1,2, \dots, M$)is given by:

$$A^{(k)}(\boldsymbol{r_j}) = -\int_{v_k} \boldsymbol{m}_k \cdot \boldsymbol{\nabla}_{QP_j}\left(\frac{1}{\|\boldsymbol{r} - \boldsymbol{r}_j\|}\right) dr^3 \qquad (4.4.1)$$

Where $\boldsymbol{r}$ and $\boldsymbol{r}_j$ are defined in Figure 4. 1 and the index QP_j in $\boldsymbol{\nabla}_{\mathrm{QP_j}}$ indicates that the gradient is calculate from the point Q to P_j, where Q is some point inside V.

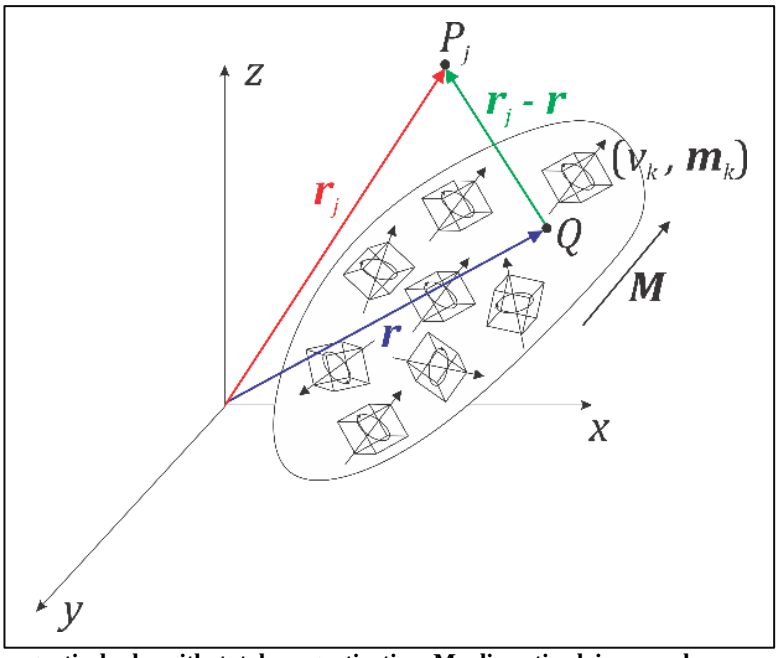

Figure 4. 1: A magnetic body with total magnetization M, discretized in v_k volumes, each with constant magnetization m_k.

The magnetic flux density $\boldsymbol{B}^{(k)}(\boldsymbol{r_j})$ due $\boldsymbol{m}_k$ is defined by:

$$\boldsymbol{B}^{(k)}(\boldsymbol{r_j}) = -\boldsymbol{\nabla}_{P_j} A^{(k)}(\boldsymbol{r_j}) = \boldsymbol{\nabla}_{P_j} \int_{v_k} \boldsymbol{m}_k \cdot \boldsymbol{\nabla}_{QP_j} \left(\frac{1}{\|\boldsymbol{r} - \boldsymbol{r}_j\|} \right) dr^3 \qquad (4.4.2)$$

The magnetic data used in this work is the total field anomaly (i.e., the amplitude of the magnetic flux density field already reduced by the International Geomagnetic Reference Field – IGRF). Therefore, equation (4.4.2) can be rewritten as a good approximation for crustal studies (which is the case of this research), as the field due crustal magnetic bodies is typically much smaller than the already reduced regional field[1]:

$$B_\beta^{(k)}(\boldsymbol{r_j}) = \frac{\partial}{\partial \beta} \int_{v_k} \boldsymbol{m}_k \cdot \boldsymbol{\nabla}_{QP_j} \left(\frac{1}{\|\boldsymbol{r} - \boldsymbol{r}_j\|} \right) dr^3 \qquad (4.4.3)$$

where β refers to $\widehat{\boldsymbol{\beta}}$, the direction of geomagnetic field. Assuming a convenient 3D orthogonal reference system (x', y', z') internal to V, as $\boldsymbol{m}_k$ is constant, equation (4.4.3) can be rewritten as:

[1] For a detailed discussion about this, see Section 8.3.1 from Blakely (1996).

$$B_{\beta}^{(k)}(\boldsymbol{r}_j) = \sum_{\alpha} m_{k,\alpha} \int_{v_k} \frac{\partial}{\partial \alpha}\frac{\partial}{\partial \beta}\frac{1}{\|\boldsymbol{r} - \boldsymbol{r}_j\|} dr^3 \tag{4.4.4}$$

where $\alpha = x', y', z'$.

Equation (4.4.4) defines the calculation of $B_{\beta}^{(k)}$ due a magnetic element $\boldsymbol{m}_k$. To get the complete field at P_j due $\boldsymbol{M}$, it is necessary to sum over the N magnetic elements, i.e.:

$$B_{\beta}(\boldsymbol{r}_j) = \sum_{k=1}^{N}\sum_{\alpha} m_{k,\alpha} \int_{v_k} \frac{\partial}{\partial \alpha}\frac{\partial}{\partial \beta}\frac{1}{\|\boldsymbol{r} - \boldsymbol{r}_j\|} dr^3 \tag{4.4.5}$$

which defines the complete forward problem to calculate $B_{\beta}(\boldsymbol{r}_j)$ at P_j, for a given $\boldsymbol{M} = \sum_{k=1}^{N} \boldsymbol{m}_k$, discretized in N magnetic elements, with volume v_k, each with constant magnetization $\boldsymbol{m}_k$. Equation (4.4.5) refers to equation (2) in Ellis et al. (2012).

Equation (4.4.5) can be rewritten in the matrix form as[2]:

$$\boldsymbol{B_j} = \overline{\overline{\boldsymbol{G}}}_{\boldsymbol{j}}\boldsymbol{m} \tag{4.4.6}$$

Where**:**

$$\boldsymbol{B_j} = \begin{bmatrix} B_{\beta,j}^{(1)} \\ B_{\beta,j}^{(2)} \\ \vdots \\ B_{\beta,j}^{(M)} \end{bmatrix} \tag{4.4.7}$$

$$\overline{\overline{\boldsymbol{G}}}_{\boldsymbol{j}} = \begin{bmatrix} g_{1,x'} & g_{1,y'} & g_{1,z'} & 0 & 0 & 0 & \cdots & 0 & 0 & 0 \\ 0 & 0 & 0 & g_{2,x'} & g_{2,y'} & g_{2,z'} & \cdots & 0 & 0 & 0 \\ \vdots & \vdots & \vdots & \vdots & \vdots & \vdots & \ddots & 0 & 0 & 0 \\ 0 & 0 & 0 & 0 & 0 & 0 & \cdots & g_{N,x'} & g_{N,y'} & g_{N,z'} \end{bmatrix} \tag{4.4.8}$$

[2] This matrix development is not presented in any Seequent Oasis Montaj official documentation so far, to the knowledge of the author. Furthermore, this should not be considered as the official mathematical formalization used in Oasis Montaj.

$$\boldsymbol{m} = \begin{bmatrix} m_{1,\,x'} \\ m_{1,\,y'} \\ m_{1,\,z'} \\ \vdots \\ m_{N,\,x'} \\ m_{N,\,y'} \\ m_{N,\,z'} \end{bmatrix} \tag{4.4.9}$$

In equation (4.4.8), for $\alpha = x', y', z'$:

$$g_{k,\alpha} = \int_{v_k} \frac{\partial}{\partial \alpha}\frac{\partial}{\partial \beta}\frac{1}{\|\boldsymbol{r} - \boldsymbol{r}_j\|}\, dr^3 \tag{4.4.10}$$

4.4.2. Magnetization Vector Inversion – Inverse Problem

In the Seequent Oasis Montaj software, the inverse problem for MVI is defined by the following objective function:

$$\phi(\boldsymbol{m}) = \phi_d(\boldsymbol{m}) + \lambda \phi_m(\boldsymbol{m}) \tag{4.4.11}$$

where:

$$\begin{aligned} \phi_d(\boldsymbol{m}) &= \sum_{j=1}^{M} \left| \frac{\overline{\overline{\boldsymbol{G}}}_{\boldsymbol{j}} \boldsymbol{m} - \boldsymbol{B_j}}{e_j} \right|^2 \\ \phi_m(\boldsymbol{m}) &= |w_0 \boldsymbol{m}\,|^2 + \sum_{\alpha} \left| w_\alpha \frac{\partial}{\partial \alpha} \boldsymbol{m} \right|^2 \end{aligned} \tag{4.4.12}$$

with $\boldsymbol{m}_l \leq \boldsymbol{m} \leq \boldsymbol{m}_u$, where ϕ_d and ϕ_m are the data misfit and the model objective functions, respectively, e_j is the standard deviation for the j-th observation point, w_0 and w_α are the model weights associated with minimization of the model gradient $\frac{\partial}{\partial \alpha}\boldsymbol{m}$ and λ is the Tikhonov regularization parameter. $\boldsymbol{m}_l$ and $\boldsymbol{m}_u$ are the lower and upper boundaries for the model. In this work, we have used $\boldsymbol{m}_l = \boldsymbol{0}$ and $\boldsymbol{m}_u$ not limited.

The factor λ models the tradeoff between ϕ_d and ϕ_m, and it is needed to adopt a criterion to choose its value. To conduct the inversion, Seequent Oasis Montaj (version

9.9.1)[3] adopts an automatic default procedure ("autofit", according to the software documentation) to find an optimal value for λ, which is defined to stop the process when $\phi_d(\boldsymbol{m}) \approx 1$, until 20 iterations. Usually, this is not the best criterion to choose the optimum λ for the tradeoff, especially in cases when the standard deviation of the noise level is not determined. Oldenburg and Li (2005) mention two approaches to solve this optimization process: using the L-curve criterion, proposed by Lawson and Hanson (1974), with extensive discussion by Hansen (1992, 1998) and Hansen and O' Leary (1993); and the Generalized Cross Validation (GCV), elaborated by Golub et al. (1979), Wahba (1990), Golub and Von Matt (1997).

In this work, we used the L-curve criterion, due the linear nature of the inverse problem defined in equation (4.4.12). L-curve is a parametric curve that describes the tradeoff between ϕ_d and ϕ_m. Its name is due to the usual "L-shape" that this curve may present, once the ϕ_d and ϕ_m respect a convex relationship (convex functional), at least in the vicinity of the optimal value. Hansen (1992) and proposed that the optimal value for λ is the point of maximum curvature of of the L-curve, which is usually the "corner" of the curve. Hansen and O'Leary (1993), proposed a method to calculate it, which is implemented in the "Regularization Tools" (REGU)) (Hansen, 1998, 2007), a MATLAB toolbox for analysis and solution of discrete ill-posed problems.

To evaluate the optimal value for $\lambda = \lambda_{opt}$, it was used this method available in the script lcorner.m in the REGU toolbox, version 4.1, which evaluates λ_{opt} through the adaptative pruning algorithm or calculate the point of maximum curvature using a splining function.

To initialize the inversion procedure, as the data present unknown standard deviation of the noise level, we followed the procedure described in Oldenburg and Li (2004) and detailed in Melo et al. (2017): assuming an initial constant guess for $e_j = e = 1\,nT$ to run the first inversion, using the discrepancy principle (Parker, 1994; Hanke 2017), we estimate λ_{opt}. running a large number of inversions (> 12 rounds) varying the λ 's, to build the first L-curve. The λ_{opt} is chosen following one of the two methods

[3] This is described in VOXI help documentation in the "Settings -> Regularization" menu. Also, see the tutorial video in the "Introduction" section of "Modelling Best Practices" in Seequent online documentation: https://my.seequent.com/learning/459/1427/1428.

described above and after visual inspection of their results. Then, using the discrepancy principle (Parker, 1994) in equation (4.4.12) for ϕ_d, which states that $\phi_d \approx N$ (N is the number of data points), we estimate the adjusted error of the data e_{adj}, by:

$$e_{adj} = \sqrt{\frac{1}{M}\sum_{j=1}^{N}\left|\overline{\overline{\boldsymbol{G}}}_j\boldsymbol{m} - \boldsymbol{B}_j\right|^2} \tag{4.4.13}$$

This procedure is repeated until two or three times for fine tuning of the models.

.

4.4.3. Resulting Output for The Magnetic Susceptibility Model From VOXI MVI

In Exploration Geophysics, magnetic modeling problems usually seek to model the spatial distribution of the scalar magnetic susceptibility k in subsurface, related to the magnetization vector $\boldsymbol{M}$ by:

$$\boldsymbol{M} = k\boldsymbol{H}_e \tag{4.4.14}$$

where $\boldsymbol{H}_e$ is the external magnetic field (geomagnetic field, or a regional field already reduced by the IGRF). The Seequent VOXI MVI algorithm solves it considering the anisotropic nature of the magnetic susceptibility related to the survey geological environment and models the effective magnetic susceptibility $\boldsymbol{M}_{eff}$. In this case, k is generalized as a 3D vector in an orthogonal reference system. Thereby, equation (4.4.14) is rewritten as:

$$\boldsymbol{M} = \boldsymbol{k}H_e \tag{4.4.15}$$

where $H_e = |\boldsymbol{H_e}|$ and $\boldsymbol{k} = (k_x, k_y, k_z)$ in the reference system. This generalization is described in Ellis (2015). This author describes $\boldsymbol{M}_{eff}$ as a combination of $\boldsymbol{M}$ and the Normal Remanent Magnetization (NMR) $\boldsymbol{M}_{NMR}$.

$$\boldsymbol{M}_{eff} = \boldsymbol{M} + \boldsymbol{M}_{NMR} \tag{4.4.16}$$

where:

$$\boldsymbol{M}_{NMR} = \boldsymbol{k}_{NMR} H_e \tag{4.4.17}$$

where $\boldsymbol{k}_{NMR}$ is the pseudo-magnetic susceptibility related to the NMR. In this work, we do not investigate the nature of $\boldsymbol{M}_{NMR}$, but just consider its inclusion in the calculation of $\boldsymbol{M}_{eff}$. By equations (4.4.15) and (4.4.17) in equation (4.4.16), $\boldsymbol{M}_{eff}$ is rewritten as:

$$\boldsymbol{M}_{eff} = \boldsymbol{k}_{MVI} H_e \tag{4.4.18}$$

where:

$$\boldsymbol{k}_{MVI} = \boldsymbol{k} + \boldsymbol{k}_{NMR} \tag{4.4.19}$$

The Seequent VOXI MVI outputs $\|\boldsymbol{k}_{MVI}\|$ and its spatial components in equation (4.4.18) in three different ways[4]:

1. As components parallel and perpendicular to $\boldsymbol{H}_e$: $\boldsymbol{k}_{MVI}^{proj} = \boldsymbol{k}_{MVI} \cdot \boldsymbol{H}_e$ and $\boldsymbol{k}_{MVI}^{perp} = \boldsymbol{k}_{MVI} \perp \boldsymbol{H}_e$, respectively;
2. $\boldsymbol{k}_{MVI} = \left(k_x^{MVI}, k_y^{MVI}, k_z^{MVI}\right)$, described in an orthogonal reference system (x, y, z); where y is North-South oriented, towards to North; x is East-West Oriented, towards to East; and z is the vertical direction, increasing upwards and;
3. $\boldsymbol{k}_{MVI} = (k_U^{MVI}, k_V^{MVI}, k_W^{MVI})$, described in an orthogonal reference system (U, V, W), where U is oriented to the geomagnetic field, increasing towards its direction.

[4] This is also detailed described in the tutorial video "Understanding MVI" in Seequent online documentation: https://my.seequent.com/learning/459/1427/1432.

Chapter 5: Geophysical Data and Data Preparation

5.1. Brief Description About Previous Airborne Geophysical Surveys and Related Works in the Quadrilátero Ferrífero Area

Besides this thesis concerns about the latest HTEM survey and its associated airborne magnetic data in the QF area, it is worthy to mention some previous airborne geophysical surveys in the area and related works. The latest HTEM survey is known as Rio das Velhas – Phase 2 (RVPh2) internally in the SGB-CPRM and this is the nomenclature used in this thesis. This dataset is public available in http://geosgb.cprm.gov.br/geosgb/downloads.html as project number 1116. However, before to describe it with more detail, the brief description below intends to provide useful information of previous works that might help to guide future works with geophysics in the QF area, in addition to the results presented in this thesis.

The first surveys were conducted in the "Brazil-Germany Agreement", which was conducted during the early 1970's by fixed-wing surveys, with 2km flight lines spacing and 350 m nominal flight height, oriented to N-S. These surveys were composed by regional airborne magnetic surveys and covered almost the totality of the Minas Gerais State (MG), with the exception of the Western portion, a region know as the "Triângulo Mineiro". It aimed to contribute to the regional geological mapping in MG. It was contracted by the Brazil's National Mining Agency, and partially executed by the SGB-CPRM. In the GeoSGB, the SGB-CPRM database, it can be found as project number 1009 from the Series 1000, which is publicly available at http://geosgb.cprm.gov.br/geosgb/downloads.html.

The most recent regional surveys in the MG focused on regional geological mapping and mineral exploration were contracted by the Development Company of Minas Gerais (CODEMGE) and partially coordinated/fiscalized by the SGB-CPRM. These surveys were conducted during the 2000's and 2010's, as fixed-wing surveys, which are composed by airborne magnetics and radiometrics data. The flight line spacing

varies between 250-500 m, with 100 m nominal flight and N-S orientation. In the GeoSGB database it can be found within the Series 2000. However, they are publicly available only for research and academic training purposes at the CODEMGE website: http://www.codemge.com.br/atuacao/mineracao/informacoes-geologicas-e-geofisicas/levantamento-aerogeofisico/.

However, the CODEMGE data do not cover the GBRV area, which was first covered by a helicopter-borne survey, conducted in 1992, by a consortium between mining companies operating in the QF area, Brazil's National Mining Agency and the Gorceix Foundation. This survey was composed by airborne magnetic, radiometrics and FDEM data, with 250 m line-spacing, average flight height of 80 m and varying flight line direction, with N40W and N50E divided in four blocks. These data can be found in the GeoSGB database as the project number 3007 from the Series 3000, but are not publicly available. The aim of this project was to provide detailed geophysical data for regional mapping of the GBRV and provide useful information for mineral exploration in the area. Internally to SGB-CPRM, this survey has been informally named as Rio das Velhas – Phase 1 (RVPh1), to be distinguished from the newer HTEM survey used in this thesis.

Among the works that used the above mentioned airborne geophysical data, some might be interesting to bring a good understand of their relevance for the geological understanding of the QF area. The first work that integrated all of these data was conducted by Leão (2006), which also provided an extensive description about their motivation, objectives, players enrolled and technical information, besides the survey reports. This work intended to integrate all these geophysical surveys to the same datum and provide regional products for the MG State (geophysical maps). This work was continued by the SGB-CPRM, with the release of publicly geophysical maps (see GeoSGB for further information: https://geosgb.cprm.gov.br/), while the completion of the CODEMGE surveys until the mid 2010's.

However, the works related specifically to the economic potential of the gold mineralization in GBRV using the RVPh1 survey (project 3007) started with Silva et al. (2000) and Silva et al. (2003a, 2003b). The first work pioneered the use of the survey to be used in the creation of statistical predictive models for the gold mineralization in the GBRV. This work was further refined for BIF-hosted gold deposits in Silva et al. (2003b),

using the same data. In Silva et al. (2003a), the RVPh1 was studied to provide insights about the most important geophysical signatures related to economic gold mineralization and their geological context. It is worthy to mention that many conductive anomalies indicated in this survey were validated by the HTEM survey used in this thesis, including the Lamego Mine and the conductors in the Roça Grande region, during the first analyses of the HTEM data by the SGB-CPRM.

Not related to the first airborne geophysical dataset described above, it is worthy to mention the work of Oliveira (2014), that used airborne magnetics, radiometrics and ATEM data with the TEMPEST system. This survey was contracted by AngloGold Ashanti and the work focused only on the Santa Bárbara municipality region, in the Eastern portion of the QF area, with the aim to characterize the BIF-hosted gold mineralization in this region. Further works at the same area were conducted by Oliveira (2020) with the RVPh2 dataset, using conductive prismatic bodies modeling, integrated with the airborne magnetic data, following the same approach presented in Couto et al. (2016, 2017).

The RVPh2 survey is detailed described in the next subsection.

5.2. HTEM and Airborne Magnetics Survey in Quadrilátero Ferrífero Area

The RVPh2 survey (Figure 5. 1) was conducted by PROSPECTORS Aerolevantamentos e Sistemas LTDA, contracted by CPRM in 2010 and was divided in two areas: RV1 and RV2 (Prospectors, 2011). In this research, we focus on the results for Lamego Mine and in Roça Grande area, both in RV1 portion. The total survey comprises an extension of 3560 line-km, flight line spacing of 250 m and N45W flight direction. The average flight heights were 65 m for the magnetometer and 30 m for the HTEM system. The HTEM system was the Aeroquest AeroTEM^{HD}, with 17 turn-off times and 16 turn-on times channels, its main features are described in Table 5. 1. In this work, only the turn-off times data was used. For a detailed description of this system, see the technical report about the survey (PROSPECTORS, 2011).

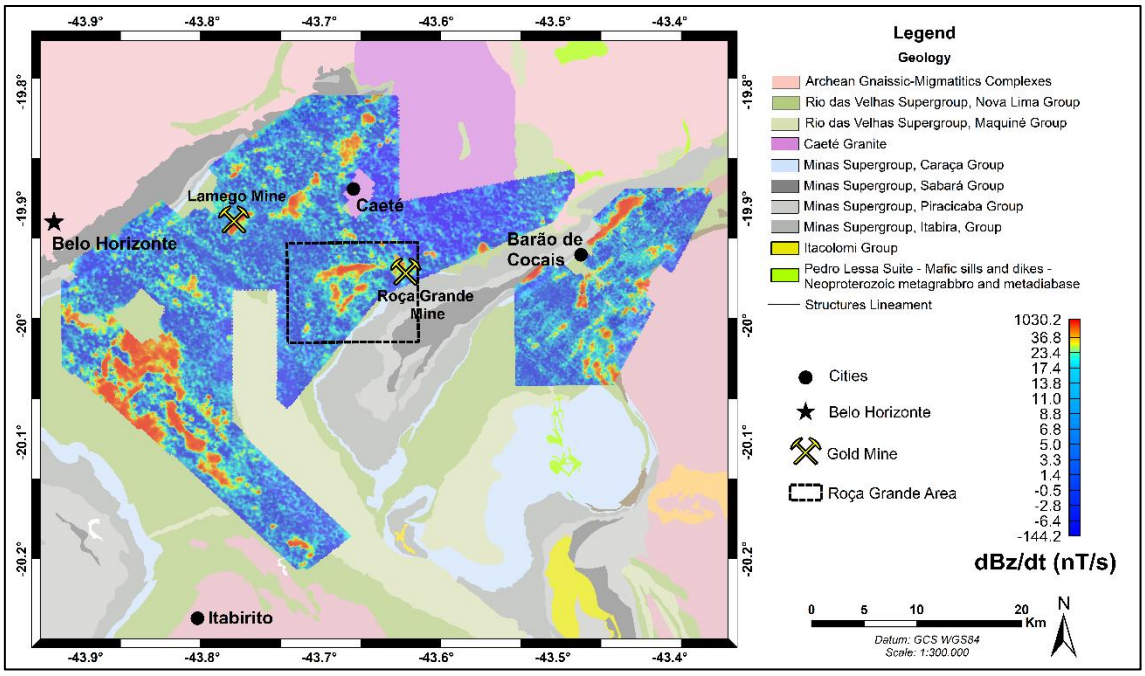

Figure 5. 1: Location map of RVPh2 survey in QF area presented as dB/dt (channel 7 for off times) map. The two studied areas Lamego Mine and Roça Grande area are indicated, the second as the black dashed polygon.

Table 5. 1: AeroTEM^{HD} specs parameters used in QF survey.

	Parameter	Value
Transmitter	Loop diameter	20 m
	Peak current	323 A
	Peak moment	711,000 NIA
	Repetition frequency	30 Hz
	Turn-on time	- 4,476 µs
	Peak current time	- 2,133 µs
	Turn-off time (when 0 current is reached) *	0
	Waveform	Triangular
Receiver	Sample rate*	10 Hz
	Number of gates (only off-time used)	17
	Time gates interval (off-times) **	87.5 to 9,532 µs

5.3. Data Preparation

Time Shift in the AeroTEM^{HD} Waveform

To process the AeroTEM^{HD} data we used the processing tools in the Aarhus Workbench (version 6.4.1.0). According to its documentation (http://www.ags-cloud.dk/Wiki/W_AirborneTEMGuides), to be able to work with AeroTEM^{HD} data in this software, it is necessary to set the zero-time (the origin of the time interval) of the current waveform to the turn-off time, due to the characteristics of the AeroTEM^{HD} system. For this system, it is provided in the database a specific waveform for each sounding point, which may present slightly variations between them. Workbench actually works with these specific waveforms for each sounding point and with the zero-time defined at the turn-off time. In this way, it was necessary to shift the waveform and time gates as presented in Prospectors (2011), referenced to the new zero time. Table 5. 2 presents the converted time gates for the off-time interval and Figure 5. 1 presents the shifted waveform. The geometric file (".gex" file) used in this research is presented in Annex 1.

It is worthy to mention that the on-time interval presented very poor signal-to-noise ratio. Thereby, we did not use them in this research.

Table 5. 2: Off-times shifted time channels for the AeroTEM^{HD} system (it was subtracted 4.509 μs as shown in Prospectors, 2011)).

Gate Number	Gate Center (µs)	Gate Start (µs)	Gate Width (µs)
0	87.50	73.60	27.80
1	115.30	101.40	27.80
2	143.10	129.00	27.80
3	170.90	157.00	27.80
4	212.50	184.70	55.60
5	282.00	240.35	83.30
6	379.20	323.65	111.10
7	504.20	434.75	138.90
8	684.80	573.70	222.20
9	948.70	795.90	305.60
10	1309.80	1101.45	416.70
11	1809.80	1518.15	583.30
12	2518.10	2101.45	833.30
13	3518.10	2934.75	1166.70
14	4920.90	4101.45	1638.90
15	6893.10	5740.30	2305.60
16	9532.00	8045.90	2972.20

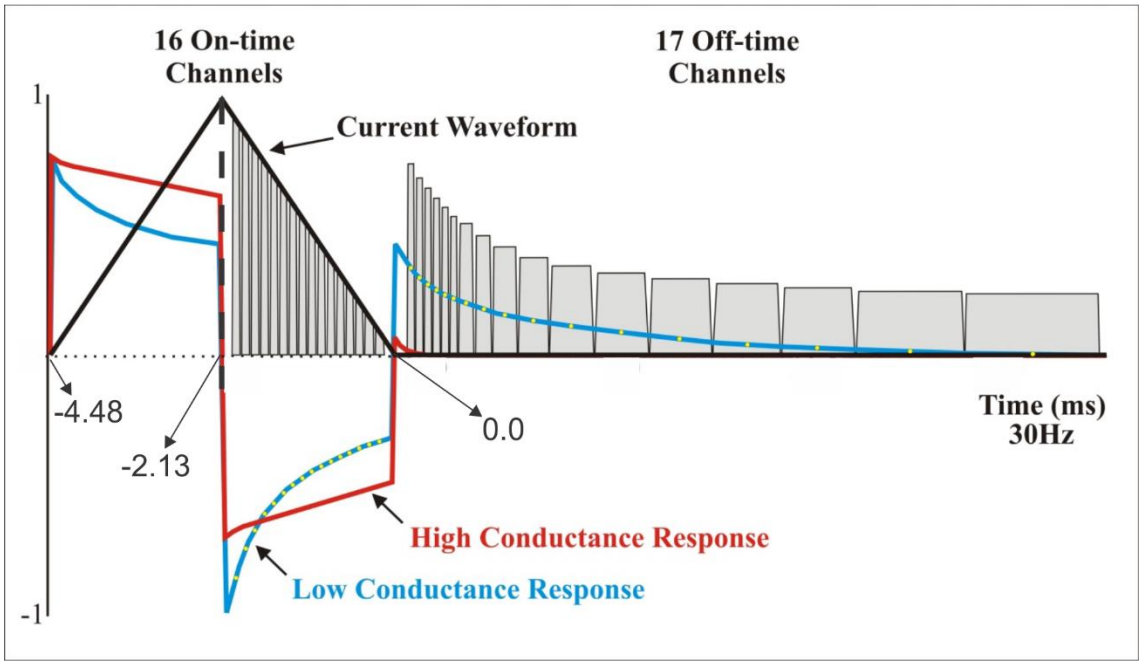

Figure 5. 2: Shifted AeroTEM^{HD} waveform used in this research (modified from Prospectors, 2010).

5.4. Limitations of the waveform used in Aarhus Workbench

Aarhus Workbench allows the possibility to input the waveform parameters considering their average values or the values for each data point sampled during the acquisition, if this is present in the database, as discussed in the last section. This is a good advantage to Aarhus Workbench because many HTEM systems (like AeroTEM) present small oscillations in their turn-off time. Christiansen et al. (2011) made a complete discussion about the limitations of the TEM systems current waveforms described by inaccurate descriptions and their implications of the subsurface resistivity models generated by them. One of their conclusions is the early times of the dB/dt decay curve could be badly modeled and cause misinterpretations of the data. Furthermore, the best way to work with it is to input the variable turn-off time available in the database, which each datapoint will be modeled individually[5]. In this sense, we choose to use the variable waveform parameters in the AeroTEM^{HD} input database for the Aarhus Workbench. These input values also were shifted as described in the previous section.

Another aspect about the input waveform discussed in Christiansen et al. (2011) is the change of polarity during the repetition of the current pulse in TEM systems. They argue that every TEM system works alternating polarity current pulses with frequencies multiple of the power lines frequency, to avoid their influence in the data (in the AeroTEM ^{HD}, the base frequency is 30 Hz). However, most TEM inverse modeling is done with just one current pulse, which is the case in Aarhus Workbench LCIs and SCIs routines. This means that the database presents less response than what is being modeled and could cause misinterpretations for the late times response (i.e., deeper layers) when compared with two or more pulses modeling, as demonstrated in Christiansen et al (2011). This is not a problem only for high resistive environments, but could be a problem when a deep conductor is presented beneath the resistive layer. In QF area, Au sulfide mineralization is often in a scenario like this and the understanding of its implications in the AeroTEM ^{HD} data used in this survey is relevant.

[5] The database in Aarhus Workbench demands a processing workflow before any inversion/forward modeling, which might be related to data averaging. In this case, a 1D model may be associated with a group of TEM soundings.

To understand this limitation, we conducted a forward modeling for the input waveform of the AeroTEM ^{HD} system used in this work, considering one and two waveform pulses. The reference model is a three-layer half space model, with the following resistivity/thickness pairs: 500 Ω.m/30 m, 5000 Ω.m/150 m and 0.3 Ω.m/infinity. Figure 5. 3 presents the comparison between the one and two waveform pulses responses. In Figure 5. 3– a the forward responses are presented, Figure 5. 3– b and Figure 5. 3 – c is the inversion considering only one pulse for the one waveform pulse and two waveform pulses forward responses, respectively, but with the inversions conducted with only one pulse, as discussed for the LCI case. Figure 5. 3– d is the relative ratio between the one and two waveform forward responses, calculated by $|1 - r|$, where r is the ration between the one and two waveform responses. The last two figures are the misfit for each time channel and total for one waveform inversion (Figure 5. 3– e) and two waveform (Figure 5. 3– f). These results show that in AeroTEM^{HD} system the late times is influenced with the limitation of inverting data with only one waveform pulse.

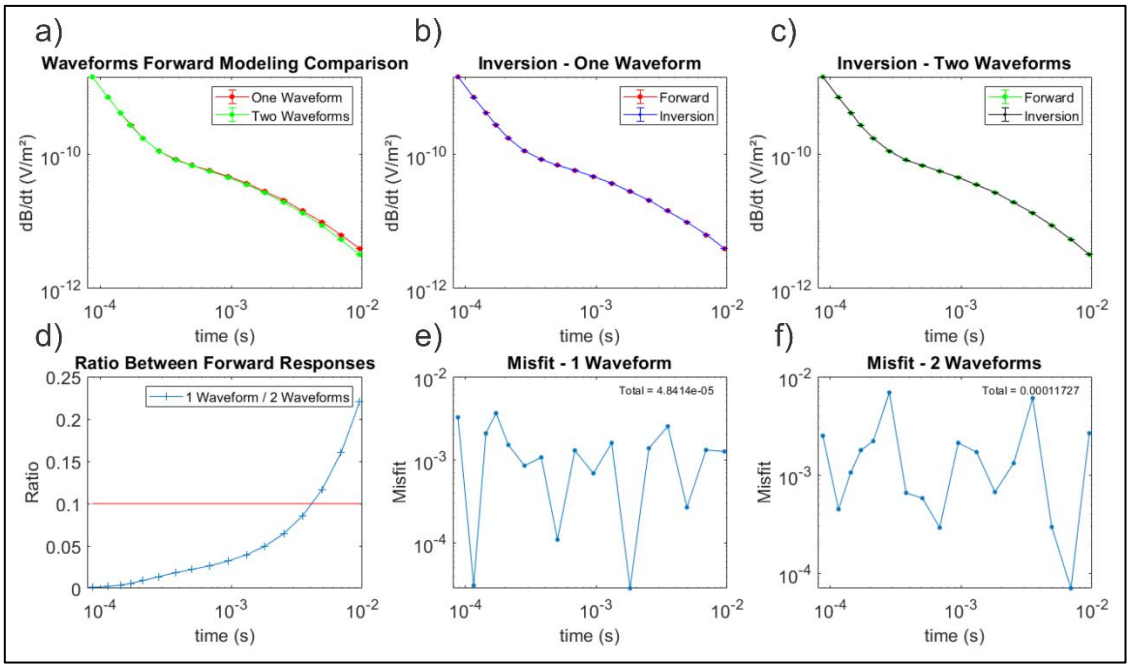

Figure 5. 3: a) Forward transient decay responses for 1 and 2 waveforms pulses for the AeroTEM^{HD} system. b) and c) are the comparison between the forward and inversion results for 1 and 2 waveforms inputs in inversion process, respectively. d) Relative ratio between 1 waveform / 2 waveforms forward responses. e) and f) are the data misfit for 1 and 2 waveform pulses input, respectively. The inversions were conducted with only one waverform pulse in AarhusInv.

Figure 5. 4 presents the results of the inversion with one waveform pulse, but with a forward input with two pulses. Figure 5. 4-b shows that the geoelectrical model could be misinterpreted about of 70-80 m in depth values for the deeper layer (the top of the

conductor). Furthermore, the interpretation of the conductors associated with sulfide mineralization in a scenario like this in QF area must consider this limitation, which may cause an ambiguity around a few tens of meters.

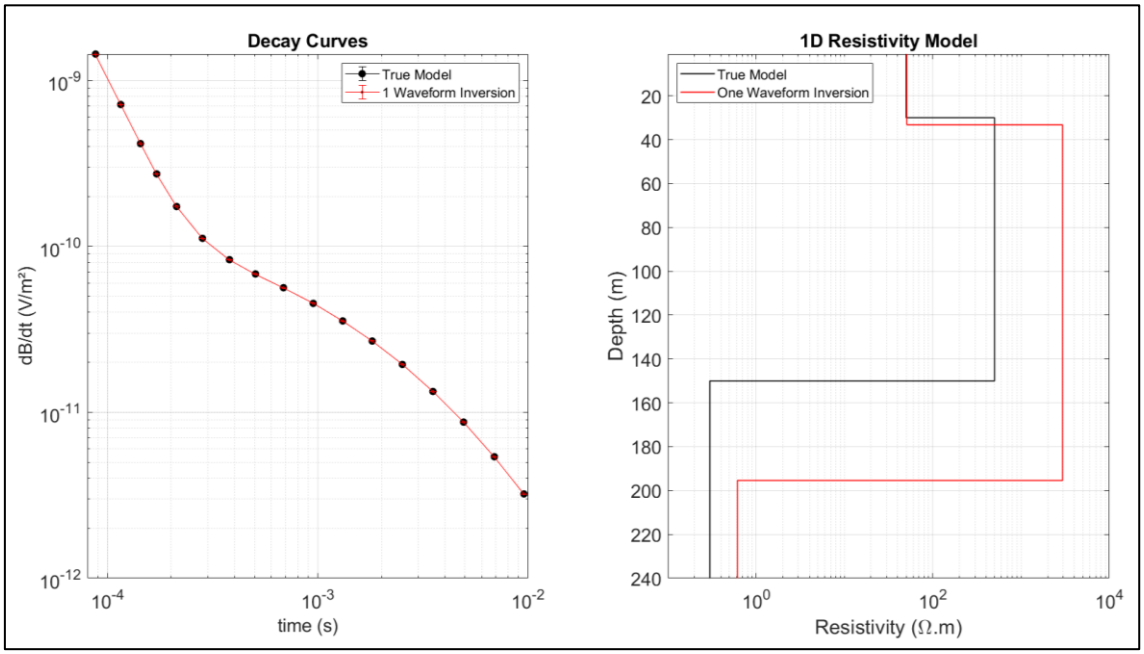

Figure 5. 4: Comparison between true and inverted models with 2 waveform pulses inputed and inversion with 1 one waveform pulse from the LCI algorithm.

Chapter 6: Results

6.1. MPA Robust Inversion Scheme Validation and Testing

In this section, the the validation and testing of the robust inversion scheme using the MPA parameterization is presented. The methodology was commented in Section 4.2 and it is fully presented in Lin et al. (2019), which is reproduced in Appendix 1. The results in this section presents the application of this methodology for synthetic data and also for real data, a SkyTEM516 survey in the Hope Bay volcanic belt area. Nunavut Territory, Canada, a gold mineral province. According to Kaminski et al. (2016), it is expected the occurrence of strong IP anomalies related to Au mineralization styles and, in addition, this dataset could not be inverted to recover a reliable resistivity model, if the IP effect was not considered. In this way, this dataset makes a good example to test the robust inversion scheme proposed in Lin et al. (2019).

I co-authored this paper, in which my participation was focused on the real data processing and modeling. The whole data processing and anomaly choice was conducted by me and oriented by the coauthors. During the field data modeling process, I collaborated testing different inversions settings (the input $\boldsymbol{m}_{MPA} = (\rho_0, \varphi_{max}, \tau_\varphi, C)$ parameter vector, number of initial iterations to lock the parameters to initialize MPA inversion and damping factor) seeking to test the limits of the methodology and improve the resistivity models. The MPA parameterization was chosen in order to decrease the spatial correlation between the multiparametric inversion that the Cole-Cole model demands, as demonstrated by Fiandaca et al. (2018) and commented in Section 4.3.1. The robust inversion scheme is detailed discussed in the paper and in Section 4.3. My collaboration in this research was focused on the understanding of the overall methodology and how to apply it in the QF case. These discussions were key to improve the methodology application in real data processing and preparation for inversion, concerning the anomalies selection based on the analysis of steep decays and negative decays anomalies possibly associated with IP phenomena.

The research was conducted evaluating the comparison between the Resistivity-Only (RO) inversions and MPA inversions using the robust inversion scheme. The RO inversions considered only the ordinary real resistivity function in the TEM data

(Nabighian and Macnae, 1991). The synthetic data study presented three geometrical configurations for conductive and polarizable bodies in two geoelectrical environments: i) one non-polarizable and conductive ($\sim 100\ \Omega \cdot \mathrm{m}$) host rock and; ii) the other in a non-polarizable very resistive ($\sim 1000\ \Omega \cdot \mathrm{m}$). A 2D forward modeling algorithm was developed by the co-authors to simulate the IP response and this data was inverted using the MPA robust inversion scheme by the coauthors. The main conclusion of this part is that the robust inversion scheme MPA recovered the geometry and the resistivity model of the anomalous bodies in a better way than the RO inversions, avoiding the occurrence of a very resistive base for the polarizable body, which could cause erroneous interpretations.

Figure 6. 1 reproduces one of the synthetic data results (model 1 in Lin et al., 2019) presented in the paper and elaborated by the coauthors, which illustrates the main results from this part. The synthetic model is composed by a resistive host rock, with a conductive and chargeable body at the edge of the domain (Figure 6. 1-a). The details about the parameters are described in the box in the lower left corner of Figure 6. 1. The RO results (Figure 6. 1-b) show a conductive model, with a significant resistive basement and shallower in comparison to the true model in Figure 6. 1-a. It is important to emphasize that all RO modeling was conducted without the negative data in the decay curves. As this parameterization does not assume negatives in its formulation. The MPA results (Figure 6. 1-c) present a conductive model in better agreement with the geometry and resistivity values of the true model. The φ_{max} spatial distribution also indicates a better recovery of the polarizable body. The other parameters (τ_ρ and C) in MPA parameterization indicates the existence of the polarizable body, as well. The data misfit is much higher in the RO model (reaching values higher than 10) than in the MPA model, indicating that the first parameterization approach does not reproduce a reliable resistivity model and the robust inversion scheme using MPA is needed to achieve that.

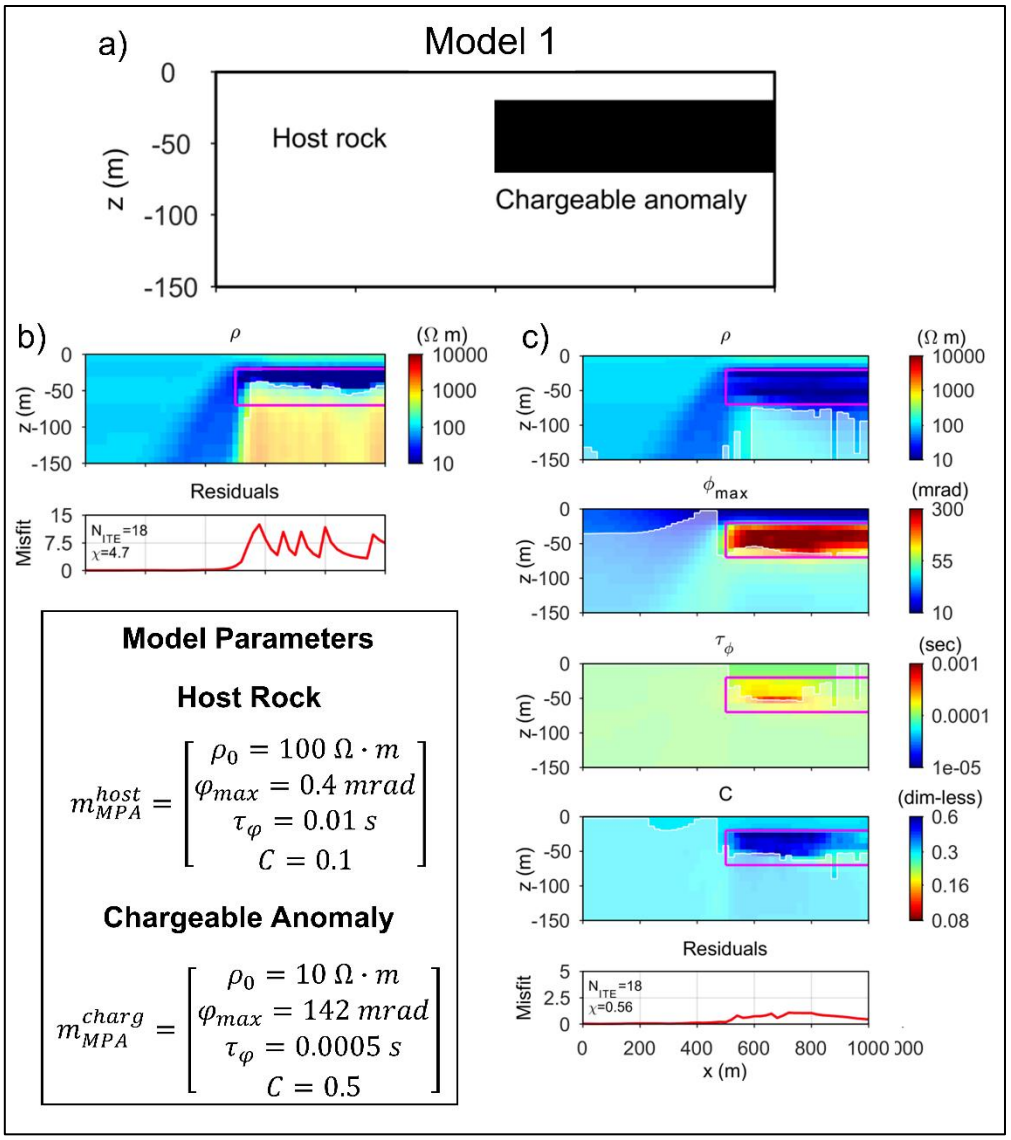

Figure 6. 1: a) Synthetic model 1 developed in Lin et al. (2019). b) Model profile for the RO parameterization. c) Model profile for the MPA robust inversion scheme. The model parameters are described in the box in the lower left corner of the figure.

For the real data study, there were important strong IP anomalies in the Hope Bay area that may be associated with gold mineralizations, which made it an ideal case to be studied using the robust MPA inversion scheme, as mentioned above. Kaminski et al. (2016) indicated three conductive anomalies in the Northern portion of the survey area, with significant distortion in the dB/dt decays, which could not be inverted using the RO approach. It needed an IP effect modeling multiparametric inversion in order to recovery a reliable resistivity model. In fact, these anomalies generated very steep decays and negative transients in the SkyTEM data.

From the three anomalous regions indicated by Kaminski et al. (2016), we choose to test the MPA robust inversion scheme in a profile over the chargeable anomalies presented in Figure 6. 2, related to the anomalous anomaly 3 in Kaminski et al. (2016). Figure 6. 3 presents a sounding point over the chargeable anomaly. As can be noted in Figure 6. 3-a, the data presents very steep dB/dt decays in both low and high moments (LM and HM, respectively), with strong negatives in both acquisition modes. In fact, the anomalies in the HM regime are fully negative above the noise floor. Still, the MPA robust scheme was able to invert the data. The resulting resistivity and φ_{max} 1D are presented in Figure 6. 3-b, which shows a very resistive environment, which is expected in the mafic background in the Hope Bay area. Also, φ_{max} model presents a shallow (depth < 15 m) polarizable ($\varphi_{max} > 200$ mrad) layer, associated with the strong IP effect in this sounding.

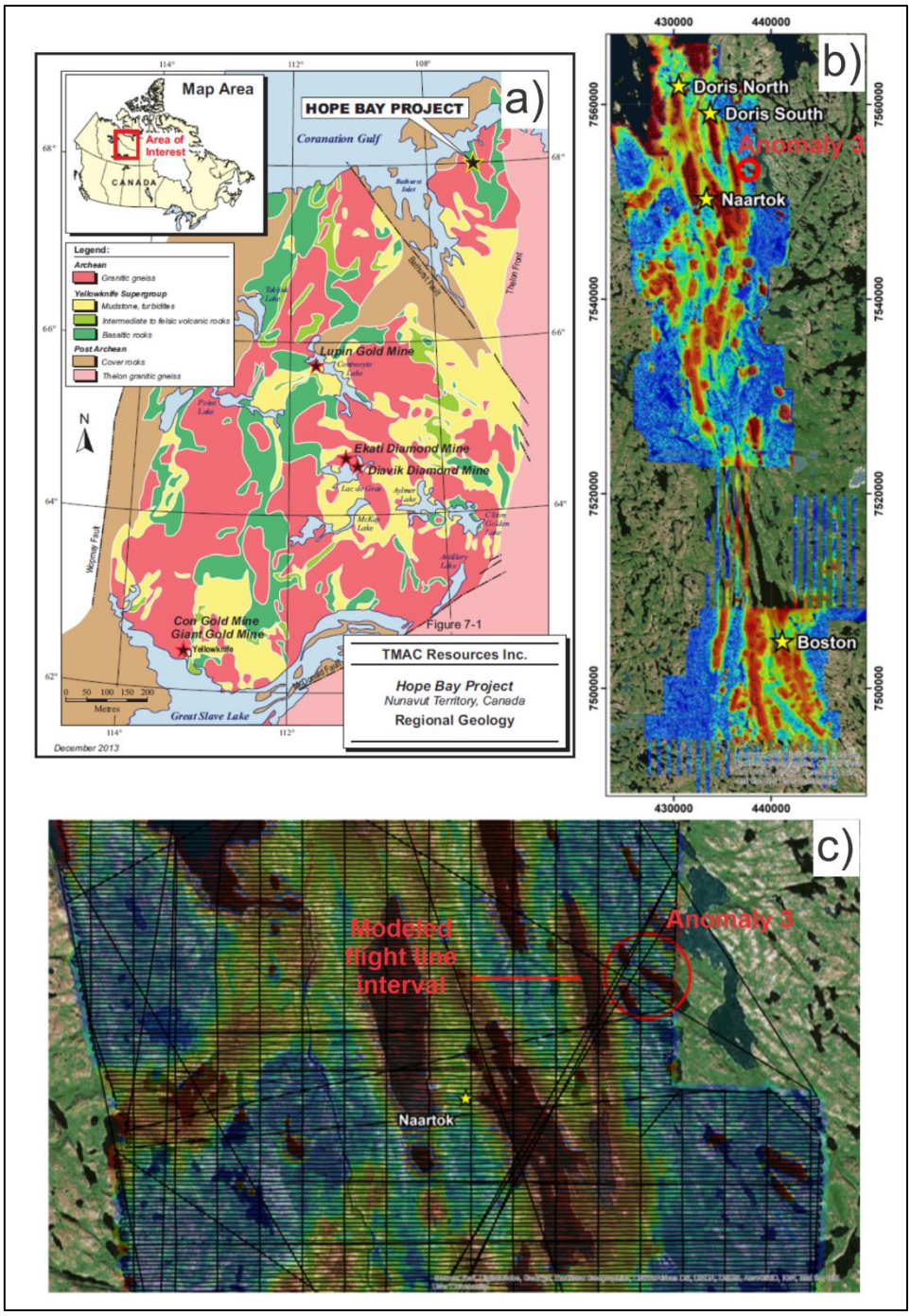

Figure 6. 2: a) Hope Bay project location in Canada (figure from Clow et al., 2013). b) SkyTEM516 survey in the area. c)Location of the chosen modeled profile over the anomaly 3 in the Northern portion of the survey, as indicated by Kaminski et al. (2016).

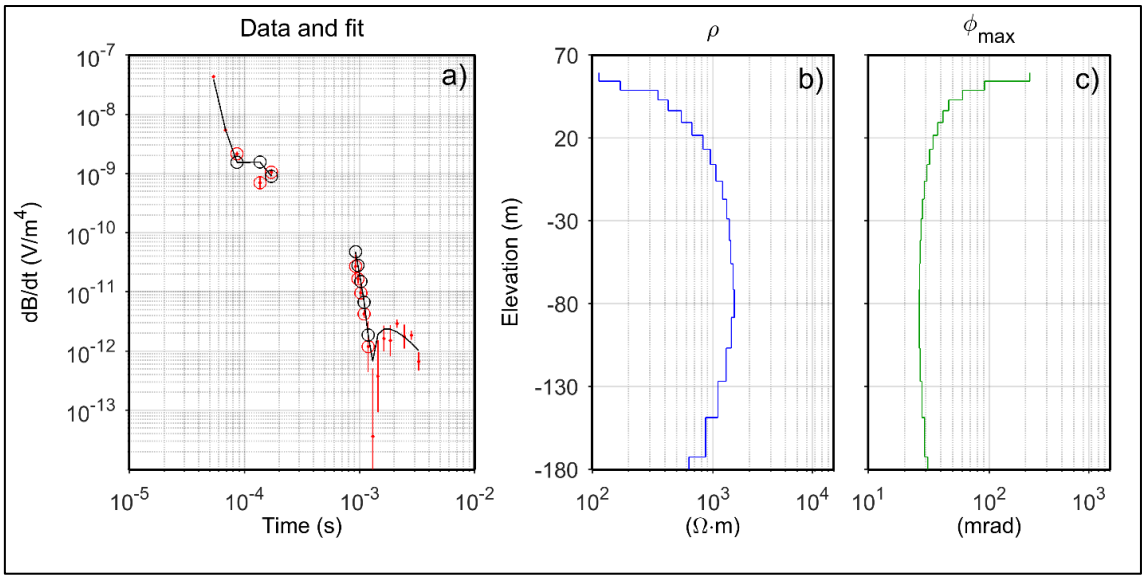

Figure 6. 3: Example of MPA robust inversion for one sounding over the polarizable anomalies in the Hope Bay data. a) dB/dt decay, the negatives values are represented as circles, the black line is the fitted model and the red marks are the data. b) Resistivity model. c) φ_{max} model – (adapted from Lin et al., 2019).

In fact, these characteristics about the resistivity and φ_{max} models are extended over the whole profile (Figure 6. 4). The central and Eastern portion of the profile is very resistive ($> 1000\ \Omega \cdot m$) with a strong polarizable shallow layer (depths around 12 m and $\varphi_{max} > 200$ mrad). This shallow polarizable environment might explain the full negative decays in the HM data, which have made the RO approach ineffective to invert this dataset.

The processing of these data, delimitating the noise level and discriminating it from the signal level was a good training to continue to process the data in QF region, commented in the next section, especially due to the high noise level of the AeroTEM^{HD} data used in this research.

The main conclusion of this part of the research is that the MPA robust inversion scheme performed better than the RO parameterization, even in a 2D situation, as simulated in the synthetic tests. In the case of a polarizable environment, the RO parameterization could not recover a reliable resistivity model, which could lead to erroneous interpretation. In fact, the field data example illustrated a marginal situation, in which RO approach could not be even applicable, due to the full negative decays in the data. For further details about these results, the paper is fully reproduced in Appendix 1.

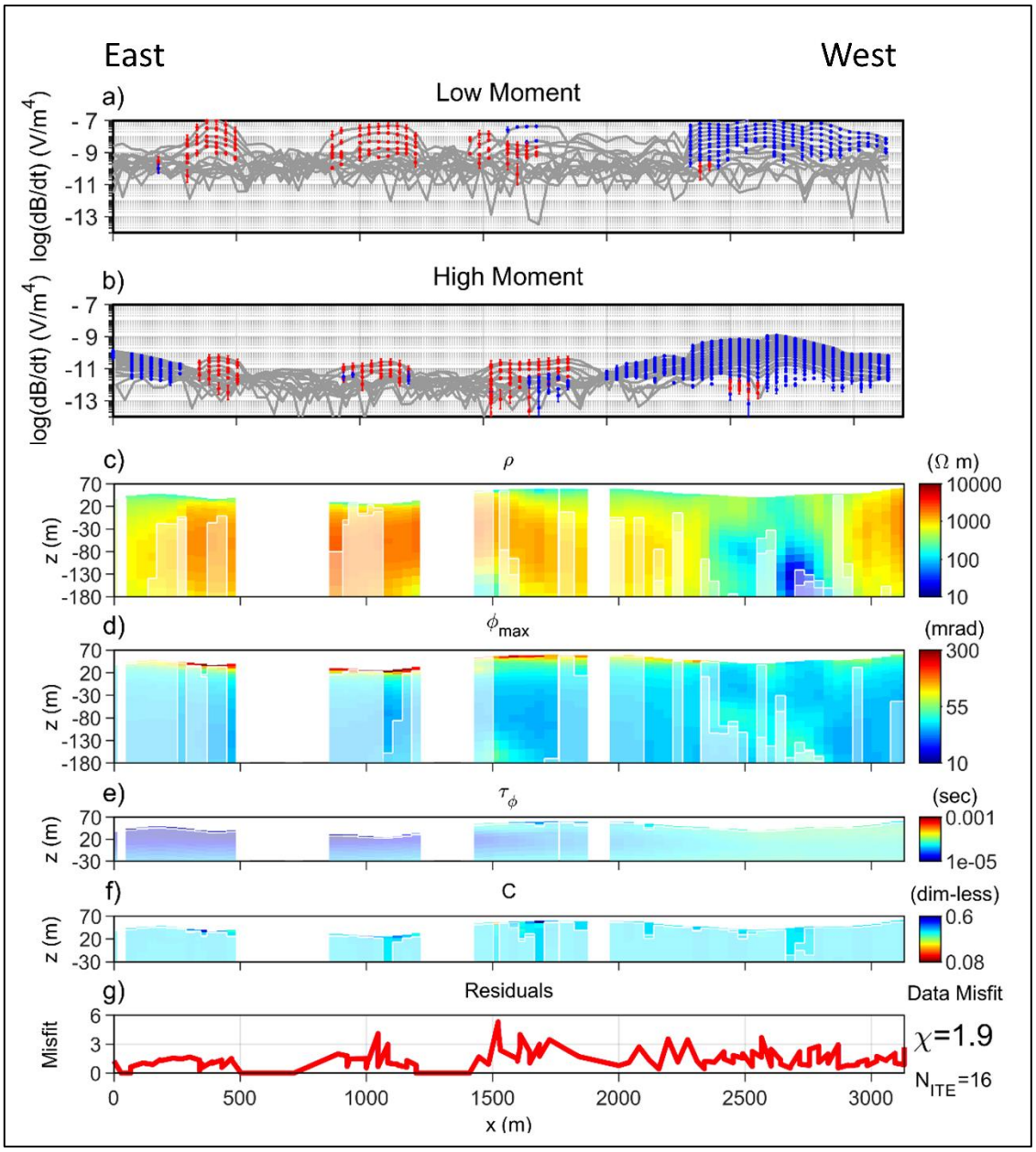

Figure 6. 4. MPA robust inversion results for the profile in Hope Bay area, reproduced from Lin et al. (2019). a) LM and b) HM data, in which blue and red marks indicate the positive and negative data, respectively. The grey lines represent all measured data, including the culled out data removed during the processing. Inverted models sections for c)ρ_0, d) φ_{max}, e) τ_φ and f) C parameters. The DOI is represented as the top of shaded vertical rectangles. g) Data misfit section.

6.2. Case Study 1: AIP In The Lamego Mine

After the discussion brought in Li et al. (2019) - Appendix 1, commented in last section, which validated the MPA robust inversion scheme, we moved to model the AeroTEM^{HD} in the QF region, in Brazil. As commented in Chapter 2, QF region is a world class gold province, with important orogenic gold deposits associated with metallic sulfides dissemination. In this way, AeroTEM^{HD} modeling seeks to identify potential zones for these mineralizations in the Rio das Velhas Greenstone Belt, as discussed in Section 2.2, in terms of geoelectrical parameters. In order to conduct this work, it was necessary to choose a portion of the dataset to understand how the IP effect may behave. The Lamego Mine is one of the most important gold mines in QF region and meets this demand, as its structural and lithological control are well known (Martins et al., 2016), with available borehole lithological data (provided by Anglo Gold Ashanti).

Thereby, we conducted this analysis in the Lamego Mine area, which resulted in the publication presented in Couto et al. (2020), fully reproduced in Appendix 2. The processing settings used in this work in the Aarhus Workbench (.gpr file) is presented in Annex 2. I am the first and correspondent author of this paper, in which I was responsible for the data processing, modelling, interpretation of the results and paper writing. During the development of this research, many discussions emerged with the coauthors that helped not just to improve the results presented in this very publication, but also in Li et al. (2019), as well, as both results were developed jointly, in a synergic way. The learning related to data processing and estimation of the input parameters nurture both works.

The geological environment in Lamego Mine can be briefly described as: disseminated sulfides associated with the contacts of iron formations/carbonaceous units hosted in a metamafic/metaultramafic environment. The Appendix 2 and Martins et al., 2016 presents the detailed description. According to petrophysical data from Anglo Gold Ashanti[6], it is expected that the mafic and ultramafic units are very resistive and non-polarizable. On the other hand, the carbonaceous units might be resistive (or conductive, if it presents graphite composition) and polarizable; the iron formation are expected to be

[6] This data was not fully available for this research, as Anglo Gold Ashanti provided only the main resistivity and chargeability values for some lithologies, which were used as a guiding direction to set our models.

less resistive than metamafic/metaultramafic environment and non-polarizable, unless it presents disseminated sulfides within it. Figure 1 from the Appendix 2 illustrates the location and geology of Lamego Mine.

It is important to note that there are occurrences of steep decays and late times negative values over Lamego's structure (Figure 2 in Appendix 2). The main approach for the data processing was to use filtering parameters that keep as much as possible the original negatives and steep decays above the noise floor for the MPA inversions, which can be seen in Figures 2-a and 2-c in Appendix 2. It is also important to mention that the same data was used to conduct RO inversions for comparison, with only the exclusion of the negatives, as this parameterization does not accept negative values. This is detailed in the Section "Data processing and anomaly selection" in Appendix 2, as well.

Before moving to the field data results, it was necessary to run a synthetic study of the AeroTEM^{HD} response over Lamego's geological environment, in order to identify what type of resistivity model we would expect from both RO and MPA parameterizations in the survey data. These results are presented in Figure 6. 5. The true model for this synthetic test is presented in Table 2 in the Appendix 2, which simulates a 3-layer 1D model, with a mafic background (first and last layer), intercalated with layers of carbonaceous/graphite schists (layer 2). In this simulation, we kept fixed all parameters in the Table 2 in the Appendix 2, with the exception for φ_{max} in the layer 2, which varied from 10 mrad to 500 mrad, i.e., going from very weak polarizable contrast within the mafic background, towards to a strong polarizable layer, as this is the expected polarizable lithology in a geological environments like Lamego (Smith, 1983). Compared to the true model, it is noted in the resistivity 1D sections in Figure 6. 5 that as φ_{max} increases, the RO resistivity model (blue curves) is distorted, the conductive layer (related to the carbonaceous units) becomes much more conductive and thinner, while the top layer may become shallower in the upper bound of φ_{max} interval. A strong resistor becomes shallower, reaching depths above the DOI, which could lead to erroneous interpretation. On the other hand, the MPA results presented a more similar resistivity model, in comparison with the true model. The top of the layer and its resistivity order of magnitude are better recovered. These results are in a good agreement with the results in Lin et al. (2019), presented in the last section.

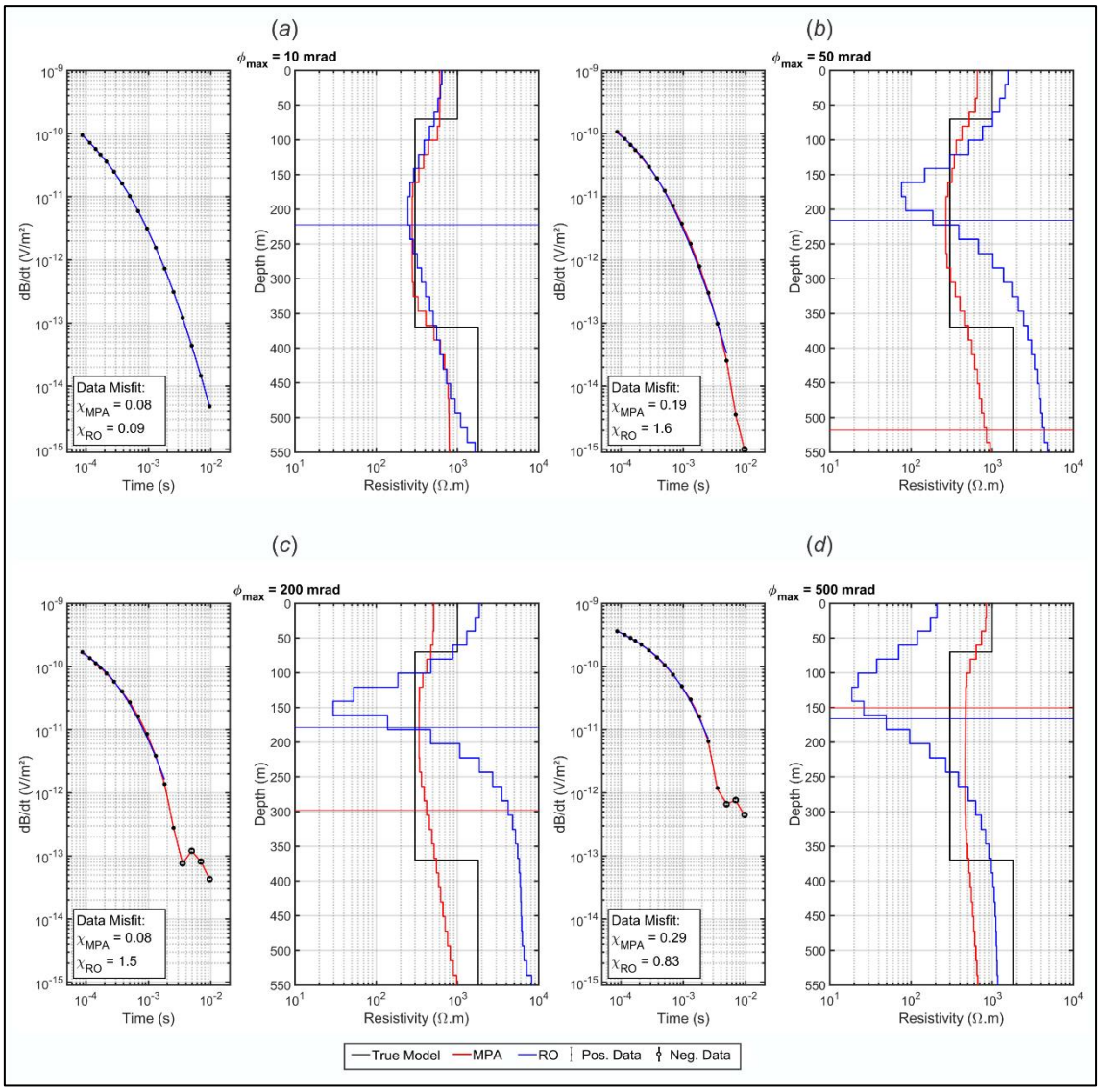

Figure 6. 5: MPA (red curves) and RO (blue curves) resistivity inversion results for the synthetic model presented in Table 2 in Appendix 2, with $10\ mrad \leq \varphi_{max} \leq 500\ mrad$, for a) $\varphi_{max} = 10\ mrad$; b) $\varphi_{max} = 50\ mrad$; c) $\varphi_{max} = 200\ mrad$ and d) $\varphi_{max} = 500\ mrad$. The horizontal lines indicate the DOIs. The true model response is indicated by the black or white dots in the decay curves, in which negatives are represented in white. The resistivity true model is represented by the black curve in the resistivity profiles. Figure reproduced from Couto et al. (2020).

The inversions of the field data presented similar behavior to the synthetic study, as can be seen in Figure 6. 6 and Figure 6. 7, which presents the result for a profile over Lamego's structure (L20810 in Figure 2 in the Appendix 2). The NW portion of the profile presents a resistive artifact in the RO model (Figure 6. 6-a), in the region of the late times negatives decays, while the robust MPA inversion does not present it. Also, for the conductive layer in the profile, RO recovered a much more conductive environment than the robust MPA (Figure 6. 7-a), similarly to the synthetic study. The φ_{max} model (Figure 6. 7-b) recovered the top of an important polarizable layer, dipping towards SE, which vertical position is in good agreement with the top of the carbonaceous schists, as

can be seen in the borehole lithological data. The τ_φ model (Figure 6. 7-c) presents shallow DOIs, except for the soundings with the presence of preserved negative decays. Which may indicate that this model was not well resolved in this profile, possibly due the amount of full positive dB/dt decays and the culled-out negatives within the noise floor. The C model (Figure 6. 7-d) presented a constant model, around 0.5, which is a good indicative that a Cole-Cole spectral domain is preferred over a constant phase parameterization to invert these data.

The main conclusion of this part of the research is that it is possible to achieve reliable resistivity models with the AeroTEM^{HD} data, for a typical QF-like geological environment. In this case, the IP effect was crucial to characterize the structural behavior of the top of the carbonaceous layer, which may be a guide to the define the structural control of Lamego mineralization. Like the results presented in Lin et al. (2019) and Appendix 1, the robust MPA inversion scheme recovered better resistivity models in comparison to the RO parameterization, which helps to avoid erroneous interpretations in this data. The detailed discussion about these results is presented in Appendix 2, in which Couto et al. (2020) is fully reproduced.

The methodological approach for the data processing and modeling presented in this part of the research was intended to be used as a guide to the rest of the AeroTEM^{HD} data in QF region. However, due to the low signal-to-noise ratio of this AeroTEM^{HD} data and the geological differences of the QF's gold deposits, it may be important to evaluate different processing approaches for each area, as discussed in the next section.

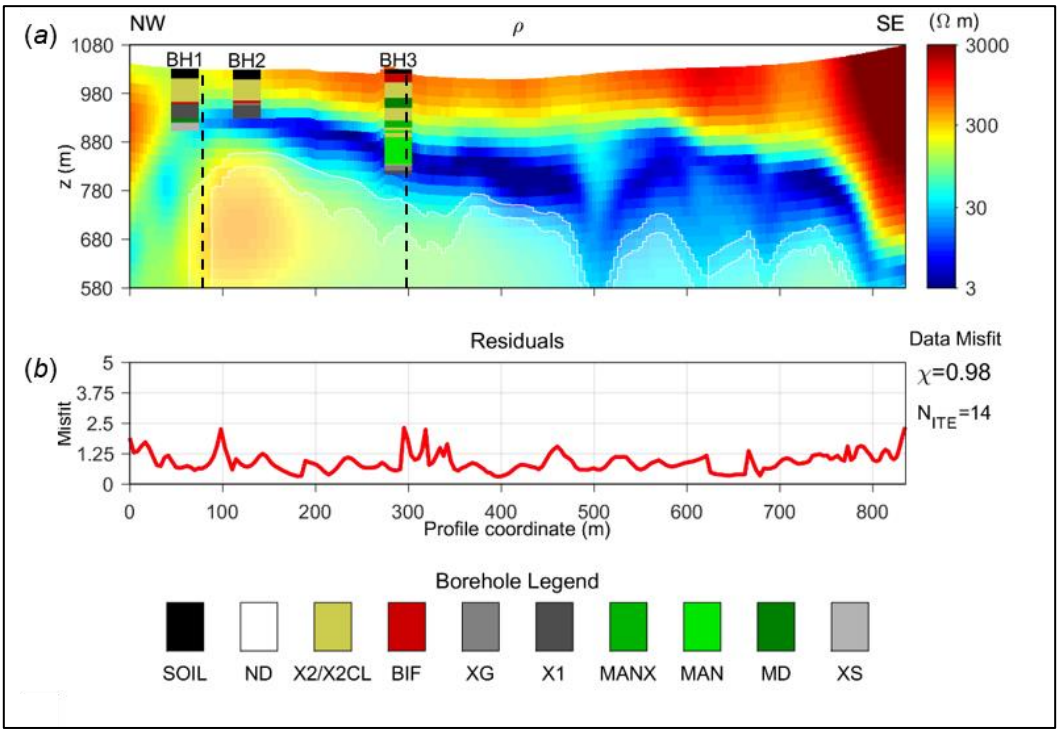

Figure 6. 6: Reproduction of Figure 5 of Paper 2. Resistivity-only LCI for flight line L20810 interval over the Lamego structure. (a) Resistivity section. (b) Data misfit. In the borehole lithological legend: SOIL is the soil layer, ND is the non-descripted interval, X2/X2CL is the micaceous metapelite, BIF represents the banded iron formation layers, XG is the carbonaceous-graphite schists, X1 is the metapelite enriched with carbonaceous material, MAN is the metabasalt/metandesite, MANX is the MAN interval with chloritization alteration, MD is the metadiabase layer and XS is the altered felsic metavulcanoclastic layer. The vertical dashed lines represent the positions of the sounding 19 and 74, presented in Figure 8-a and 8-b in the Appendix 2, respectively.

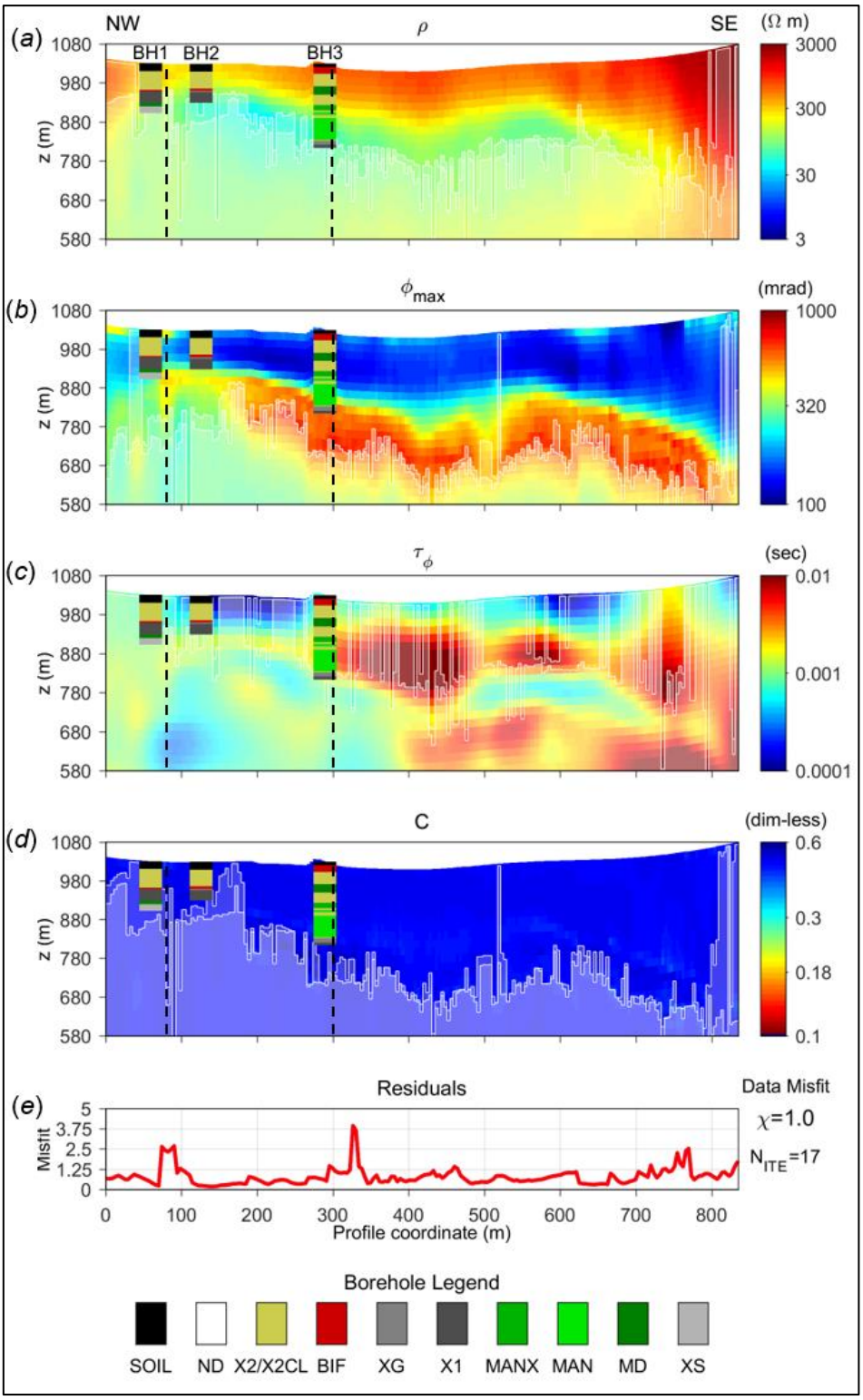

Figure 6. 7: Reproduction of Figure 6 of Paper 2 MPA LCI for flight line L20810 interval over the Lamego structure. (a) Resistivity section. (b) ϕ_{max} section. (c) τ_φ section. (d) C section. (e) Residuals. The borehole description is associated with the borehole legend presented in Figure 4 of Appendix 2. The vertical dashed lines represent the positions of the sounding 19 and 74, presented in Figure 8-a and 8-b in the Appendix 2, respectively

6.3. Case Study 2: AIP and Magnetic Integration in Roça Grande Area

In this section, it is presented the results for the Roça Grande area (see Figure 5. 1 for location context in QF). The aim of this case study is the application of the MPA robust inversion scheme in a regional/district context and less exploited area in QF region, in order to verify its results in a complex 3D structural environment and provide useful information that may conduct further exploration activities. As ancillary information, it was used the airborne magnetic data from RVPh2 survey and the MVI model for the area was integrated in a 3D environment. In the next subsections, it is briefly commented about the local geology in Roça Grande area, the HTEM and magnetic data processing, as well. In the final subsection, we present the inversion results and its integration.

6.3.1. HTEM Data Processing

For the HTEM survey over Roça Grande area, the data processing was conducted similarly to the results presented in Section 6.2 and Couto et al. (2020), but with a slightly difference related to the negative data in the late times. Due to the low signal-to-noise ratio in this part of the survey, the negatives were mostly below the noise floor. However, as discussed in the last section and Couto et al. (2020), the IP effect can be detected in the positive part of the dB/dt decay. In this way, seeking to avoid misinterpretations in our data, during the set-up of the automatic voltage and altitude processing in Aarhus Workbench (Auken et al., 2009), the negative data were culled out, but keeping the steep decays that might be associated with the IP effect. To conduct that, it was used limited lateral average and slope filtering, to preserve the original characteristics of the data, followed by manual processing, similarly to the workflow presented in Kaminski and Viezzoli (2017).

Figure 6. 8 presents pre-processed and processed data for flight line L20950, which is detailed in the following sections. The first one results from the data delivery by Prospectors to CPRM (Prospector, 2011), followed by the waveform alteration discussed

in Section 5.2 and the application of cap filters in Aarhus Workbench[7]. The second results from the processing discussed in the last paragraph. The processing parameters are detailed in Annex 2.

[7] For further information, see http://www.ags-cloud.dk/Wiki/WH_AutomaticProcessingAEMVoltageData?highlight=cap%20filter

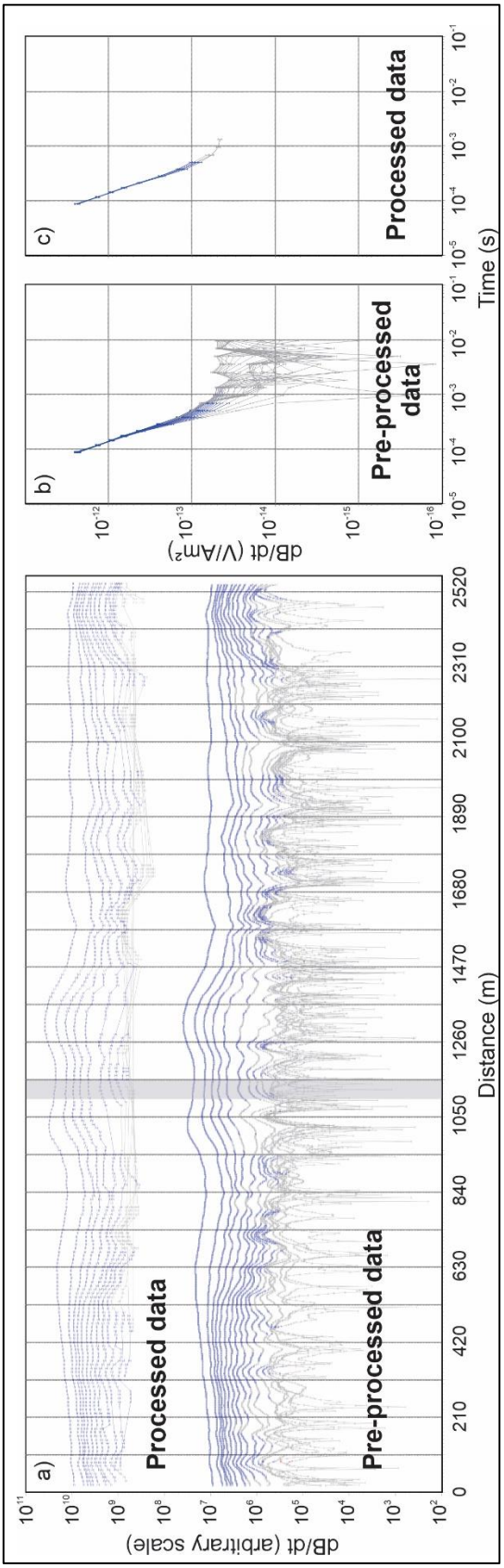

Figure 6. 8 a) Example of ore-processed and processed data for flight line L20950. dB/dt decay detail of the group of soundings for b) Pre-processed data and c) Processed data; The group of soundings presented in b) and c) are indicated by the transparent vertical rectangle in a).

6.3.2. Airborne Magnetic Data Processing

The data processing for the magnetic survey was conducted through two process:

1. **Decorrugation:** in addition to processing described in (CPRM, 2011) to remove any residual flight line influence in the data, through decorrugation process using the combination of butterworth and directional cosine filters. Even though the delivered data within the survey was already microlleved, it was noticed that there still some flight line interference. Then, the processing was conducted in the frequency domain (FFT filters) using the high pass butterworth filter of first order, degree 8 and wavelength 120; and the direction cosine of order 0.5 in to pass data in the lines direction (azimuth 135º). This grid was subtracted from the original microlleved data from the database, then gridded again using the Bigrid algorithm with the de-trend filter perpendicular to the flight lines in Seequent Oasis Montaj software. The result was resampled to database, in which it was subtracted the IGRF reference field, resulting in the final magnetic anomaly field. This procedure was executed for the whole survey. Then, the database was selected to the Roça Grande area.
2. **Regional-residual separation:** in Roça Grande area there is a presence of a regional trend of the magnetic field (Figure 6. 9-a), increasing towards SE. In order to remove any regional influence and prepare the magnetic data to be comparable with the HTEM survey depth scale, it was subtracted a regional magnetic field from the processed data describe in item 1. This regional field was chosen to be the upward continuation filter of 800 m (Figure 6. 9-b). This choice was determined after testing linear and polynomial regressions trends, and other values for upward continuation filters as well. The result is presented in Figure 6. 9-c. The upward continuation filter was performed in the frequency domain in the gridded data processed as described in the last item. Then, it was resampled to database, where the residual calculation was performed.

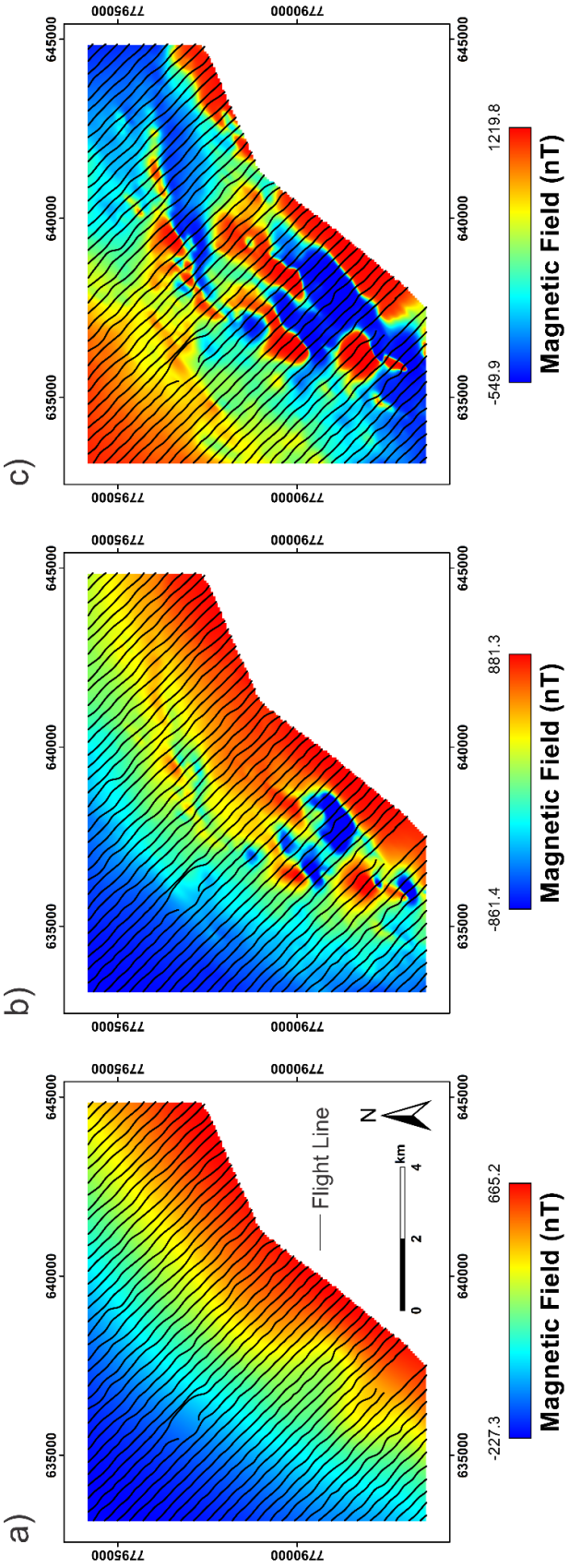

Figure 6. 9: Regional-residual removal for the aeromagnetic data in the Roça Grande area. a) Upward continuation field to 800 m. b) Magnetic anomaly (with IGRF already discounted). c) Residual magnetic field..

6.3.3. Roça Grande Area Local Geology and Geophysical Characterization

The Roça Grande area geology is characterized regional Archean-Paleoproterozoic WSW-ENE thrust fault system, deformed during the Brasiliano Orogeny (Baltazar and Zuchetti, 2007). Lithologicaly (Figure 6. 10), it is composed by the rocks from the Nova Lima Group, in which predominantly occurs mafic-ultramafic metavolcanic sequences, sericite-quartz schists, carbonaceous metapelites, quartzites and BIFs. The Au mineralization is controlled by the ENE-WSW lineaments system and commonly associated with the elongated BIFs layers along these structures, in which may be present in the form of metallic sulfide dissemination zones within these horizons. The mines presented in Figure 6. 10 are both active and inactive. The most economically relevant gold mine in this area so far is Roça Grande Mine, controlled by Jaguar Mining.

Figure 6. 11 presents the geological map and geophysical anomalies in the Roça Grande area. The magnetic anomalies for the residual field (Figure 6. 11-b), 1st order vertical derivative (DZ1 - Figure 6. 11-c) and the total gradient amplitude (TGA – Figure 6. 11-d) identify a magnetic trend oriented according to the NNE-SSW regional structural control of the area (Figure 6. 11-a), with many dipoles along this trend, with variable dipole orientation in between NW-SE and N-S directions, which could indicate the strong remanent magnetization in this area, can be observed in the residual field and DZ1 maps (Figure 6. 11-a and Figure 6. 11-b, respectively). Thereby, the MVI approach was chosen to model this data. These magnetic anomalies are in good positional agreement with the BIFs layers along the NNW-SSE structure, suggesting that these iron formations might be strongly magnetic in comparison to the mafic background. As suggested by Couto et al. (2016), these magnetic bodies might dip towards to SE, following the regional structural control. All magnetic products presented in this figure were derived from the data processing described in Subsection 6.3.2.

The AeroTEM^{HD} data (Figure 6. 11-e) presents high transient (dB/dt) contrast in the late-times interval (channel 7 in the off-times) oriented according to the BIFs/magnetic trend, suggesting conductive contrast in these lineaments. This result suggest that these lineaments might present lower conductivity contrast in comparison to the mafic/ultramafic resistive background, which could be potential targets to identify metallic sulfide zones associated with the BIFs layers and Au mineralization, as discussed in the first paragraph of this section. The AeroTEM^{HD} product presented in

Figure 6. 11-e was derived from the original delivered dataset, without any previous processing.

In the following subsections, the results for the magnetic and AeroTEM^{HD} data are presented.

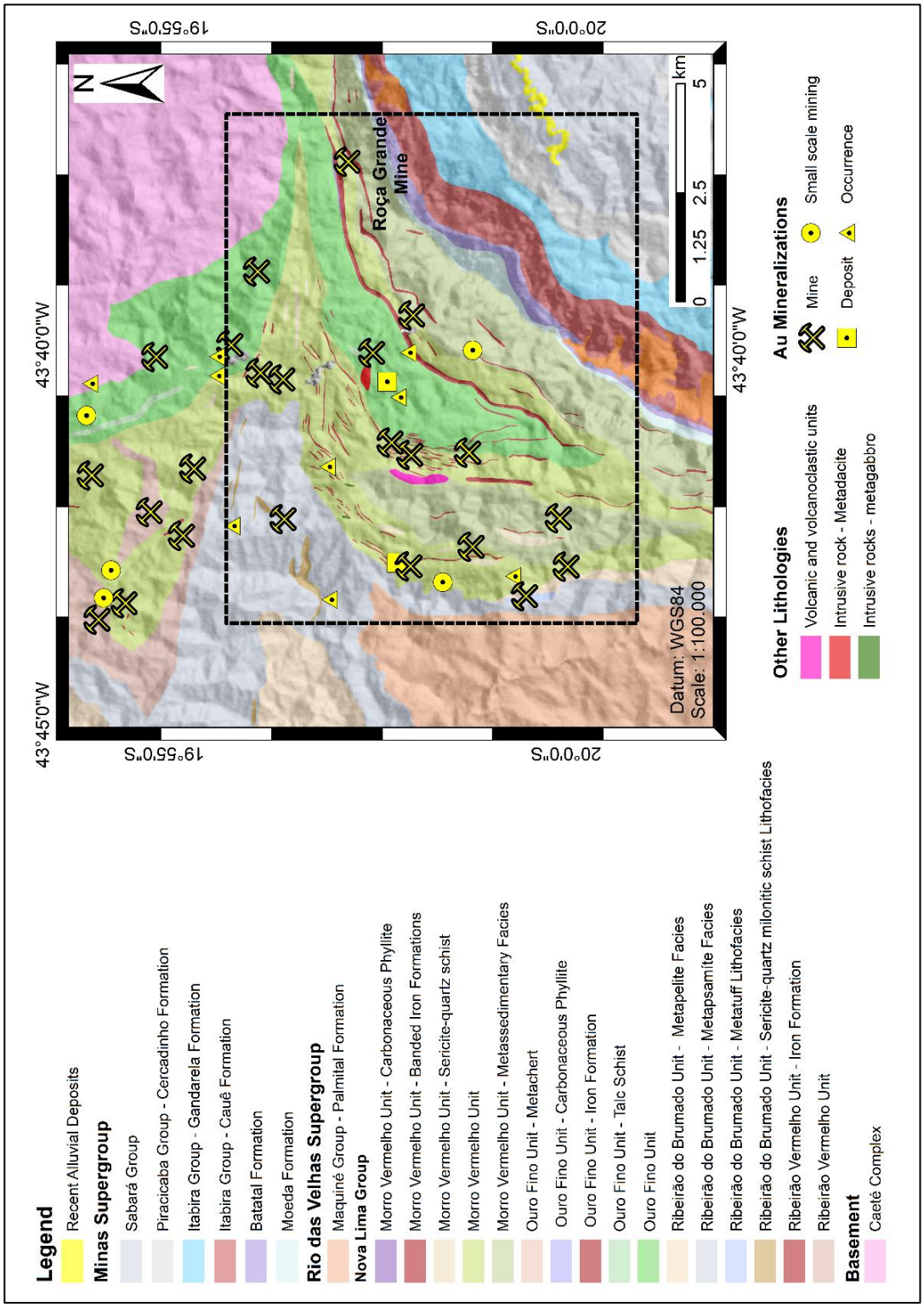

Figure 6. 10: Simplified geological map and main Au mineralization for the Roça Grande area. The Roça Grande Mine is indicated in the East portion of the area. This map is a based on Silva et al. (2020).

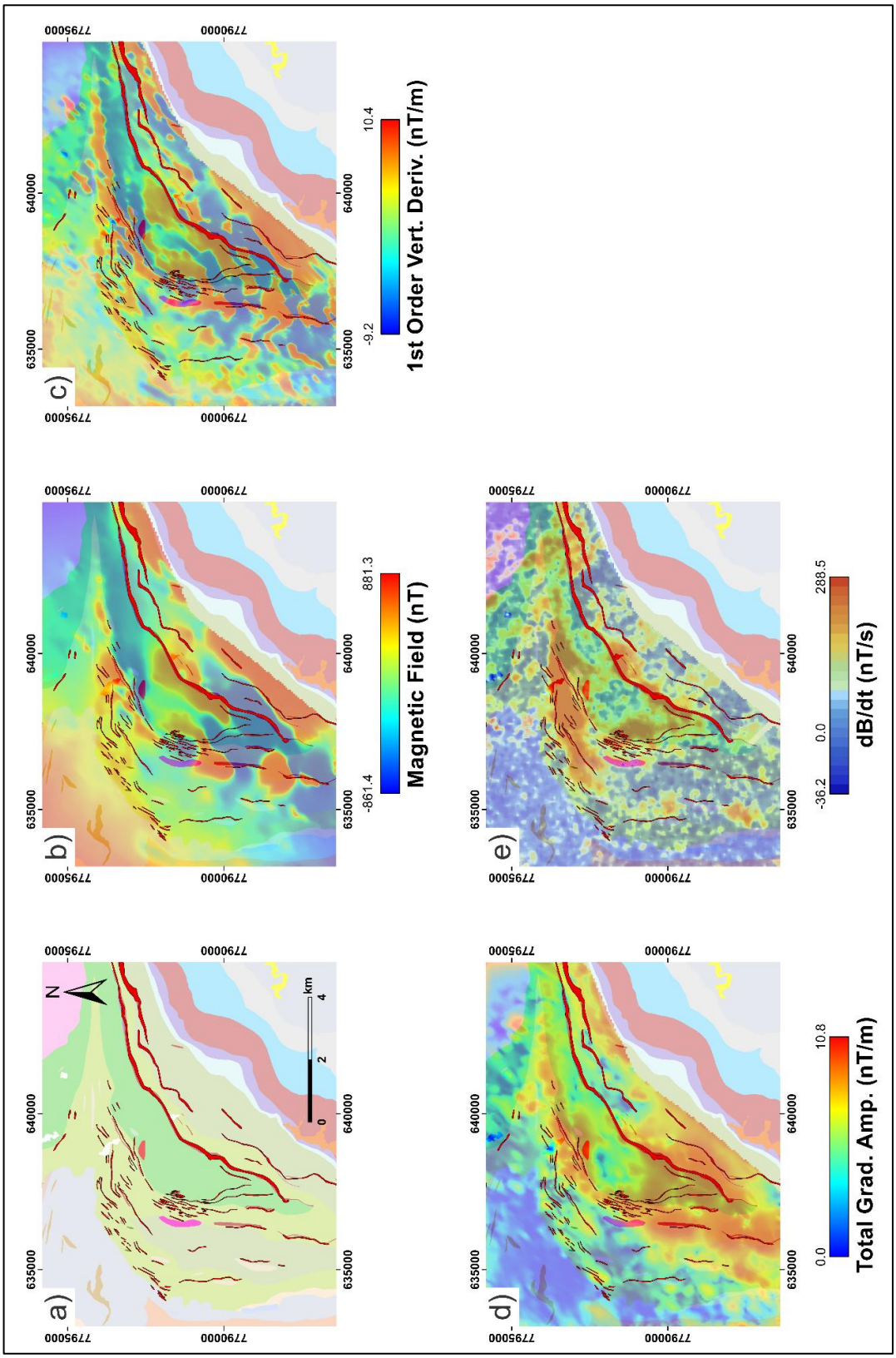

Figure 6. 11: Geophysical signatures compared to the geology in Roça Grande area. a) Simplified geological map. b) Residual magnetic field. c) First order vertical derivative of the residual field. d) Total gradient amplitude of the residual data. e) AeroTEM^{HD} dB/dt for the 7th channel in off-times regimes.

6.3.4. MVI General Results in Roça Grande Area

In order to evaluate the magnetic BIFs bodies extension along the NNE-SSE lineament in a regional scale, the magnetic data in the Roça Grande area was inverted using the MVI algorithm, as discussed in Section 4.4, seeking to avoid remanent magnetization issues in the data. It is not discussed the nature of the remanent magnetization in this research, only the implications of the MVI models for the geology in Roça Grande area. In addition, all discussions were made based on the results for the amplitude of the $\boldsymbol{k}_{MVI}$, as presented in equation 4.4.18.

The standard deviation of the noise level for this magnetic data is unknown, which is necessary to estimate the misfit function in the inversion process, as seen in equation 4.4.11. Thereby, we followed the procedure as presented in Oldenburg and Li (2005) and Melo et al. (2017), already described in subsection 4.4.2, using the L-Curve criterion (Hansen, 1992). Setting up the first estimate to 1 nT, we repeated the process three times using the L-curve criterion, ending up to a final estimation of the standard deviation of the noise level as 1.4771 nT, with best Tikhonov regulation parameter for the trade-off parameter equals to 750. This model was chosen after comparison between the use of the spline option and pruning algorithm in the REGU toolbox (Hanson, 2007). The chosen model was the one indicated by the spline method, through visual inspection and comparison with the models around the vicinity of the accepted regularization parameter.

In the L-Curve analysis, all inversions were conducted using the IRI-focus and the lower bound constrains. This second constrain was fixed in zero. The mesh discretization used to all models was composed by cells with 50x50x25 m, following the suggestion of VOXI documentation[8]. The model bottom depth was set up to 2000 m and the top to the digital terrain model for the area (Shuttle Radar Topography Mission - SRTM model, with 30 m lateral resolution).

The results are presented in Figure 6. 12 and Figure 6. 13. The first figure presents the comparison between the predicted response (Figure 6. 12-a) and the measured data (Figure 6. 12-b), as well the data residual between these two grids (predicted subtracted from the measured data). It is observed in Figure 6. 12-c that the data residual over Roça

[8] See https://my.seequent.com/learning/459/1427/1949 for further information.

Grande area is described by a symmetric statistical distribution (Figure 6. 12-d) with mean value and median compatibles to zero and between each other in one standard deviation. These results indicate a good data fitting for the chosen model.

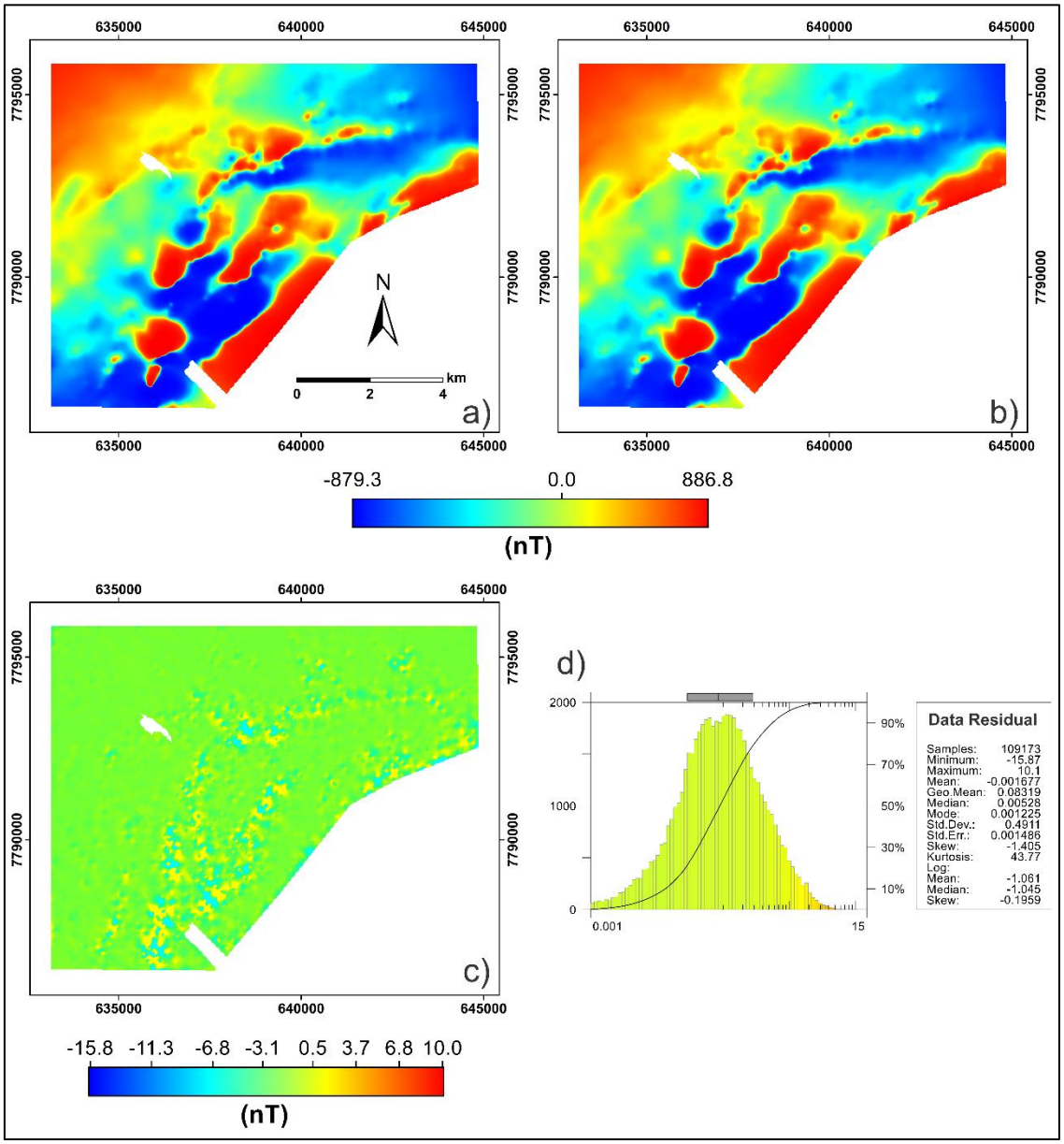

Figure 6. 12: Data residual analysis for the chosen model in Roça Grande area, after the application of L-curve criterion. a) Predicted data. b) Measured data. c) Data residual (predicted minus measured data). d) Log-normalized distribution of the data residual in the area, with the statistical summary.

For the shallow and intermediate depths (50 m to 300 m) – Figure 6. 13-a, Figure 6. 13-b, Figure 6. 13-c, Figure 6. 13-d, the high magnetic susceptibility anomalies (> 0.012 SI) are strongly correlated with the BIFs layers along the ENE-WSW lineament. In fact, previous field work in this area confirmed that these BIFs bodies are strongly magnetized in relation to the background, although petrophysical data is still absent to

this area, to the knowledge of the author so far. For higher depths (> 500 m), the magnetic susceptibility anomalies start blurring for both East and SW portions of the area (Figure 6. 13-e and Figure 6. 13-f), achieving smoother solutions, while it considerably decreased in the NNE portion at the 1000 m depth. The "blurring effect" is due to the ambiguity of the magnetic method (Fedi et al., 2005 and 2007) related to the indetermination to define the bottom limit of potential field sources, as the inversions were conducted with no depth constrain model. However, the structural control of the magnetic susceptibility is still preserved, as can be seen in Figure 6. 13 and Figure 6. 14.

In Figure 6. 14 a general view of the MVI magnetic susceptibility above 0.012SI is presented. The model was limited to depth 1000 m, to facilitate the visualization. It can be observed that the magnetic bodies in the Eastern portion were recovered preserving the SE dipping general direction (Figure 6. 14-a and Figure 6. 14-b), in agreement with the structural control of this area (Couto et al., 2017; Baltazar and Zuchetti, 2007), with shallower extension in contrast to the magnetic bodies in the Western portion. This might be an effect of the smaller spatial density of BIFs layers to the East. The section L20950 is discussed with more detail in the following sections.

In the next sections, the AeroTEM^{HD} MPA inversions models are discussed and compared with the RO models, followed by an integrated interpretation with the MVI results.

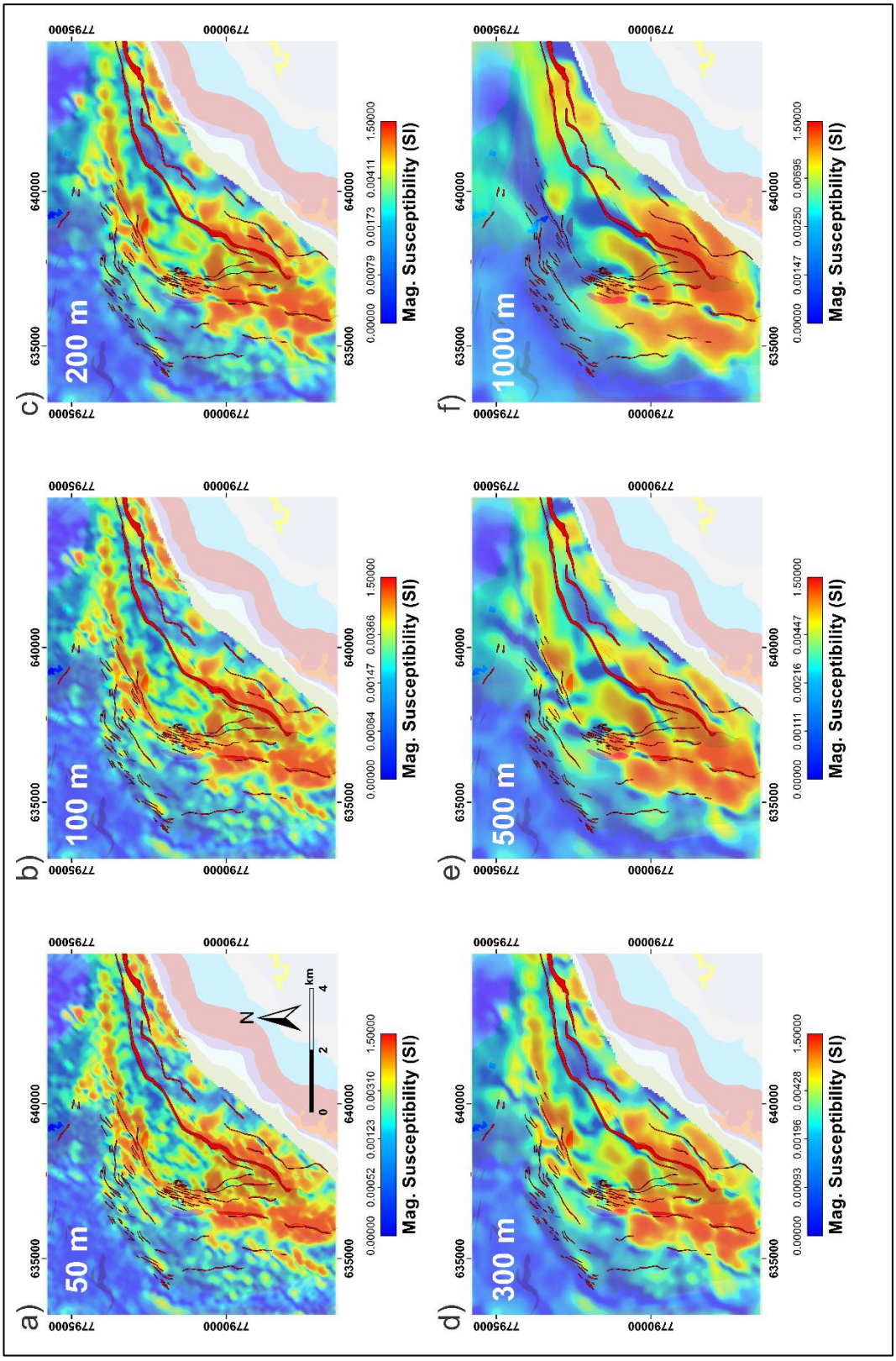

Figure 6. 13: MVI depth slices for a) 50 m, b) 100 m, c) 200 m, d) 300 m, e) 500 m e f) 1000 m.

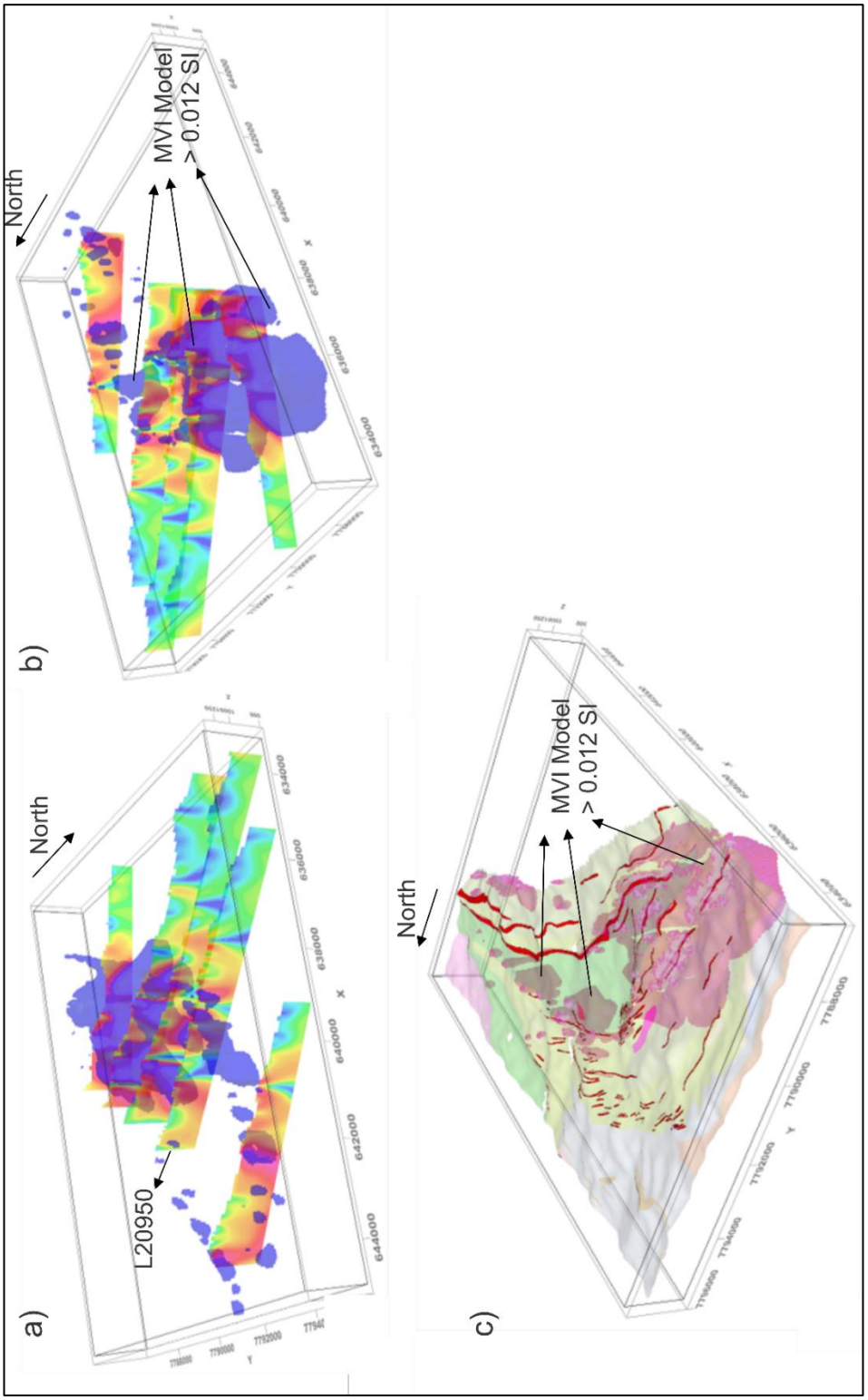

Figure 6. 14: General view of MVI susceptibility model in Roça Grande area. A) View from Northeast. B) View from Southwest. C) View from Southwest integrated with the geological map. In all three models the cells present magnetic susceptibility above 0.012 SI. Section L20950 is commented in the following sections. The vertical exaggeration factor of this is figures is 1.5.

6.3.5. AeroTEM^{HD} MPA Inversions Results

In this subsection, the MPA inversions are presented. For comparison, RO and MPA inversions were conducted. For the MPA inversions, the input resistivity model was defined using the robust scheme (Li et al., 2019), as discussed in Sections 6.1 and 6.2 (Appendix 1 and B, respectively). The φ_{max} was set to 100 mrad, while the $\tau_\rho = 1$ ms and $C = 0.5$. As any a-priori information about the phase value background was available in the area, the initial φ_{max} was defined based on the greenstone metabasalts values presented in Smith et al. (1983), which reported values above 70 mrad for this type of lithology in the AeroTEM^{HD} frequency operation range (100 to 1000 Hz). It was used loose constrains (bigger than 4) both for lateral and value variations of ρ and φ_{max}, in order adequate the model for a regional/district investigation. The other two MPA parameters were not constrained. The LCI models were discretized in 30 layers, using the L_2 norm for minimizing both RO and MPA inversions. The same initial resistivity model was used for the RO inversions.

In Figure 6. 15 it is presented the comparison between RO and MPA data residuals for the inversion in Roça Grande area. In RO data residual (Figure 6. 15-a), the higher levels (> 3.0) occur associated with the general ENE-WSW structural control, in some portions over the mafic units and in other around the BIFs bodies. These results indicates that the RO parameterization is not fitting the data properly in these areas. On the other hand, the MPA presents data residual (Figure 6. 15-b) considerably lower in the overall area (< 1.5), indicating a best model fitting in comparison to RO results. This result could be expected, as MPA is a multiparametric inversion considering four parameters to be inverted ($\rho_{MPA}, \varphi_{max}, \tau_\varphi, C$), while RO takes into account only the resistivity.

However, it is also noted that the DOI of these two parameterizations are considerably different, as presented in Figure 6. 16. For RO (Figure 6. 16-a), the DOIs go down to 100 m for the mostly part of the model. For MPA (Figure 6. 16-b) it smaller than 10 m in the region of the mafic units, but can goes below 100 m around the BIFs zones, both for the ρ_{MPA} and φ_{max} models. It is also observed a strong spatial correlation between the DOIs and the ENE-WSW lineament in the BIFs zones in the Northern and Southern portions of the area. The DOI calculation method vary between RO and MPA. The “flight line” pattern that can be seen in these figures are not related to flight issues,

but to the nature of the LCI algorithm, which does not consider lateral variations between the flight lines.

The |RO DOIs use the methodology presented in Christiansen and Auken (2012), which bases the calculation on the model output and its relation to the system response, as described in Section 4.2.1. The MPA DOIs use the methodology developed by Fiandaca et al. (2015), which is an evolution of the one used in the RO parameterization. It includes the cross-correlation analysis between MPA parameters, seeking to decreasing the correlation between them. It also uses the system response due to model output, likely the one in the RO parameterization. In this way, both DOI sensitivity methods are related to the model parameterization.

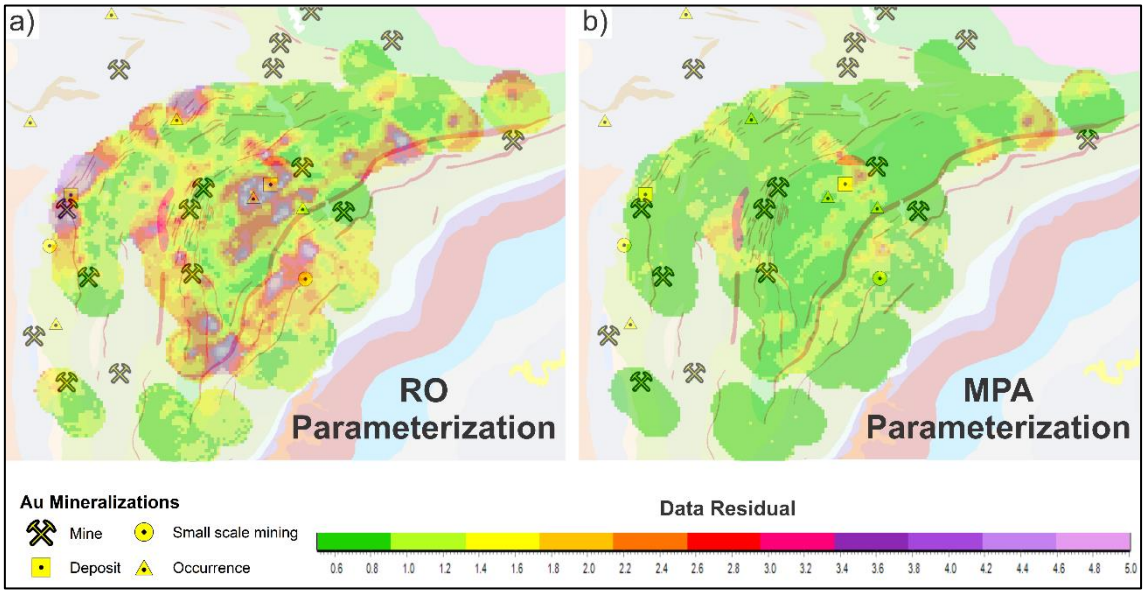

Figure 6. 15: Data residual for a) RO and b) MPA parameterizations. Note the low definition of the RO results , while MPA presents data residuals below 1.5 for mostly parts of the area.

As could be seen in Figure 6. 16, the RO parameterization could not define the resistivity model in the mafic units areas, while the MPA results presented a best data fit. Also, MPA did not defined the deep layers.

The difference in the behavior of these two models can be related to the so called “AIP trap” for airborne TEM systems, extensively discussed in Viezzoli et al. (2020), which is discussed further in the text. These authors discuss that shallow polarizable layers can be determinant do define the sensitivity for airborne TEM system to characterize the shallow depth intervals. Due to the shallow chargeable layers, the IP transient currents may be dominant over the pure EM induction (the transient without the

IP effect) and dominate the voltage measurement in the AEM receiver. As consequence, not considering the IP effect in a situation with shallow polarizable layers can lead to erroneous definition of the resistivity model. In a situation with shallow conductive layers over a resistive basement, the RO parameterization can overestimate the resistivity and depth of the top of the deep resistor, while an IP parameterization can be able to recover a more reliable model. Examples of this situation were presented in Section 6.1 and 6.2. Viezzoli et al. (2020) also present a case study like this.

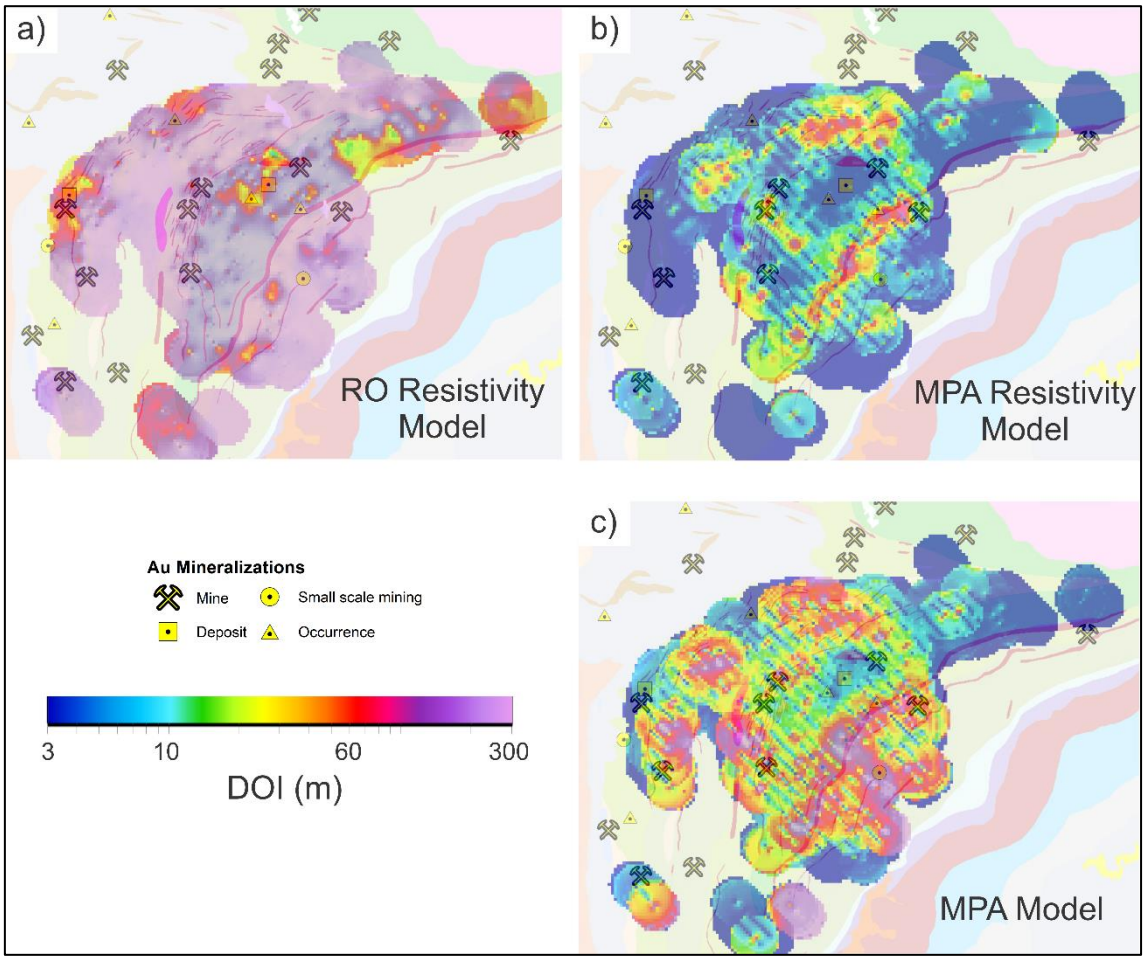

Figure 6. 16: DOIs for the a) resistivity RO model, b) resistivity MPA model and c) φ_{max} model.

This effect can be seen in the data results for Roça Grande area, as well. In Figure 6. 17 two sections for flight lines L20901 and L20901 are presented with resistivity and φ_{max} models for RO and MPA parameterizations. It can be noted that the resistive bodies associated with the mafic domains are more resistive and shallower in the RO models than in MPA. However, in the MPA model, it is not safe to infer the depth to the top of these resistive layers, as they are bellow DOI. What can be noted about the resistivity

models for MPA and RO is that the shallow layers (down to 4 m) are very conductive (< 100 Ohm.m) in both models.

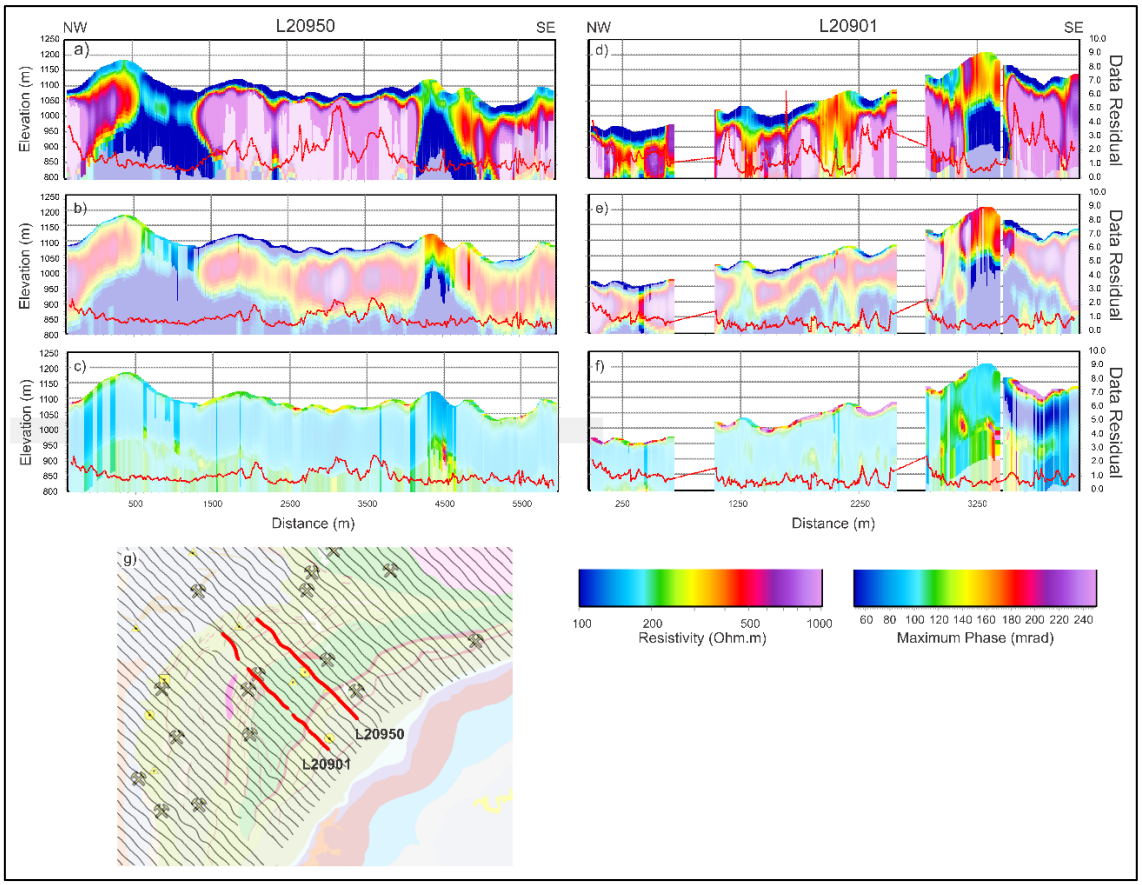

Figure 6. 17 . Section models for RO (upper panels) and MPA (lower panels) for flight lines L20950 (left) and L20901 (right). a) Resistivity RO, b) resistivity MPA and c) φ_{max} models for L20950, with vertical exaggeration factor of 13. d) Resistivity RO, resistivity MPA and φ_{max} models for L20901, with vertical exaggeration of 9.4. g) The location map for these flight lines. In the sections, the red line in the bottom represents the data residual. DOIs are represented by the vertical white transparent rectangles.

In fact, in these shallow layers (< 10 m), these models seem to present compatible spatial distribution, as can be observed in Figure 6. 18-a (RO) and Figure 6. 18-e (MPA), with low resistivity values and spatial related within the areas of mafic units. However, as it goes deeper, RO becomes more resistive and spatially blurry within the mafic units, while it presents conductive lineaments parallel to the ENE-WSW oriented BIFs bodies in the Northern and Central portion of the area (Figure 6. 18-b, Figure 6. 18-c a Figure 6. 18-d). These deep conductive horizons can be observed in the sections of Figure 6. 17, in the NW and SE portions as well. For the MPA resistivity model it can be observed that in the regions where DOI goes below 100 m, these conductors along the BIF lineament are still preserved as well, while it is not possible to infer other geoelectrical structures in the deep part of this model, due to the DOI limitation.

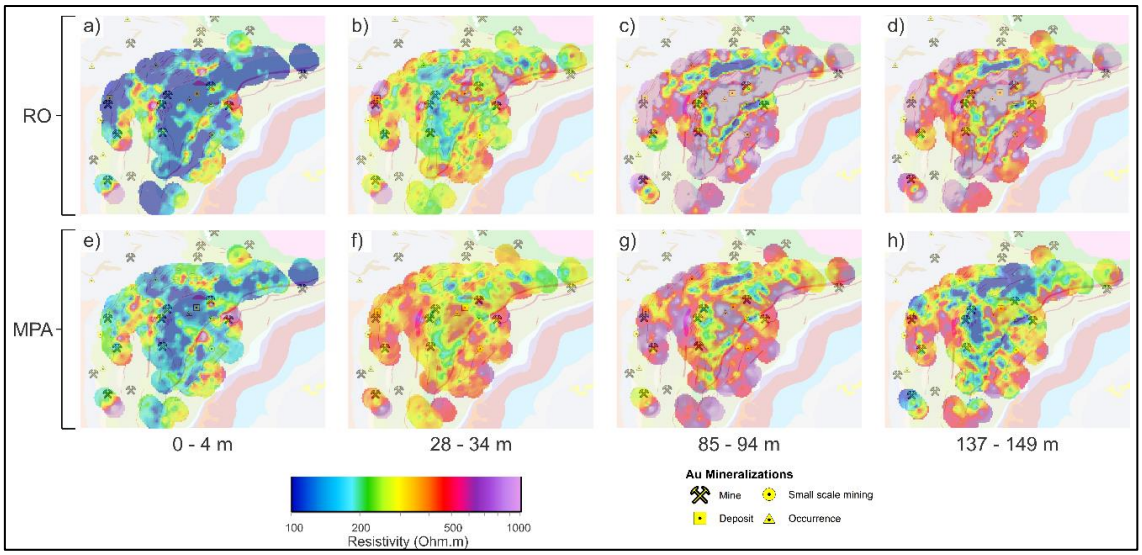

Figure 6. 18: Resistivity depth slices for depth intervals a) 0-4 m, b) 28-34 m, c) 85-94 m and d) 137-149 m for RO model. e), f), g) and h) present the same depth slices for MPA model.

In Figure 6. 19, it is presented the φ_{max} depth slices. It is clear that the first 4 m depth within the Ouro Fino Formation mafic domain are highly polarizable, with φ_{max} above 150 mrad. These shallow polarizable layers can be seen in the φ_{max} sections in Figure 6. 17-c and Figure 6. 19-f. As commented above, this result could be related to an "AIP trap" process, as described in Viezzoli et al. (2020), and might justify the very shallow DOI behavior within this domain seen in Figure 6. 16. According to Viezzoli et al. (2020), if the IP induced currents were imprisoned in the first polarizable layers at the point to domain the system response in the early times, then the model will present high sensitivity for the shallow layers. Thereby, MPA may not recover deeper information properly. On the other hand, the RO parameterization will "see" the model space as a conductive/resistive interface and will look for the accordingly resistivity model. As both DOIs calculation methodologies described above are based in the system response to a defined parameterization, they may vary. The shallow part of the model in the mafic zones (depth < 10m) is presented as conductive and very chargeable layer.

For the deeper parts of the model, it is noted that polarizable structures emerge in zones where MPA DOI is below 100 m (Figure 6. 19-b, Figure 6. 19-c and Figure 6. 19-d). In fact, in the Northern portion of the area, a polarizable anomaly (>150 mrad) emerges in a BIF zone. At deeper depths, this polarizable zone increases laterally along the ENE-WSW trend, following the structure control of the BIF zones. In the Southern portion, another chargeable horizon emerges below 137 m, along the ENE-WSW trend. These

deep polarizable bodies can be seen in SE portion in the sections of Figure 6. 17-c and Figure 6. 17-f, deeping towards SE. These anomalies may be positioned nearby carbonaceous schist horizons, according to borehole information. The discussion for these results were detailed in the next subsection.

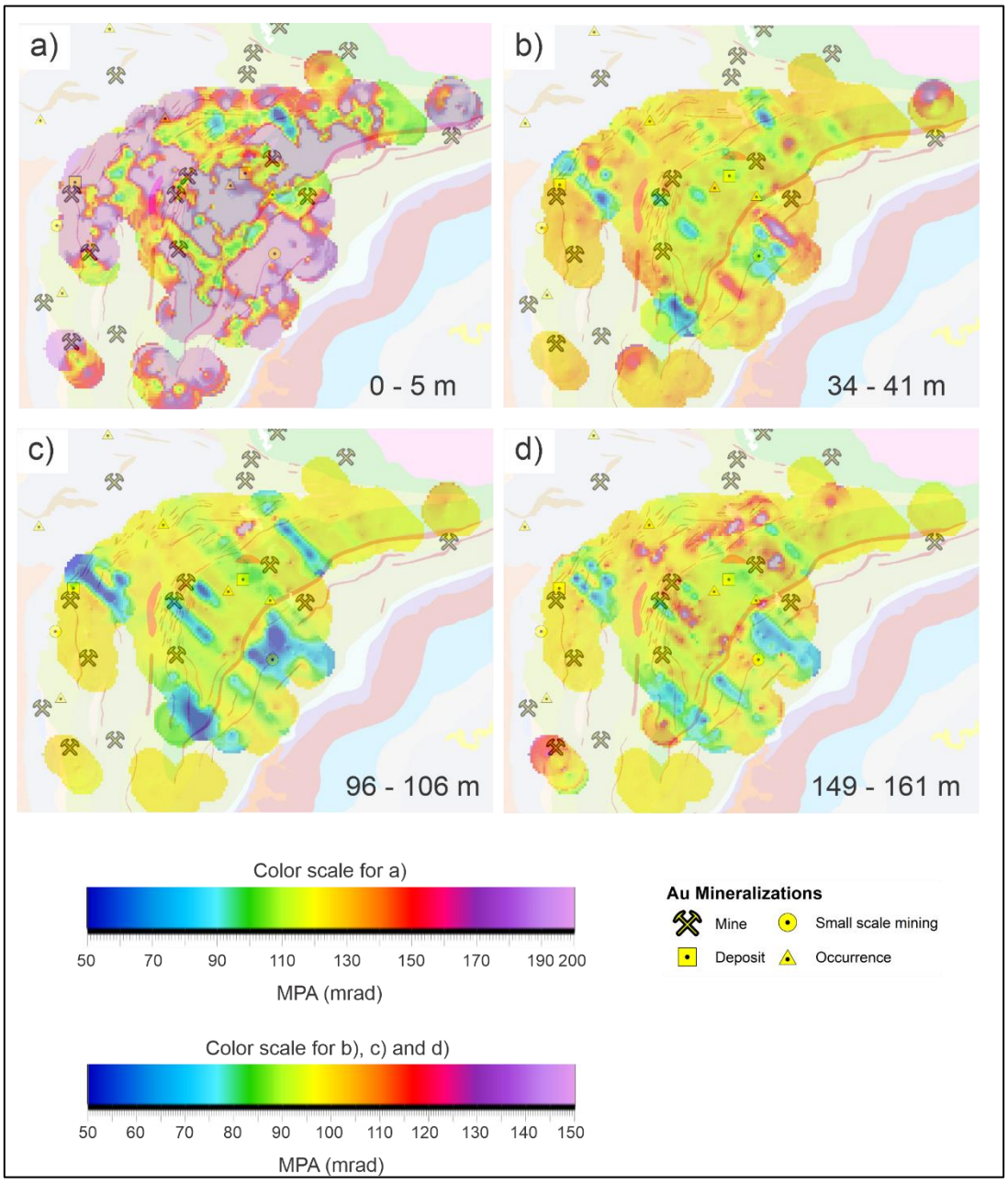

Figure 6. 19: φ_{max} depth slices for a) 0-4 m, b) 28-34 m, c) 85-84 m and d) 137-149 m.

The strong shallow IP effect seen in Figure 6. 19-a may be a result of overburden process over the metamafic units (Ouro Fino and Morro Vermelho Formations) in the QF region, more intensively in the Ouro Fino Formation. Although there are occurrences of other lithological types, like carbonaceous, BIFs and felsic units, they occur subordinately

(Silva et al., 2020). Most part of the outcrops in this area occur as thick layers affected by strong weathering, as can be seen in Figure 6. 20-c. The comparison between the simplified geological map and the gamaspectrometric data (Figure 6. 20-a and Figure 6. 20-b, respectively) also presents lower counting all over the Ouro Fino unit, a typical characteristic of mafic domains. In fact, two boreholes from Jaguar Mining at central portion of Ouro Fino unit show soil+saprolite combination with 43 m tick starting from the surface, formed over the metabasalts.

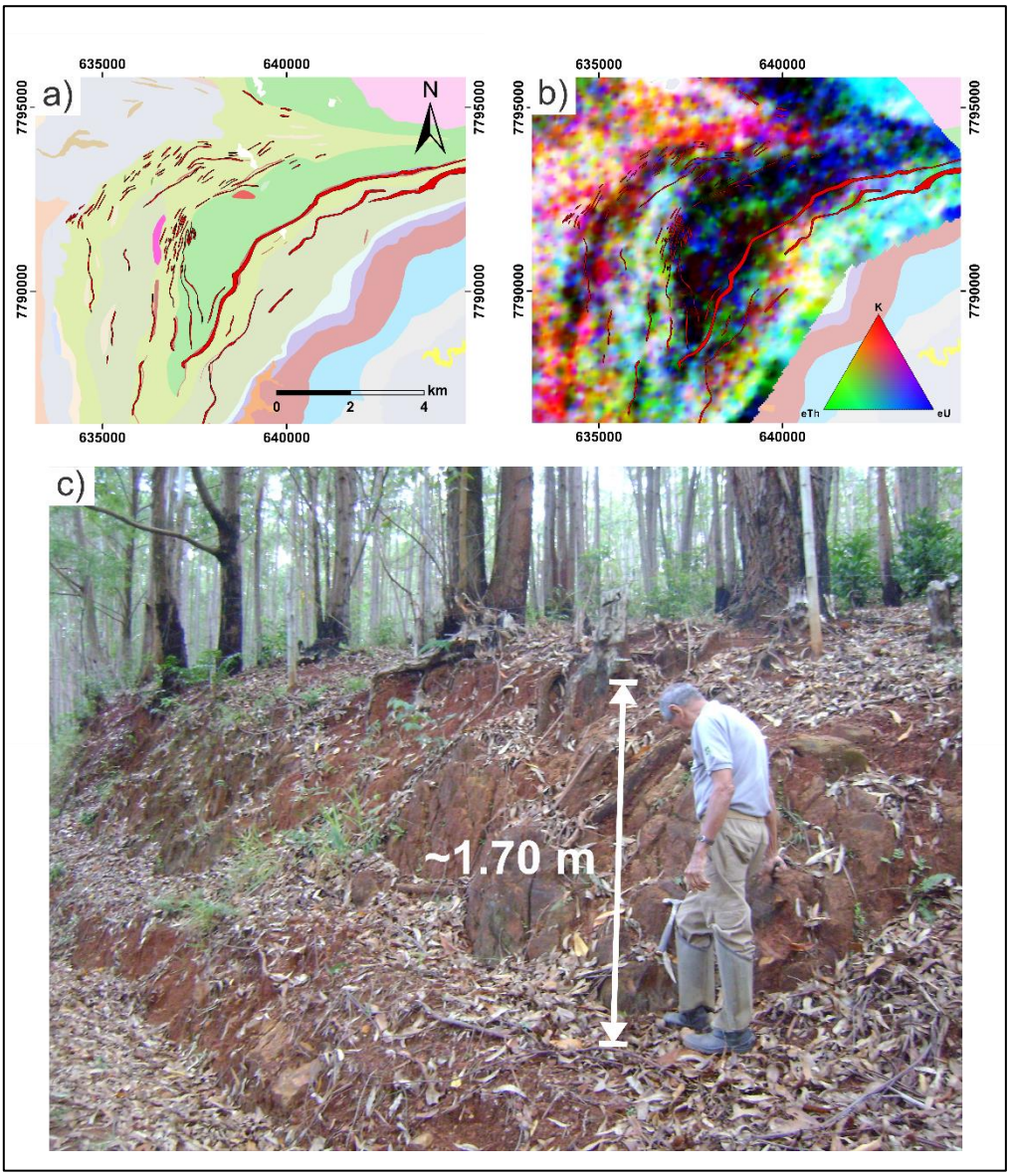

Figure 6. 20: a) Simplified geological map of Roça Grande area for reference. b) RGB ternary image of K(%), eTh (ppm) and eU (ppm) data from the gamascpectrometic survey in the area, the BIFs layer (in red) are presented for reference. c) Typical strongly altered metabasalt outcrop from Ouro Fino Formation, most outcrops in the area are like this one in the picture (Credits for the photo: Joanna Chaves Souto Araújo).

In the data, the shallow IP effect can be observed as very steep decay in the early times following to the late times, suggesting an AIP trap, as commented in Viezzoli (2020). It can be seen that (Figure 6. 21-a) for soundings within the Ouro Fino Formation mafic domain with strong soil+saprolite formation process (point B in Figure 6. 21-b), the data presents a very steep decay starting from the early times. However, outside of this domain, in parts of the BIFs zones trend, the decay is slower and can become steep in the late times (point A in Figure 6. 21-b), suggesting the influence of deep IP effect which justify the polarizable anomalies in the SE portion of the φ_{max} sections in Figure 6. 17.

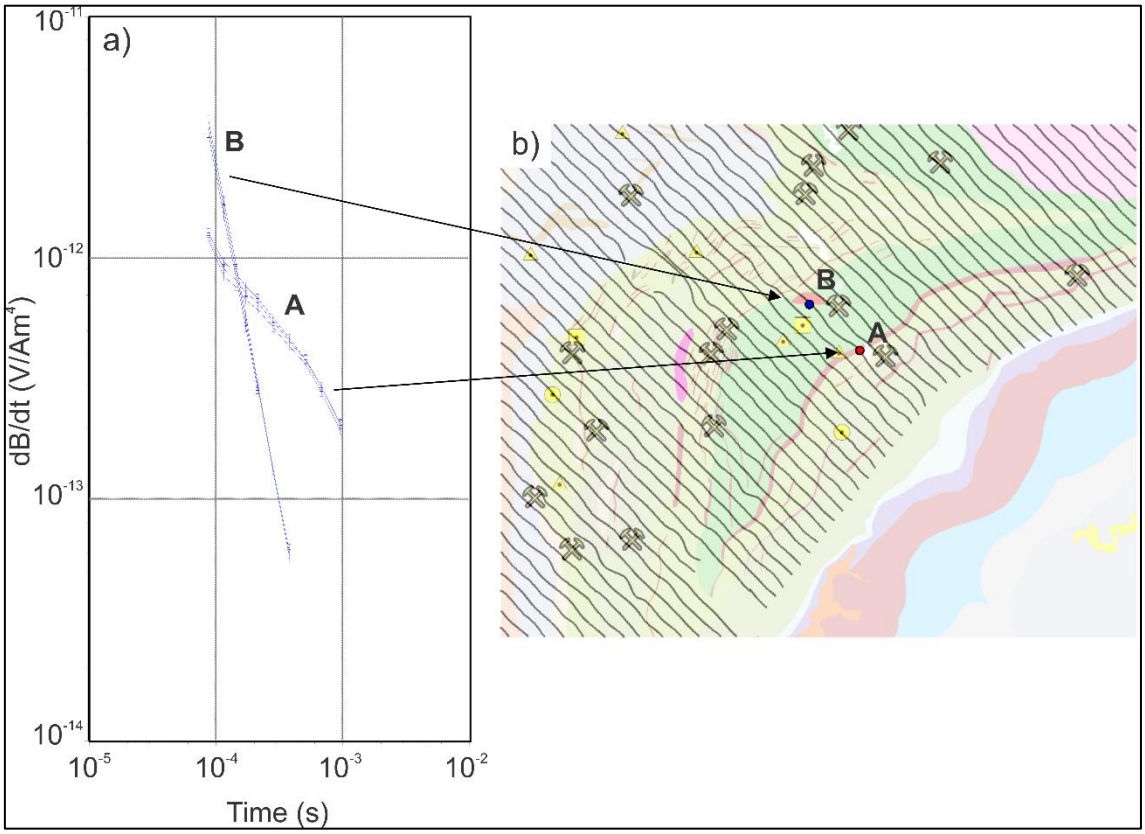

Figure 6. 21: a) dB/dt decays for two set of processed soundings in the region of point A and B. b) Location map of point A and B.

In the next subsection, the chargeable anomalies presented in the depths below 100 m in the Northern and Southern (Figure 6. 22) parts of the area are detailed discussed and interpreted under an mineral exploration paradigm.

6.3.6. Interpretation of Results for Exploration Targets

In this subsection, it is presented the joint interpretation of both AeroTEM^{HD} and magnetic results to study economical potentiality in the Roça Grande area. The aim of this subsection is to identify chargeable and magnetic susceptibility targets, possible related to exploration targets.

As commented in Subsection 6.3.3, the Au mineralizations in the Roça Grande area are predominantly related to the BIFs bodies and carbonaceous horizons (Pressaco and Sepp, 2018). In this way, the deeper AIP anomalies at depths below the apparent shallow IP effect, associated with magnetic anomalies in the BIFs zones and their structural control, should be targets of interest.

In Figure 6. 22, it is presented depth slices comparing two depths intervals for the φ_{max} and the amplitude of the MVI magnetic susceptibility models: 96–106 m and (Figure 6. 22-a and Figure 6. 22 - b) and 150 – 161 m (Figure 6. 22-c and Figure 6. 22-d). Following the criteria described in the last paragraph, two interesting φ_{max} anomalies emerged in the Southern and Northen portions of Roça Grande area, which will be called from now on as Anomaly 1 and Anomaly 2, respectively.

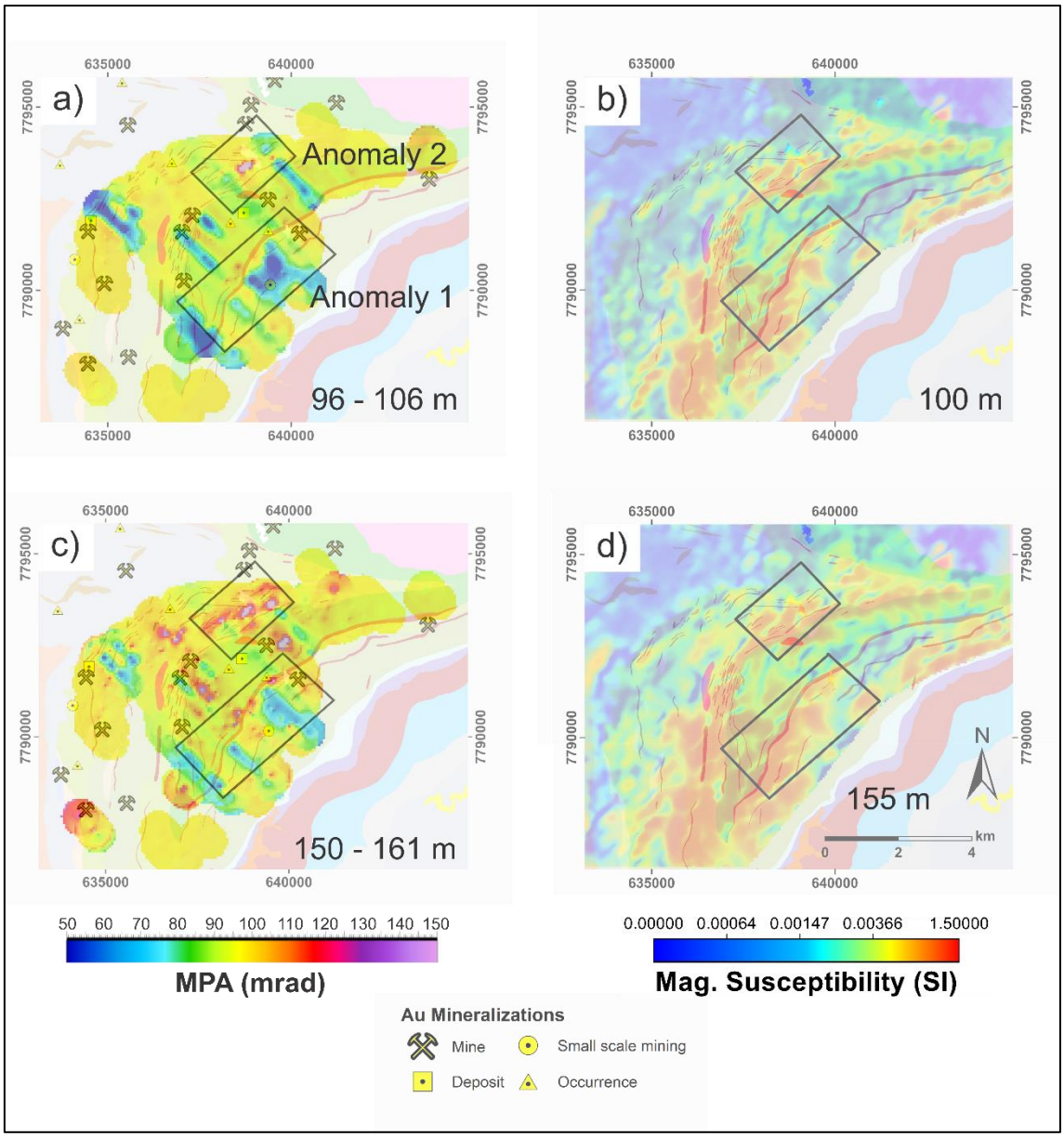

Figure 6. 22: Depth slices for φ_{max} and amplitude of MVI magnetic susceptibility model for a)96-106 m for φ_{max}, b) 100 m for MVI, c) 150-161 m for φ_{max} and 155 m for MVI. The Anomalies 1 and 2 areas are indicated by the black polygon in the figures.

From Figure 6. 22, it can be observed that Anomaly 1 begin to emerge at depth interval 96-106 m, which becomes stronger (> 120 mrad) at depth interval 150-161 m, with two chargeable anomalies following the ENE-WSW trend. The MVI model shows strong magnetic susceptibility anomalies (> 1.0 SI) oriented to this trend and same depths intervals, following the BIFs layers as well.

The detail of this anomalous area is presented in Figure 6. 23, which indicates polarizable anomaly (φ_{max}>150 mrad) following the ENE-WSW trend (Figure 6. 23-a), as the above-mentioned. The MVI magnetic susceptibility (> 0 05 SI) model identified a

magnetic lineament that is positioned according to the regional trend, as well (Figure 6. 23-b).

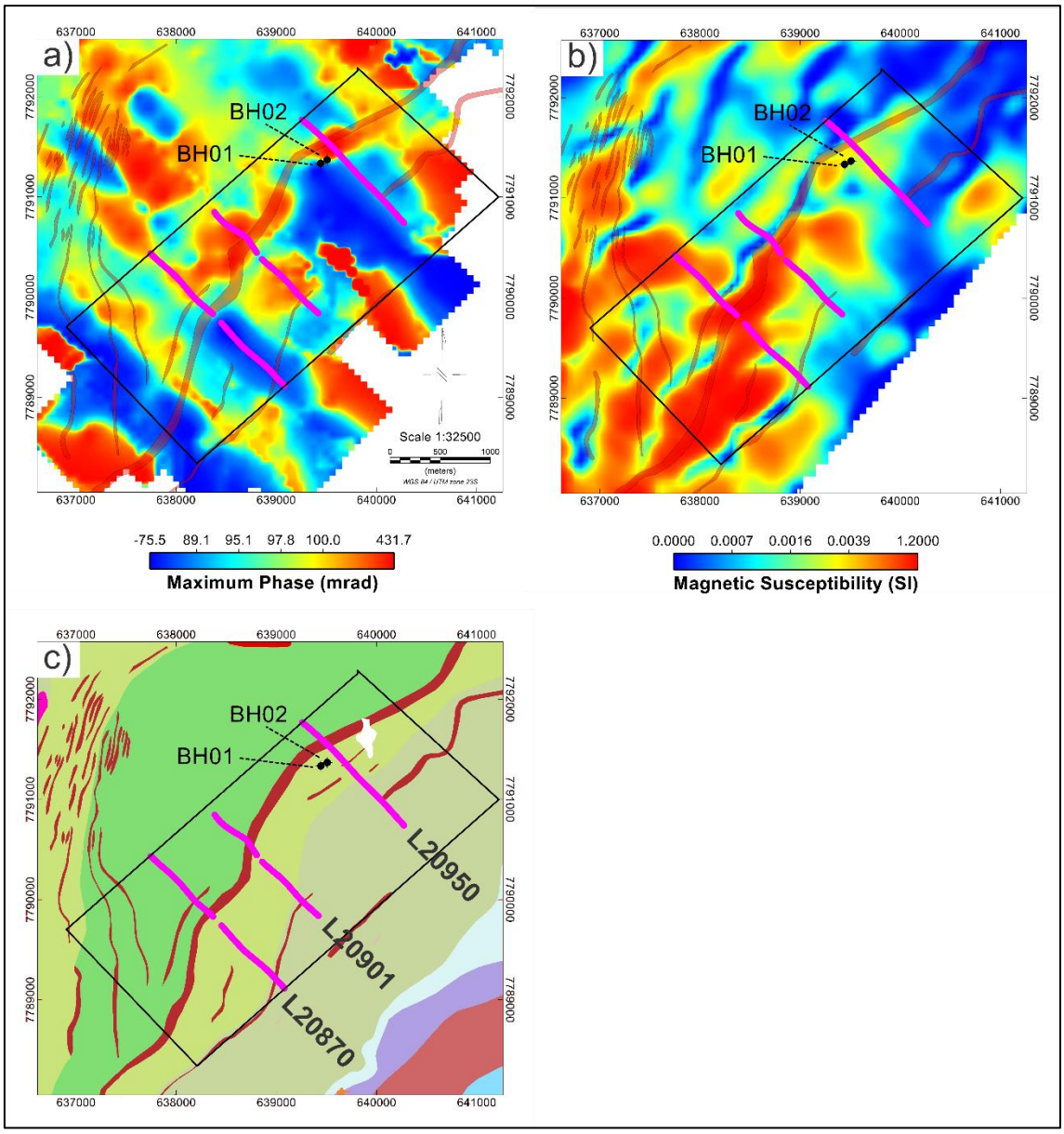

Figure 6. 23: Detail in Anomaly 1 area. a)φ_{max} slice at 150-161 m depth, b) MVI magnetic suscptibility slice at 155 m and c) geological map of the area for reference. The modelled flight lines intervals presented in Figure 6. 24 and Figure 6. 25 are indicated (L20870, L20901 and L20950) by the magenta lines. The position of the two boreholes (BH01 and BH02) provided by Jaguar Mining are indicated by the black dots.

Three φ_{max} sections intervals were extracted in the Anomaly 1 area, presented in Figure 6. 24, for the following flight lines L20870 (Figure 6. 24-a), L20901 (Figure 6. 24-b) and L20950 (Figure 6. 24-c). The positions of these sections are indicated in Figure 6. 23. It can be seen the lateral continuity of the chargeable body below DOI along the ENE-WSW structure in depth, around the altitude interval 1000-1090 m, and an apparent

dipping towards SE, following the known regional structural control of the area (Baltazar and Zuchetti, 2007). Close to the flight line L2950 (~100 m distance), there are two boreholes (BH01 and BH02) from Jaguar Mining that indicate two BIFS and graphite schists horizons, around depths 95 m and 100 m (thickness around 2.5 m) for the BIFs layers and 160 depth (~8 m thickness) for the graphite schist. This layer seems to be close to the top of the chargeable body around the altitude 950 m (160 m depth). It can be noted in all sections that DOI goes shallow (< 10 m) below the shallow chargeable zones, which may be associated with the mafic saprolite+soil layer in the area, as commented in the previous section. In fact, BH01 shows a thick layer of this typical cover around 53 m thickness from the top in this area, as well.

The section for flight line L20950 is detailed and integrated with the amplitude of the MVI magnetic susceptibility model (Figure 6. 25). The MVI model presents a steep magnetic body dipping towards SE (Figure 6. 25-b), in agreement with the regional dipping direction in the area around 50º to SE (Couto et al., 2016). A second BIF horizon is identified in BH02 at depth 200 m (~2.5 m thickness), which is compatible with the depth of the deepest part of the magnetic body. The shallow depth interval of magnetic may be related with the BIF horizon at 95-100 m depths. The borehole BH01 also identified a ~12 m thick chlorite schist enriched with magnetite, at depth 141 m, which could be pronounceable in the magnetic response as well.

A general 3D view of the chargeable body and the MVI magnetic susceptibility model is presented in Figure 6. 26. It can be seen that the magnetic model (Figure 6. 26-a) recovered the general dipping direction of the BIFs bodies along the NE-SW trend. The chargeable body (3D voxel clipped to φ_{max}>120 mrad and altitude 1000 m for the top) follows the main structural direction (Figure 6. 26-b and Figure 6. 26-c) and shows lateral continuity along it, above the DOI surface (Figure 6. 26-d). These results may indicate that the chargeable body could be related with carbonaceous units in the area, within the mafic domain of Ouro Fino Formation, and, in that case, may suggest the lateral continuation of these units towards SW in the main structure. Future exploration campaigns may evaluate this hypothesis, as there is no available lithological borehole data in the Western portion of the trend to confirm its extension.

There is no information about the Au content in the provided borehole data, which make any direct inference about its potentiality impossible in these results. However, as

described in Subsection 6.3.3, the Au mineralization is controlled by the BIFs horizons in this area. It is also known that the BIFs and carbonaceous units may be strong related, following an interbedded depositional structure along this regional trend (Pressaco and Sepp, 2018), according to the example in Roça Grande Mine, which is in the same regional structure, as can be observed in the map of Figure 6. 10. In this way, these results may suggest potential zones to develop any further exploration studies in this area, as AIP and the magnetic data apparently indicate the lateral continuity of potential lithologies associated with the typical mineralization style along the main NE-SW structure.

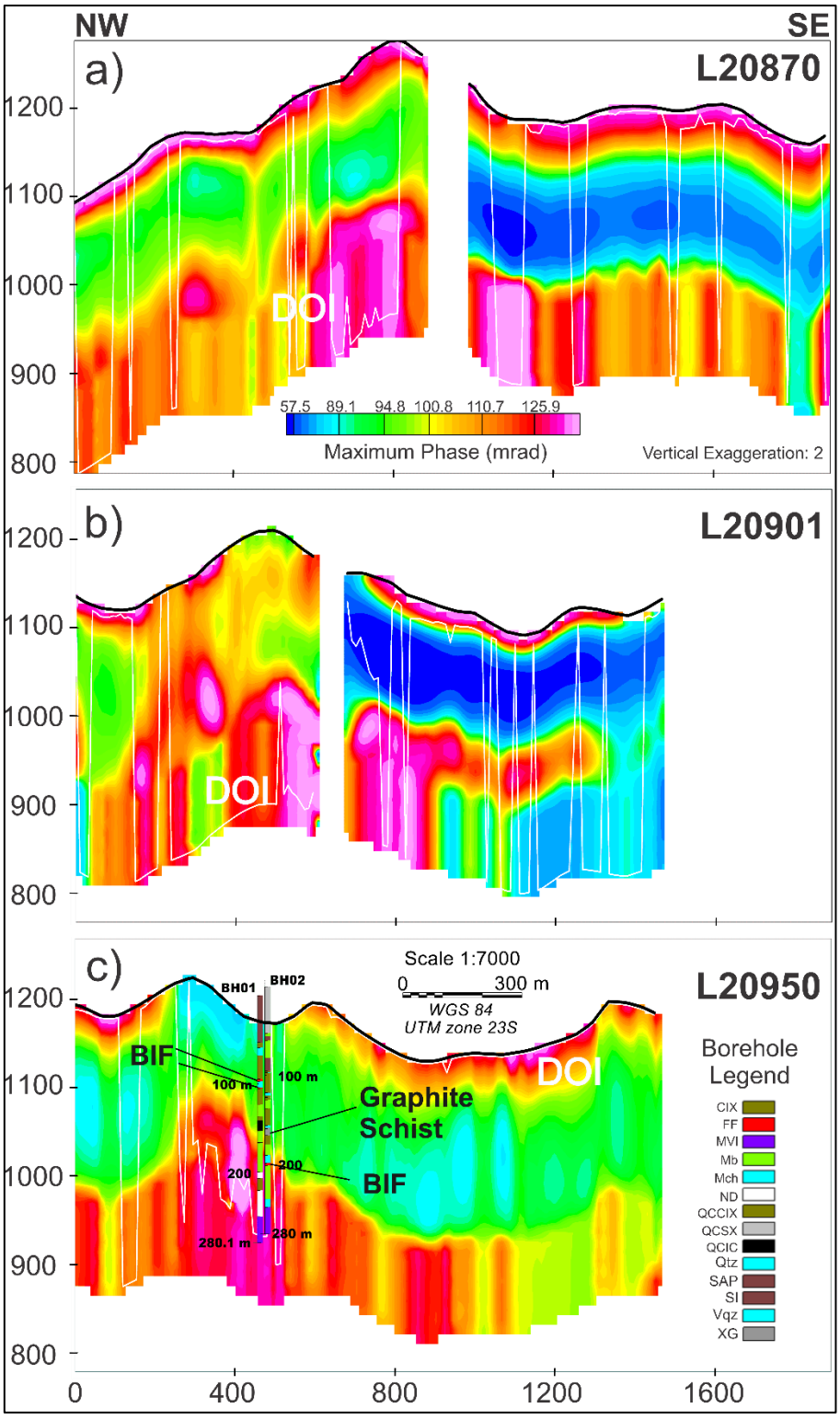

Figure 6. 24: φ_{max} sections for flight lines indicated in Figure 6. 23: a) L20870, b) L20901 and c) L20950. In c), the borehole legend describes: CIX – chlorite schist, FF – banded iron formation, MVI-metavolcanic rock, Mb-metabasalt, Mch-metachert, ND-not described interval, QCCIX-chlorite schist, QCSX-carbonaceous schist, QCIC-chlorite schist enriched with magnetite, Qtz-quartz, SAP-saprolite, SI-soil and XG-graphite schist. All sections are NW-SE oriented, being NW to the left. The topography is indicated as the black line, while the DOI is as the white line, while topography as the black line. Left axis represents the altitude and the bottom axis the distance, both in meters.

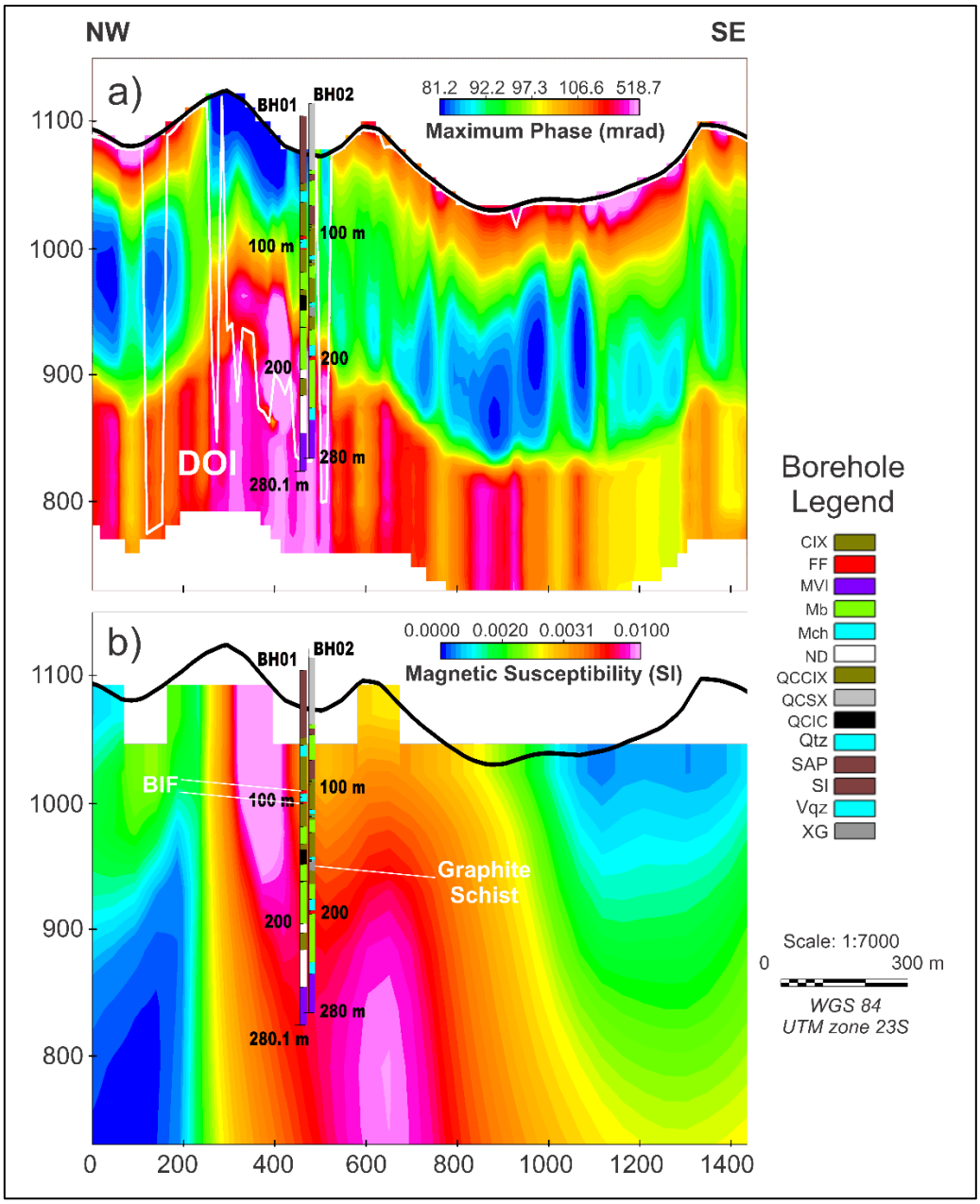

Figure 6. 25: Detail for section L20950. a) φ_{max} section and b) Amplitude of MVI magnetic susceptibility section. The borehole legend is describe in Figure 6. 24. DOI is indicated as the white line, while topography as the black line. Left axis represents the altitude and the bottom axis the distance, both in meters.

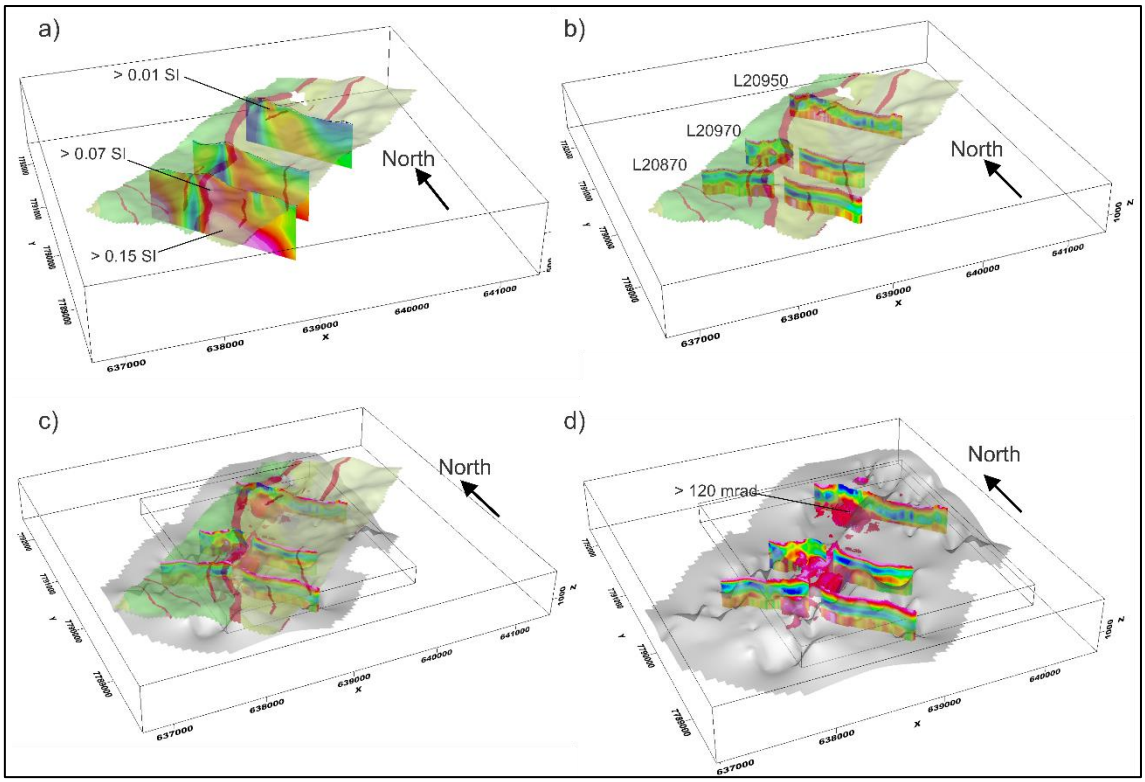

Figure 6. 26: 3D view of Anomaly 1 area. a) Amplitude of MVI magnetic suscptibility sections. b) φ_{max} sections. c) Chargeable body clipped with φ_{max}>120 mrad and topography clip at altitude 1000 m integrated with the geological map and sections. c) The same chargeable body in the DOI (grey surface) and sections perspective. Not most part of the body is above DOI. The sections refer to the flight lines L20870, L20901 and L20950 intervals, indicated in b).

For the Anomaly 2 area, the detailed view is presented in Figure 6. 27. The chargeable anomaly emerges around 100 m depth (Figure 6. 27-a), confirmed by four flight lines intervals from L20960, L20970, L20980 and L20990, although the flight line L20960 identified it less pronounced. The amplitude of MVI magnetic susceptibility model indicates a magnetic zone oriented to NE-SE regional trend at the same depth interval (Figure 6. 27-b and Figure 6. 27-c).

The φ_{max} sections for the full flight lines presented in Figure 6. 27are presented in Figure 6. 28. The anomaly at the 100 m depth is indicated by the dashed black circles. It is noted that the top of the chargeable body was found around 80-100 m depth, and shows apparent dipping towards SE with estimated 20-30º. Dipping values within this interval for non IP effect modeling, using thin plates geometry and the same AeroTEM^{HD} data, were found for conductive bodies in this area, presented in Couto et al. (2016).

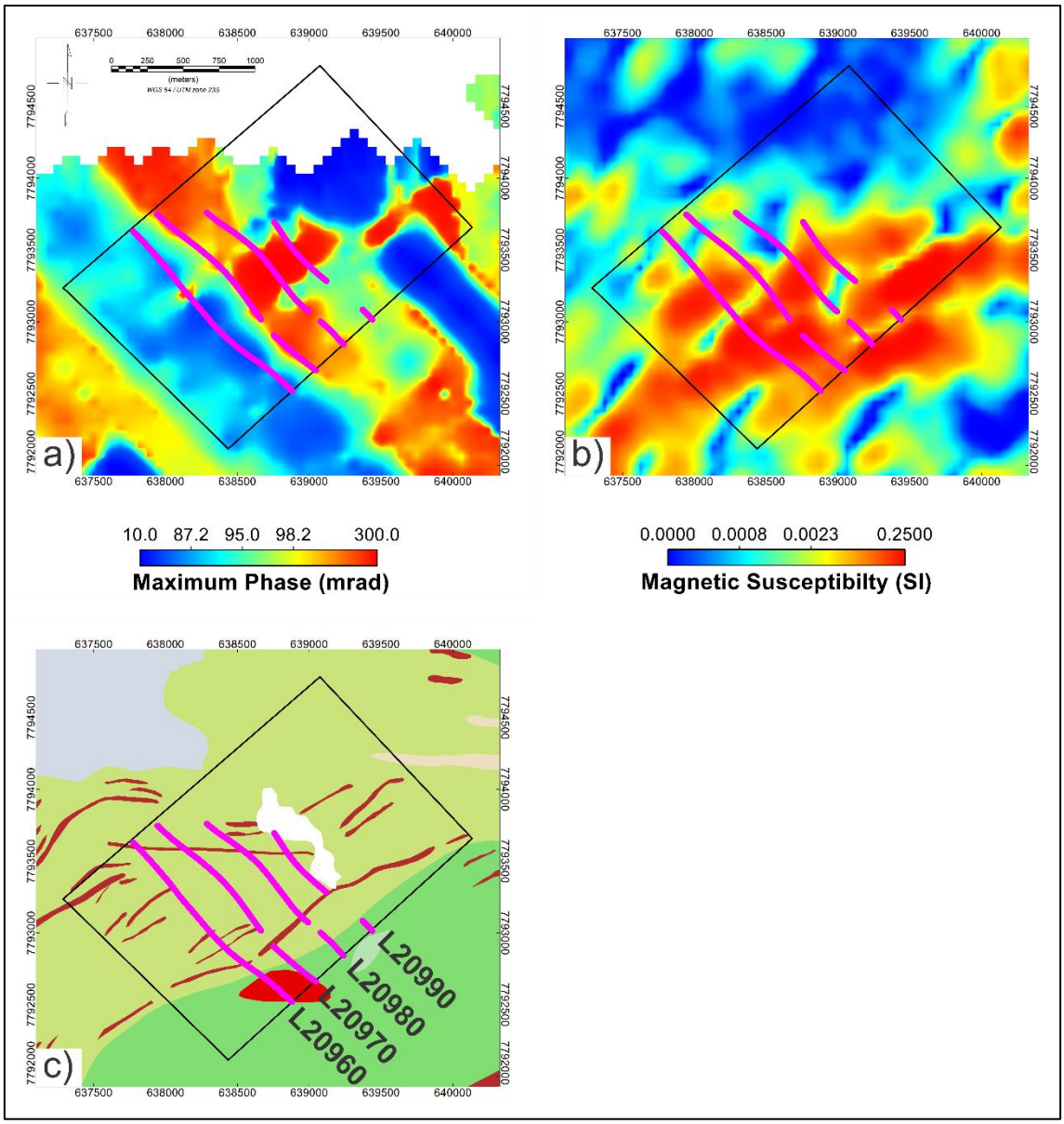

Figure 6. 27: Detail in Anomaly 2 area. a) φ_{max} slice at 96-106 m depth, b) MVI magnetic suscptibility slice at 100 m and c) geological map of the area for reference. The modelled flight lines intervals within the area presented in Figure 6. 27 are indicated (L20960, L20970 and L20980, L20990) by the magenta lines.

In this area, there are no available borehole lithological data, to the knowledge of the author so far. In this way, it is not possible to directly relate these chargeable anomalies to any lithology by now, as conducted in the case of Anomaly 1. However, as can be seen comparing Figure 6. 11 and Figure 6. 16 (DOI, in the second case), the AeroTEM^{HD} data presents significant response following the NE-SW trend, which structural behavior agrees with the MVI model as well, as observed in Figure 6. 22. Also, previous geological mapping campaigns conducted by the Geological Survey of Brazil-CPRM identified carbonaceous/graphite schists horizons in this area, although they are not cartographically represented in the map of Figure 6. 10. In this way, it may be

suggested that following geophysical surveys and exploration campaigns should be of interest to evaluate the IP response with more detail in this area, seeking to better understand its relation to the lithological types and possible mineralizations in this area.

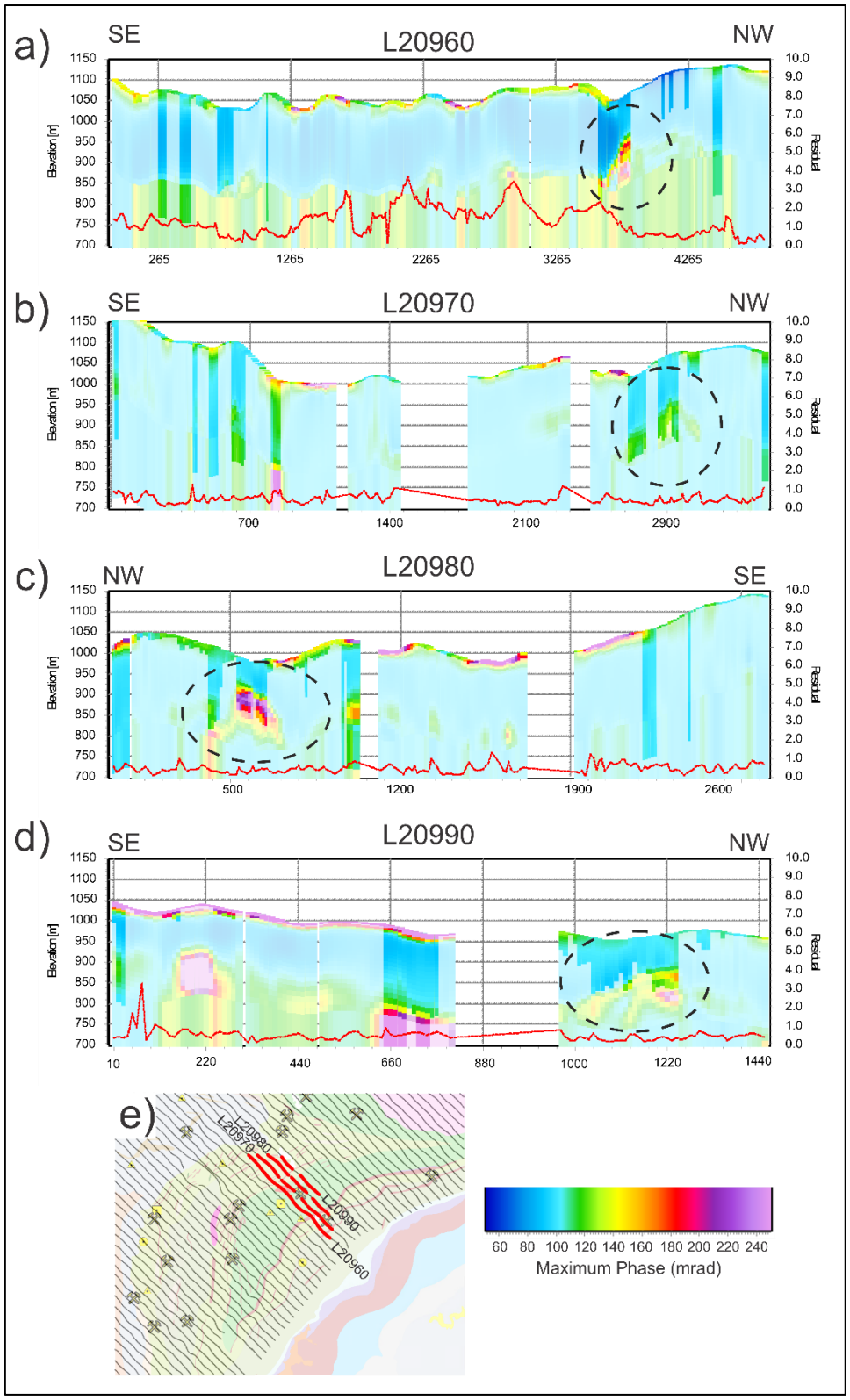

Figure 6. 28: φ_{max} sections for flight lines indicated in Figure 6. 27: a) L20960, b) L20970, c) 20980 and d) L20990. e) Location maps of full flight lines modeled intervals for reference. DOI is indicated as the shaded white vertical rectangles. The dashed circles indicate the chargeable anomaly with depth to the top around 100 m.

Figure 6. 29 presents a 3D view of the Anomaly 2 area, combining the φ_{max} model clipped above 110 mrad and at the top on the altitude of 968 m (Figure 6. 29-a), the amplitude of MVI magnetic susceptibility model (Figure 6. 29-b) and the spatial distribution of the chargeable model compared to DOI surface and geological map (Figure 6. 29-c and Figure 6. 29-d, respectively). It is possible to note that the magnetic model also indicates dipping direction towards SE, as previously discussed in Couto et al. (2016). The lateral continuation of the chargeable body above DOI apparently follows the SW-NE trend, as well, following the BIFs lineament in this area.

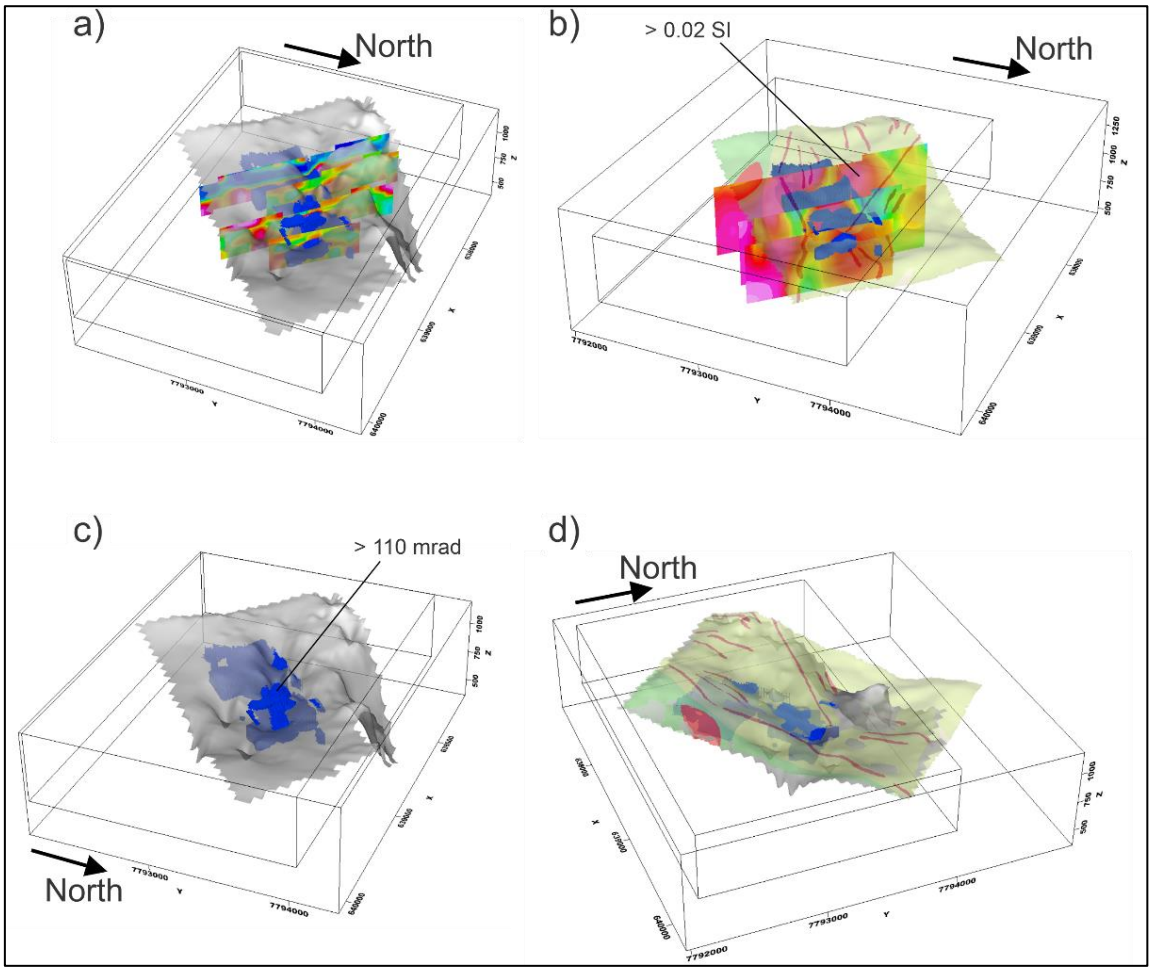

Figure 6. 29: 3D view of Anomaly 2 area. a) φ_{max} sections refered to L20960, L20970, L20980 and L20990. b) Amplitude of MVI magnetic suscptibility sections refered to the same flight lines intervals. c) Chargeable body clipped with φ_{max}>110 mrad and topography clip at altitude 968 m in the DOI (grey surface) perspective. c) The same chargeable body integrated with the geological map.

6.3.7. Discussions of Section 6.3

In the Roça Grande area, the AeroTEM^{HD} brought important insights for the AIP effect in a regional/district geological perspective, despite the low signal-to-noise level in the area, as presented in Figure 6. 8. Regionally, it identified a high polarizable shallow layer (< 15 m) in a significant portion off the area, with φ_{max} values reaching above 200 mrad. Particularly, it presents a spatial distribution related to the Ouro Fino Formation in the center of the area, although it extends to the Southern and Northern portions of the area, as well (Figure 6. 19). This strong shallow IP effect may justify why the RO parameterization could not fit the data (misfits above 4.0) in the central portion of the area, over many regions of the Ouro Fino Formation. On the other hand, the MPA parameterization could have achieved data misfits smaller than 1.4 in the same areas (Figure 6. 15). In this way, the choice of MPA parameterization using the robust inversion scheme presented in Section 6.1 to invert the data is justified, instead of RO parameterization. Although other IP parameterizations are strongly encouraged to be tested in a case like this. The MPA was chosen in the sense that it is known that it can decrease the correlation between the multiparametric Cole-Cole model, as demonstrated by Fiandaca et al. (2018).

The shallow strong IP effect over the Ouro Fino Formation might be related with the soil/saprolite formation process in the mafic and ultramafic units, as it is known that this process is quite intense in the area (Figure 6. 20), reaching depths around 50 m according to borehole information. The alteration cover seems to be worked as an AIP trap, as described in Viezzoli et al. (2020), which increased the sensitivity of the AeroTEM^{HD} data in the shallow layers, limiting the DOI to a few meters in the IP parameterization (Figure 6. 16-b and Figure 6. 16-c), while the RO parameterization "interpreted" this effect as a strong resistor, with DOIs down below its top layer, as can be observed in Figure 6. 17-a. However, this could not justify the data in a significant portion of the area due to high misfit values, as discussed above. To corroborate this hypothesis, subject soil samples to petrophysical analysis is necessary. In particular, spectral induced polarization (SIP) measurements should be conducted as a priority.

Despite the DOI limitation in the most part of the area, in the BIFs trends in the Northern and Southern portion of the area, deeper DOIs (> 100 m) could be identified for the MPA parameterization (Figure 6. 16) and interesting deeper chargeable anomalous

areas (> 150 mrad) could be identified: Anomaly 1 and Anomaly 2 (Figure 6. 22). In fact, in these areas, the NE-SW oriented BIFs trends seems to be described quite well with the magnetic anomalies (Figure 6. 11) and the MVI magnetic susceptibility model (Figure 6. 22).

In the Anomaly 1 area (Figure 6. 23), the depth to the top of the chargeable anomaly agrees with the position of a graphite schist layer in the NE portion of this smaller area, while steep SE-dipping magnetic bodies might be justified by BIFs horizons and magnetite enriched chlorite schists (Figure 6. 25). As it is known to this area that the BIFs and the graphite horizons follow an interbedded structure, in which the Au mineralization is strongly related to the bedding of the iron formations in the area, the identified chargeable body, combined with the magnetic models, might be useful as a structural guide for exploration activities. The lateral continuation to the SW portion of this polarizable body is suggested due to the lower DOIs towards this direction (Figure 6. 24 and Figure 6. 26). Further geophysical and exploration campaigns are encouraged to this area. In particular, ground TEM surveys associated with boreholes campaigns should be conducted as a priority in order to be able to detect possible IP effects that could be detected in the AeroTEM^{HD} data.

In the Anomaly 2 area, it is not possible to make direct inferences about the lithological nature of the IP effect response as conducted in the Anomaly 1 area, due to the lack of borehole lithological data. However, it can be observed that four flight lines identified an important chargeable anomaly around 100 m depth. Previous CPRM geological mapping campaigns identified graphite schist occurrences within this area, with the closest one around 330 m from flight line L20960. The magnetic data indicated by the MVI model suggests the continuation in depth of the BIFs horizons towards to SW, as can be seen in Figure 6. 27-b and Figure 6. 27-c. In this way, this chargeable anomaly should be investigated in detail with further geophysical and exploration campaigns, in order to be better evaluated.

After this discussion, it is possible to identify two levels of priorities for the two identified anomalous areas, to guide further investigations activities, as follows:

- Anomaly 1: priority 1
- Anomaly 2: priority 2

These levels of priorities were based on the possibility of constrains to be used in future works. As Anomaly 1 presented in the depth a possible association between the graphite horizons and the polarizable anomaly, with suggestion of lateral continuation to SE, it should be prioritized in the sense of exploration expenses. On the other hand, Anomaly 2 might be interesting to be investigated, after all the exposed discussion above, as well.

In addition to all these discussions, petrophysical data needs to be integrated in further analysis of these data or future surveys in the area, seeking to better constrain these models. For the IP effect evaluation in TEM systems, using the MPA approach should be easier to be compared with SIP measurements, as it provides the information of the maximum phase in the spectra of any lithological type. In this way, SIP measurements should retain a more relevant attention, as its use is not quite common in the gold mining activities in QF area.

6.3.8. Conclusions of Section 6.3

An AeroTEM^{HD} survey over the Roça Grande area, QF region, was processed, modeled and integrated with magnetic data, through the direct comparison with MVI models in the Roça Grande area. It might be suggested that the HTEM data is strongly affected over the mafic/ultramafic domain alteration cover, indicating a significant AIP trap process in these lithologies, which confined the TEM signal to the shallow layers in the most part of the area.

However, two areas associated with AIP chargeable anomalies were identified in the Au economic potential evaluation sense. These anomalies are controlled by a regional NE-SW trend, in which mineralization occur over locally structures, controlled by magnetic iron formations layers, intrinsically related to graphite horizons. For one of these anomalous regions (Anomaly 1), the magnetic data suggests spatial association with iron formation layers and the polarizable unit, that seems to be related with the graphite layers, according to borehole lithological data. For the second anomalous area (Anomaly 2), the regional structural control of the iron formations could be noted in the magnetic data. The identified polarizable anomaly is apparently related with these iron formation horizons and its structural control, as well. However, the lack of borehole lithological data

in this part of the survey cannot allow the direct association with the AIP anomaly. In this way, these two areas were classified in order of priorities, according to the higher level of a-priori information each one presents so far.

The AIP analysis in this data contributed to the regional/district geological mapping campaigns in the Roça Grande area, as it seems to be able to map alteration covers over the mafic units. Also, it provided insights about two possible exploration targets in the area.

Chapter 7: Conclusions

In this thesis, a Helicopter Transient Electromagnetic (HTEM) data from a AeroTEM^{HD} survey in the Quadrilátero Ferrífero (QF) region was processed and modeled, in order to investigate geological domains and potentiality for Au mineralization zones. To achieve that, it was decided to test the viability of the application of Airborne Induced Polarization (AIP) effect in the area.

The approach considered using the robust inversion scheme described in Section 6.1 and published in Lin et al. (2019), which I am one of the coauthors. The paper is entirely reproduced in the Appendix 1, as well. This discussion illustrated that some considerations should be taken related to the model space in AIP inversions, that are summarized by: 1) the use of Maximum Phase Angle (MPA), seeking to decrease the correlation between the Cole-Cole parameters; 2) the use of an initial resistivity starting model seeking to decrease the ill-posedness issues of the multiparametric induced polarization (IP) inversion; 3) fixing τ_{φ} and C for the first few iterations are a good way to control the convergence of the inverted model; 4) variations of the data standard deviations around negatives transients may help the convergence as well, in case the data present negatives decays possibly associated with polarization effect; and 5) the modification of the damping scheme during the inversion process, seeking the balance of the multi-parameter model space.

In the first publication, this approach was tested in synthetic and a field example, a SkyTEM516 survey in the Hope Bay area, Nunavut Territory, Canada. The test was conducted comparing the resistivity-only (RO) and the MPA approach. The synthetic examples in the paper, elaborated by the coauthors, showed that the robust inversion scheme recovers the geometry of conductive and polarizable bodies in better agreement with the actual geometry. The field data, processed and modeled by me, under the orientation of the coauthors, indicated that it is impossible to invert the data using the RO parameterization for the SkyTEM survey in a portion of the Hope Bay area, while the MPA parameterization successfully achieved it. These results indicated the importance to consider the AIP effect in an Airborne Transient Electromagnetic (ATEM) survey.

Following the discussion presented in Lin et al. (2019), I moved to work with the AeroTEM^{HD} data in the QF region. Firstly, as a case study, we started testing the MPA robust inversion scheme in the Lamego Mine area, seeking to understand the system response in the case of possible AIP effect, as expected in the Lamego area, due to carbonaceous layers and metallic sulfide dissemination associated with the gold mineralization. This discussion is commented in Section 6.2 and published in the paper presented in Appendix 2. Before moving to the real data, we conducted a synthetic model study compatible with Lamego's geology. Our results indicated that the IP effect can be pronounced as very steep decays in the early times, while possible negative data in the late times could be detected, which could be better modeled with the MPA robust inversion scheme, in comparison with the RO parameterization. This understanding was extended to the AeroTEM^{HD} data over the mine, which results demonstrated that the MPA inversions lead to recover a better resistivity model than the RO approach, partially recovering the depth to the top of the carbonaceous units in the geology framework, which might be helpful as a structural guide to the gold mineralization. However, we observed that ancillary information must be integrated in a real case study, like petrophysical and borehole data, to better constrain the input setup of the MPA parameters. The results for Lamego Mine case indicated that it is possible to model AIP affected data in the QF's AeroTEM^{HD} survey.

A second case study is presented in Section 6.3, in the Roça Grande area, central part of QF region. We choose this area to be studied under the AIP point of view as the application of the method in a regional/district context, in a less explored/exploited area in the QF area, so far. As ancillary information, the airborne magnetic survey associated with with the AeroTEM^{HD} data was integrated in the analysis, seeking to provide any structural a priori information to interpret the AIP models. The processing scheme was conducted differently from the Lamego Mine case: due to low signal-to-noise ratio in this portion of the data, it was ambiguous to define late times negative transients, that might be related with the IP effect. However, as demonstrated in the Lamego's case, the IP effect may be pronounced without these negatives, causing distortion in the early and late times transients. We conducted tests with both RO and MPA parameterization using the robust inversion scheme, concluding that the RO approach could not model the data in many portions of the survey, which lead to choose the MPA parameterization do continue the study. In particular, the data could not be inverted over the Ouro Fino Formation,

mainly composed by mafic/ultramafic rocks, with a considerably thick cover of soil and saprolite combination, resulted from the alteration of the metamafic units. Using the MPA approach, it was observed that, for this area, the AeroTEM^{HD} data indicated very shallow polarizable layers in the most regions of the study area, but expressive occurrence within the Ouro Fino Formation area. This result might suggest that the IP effect from the cover layers over this geological formation work as an "AIP trap", already described in the literature. The "AIP trap" is capable to domain the HTEM signal in the early times, avoiding it to thoroughly investigate deeper depths under the AIP approach. However, some portions related with possible Au-mineralized structured controlled banded iron formations (BIFs), could be modeled for deeper intervals. The magnetic data was used to constrain the position of these BIFs horizons. The results made possible to indicate two potential areas in prospective terms, one corroborated with borehole lithological information that might suggest the deeper AIP effect relation to graphite schists, which could be used as a structural guide jointly with the BIFs units to constrain future exploration campaigns. The results in the Roça Grande area indicated that it is possible to use the AIP method to evaluate mineralization potentiality in a regional/district scale study, contributing to geological mapping studies as well.

The results of the Chapter 6 presented in this thesis demonstrated that considering the AIP effect to invert ATEM data recovered better resistivity models, even though the presence of negatives transients in the late times are not so clear, like the case in some portions in Roça Grande area, discussed in Section 6.3. Accordingly, it is suggested that using the AIP approach to invert ATEM data may be necessary in the context of geological mapping and mineral exploration, in order to avoid erroneous interpretations of the resistivity models.

However, some important considerations are presented:

- Firstly, the data processing procedure must be conducted very carefully to avoid false IP anomalies, especially in the case of very noisy data, like the AeroTEM^{HD} data in QF region. This process should be conduct with a-priori geological information, like geological maps, other geophysical data and/or boreholes information, for example. The spatial continuity of possible IP anomalies could be a good indicator for reliable polarizable bodies affecting the ATEM data. Even though negatives decays are not so clear in some cases, the

changes in the slope of the dB/dt decay my indicate IP effect. The data processing part consumes most of the time working with the ATEM data, even using automatic voltage processing routines, like the one used in Aarhus Workbench, once it needs to be less aggressive than the ordinary approach to process the data for RO inversions, in order to not remove or considerably affect the IP affected data.

- Secondly, the use of ancillary data is fundamental for the definition of starting models and interpretation of results. In Lamego Mine case (Section 6.2 and Appendix 2), for example, the use of borehole information and petrophysical information was completely necessary to define initial robust models and evaluate the results. In Roça Grande area, the integration with airborne magnetic data, geological map and borehole lithological information was mandatory to identify polarizable structures that might present some potential to host gold mineralization associated with BIF bodies.

In this way, the geoscientific community should better consider the AIP problem when using ATEM data, not only in the data processing scheme, but as in the survey planning as well, especially because these type of surveys demands substantial investments. This is already happening abroad, in the ATEM research groups around the world, but it seems it is not so clear that this discussion is being conducted frequently in Brazil, to my knowledge. The two study cases in Lamego Mine and Roça Grande area should be considered as a good example about the importance of this issue, that might be helpful in the case of ATEM surveys planning, together with many other examples in other countries that can be found in the literature. It might be noted that a good quality control is crucial to determine valuable AIP data, as illustrated negatively in the Roça Grande area, where we had to cull out negatives below the high noise level in the area, which could have limited our IP interpretation. Considering this discussion and encouraging new proposals for ATEM surveys might be helpful for planning and designing in further mining exploration campaigns and regional geological mapping, usually conducted by geoscientific government agencies/institutions, like SGB-CPRM and Agência Nacional de Mineraçao, for example.

7.1. Future Work Directions

IP affected data in ATEM surveys are being detected with increasing frequency in the last decades, which configurates this study as a “hot topic” to be addressed in the international geoscientific community. The ATEM community abroad is learning fast how to deal with AIP issues and novel methodologies have been proposed for automatic processing and modeling of such type of the data (see Viezzoli et al, 2021, for example). To my knowledge, this study is the first one to consider AIP effect in HTEM data in Brazil, which makes this topic poorly explored in the country yet. In this sense, researches to deal better with IP effect should be encouraged by the Brazilian geoscientific community. As a first step, historical data that might be affected by AIP should be reinvestigated, even the ones conducted by private companies.

Automatic processing and modeling approaches for AIP seems to be the next frontier in this matter and should be considered for future research in the country. However, the availability of national public ATEM surveys for testing and calibration of new methodologies development is still scarce and relies predominantly in the public sector, which may limit this research topic in the country. Considering not only the AIP studies in Brazil, but seeking to create a productive national ATEM, the effectively participation in the international debate should be strongly encouraged, as well the proposals of new ATEM surveys to meet social demands. Government agencies, academia and the private sector are key to achieve it and should work together, in a synergic way, seeking the mutual benefit in terms of the useful information that ATEM surveys can bring to their activities, like mining, groundwater exploration and risk management. A good example in this direction can be found in the AusAEM program (https://www.ga.gov.au/eftf/minerals/nawa/ausaem), which pioneered this discussion in the world. In this way, such future partnerships and research programs should be conducted, pursuing the expansion of the national debate about the ATEM methodology.

References

Alkmim, F.F. and Noce, C.M. (eds.) 2006. The Paleoproterozoic Record of the São Francisco Craton. IGCP 509 Field workshop, Bahia and Minas Gerais, Brazil. Field Guide & Abstracts, 114 p

Allard, M. (2007). On the Origin of the HTEM Species. Advances in Airborne Geophysics. In Proceedings of Exploration 07: Fifth Decennial International Conference on Mineral Exploration, p. 355-374.

Almeida, E.R., Porsani, J. L., Monteiro-Santos, F.A., Bortolozo, C.A. (2017). 2D TEM Modeling for a Hydrogeological Study in the Paraná Sedimentary Basin, Brazil. International Journal of Geosciences (on-line), v.08, p.693-710. https://doi.org/10.4236/ijg.2017.85038

Almeida, F. F. M. (1967) Origem e Evolução da Plataforma Brasileira. Departamento Nacional da Produção Mineral. Boletim da Divisão de Geologia e Mineralogia, Rio de Janeiro, n. 241. 38 p.

Auken, E., & Christiansen, A. V. (2004). Layered and laterally constrained 2D inversion of resistivity data. Geophysics, 69(3), 752–761. https://doi.org/10.1190/1.1759461

Auken, E., Christiansen, A. V., Jacobsen, B. H., Foged, N., & Sorensen, K. I. (2005). Piecewise 1D laterally constrained inversion of resistivity data. Geophysical Prospecting, 53(4), 497–506. https://doi.org/10.1111/j.1365-2478.2005.00486.x

Auken, E., Christiansen, A. V., Westergaard, J. H., Kirkegaard, C., Foged, N., & Viezzoli, A. (2009). An integrated processing scheme for high-resolution airborne electromagnetic surveys, the SkyTEM system. Exploration Geophysics, 40(2), 184–192. https://doi.org/10.1071/eg08128

Auken, E., Christiansen, A. V., Kirkegaard, C., Fiandaca, G., Schamper, C., Behroozmand, A. A., Binley, A., Nielsen, E., Effersø, F., Christensen, N. B., Sørensen, K., Foged, N., & Vignoli, G. (2015). An overview of a highly versatile forward and stable inverse algorithm for airborne, ground-based and borehole electromagnetic and electric data. Exploration Geophysics, 46(3), 223–235. https://doi.org/10.1071/eg13097

Baltazar, O. F., & Zucchetti, M. (2007). Lithofacies associations and structural evolution of the Archean Rio das Velhas greenstone belt, Quadrilátero Ferrífero, Brazil: A review of the setting of gold deposits. Ore Geology Reviews, 32(3–4), 471–499. https://doi.org/10.1016/j.oregeorev.2005.03.021

Bortolozo, C. A., Porsani, J. L., Santos, F. A. M. dos, & Almeida, E. R. (2015). VES/TEM 1D joint inversion by using Controlled Random Search (CRS) algorithm. Journal of Applied Geophysics, 112, 157–174. https://doi.org/10.1016/j.jappgeo.2014.11.014

Bortolozo, C. A., Couto, M. A., Jr., Porsani, J. L., Almeida, E. R., & Monteiro dos Santos, F. A. (2014). Geoelectrical characterization using joint inversion of VES/TEM

data: A case study in Paraná Sedimentary Basin, São Paulo State, Brazil. Journal of Applied Geophysics, 111, 33–46. https://doi.org/10.1016/j.jappgeo.2014.09.009

Blakely, R. J. (1995). Potential Theory in Gravity and Magnetic Applications. Cambridge University Press. https://doi.org/10.1017/cbo9780511549816

Campaña, J. D. R., Porsani, J. L., Bortolozo, C. A., Serejo de Oliveira, G., & Monteiro dos Santos, F. A. (2017). Inversion of TEM data and analysis of the 2D induced magnetic field applied to the aquifers characterization in the Paraná basin, Brazil. Journal of Applied Geophysics, 138, 233–244. https://doi.org/10.1016/j.jappgeo.2017.01.024

Christensen, N. B. (1990). Optimized Fast Hankel Transform Filters1. Geophysical Prospecting, 38(5), 545-568. https://doi.org/10.1111/j.1365-2478.1990.tb01861.x

Christensen, M. S. (2013). Induced Polarization Effect in the Transient Electromagnetic Method. Bachelor Thesis. Department of Physics and Astronomy, Aarhus University.

Christiansen, A. V., & Auken, E. (2012). A global measure for depth of investigation. Geophysics, 77(4), WB171–WB177. https://doi.org/10.1190/geo2011-0393.1

Christiansen, A. V., Auken, E., & Viezzoli, A. (2011). Quantification of modeling errors in airborne TEM caused by inaccurate system description. Geophysics, 76(1), F43–F52. https://doi.org/10.1190/1.3511354

Clow, G. G., Lecuyer, N. L., Valliant, W. W., Krutzelmann, H.,Chubb, D., Martiz, R. (2013). Preliminary Economic Assessment Study on the TMAC-Hope Bay Project, Nunavut, Canada. RPA Technical Reports.

Cole, K. S., & Cole, R. H. (1941). Dispersion and Absorption in Dielectrics I. Alternating Current Characteristics. The Journal of Chemical Physics, 9(4), 341–351. https://doi.org/10.1063/1.1750906

Couto, M. A., Fiandaca, G., Maurya, P. K., Christiansen, A. V., Porsani, J. L., & Auken, E. (2020). AEMIP robust inversion using maximum phase angle Cole–Cole model re-parameterisation applied for HTEM survey over Lamego gold mine, Quadrilátero Ferrífero, MG, Brazil. Exploration Geophysics, 51(1), 170–183. https://doi.org/10.1080/08123985.2019.1682458

Couto, M. A., Aisengart, T., Barbosa, D., Ferreira, R. C. R., Baltazar, O. F., de Souza Marinho, M., Cavalcanti, J. A. D., & Araújo, J. C. S. (2017a). Magnetization Vector Inversion Application in Quadrilatero Ferrifero Region, MG, Brazil. 15th International Congress of the Brazilian Geophysical Society & EXPOGEF, Rio de Janeiro, Brazil, 31 July-3 August 2017. https://doi.org/10.1190/sbgf2017-103

Couto, M. A., Wosniak, R., Marques, E. D., Duque, T. R. F., & de Carvalho, M. T. N. (2017b). VTEM and Aeromagnetic Data Modeling Applied to Cu, Zn and Pb Prospection in Palmeirópolis Project, TO, Brazil. 15th International Congress of the Brazilian Geophysical Society & EXPOGEF, Rio de Janeiro, Brazil, 31 July-3 August 2017. https://doi.org/10.1190/sbgf2017-104

Couto, M.A., Baltazar, O. F., Ferreira, R. C. R., Marinho, M. S., Araújo J. C. S. Modelagem e Integração Geofísica (HTEM, Magnetometria e Gamaespectrometria) no Greenstone Belt Rio das Velhas, Quadrilátero Ferrífero, MG. VII Simpósio Brasileiro de Geofísica, SBGf, Ouro Preto, MG, Brazil, 2016.

CPRM (2011). Projeto Aerogeofísico Rio das Velhas–Etapa II e Projeto Aerogeofísico Nova Redenção. Relatório Final do Levantamento e Processamento dos Dados Eletromagnético e Magnéticos. Volume 1, Texto Técnico.

Danielsen, J. E., Auken, E., Jørgensen, F., Søndergaard, V., & Sørensen, K. I. (2003). The application of the transient electromagnetic method in hydrogeophysical surveys. Journal of Applied Geophysics, 53(4), 181–198. https://doi.org/10.1016/j.jappgeo.2003.08.004

Dentith, M., & Mudge, S. T. (2014). Geophysics for the Mineral Exploration Geoscientist. Cambridge University Press. https://doi.org/10.1017/cbo9781139024358

Ellis, R. 2015. Quantitative Analysis of MVI, ASEG-PESA 2015–-24th International Geophysical Conference and Exhibition, Perth, Australia.

Elllis, R. G., de Wet, B., & Macleod, I. N. (2012). Inversion of Magnetic Data from Remanent and Induced Sources. ASEG Extended Abstracts, 2012(1), 1–4. https://doi.org/10.1071/aseg2012ab117

Fedi, M., Hansen, P. C, & Paoletti, V. (2007). Ambiguity and Depth Resolution in Potential Field Inversion. Communications to SIMAI Congress, 2. https://doi.org/10.1685/CSC06155

Fedi, M., Hansen, P. C., & Paoletti, V. (2005). Analysis of depth resolution in potential-field inversion. Geophysics, 70(6), A1–A11. https://doi.org/10.1190/1.2122408

Fiandaca, G., Ramm, J., Binley, A., Gazoty, A., Christiansen, A. V., & Auken, E. (2012). Resolving spectral information from time domain induced polarization data through 2-D inversion. Geophysical Journal International, 192(2), 631–646. https://doi.org/10.1093/gji/ggs060

Fiandaca, G., Christiansen, A., & Auken, E. (2015). Depth of Investigation for Multi-parameters Inversions. Near Surface Geoscience 2015 - 21st European Meeting of Environmental and Engineering Geophysics. https://doi.org/10.3997/2214-4609.201413797

Fiandaca, G., Madsen, L.M., and Maurya, P.K. (2018). Re-Parameterizations of the Cole-Cole Model for Improved Spectral Inversion of Induced Polarization Data. Near Surface Geophysics 16, 385-99. https://doi.org/10.3997/1873-0604.2017065

Flis, M. F., Newman, G. A., & Hohmann, G. W. (1989). Induced-polarization effects in time-domain electromagnetic measurements. Geophysics, 54(4), 514–523. https://doi.org/10.1190/1.1442678

Flores, C., & Peralta-Ortega, S. A. (2009). Induced polarization with in-loop transient electromagnetic soundings: A case study of mineral discrimination at El Arco

porphyry copper, Mexico. Journal of Applied Geophysics, 68(3), 423–436. https://doi.org/10.1016/j.jappgeo.2009.03.009

Fournier, D., Heagy, L. J., & Oldenburg, D. W. (2020). Sparse magnetic vector inversion in spherical coordinates. Geophysics, 85(3), J33–J49. https://doi.org/10.1190/geo2019-0244.1

Golub, G. H., & von Matt, U. (1997). Generalized Cross-Validation for Large-Scale Problems. Journal of Computational and Graphical Statistics, 6(1), 1. https://doi.org/10.2307/1390722

Golub, G. H., Heath, M., & Wahba, G. (1979). Generalized Cross-Validation as a Method for Choosing a Good Ridge Parameter. Technometrics, 21(2), 215–223. https://doi.org/10.1080/00401706.1979.10489751

Gubatyenko, V. P. Tikshaeyv, V. V. On the variation of sign of the electromagnetic force of induction in the transient electromagnetic field method. Akad. Nauk USSR, Earth Phys., v. 15, p217-219, 1979.

Hamada, L. R., Porsani, J. L., Bortolozo, C. A., & Rangel, R. C. (2018). TDEM and VES soundings applied to a hydrogeological study in the central region of the Taubaté Basin, Brazil. First Break, 36(8), 49–54. https://doi.org/10.3997/1365-2397.n0111

Hanke, M. (2017). A Taste of Inverse Problems. Society for Industrial and Applied Mathematics. https://doi.org/10.1137/1.9781611974942

Hansen, P. C. (1992). Analysis of Discrete Ill-Posed Problems by Means of the L-Curve. SIAM Review, 34(4), 561–580. https://doi.org/10.1137/1034115

Hansen, P. C. (1994). REGULARIZATION TOOLS: A Matlab package for analysis and solution of discrete ill-posed problems. Numerical Algorithms, 6(1), 1–35. https://doi.org/10.1007/bf02149761

Hansen, P. C. (2007). Regularization Tools version 4.0 for Matlab 7.3. Numerical Algorithms, 46(2), 189–194. https://doi.org/10.1007/s11075-007-9136-9

Hansen, P. C., & O'Leary, D. P. (1993). The Use of the L-Curve in the Regularization of Discrete Ill-Posed Problems. SIAM Journal on Scientific Computing, 14(6), 1487–1503. https://doi.org/10.1137/0914086

Johansen, H. K., & Sorensen, K. (1979). Fast Hankel Transforms*. Geophysical Prospecting, 27(4), 876-901. https://doi.org/10.1111/j.1365-2478.1979.tb01005.x

Kaminski, K., Viezzoli, A. (2016). Case studies: Hope Bay gold deposits. AarhusGeo Technocal Notes.

Kaminski, V., & Viezzoli, A. (2017). Modeling induced polarization effects in helicopter time-domain electromagnetic data: Field case studies. GEOPHYSICS, 82(2), B49–B61. https://doi.org/10.1190/geo2016-0103.1

Kang, S., & Oldenburg, D. W. (2015). Recovering IP information in airborne-time domain electromagnetic data. ASEG Extended Abstracts, 2015(1), 1–2. https://doi.org/10.1071/aseg2015ab102

Kang, S., & Oldenburg, D. W. (2016). On recovering distributed IP information from inductive source time domain electromagnetic data. Geophysical Journal International, 207(1), 174–196. https://doi.org/10.1093/gji/ggw256

Kang, S., Fournier, D., & Oldenburg, D. W. (2017). Inversion of airborne geophysics over the DO-27/DO-18 kimberlites — Part 3: Induced polarization. Interpretation, 5(3), T327–T340. https://doi.org/10.1190/int-2016-0141.1

Kauffman, A., Keller, G.V. Frequency and Transient Soundings. First Edition. Elsevier, Amsterdam, 1983.

Kratzer, T., & Macnae, J. C. (2012). Induced polarization in airborne EM. Geophysics, 77(5), E317–E327. https://doi.org/10.1190/geo2011-0492.1

Kwan, K., Prikhodko, A., Legault, J. M., Plastow, G., Xie, J., & Fisk, K. (2015). Airborne Inductive Induced Polarization Chargeability Mapping of VTEM Data. ASEG Extended Abstracts, 2015(1), 1–4. https://doi.org/10.1071/aseg2015ab104

Kwan, K., & Müller, D. (2020). Mount Milligan alkalic porphyry Au--Cu deposit, British Columbia, Canada, and its AEM and AIP signatures: Implications for mineral exploration in covered terrains. Journal of Applied Geophysics, 180, 104131. https://doi.org/10.1016/j.jappgeo.2020.104131

Ladeira, E. A. (1980). Metalogenesis of gold at the Morro Velho mine, and in the Nova Lima District, Quadrilátero Ferrífero, Minas Gerais, Brazil. PhD thesis, Department of Geology, University of Western Ontario. London, Canada, 272 pp.

Lana, C., Alkmim, F. F., Armstrong, R., Scholz, R., Romano, R., & Nalini, H. A. (2013). The ancestry and magmatic evolution of Archaean TTG rocks of the Quadrilátero Ferrífero province, southeast Brazil. Precambrian Research, 231, 157-173. https://doi.org/doi:10.1016/j.precamres.2013.03.008

Lawson, C. L., & Hanson, R. J. (1995). Solving Least Squares Problems. Society for Industrial and Applied Mathematics. https://doi.org/10.1137/1.9781611971217

Lee, T. (1975). Sign reversal in the transient method of electrical prospecting (one loop version). Geophysical Prospecting, 23(4), 653–662. https://doi.org/10.1111/j.1365-2478.1975.tb01551.x

Lee, T. (1981). Transient electromagnetic response of a polarizable ground. GEOPHYSICS, 46(7), 1037–1041. https://doi.org/10.1190/1.1441241

Leite, D. N., Bortolozo, C. A., Porsani, J. L., Couto, M. A., Jr, Campaña, J. D. R., dos Santos, F. A. M., Rangel, R. C., Hamada, L. R., Sifontes, R. V., Serejo de Oliveira, G., & Stangari, M. C. (2018). Geoelectrical characterization with 1D VES/TDEM joint inversion in Urupês-SP region, Paraná Basin: Applications to hydrogeology. Journal of Applied Geophysics, 151, 205–220. https://doi.org/10.1016/j.jappgeo.2018.02.022

Lelièvre, P. G., & Oldenburg, D. W. (2009). A 3D total magnetization inversion applicable when significant, complicated remanence is present. GEOPHYSICS, 74(3), L21–L30. https://doi.org/10.1190/1.3103249

Lin, C., Fiandaca, G., Auken, E., Couto, M. A., & Christiansen, A. V. (2019). A discussion of 2D induced polarization effects in airborne electromagnetic and inversion with a robust 1D laterally constrained inversion scheme. GEOPHYSICS, 84(2), E75–E88. https://doi.org/10.1190/geo2018-0102.1

Liu, S., Hu, X., Xi, Y., Liu, T., & Xu, S. (2015). 2D sequential inversion of total magnitude and total magnetic anomaly data affected by remanent magnetization. Geophysics, 80(3), K1–K12. https://doi.org/10.1190/geo2014-0019.1

Lobato, L. M., Ribeiro-Rodrigues, L. C., & Vieira, F. W. R. (2001). Brazil's premier gold province. Part II: geology and genesis of gold deposits in the Archean Rio das Velhas greenstone belt, Quadrilátero Ferrífero. Mineralium Deposita, 36(3–4), 249–277. https://doi.org/10.1007/s001260100180

Macnae, J. (2016). Airborne IP detects only fine-grained minerals when compared to conventional IP. ASEG Extended Abstracts, 2016(1), 1–4. https://doi.org/10.1071/aseg2016ab141

Marchant, D., Haber, E., Beran, L., & Oldenburg, D. W. (2012, September). 3D modeling of IP effects on electromagnetic data in the time domain. SEG Technical Program Expanded Abstracts 2012. SEG Technical Program Expanded Abstracts 2012. https://doi.org/10.1190/segam2012-1454.1

Marchant, D., Haber, E., & Oldenburg, D. (2013). Recovery of 3D IP distribution from airborne time-domain EM. ASEG Extended Abstracts, 2013(1), 1–4. https://doi.org/10.1071/aseg2013ab217

Marchant, D., Haber, E., & Oldenburg, D. W. (2014). Three-dimensional modeling of IP effects in time-domain electromagnetic data. GEOPHYSICS, 79(6), E303–E314. https://doi.org/10.1190/geo2014-0060.1

Martins, B. S., Lobato, L. M., Rosière, C. A., Hagemann, S. G., Santos, J. O. S., Villanova, F. L. dos S. P., Figueiredo e Silva, R. C., & de Ávila Lemos, L. H. (2016). The Archean BIF-hosted Lamego gold deposit, Rio das Velhas greenstone belt, Quadrilátero Ferrífero: Evidence for Cambrian structural modification of an Archean orogenic gold deposit. Ore Geology Reviews, 72, 963–988. https://doi.org/10.1016/j.oregeorev.2015.08.025

McNeill, J.D. (1994). Principles and application of time domain electromagnetic techniques for resistivity soundings. Tech. Note TN-27, Geonics Ltd., Mississauga, Ont., Canada.

Melo, A. T., Sun, J., & Li, Y. (2017). Geophysical inversions applied to 3D geology characterization of an iron oxide copper-gold deposit in Brazil. GEOPHYSICS, 82(5), K1–K13. https://doi.org/10.1190/geo2016-0490.

Nabighian, M. N., & Macnae, J. C. (1991). 6. Time Domain Electromagnetic Prospecting Methods. In Electromagnetic Methods in Applied Geophysics (pp. 427–520).

Society of Exploration Geophysicists. https://doi.org/10.1190/1.9781560802686.ch6

Noce, C. M., Tassinari, C., & Lobato, L. M. (2007). Geochronological framework of the Quadrilátero Ferrífero, with emphasis on the age of gold mineralization hosted in Archean greenstone belts. Ore Geology Reviews, 32(3–4), 500–510. https://doi.org/10.1016/j.oregeorev.2005.03.019

Oldenburg, D. W., & Li, Y. (1994). Inversion of induced polarization data. Geophysics, 59(9), 1327–1341. https://doi.org/10.1190/1.1443692

Oldenburg, D. W., & Li, Y. (2005). 5. Inversion for Applied Geophysics: A Tutorial. In Near-Surface Geophysics (pp. 89–150). Society of Exploration Geophysicists. https://doi.org/10.1190/1.9781560801719.ch5

Oliveira, D. S. (2014). Interpretação de dados aerogeofísicos para exploração aurífera na área do Projeto Córrego do Sítio, NE do Quadrilátero Ferrífero. Dissertação de Mestrado, Instituto de Astronomia, Geofísica e Ciências Atmosféricas, Universidade de São Paulo.

Oliveira, G. S. (2020). Modelagem de Anomalias de Dados HTEM para Exploração Mineral no Quadrilátero Ferrífero (MG). Dissertação de Mestrado, Instituto de Astronomia, Geofísica e Ciências Atmosféricas, Universidade de São Paulo.

Parker, R. L. (1994). Geophysical Inverse Theory. Princeton University Press. https://doi.org/10.1515/9780691206837

Pelton, W. H., Ward, S. H., Hallof, P. G., Sill, W. R., Nelson, P. H. (1978). Mineral discrimination and removal of inductive coupling with multi-frequency IP. Geophysics, 43(3), 588–609. https://doi.org/10.1190/1.1440839

Porsani, J. L., Almeida, E. R., Bortolozo, C. A., & Santos, F. A. M. dos. (2012). TDEM survey in an area of seismicity induced by water wells in Paraná sedimentary basin, Northern São Paulo State, Brazil. Journal of Applied Geophysics, 82, 75–83. https://doi.org/10.1016/j.jappgeo.2012.02.005

Porsani, J. L., Bortolozo, C. A., Almeida, E. R., Sobrinho, E. N. S., & Santos, T. G. dos. (2012). TDEM survey in urban environmental for hydrogeological study at USP campus in São Paulo city, Brazil. Journal of Applied Geophysics, 76, 102–108. https://doi.org/10.1016/j.jappgeo.2011.10.001

Pressaco, R., Sepp, J. (2018). Technical Report on The Roça Grande and Pilar Mines, Minas Gerais State, Brazil. RPA Technical Reports.

Prospectors Corporation. (2011) Report on a Helicopter-BorneAeroTEM System Electromagnetic & Magnetic Survey - Nova, Rio1 and Rio2 Projects.

Rangel, R. C., Porsani, J. L., Bortolozo, C. A., & Hamada, L. R. (2018). Electrical Resistivity Tomography and TDEM Applied to Hydrogeological Study in Taubaté Basin, Brazil. International Journal of Geosciences, 09(02), 119–130. https://doi.org/10.4236/ijg.2018.92008

Santos, M. H. L. (2006). Processamento, Nivelamento e Integração de Levantamentos Aerogeofísicos Magnetométricos no Estado de Minas Gerais e sua Contribuição à Geologia da Porção do Sul do Cráton São Francisco. Dissertação de Mestrado, Instituto de Geociências, Universidade de Brasília.

Schorscher, H. D. Polimetamorfismo do Pré-Cambriano na Região de Itabira, Minas Gerais. In: SBG, Congresso Brasileiro de Geologia, 29. Anais SBG. Ouro Preto: Abstracts, 194- 195, 1976.

Silva, A. M., Mccafferty, A., Pires, A. C., & Rodrigues, L. C. (2000). Predictive Geophysical Model For Gold Mineralization In The Quadrilatero Ferrifero, Brazil: The Case Of Cuiabá Mine. Revista Brasileira De Geociências, 30(3), 543-546. https://doi.org/10.25249/0375-7536.2000303543546

Silva, A. M., Pires, A. C., Mccafferty, A., Moraes, R. A., & Xia, H. (2003). Application of airborne geophysical data to mineral exploration in the uneven exposed terrains of the Rio das Velhas greenstone belt. Revista Brasileira De Geociências, 33(2), 17-28. https://doi.org/10.25249/0375-7536.200333s21728

Silva, A. M., Mccafferty, A. E., & Pires, A. C. (2003). An integrated exploration approach to map bif-hosted gold deposits in the Rio das Velhas greenstone belt, Quadrilátero Ferrífero, Brazil. Revista Brasileira De Geociências, 33(2), 29-36. https://doi.org/10.25249/0375-7536.200333s22936

Silva, M A. Cavalcanti, J. A. D., Araújo, J. C. S., Ferreira, R. C. R., Freitas, F. M. (2020). Mapa geológico e de recursos minerais integrado do Quadrilátero Ferrífero - Subárea Central. CPRM. http://rigeo.cprm.gov.br/jspui/handle/doc/20490

Smith, B.D., Tippens, C., Flanigan, V., and Sadek, H., 1983, Preliminary Results of Spectral Induced Polarization Measurements, Wadi Bidah District, Kingdom of Saudi Arabia. US Geological Survey, Open-File Report, 83-612

Smith, R. S., & Klein, J. (1996). A special circumstance of airborne induced-polarization measurements. Geophysics, 61(1), 66–73. https://doi.org/10.1190/1.1443957

Smith, R. S., & West, G. F. (1989). Field examples of negative coincident-loop transient electromagnetic responses modeled with polarizable half-planes. Geophysics, 54(11), 1491–1498. https://doi.org/10.1190/1.1442613

Smith, R. S., Walker, P. W., Polzer, B. D., West, G. F. (1988a) The Time-Domain Electromagnetic Response of Polarizable Bodies: An Aproximate Convolution Algorithm Geophysical Prospecting, 36(7), 772–785. https://doi.org/10.1111/j.1365-2478.1988.tb02192.x

Smith, R. S., & West, G. F. (1988b). Inductive interaction between polarizable conductors: An explanation of a negative coincident-loop transient electromagnetic response. Geophysics, 53(5), 677–690. https://doi.org/10.1190/1.1442502

Smith, R. S., & West, G. F. (1988c). An Explanation of Abnormal TEM Responses: Coincident-Loop Negatives, and the Loop Effect. Exploration Geophysics, 19(3), 435–446. https://doi.org/10.1071/eg988435

Smith, R. S., & West, G. F. (1988d). TEM Coincident Loop Negatives and the Loop Effect. Exploration Geophysics, 19(1–2), 354–357. https://doi.org/10.1071/eg988354

Soares, M. B., Neto, A. V., & Fabricio-Silva, W. (2020). The development of a Meso- to Neoarchean rifting-convergence-collision-collapse cycle over an ancient thickened protocontinent in the south São Francisco craton, Brazil. Gondwana Research, 77, 40-66. https://doi.org/10.1016/j.gr.2019.06.017

Spies, B. R. (1980). A field occurrence of sign reversals with the transient electromagnetic method Geophysical Prospecting, 28(4), 620–632. https://doi.org/10.1111/j.1365-2478.1980.tb01247.x

Telford, W. M., Geldart, L. P., & Sheriff, R. E. (1990). Applied Geophysics. Cambridge University Press. https://doi.org/10.1017/cbo9781139167932

Thomson, S., D. Fountain, and T.Watts. (2007). Airborne geophysics - Evolution and revolution. In Proceedings of Exploration 07: Fifth Decennial International Conference on Mineral Exploration, vol.1, p. 19–37.

Viezzoli, A., Christiansen, A. V., Auken, E., & Sørensen, K. (2008). Quasi-3D modeling of airborne TEM data by spatially constrained inversion. GEOPHYSICS, 73(3), F105–F113. https://doi.org/10.1190/1.2895521

Viezzoli, A., Fiandaca, G., Auken, E., Christiansen, A. V., & Sergio, S. (2013). Constrained inversion of IP parameters from Airborne EM data. ASEG Extended Abstracts, 2013(1), 1–4. https://doi.org/10.1071/aseg2013ab274

Viezzoli, A., Kaminski, V., Cooper, Y. L., Hardy, L., & Fiandaca, G. (2015). Improving modelling of AEM data affected by IP, two case studies. ASEG Extended Abstracts, 2015(1), 1–5. https://doi.org/10.1071/aseg2015ab213

Viezzoli, A., & Kaminski, V. (2016). Airborne IP: examples from the Mount Milligan deposit, Canada, and the Amakinskaya kimberlite pipe, Russia. Exploration Geophysics, 47(4), 269–278. https://doi.org/10.1071/eg16015

Viezzoli, A., Kaminski, V., & Fiandaca, G. (2017). Modeling induced polarization effects in helicopter time domain electromagnetic data: Synthetic case studies. GEOPHYSICS, 82(2), E31–E50. https://doi.org/10.1190/geo2016-0096.1

Viezzoli, A., Minsley, B., & Menghini, A. (2019). Insight from AIP modelling of VTEM ET data from Colorado. ASEG Extended Abstracts, 2019(1), 1–6. https://doi.org/10.1080/22020586.2019.12073178

Viezzoli, A., & Manca, G. (2019). On airborne IP effects in standard AEM systems: tightening model space with data space. Exploration Geophysics, 51(1), 155–169. https://doi.org/10.1080/08123985.2019.1681895

]Viezzoli, A., Manca, G., & Wjins, C. (2020). Causes and effects of the AIP trap in AEM data. Journal of Applied Geophysics, 175, 103970. https://doi.org/10.1016/j.jappgeo.2020.103970

Viezzoli, A., Dauti, F., & Wijns, C. (2021). Robust scanning of AEM data for IP effects. Exploration Geophysics, 1–12. https://doi.org/10.1080/08123985.2020.1856624

Wahba, G. (1990). Spline Models for Observational Data. Society for Industrial and Applied Mathematics. https://doi.org/10.1137/1.9781611970128

Walker, S. E. (2008). Should we care about negative transients in helicopter TEM data? SEG Technical Program Expanded Abstracts 2008. SEG Technical Program Expanded Abstracts 2008. https://doi.org/10.1190/1.3059116

Ward, S. H., & Hohmann, G. W. (1988). 4. Electromagnetic Theory for Geophysical Applications. In Electromagnetic Methods in Applied Geophysics (pp. 130–311). Society of Exploration Geophysicists. https://doi.org/10.1190/1.9781560802631.ch4

Weidelt, P. (1982). Response characteristics of coincident loop transient electromagnetic systems. Geophysics, 47(9), 1325–1330. https://doi.org/10.1190/1.1441393

Yu, C.-T., Liu, H.-F., Zhang, X.-J., Yang, D.-Y., & Li, Z.-H. (2013). The analysis on IP signals in TEM response based on SVD. Applied Geophysics, 10(1), 79–87. https://doi.org/10.1007/s11770-013-0366-4

Zhu, Y., Zhdanov, M. S., & Čuma, M. (2015). Inversion of TMI data for the magnetization vector using Gramian constraints. SEG Technical Program Expanded Abstracts 2015. https://doi.org/10.1190/segam2015-5855046.1

Appendix 1: Paper 1

A discussion of 2D induced polarization effects in airborne electromagnetic and inversion with a robust 1D laterally constrained inversion scheme

Changhong Lin, Gianluca Fiandaca, Esben Auken, Marco Antonio Couto, and Anders Vest Christiansen

GEOPHYSICS, VOL. 84, NO. 2 (MARCH-APRIL 2019); P. E75–E88, 17 FIGS., 3 TABLES. https://doi.org/10.1190/geo2018-0102.1

ABSTRACT

Recently, the interest in the induced polarization (IP) phenomenon in airborne time-domain electromagnetic (ATEM) data has increased considerably. IP may affect the ATEMdata significantly and mask underlying geologic structures. To simulate 2D airborne IP data, a 2D finite-element forward-modeling algorithm has been developed with the dispersive conductivity described by the wellknown Cole-Cole model. We verify our algorithm by comparison with the 1D solution of the AarhusInv code. Two-dimensional forward responses on six synthetic models,mimicking archetypal 2D conductive and chargeable anomalies, have been generated, and the results indicate that 2D IP affects the data significantly. Differences between the 2D IP responses and the 1D IP responses are evident above the 2D anomalies and at their edges. These differences are similar to what is found when comparing 2D and 1D forward responses over conductive 2D anomalies without considering IP. We evaluate an effective robust inversion scheme to recover the 2D IP parameters using the 1D laterally constrained inversion (LCI) scheme. The inversion of the synthetic data using the robust scheme indicates that not only can the IP parameters be recovered, but also the IP inversions can provide more accurate resistivity sections than a resistivity-only inversion, in terms of resistivity values and anomaly thickness/depth. The field example from Hope Bay area in Canada is even more valuable, considering that part of the profile consists of only negative data, which cannot be inverted with a resistivity-only scheme. Furthermore, the edge effects at the

anomaly boundaries are less pronounced in the IP parameters than in the resistivity parameter on the synthetic models with more conductive backgrounds.

INTRODUCTION

The induced polarization (IP) phenomenon in airborne electromagnetic (AEM) data presents a problem to exploration in many parts of the world. It is a well-known phenomenon and since Smith and Klein (1996) first demonstrate the presence of IP effects, which have been further discussed by several authors (e.g., Marchant et al., 2014; Macnae, 2016; Kaminski and Viezzoli, 2017). The advances in electronic and data processing especially for airborne time-domain electromagnetic (ATEM) systems have led to a much larger decay time recording and better signal-to-noise ratios, which in turn have revealed that IP is a severe problem and cannot be neglected during modeling.

Kozhevnikov and Antonov (2008, 2010) discuss numerical experiments exploring the potentialities and limitations in the 1D IP inversion of ground-based transient electromagnetic responses of a uniform and a two-layer earth. Kratzer and Macnae (2012) develop an approximate interpretation tool to invert ATEM IP responses. Fiandaca et al. (2012) present a laterally constrained 1D inversion scheme to model the complex resistivity in terms of the Cole-Cole IP model (Cole and Cole, 1941; Peton et al., 1978), and Viezzoli et al. (2017) use the approach of Fiandaca et al. (2012) to study the recovering of IP parameters from AEM data. Kang and Oldenburg (2016) and Kang et al. (2017) propose a 3D inversion method for ATEM IP data, where they do a 3D resistivity only in- version of the early time data not significantly affected by IP, subtract the forward responses from the data and by this decouple the IP model from the resistivity model. However, the computation power involved is significant for a 3D inversion and the decoupling approach neglects the correlations between the resistivity and the IP parameters (by assuming that the early-time data are not affected by IP).

Two-dimensional forward modeling of ATEM IP has, to the best of our knowledge, not been presented before, and we use it to gain insight into IP responses over 2D chargeable bodies and to develop a robust inversion scheme. We have developed a 2D finite-element (FE) modeling algorithm for ATEM data, where the model is defined in two dimensions and the source is a finite rectangular loop. To simulate airborne IP data, our 2D forward

code uses the resistivity Cole-Cole (RCC) parameterization (Cole and Cole, 1941; Pelton et al., 1978) and the maximum phase angle (MPA) reparameterization of the RCC model (Fiandaca et al., 2018) to compute the electrical complex resistivity (Maclennan et al., 2014).

As described in Auken et al. (2008), 1D inversion of ATEM data in a 3D environment is possible and gives a good recovery of the true model in many cases. Nevertheless, even in one dimension, the ATEM IP inversion is significantly ill-posed and it is a challenging problem to recover the four parameters simultaneously. Here, a robust inversion scheme, based on the multiparametric 1D laterally constrained inversion (LCI) scheme (Auken and Christiansen, 2004), is proposed and tested on the 2D data. The inversion scheme relies on 1D forward/Jacobian computations, but without any decoupling approximations, i.e., with a simultaneous recovery of the resistivity and the IP parameters. In addition to the standard 1D LCI scheme described in Auken et al. (2015), several modifications are introduced to improve the robustness of the inversion process.

The inversion results of the synthetic data from the 2D models and of a field example are used to illustrate the effectiveness of the robust inversion scheme, which suggests a way forward for IP inversion of large-scale field data sets for geophysical exploration and geologic mapping.

METHODOLOGY

In this section, we will describe the steps involved in the investigation, i.e., (1) the 2D modeling, (2) the system description and simulation of noise, (3) the robust inversion scheme, and (4) the synthetic models and sounding layout.

2D modeling

For simulating ATEM data, we developed a 2D modeling algorithm. In the implementation, the source is a horizontal rectangular loop. To deal with the singularity of the field at the source location, an approach separating the total electric (EM) and magnetic fields into a primary part containing the singularity and a secondary part (Wannamaker et al., 1986; Unsworth et al., 1993; Newman and Alumbaugh, 1995) is used. The EM fields generated by a horizontal electric dipole at the earth's surface on

either a uniform whole space or a layered half-space can be evaluated using the expressions presented by Ward and Hohmann (1987). By integrating numerically around the loop using the transverse electric (TE) mode of these expressions and some modifications of the reflection coefficients, the primary EM fields above the earth generated by a horizontal rectangular loop in the air on either a uniform whole space or a layered half-space can be obtained in the wavenumber (k_y) domain. The FE method is then applied to the numerical modeling of the secondary field for each k_y.

Assuming a harmonic time dependence of $e^{\mathrm{i}\omega\mathrm{t}}$, the secondary electric field Es and magnetic field $\boldsymbol{H}^S$ are described by Maxwell's equations:

$$\boldsymbol{\nabla} \times \boldsymbol{E}^S = -i\mu_0 \omega \boldsymbol{H}^S \tag{1}$$

$$\boldsymbol{\nabla} \times \boldsymbol{H}^S = \sigma \boldsymbol{E}^S + \sigma_a \boldsymbol{E}^P \tag{2}$$

where $\boldsymbol{E}^P$ is the primary electric field, ω is the angular frequency, μ_0 is the vacuum magnetic permeability (permeability variations are not considered), σ is the complex conductivity, $\sigma_a = \sigma - \sigma_P$ is the anomalous complex conductivity, and σ_P is the background conductivity used for computing the primary field. To include the IP phenomenon in the Maxwell's equation, the RCC model as in Pelton et al. (1978) is applied to model the dispersive complex conductivity in equation 2:

$$\sigma(\omega) = \frac{1}{\rho_0 \left[1 - \frac{m_0}{10^3}\left(1 - \frac{1}{1 + \left(i\omega\tau_\rho\right)^C}\right)\right]} \tag{3}$$

with four interconnected parameters: ρ_0 is the electrical resistivity (ohm-m), m_0 is the intrinsic chargeability (mV/V), τ_ρ is the relaxation time (s), and C is the frequency exponent.

Following Mitsuhata (2000), we can obtain two coupled governing differential equations for the secondary electric field $\boldsymbol{E}_y^S$ and magnetic field $\boldsymbol{H}_y^S$ in the k_y-domain after the Fourier transform is applied to equations 1 and 2 with respect to y. The other components $\boldsymbol{E}_x^S$, $\boldsymbol{E}_z^S$, $\boldsymbol{H}_x^S$, and $\boldsymbol{H}_z^S$ are calculated from the spatial derivatives of $\boldsymbol{E}_y^S$ and $\boldsymbol{H}_y^S$. To derive

the finite-element equations, the Galerkin method (Zienkiewicz, 1977) and a rectangular element with four nodes have been adopted. The simple Dirichlet condition $\boldsymbol{E}_y^S = \boldsymbol{H}_y^S = \mathbf{0}$ at the boundaries is assigned. We solve the linear system equations by the Bi-CGSTAB method (Smith, 1996; Lin et al., 2018) to obtain $\boldsymbol{E}_y^S$ and $\boldsymbol{H}_y^S$. The total EM fields in the k_y-domain are transformed to the space domain by the inverse Fourier transformation. The ATEM responses are obtained by transforming the total EM fields from the frequency domain to the time domain.

To assess modeling accuracy of the 2D code, the time derivatives of the vertical magnetic fields, $d\boldsymbol{B}\ /\ dt$, were compared with the 1D solution implemented in the AarhusInv code (Auken et al., 2015). The comparison between the 1D solution of the AarhusInv code and the 2D response on a three-layer model is shown in Figure 2.1. The three-layer model consists of a homogeneous background (ρ0 ¼ 5000 Ωm, m0 ¼ 0 mV/V), with an anomalous layer ($\rho_0 = 500$ Ωm, $m_0 = 350\ mV/V$, $\tau_\rho = 0.001$ s , $= 0.55$) embedded in it at a depth of 20 m. The consistency of the 2D response and the 1D solution is sufficiently accurate, with 6.4% maximum deviation at the gates close to the sign change and less than 2% at all others.

System description and noise: Synthetic example

The main features of the ATEM system used to simulate synthetic data are described in Table 1. Two types of errors are considered when constructing the noise model (Auken et al., 2008): (1) a uniform relative error, which simulates possible inaccuracy in the system description and (2) a contribution that depends on the signal level, which mimics the background random noise. Consequently, the total noise contribution to synthetic data is described as

$$v = G(0,1) \cdot [STD_{uni}^2 + v_{noise}^2]^{\frac{1}{2}} \tag{4}$$

where G $G(0,1)$ is the Gaussian distribution with zero mean and standard deviation 1, STD_{uni}^2 is the uniform noise, and v_{noise}^2 is the background noise contribution. Here, the uniform STD is set to 3% on all the time gates. The background noise can be approximated to a straight line with a slope of $t^{-1/2}$ in a log-log plot. From field data, we

estimated an empirical value for the background noise of 10^{-9} V/m^4, at 1 ms (Auken et al., 2008).

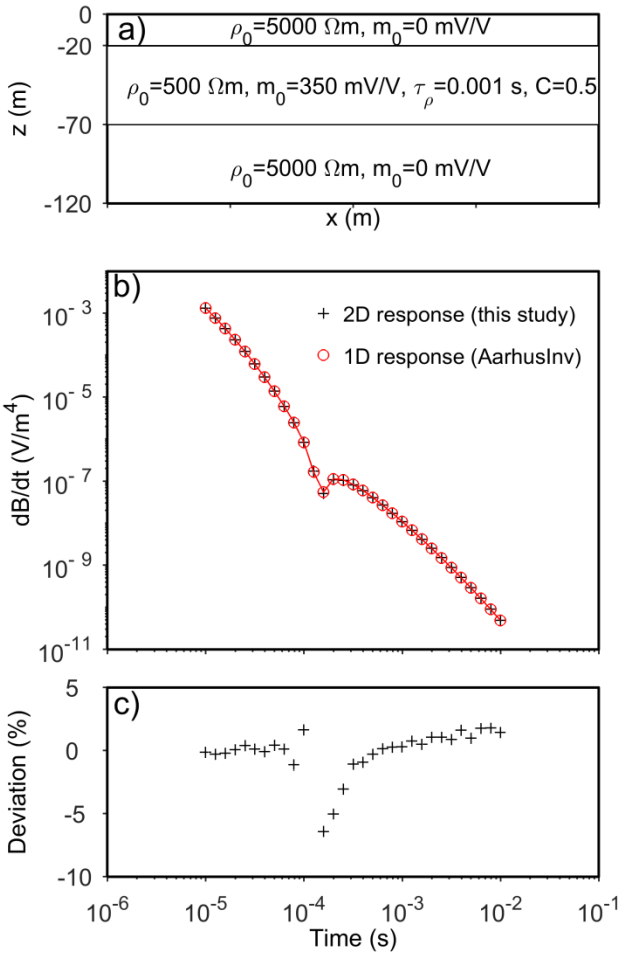

Figure 2.1. Comparison between the 1D solutions of the AarhusInv code and the 2D responses on a three-layer model. (a) The threelayer model. (b) The time derivatives of the vertical magnetic fields. (c) Deviations of our 2D solutions from AarhusInv's 1D solutions.

In the plots throughout the paper, the data are presented in volts (V) normalized by the receiver and transmitter areas (m4), but not by current and turns of the transmitter loop. This normalization is chosen to highlight the level of the signal in comparison with the background noise.

Table 1. Synthetic AEM system parameters description.

	Parameter	Value

Transmitter	Number of transmitter turns	16
	Transmitter area	300 m^2
	Peak current	100 A
	Peak moment	480,000 NIA
	Turn-on time	-10 ms
	Ramp up to peak current time	-9 ms
	Turn-off time	0 µs
	Ramp down to zero current time	5 µs
Receiver	Number of outuput gates	31
	Time gates interval	From 10 µs to 10 ms (10 gates/decade)

1D LCI robust scheme

To invert the synthetic data, we use the 1D LCI approach, which minimizes an objective function that includes 2D lateral constraints on the model parameters belonging to neighboring stations. The objective function is expressed by

$$Q = \left(\frac{\delta \boldsymbol{d}^T \boldsymbol{C}_{obs}^{-1} \delta \boldsymbol{d} + \delta \boldsymbol{r}^T \boldsymbol{C}_R^{-1} \delta \boldsymbol{r}}{N_d + N_R} \right)^{1/2} \quad (5)$$

where $\boldsymbol{C}_{obs}$ and $\boldsymbol{C}_R$ are the data and constraint covariance matrices; $\delta \boldsymbol{d} = \boldsymbol{d} - \boldsymbol{d}_{obs}$ represents the difference between the forward response d and the observed data dobs; $\delta \boldsymbol{r} = -\mathbf{Rm}$ is the roughness of the model vector m, computed through the roughness matrix **R**; N_d and N_R represent the number of data points and roughness constraints. A Gauss-Newton style minimization scheme with a Marquardt modification (Marquardt, 1963) is applied to find the set of model parameters that minimize the $L2$-misfit with

respect to observed data and regularization (and prior information, if present). The model parameters are log-transformed for reducing their dynamic range. The stopping criterion for the inversion is enforced on the relative change in the objective function between consecutive iterations and is set to 1%. More details about the LCI scheme can be found in Auken and Christiansen (2004) and Auken et al. (2015). In this study, we inverted all the soundings along a profile simultaneously to minimize a common objective function including lateral constraints. The 1D LCI algorithm is robust to 2D earth structures due to the lateral constraints (Auken et al., 2008), but edge effects such as "pants legs," that are reminiscent of diffraction hyperbolas from seismic sections (Wolfgram et al., 2003), may be found in the 1D LCI inversion models when significant lateral resistivity contrasts are present. The 1D LCI has its advantages in the reduction of the nonuniqueness, recovering the lateral continuity of the inverted model, compared with individual sounding-by-sounding 1D inversions. Finally, compared with a full 2D inversion, the 1D LCI is computationally efficient, which makes field-data inversion practical.

Compared with the standard 1D LCI scheme described in Auken et al. (2015) and used in Viezzoli et al. (2017) and Kaminski and Viezzoli (2017), five modifications have been implemented to increase the stability and parameter recovery of the ATEM IP inversion: (1) The model space has been reparameterized to minimize parameter correlations, (2) a method to establish robust starting models has been identified, (3) the τ and C parameters have been fixed in the first few iterations awaiting structure to happen in the resistivity and chargeability parameters, (4) the data standard deviations have been modified close to the sign change to improve convergence, and (5) the damping scheme has been modified to balance the multiparameter model space better. In the following, these five modifications are treated in detail.

Model Space

The model reparameterization consists of the MPA reparameterization of the RCC model introduced by Fiandaca et al. (2018) for galvanic, ground-based frequency-domain and time-domain IP inversions, described by the parameters

$$\boldsymbol{m}_{MPA} = \{\rho_0,\ \varphi_{max},\ \tau_{\varphi}, C\} \tag{6}$$

where φmax represents the MPA of the Cole-Cole complex resistivity and τ_φ is the inverse of the frequency at which φmax is reached. Figure 2 shows the absolute value and the phase (sign reversed) of the Cole-Cole complex resistivity as a function of frequency, with the classic Cole-Cole parameters (ρ_0, m_0, τ_ρ), and φ_{max} and τ_φ represented as well. The phase reaches the maximum φ_{max} at the frequency $1 / 2\pi\,\tau_\varphi$. The terms τ_φ and τ_ρ are linked through the relation $\tau_\varphi = \tau_\rho \cdot (1 - m_0)^{1/2C}$.

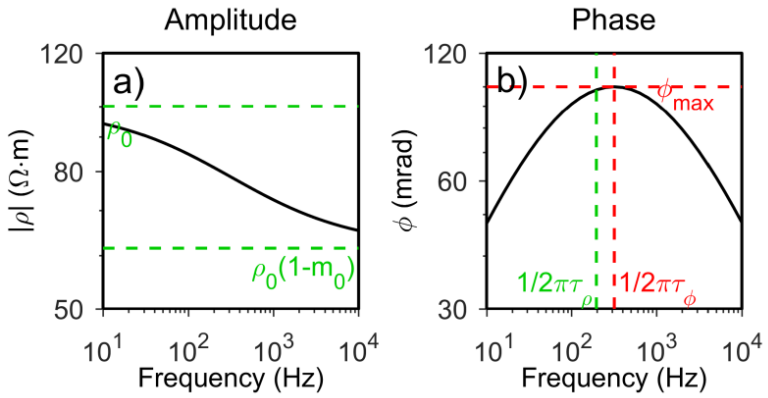

Figure 2. (a) Amplitude and (b) phase of the Cole-Cole complex conductivity spectrum for the model $m_{MPA} = \{\rho_0 = 100\ \Omega m,\ \varphi_{max} = 100\ mrad, \tau_\varphi = 5 \times 10^{-4}, C = 0.5\}$. The low- and high- frequency limits of the amplitude are ρ_0 and $\rho_0(1 - m_0)$ (with m_0 expressed in V/V).

In the inversion of galvanic, ground-based time-domain, or frequency-domain spectral IP data, the m_0 and C parameters of the RCC model are strongly correlated (Bérubé et al., 2017; Fiandaca et al., 2018), whereas the correlation between φ_{max} and C in the MPA parameterization is weaker, leading to a significantly better resolution of φ_{max} compared with m_0 (Fiandaca et al., 2017). A reduction of the $\varphi_{max} - C$ correlation in comparison with the $m_0 - C$ correlation is obtained also for ATEM data. This can be seen in Figure 3, in which the phase of the complex resistivity and the ATEM response of a homogeneous half-space are compared when varying the φ_{max} / C parameters of the MPA model and the m_0 / C parameters of the classic RCC model. In Figure 3a, the phase of the reference RCC model (gray line) is compared with the phase obtained with a 20% decrease of m_0 (green line) and a 20% decrease of C (orange line). The decrease of m_0 and the decrease of C cause similar phase variations close to the phase peak. This similarity in the phase variation is reflected into the effect on the ATEM response (Figure 3b), where the responses are practically indistinguishable (green and orange lines) above

the background noise. In Figure 3c, the phase of the MPA reference model (gray line) is compared with the phase obtained with a 20% decrease of φ_{max} (green line) and a 20% increase of C (orange line). Here, it is an increase instead of decrease because a C decrease would bring the orange line even farther from the phase of 20% φ_{max} decrease. The spectra obtained with the 20% φ_{max} decrease and the 20% C increase are significantly different close to the phase peak, and the corresponding ATEM responses (Figure 3d) are clearly distinguishable.

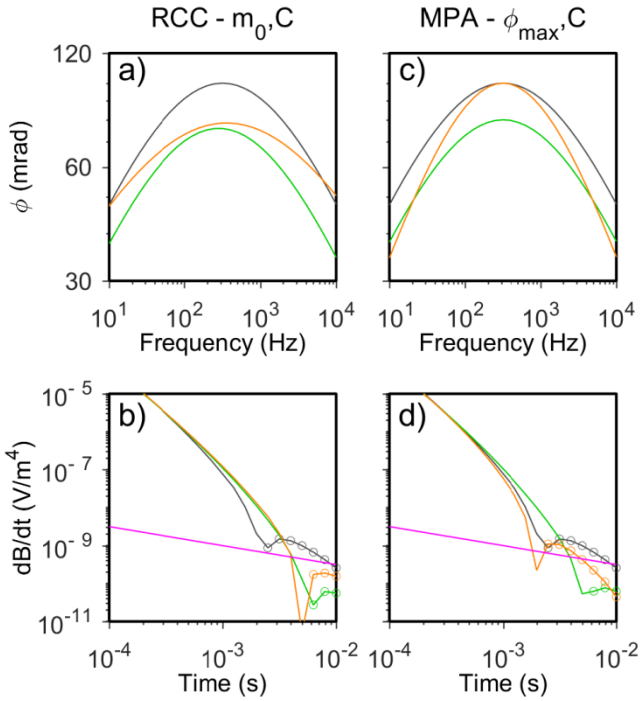

Figure 3. Phase spectra and AEM responses for the homogeneous halfspace models. Reference model: $\mathbf{m_{MPA}} = \left\{ \rho_{\mathbf{0}} = \mathbf{100\ \Omega m},\ \phi_{\mathbf{max}} = \mathbf{100\ mrad},\ \tau_{\phi} = \mathbf{5 \cdot 10^{-4}\ s}, \mathbf{C = 0.5} \right\}$. a) Reference phase spectrum (grey line), spectrum obtained with 20% $\mathbf{m_0}$ decrease (green line) and 20% C decrease (orange line) for the RCC model. b) Reference AEM response (grey line), response obtained with 20% $\mathbf{m_0}$ decrease (green line) and 20% C decrease (orange line) for the RCC model. c) Reference phase spectrum (grey line), spectrum obtained with 20% $\phi_{\mathbf{max}}$ decrease (green line) and 20% C increase (orange line) for the MPA model. d) Reference AEM response (grey line), response obtained with 20% $\phi_{\mathbf{max}}$ decrease (green line) and 20% C increase (orange line) for the MPA model. In sections b) and d) the circled data are negative. The magenta lines represent the noise level.

Robust starting models

Like any other ill-posed problem, the IP inversion problem can become unstable and sensitive to the starting parameter values. Compared with inverting for resistivity only, the choice of the starting values for the four parameters becomes significantly more critical in IP inversion. As presented by Viezzoli et al. (2017), the use of ancillary a priori information (drilling, geology, ground geophysics, etc.) can help to reduce the ambiguity of the inversion results. The question is how to choose the starting parameter values without available ancillary information, which is the normal situation. Our tests found that using starting values close to the values of the half-space host rock (i.e., ignoring an anomalous IP layer) is a good choice for all four MPA Cole-Cole parameters. If the starting value of ρ_0 or φ_{max} is far away from the values of the host rock, the inversion often converges to the wrong model. Based on this, and considering that the host rock is usually nonchargeable, our robust scheme to choose the starting MPA Cole-Cole parameters is (1) invert resistivity-only including only the nonnegative data, and using tight lateral and vertical constraints, to get a nearly homogeneous resistivity model as the starting value for ρ_0; (2) choose a low or moderate value (10–30 mrad) as the starting φmax, which does not trigger negative data (note that smaller values are needed when starting from high resistivity values and that the values depend also on the system characteristics, so that forward modeling tests might be needed for finding appropriate values); (3) set the starting value for C to 0.3, i.e., an intermediate value; (4) select a value in the interval 1e-1s to 1e-5s, which triggers the strongest IP as the staring values for τ_φ. This choice for the starting resistivity is based on the assumption that the IP-affected AEM data are only present in a portion of the profile/area and that the remaining soundings can give a reasonable estimate of the background resistivity. This is not necessarily always true, and the negative data can dominate not only spatially in the surveyed area, but also within each sounding. In this case, the resistivity of the starting model can be hard to retrieve automatically and it has to be manually set.

Locking parameters

Simultaneous recovery of four parameters increases the nonuniqueness of the inversion. To favor the structure in the ρ_0 and φ_{max} parameters and decrease nonuniqueness, the robust scheme is separated into two steps after the starting model is determined. In step

one, the parameters τ_φ. and C are fixed for several iterations, focusing the structure to ρ_0 and φmax. Then, in step two, τ_φ. and C are released and all four parameters are optimized simultaneously.

Sign changes

During the iterative inversion process, changes in model parameters that impact the timing of the sign reversal in the forward responses infer large variation in the data misfit of the objective function. This leads to instability in the inversion process, which easily traps the model in a local minimum. To mitigate the effects linked to the sign change, we increase the uniform STD at the four time gates (two positive and two negative) around the sign change (s) from 3% to 30%.

Damping scheme

The adaptive damping approach based on the Marquardt method described in Auken et al. (2015) damps all the inversion parameters through the maximum diagonal element of the matrix $\boldsymbol{G}_n'^T \boldsymbol{C}'^{-1} \boldsymbol{G}_n'$, where $\boldsymbol{G}_n'$ and $\boldsymbol{C}'$ are the Jacobian of the *n*th iteration and the data covariance matrix, respectively (extended to also contain the prior and roughness information; for details, see Auken et al., 2015). In the IP inversion, we have four inversion parameters per layer, which means that the magnitudes of the Jacobian elements differ significantly. For example, the τφ parameter usually has very small derivative values compared with the other parameters. This means that the damping scheme described in Auken et al. (2015) likely overdamps the weakly resolved parameter types, impeding their variation through the inversion process. To overcome this problem, the damping scheme was modified to evaluate the maximum of the $\boldsymbol{G}_n'^T \boldsymbol{C}'^{-1} \boldsymbol{G}_n'$ matrix block-wise for each parameter type and damping them per block.

Synthetic models and sounding layout

Fifty-one synthetic soundings simulating a profile length of 1 km (20 m sounding spacing) were used for each of the 2D forward modeling scenarios. In the 2D finite-element forward modeling, the grid has a fine central part containing the model, the transmitter,

and receivers laterally and vertically. The grid has 141 × 39 in the $x - z$ plane (a total of 5499 nodes). A nominal flight height of 30 m over a flat surface was used.

In our experiments, we consider six 2D models based on three base models. The models are displayed in Figure 4, and they all consist of a chargeable anomaly 20 m below surface. The chargeable and relatively conductive anomalies are embedded in a homogeneous and nonchargeable host rock, mimicking ore bodies. The lengths of the chargeable anomaly blocks are infinite (models 1 and 2), 320 (models 3 and 4) and 60 m (models 5 and 6). Two different sets of IP parameters (shown in Table 2) are used in the models. The Cole-Cole parameters of type 2 are the same used for the disseminated sulfide model by Viezzoli et al. (2017, Figure 2). Models using the type 2 parameters are comparatively resistive. We also consider a comparatively conductive type 1 with different IP parameters. In our six experimental models, the type 1 Cole-Cole parameters are used for models 1, 3, and 5 and the type 2 are used for models 2, 4, and 6.

Table 2. The two different MPA Cole-Cole parameters used in the 2D experimental models.

		ρ_0 (Ωm)	m_0 (mV/V)	ϕ_{max}(mrad)	τ_ρ (s)	τ_ϕ (s)	C
Type 1	Host rock	100	10	0.4	0.01	0.01	0.1
	Anomaly	10	500	142	0.001	0.0005	0.5
Type 2	Host rock	5000	0	0	0	0	0
	Anomaly	500	350	89	0.001	0.00065	0.5

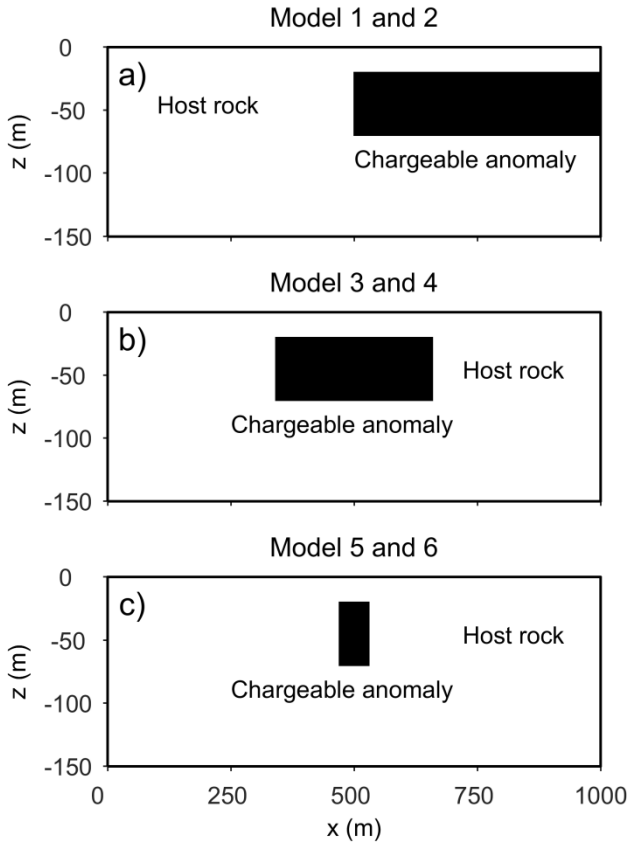

Figure 4. The three basic 2D experimental models. The horizontal lengths of anomalies are (a) infinite, (b) 320 m, and (c) 60 m. By applying two sets of IP parameters to the anomalies, a total of six models are achieved.

RESULTS

Synthetic examples

2D effects on AEM IP data

Comparisons between the 2D responses (the red and blue lines with the gray error bar) and the 1D responses (the black lines) at station A (red) and station B (blue) generated on models 1 and 2 are shown in Figure 5a and 5b and Figure 5c and 5d, respectively. Influenced by the edge of the target, significant differences between the 2D responses and 1D responses are observed at the A station (Figure 5a and 5c), which is 20 m outside the anomaly. A sign change due to the 2D effect is seen only with the comparatively resistive model 2 (Figure 5c), although the negative data are below the noise level. Edge effects

are still seen at station B, 160 m away from the anomaly edge, whereas they are negligible at 440 m from the edge (not shown).

On model 2, stronger IP effects with a much earlier sign reversal is observed at station B (Figure 5d). Similarly, on model 1, clear sign changes appear at station B (Figure 5b). The differences in the timing of the sign reversal are an effect of the relative size between the signal coming from the anomalous conductivity and the negative effect of the anomalous chargeability. To underline this, Figure 6 shows a comparison of the 2D and 1D responses on models 1b and 2b, which have the same conductivity structure as models 1 and 2, but without IP ($\varphi_{max} = 0\ mrad$). Here, 2D effects are present at stations A and B, but no sign reversals are observed. Hence, the sign reversal is an effect solely of the IP response, but the timing includes a balance with the conductivity-driven signal.

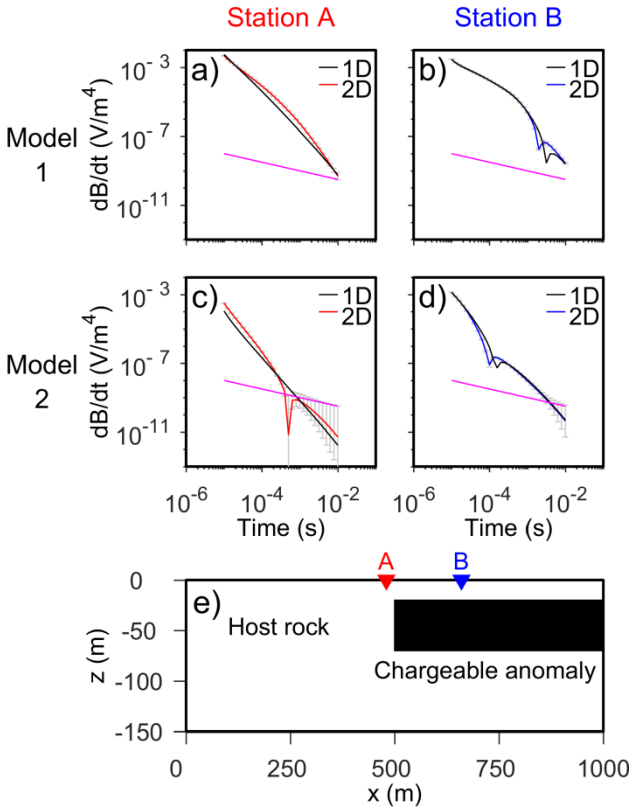

Figure 5. Comparison between the 2D responses (red and blue lines with gray error bar) and the 1D response (black lines) at station A (red) and station B (blue) generated on Models 1 (panels a and b) and 2 (panels c and d). The magenta lines represent the noise level. Stations A and B lie at 480 m and 660 m in the x-direction, respectively.

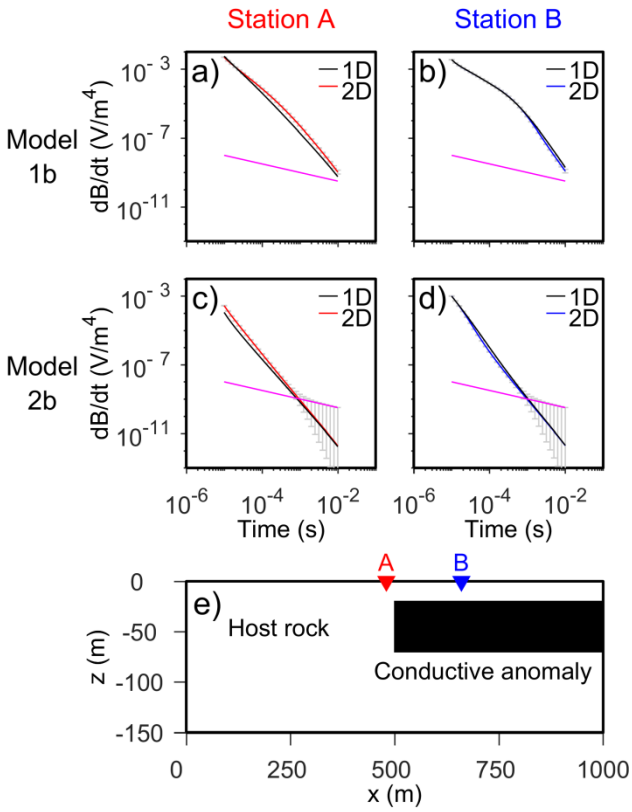

Figure 6. Comparison between the 2D responses (red and blue lines with gray error bar) and the 1D response (black lines) at station A (red) and station B (blue) generated on conductive Models 1b (panels a and b) and 2b (panels c and d), which have the same conductivity structure as Models 1 and 2 but without an IP effect ($\varphi_{max} = 0$ mrad). The magenta lines represent the noise level. Stations A and B lie at 480 m and 660 m in the x-direction, respectively.

Figure 7 shows the comparison between the 2D responses and the 1D responses at stations A and B generated on models 3 and 4. Stations A and B are again 20 and 160 m away from the target edge. The 2D responses at stations A and B have obvious differences to the 1D responses and have similar characteristics as those in Figure 5 although the IP effects on models 3 and 4 are stronger, seen as a sign reversal at an earlier time.

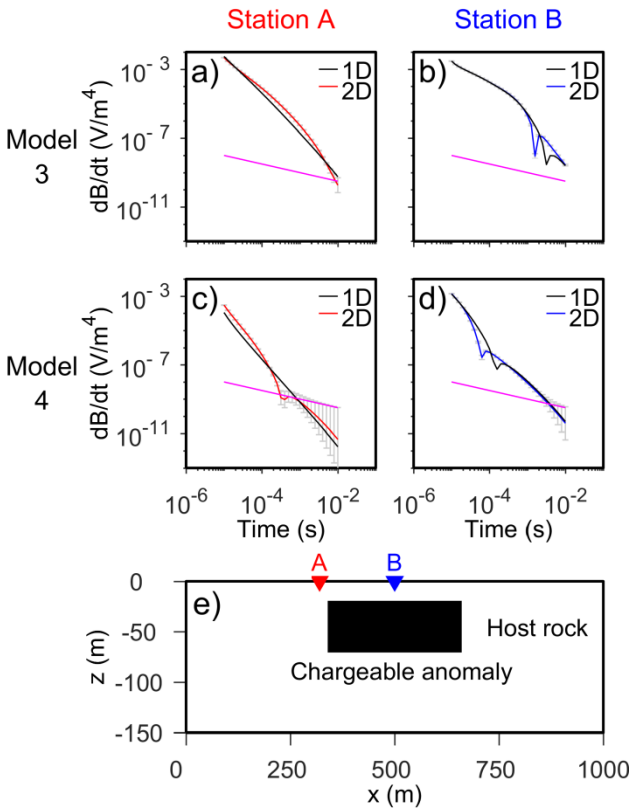

Figure 7. The same as Figure 5 but for Models 3 (panels a and b) and 4 (panels c and d). Stations A and B lie at 320 m and 500 m in the x-direction, respectively.

The comparisons between the 2D and 1D responses at stations A and B for models 5 and 6 are shown in Figure 8. The 2D responses generated by the comparatively smaller anomaly in the x-direction (models 5 and 6) are still different from the 1D responses. Looking at the 2D responses alone, there are significant differences between models 5 and 6, where model 5 does not produce a sign change, whereas model 6 creates a clear sign reversal. However, the negative data for model 6 are below the noise level. Such responses with no sign change or negative data below the noise level would be hard to interpret as IP effects.

Comparing the responses at station B on model 3 and those on model 5, which have the same Cole-Cole parameters but different model geometry, the 2D responses are obviously affected by the length of the target. A clearer sign reversal is seen because the longer target (model 3, Figure 7b) is charged up more strongly. A similar phenomenon is observed in the 2D responses at station B on models 4 and 6 (Figures 7d and 8d).

Figure 9 shows a comparison between the 2D IP responses and the 2D resistivity-only responses at station A (from Figures 5a, 5c, 7a, 7c, 8a, and 8c) for all six models. The black lines show the ratios of the 2D IP responses normalized by 2D resistivity-only responses. The negative ratios come from the negative values of the IP responses at late gate times for models 2, 4, and 6. The responses are similar at the early gate times, with ratios close to 1, but the differences become significant at later times. For models 1, 3, and 5, the (logarithmic) average deviations between the 2D IP responses and the 2D resistivity-only responses are 18%, 24%, and 32%, respectively, with the larger deviations at approximately 10 ms (the smallest ratio is 0.24 for model 1). For models 2, 4, and 6, the deviations are much larger than for the conductive models because sign reversals are present in the 2D IP responses, the smallest ratio being 0.013 for model 2 at the time gate of 0.5012 ms. Consequently, big 2D IP edge effects are present when the background is resistive and sign reversals exist in the 2D IP responses, but significant edge effects are also present when sign reversals are not observed.

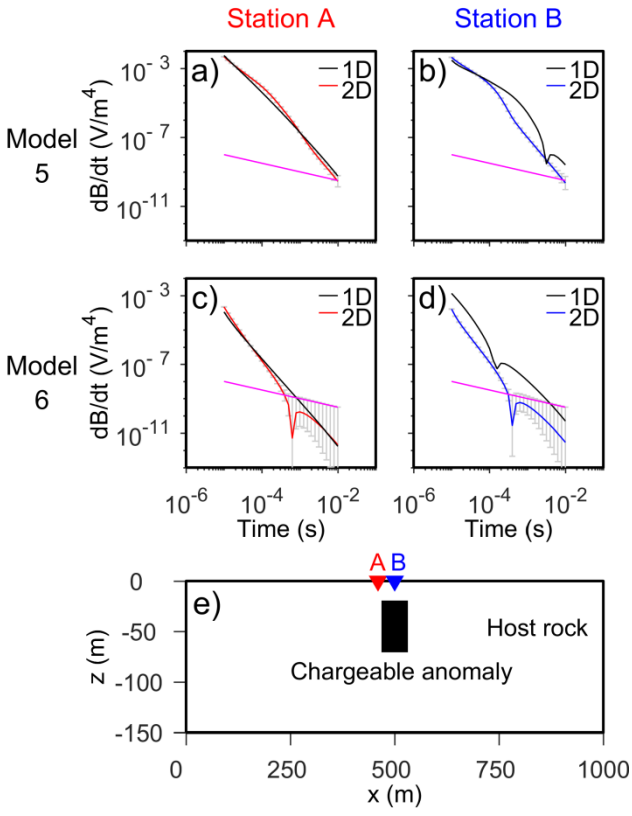

Figure 8. The same as Figure 5 but for Models 5 (panels a and b) and 6 (panels c and d). Stations A and B lie at 460 m and 500 m in the x-direction, respectively.

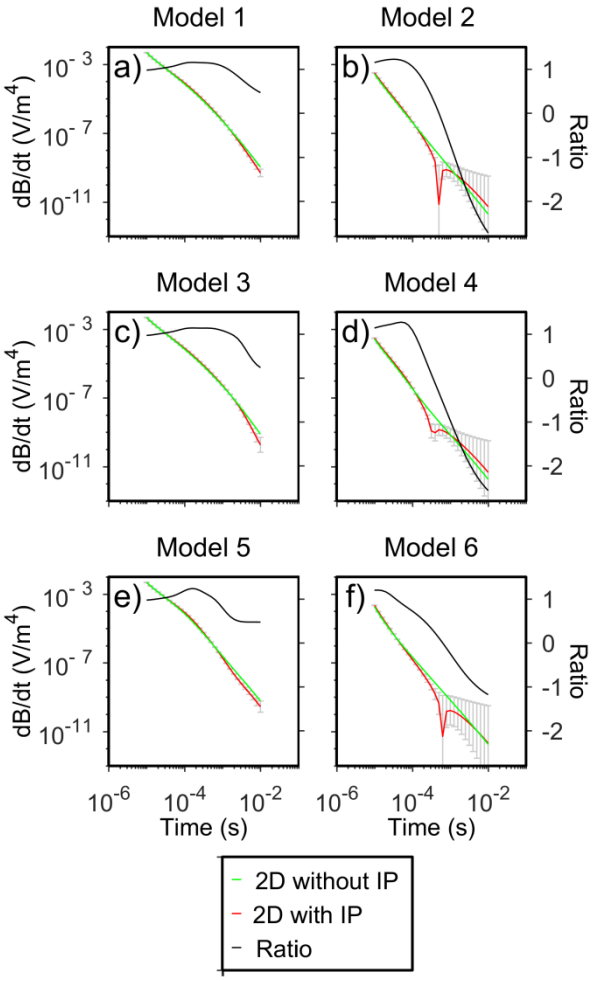

Figure 9. Comparison between the 2D IP responses (red lines with gray error bar) and the 2D resistivity-only responses (green lines) at station A (shown in Figures 5, 7 and 8 panels) generated on the Models 1 (panel a), 2 (panel b), 3 (panel c), 4 (panel d), 5 (panel e) and 2 (panel f). The black lines show the ratio of the 2D IP responses divided by 2D resistivity-only responses.

Inversion results

First, inversions with the robust 1D inversion scheme on the synthetic data from the six experimental models without noise contamination are presented. The robust scheme uses the following settings: MPA inversion; starting ρ0 from the resistivity-only inversion without negative data, $\varphi_{max} = 30\ mrad$, $\tau_\varphi = 1e-4s$, and $C = 0.3$; τ_φ and C locked for the first seven iterations; increased STD to 30% atthe four gate times at the sign reversal; and the adaptive damping approach.

Figure 2.10 shows the inversion results from the synthetic data for models 1, 3, and 5 (Figure 2.10a, 10b, and 10c, respectively). The depth of investigation (DOI) is computed following Fiandaca et al. (2015). The anomalies of the three models are recovered for all four MPA parameters, in magnitude and shape, and the data are well fitted. This means that the differences between the 1D and 2D responses seen in the synthetic studies are compensated in the inversion through small parameter variations that do not prevent the recovery of reasonable models. However, pants-leg edge effects are present in the resistivity and MPA (φ_{max}) sections. The edge effects in the φ_{max} parameter are a consequence of the 2D IP effects at the anomaly edges presented in Figure 9. The edge effects are present in φmax and not in τ_{φ} and C because φmax controls the the synthetic data for models 1, 3, and 5 in Figure 2.11. To do this, the negative data have been removed. As is clearly seen, the resistivity only inversions do not reproduce the resistivity models as well and they have a poorer data fit. strength of the IP effect in the data more than τ_{φ} and C. However, contrary to the resistivity parameter, the edge effects in φ_{max} lay below the DOI on models 1 and 3. On model 5, the φ_{max} edge effects are above the DOI, but the φ_{max} values retrieved by the inversion are smaller in the edges than in the anomaly. On the contrary, on model 5, the resistivity edge effects are as strong as the resistivity anomaly.

To investigate the effect of inverting with a full IP model with four parameters, we show 1D resistivity-only inversion results of the synthetic data for models 1, 3, and 5 in Figure 2.11. To do this, the negative data have been removed. As is clearly seen, the resistivity-only inversions do not reproduce the resistivity models as well and they have a poorer data fit.

Figure 2.12 shows the inversion results from the synthetic data for models 2, 4, and 6 using the robust 1D inversion scheme. The anomalies of the three models are decently recovered in the resistivity and phase sections, but not as well as in Figure 2.10. Furthermore, contrary to Figure 2.10, in Figure 2.12, the edge effects in φ_{max} are above the DOI and similar to the resistivity edge effects because the 2D IP edge effects in the forward data are stronger in the models with more resistive backgrounds (Figure 9). The inversion results from the synthetic data inverting resistivity-only after deleting the negative data are shown in Figure 2.13. It is found that the inversions for models 2 and 4 represent the anomalies at a much shallower depth than the true depth. Nevertheless,

compared with the results obtained from inverting resistivity only (Figure 2.13), the IP inversions have smaller data misfits and more accurate resistivity images (the first row in Figure 2.12). As shown in Figure 8c and 8d, there are no IP effects above the noise level in the 2D responses from by the smallest anomaly in model 6. Therefore, the inversions for model 6 cannot predict the true model.

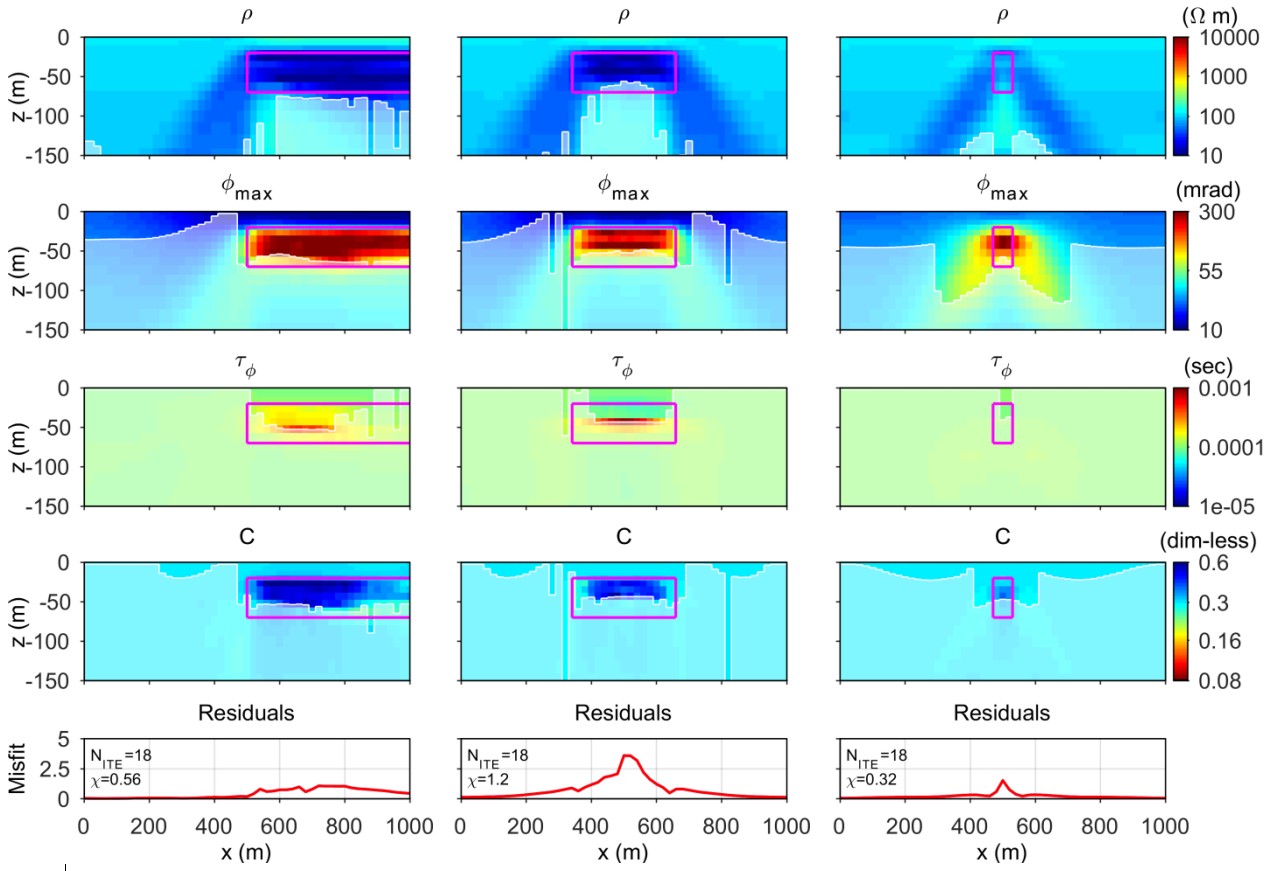

Figure 2.10. Inversion results from 1D LCI of the synthetic data for Models 1 (left column), 3 (middle column) and 5 (right column) using the robust scheme. The shaded areas represent the portions of the models below the depth of investigation (DOI).

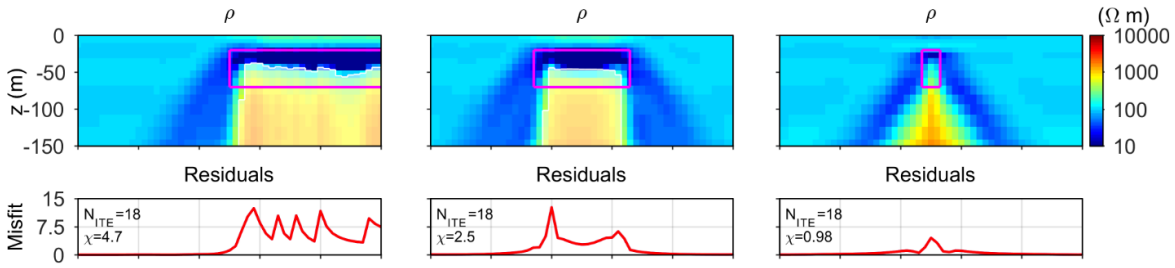

Figure 2.11. Inversion results from1D LCI of the synthetic data for Models 1 (left column), 3 (middle column) and 5 (right column) inverting resistivity only and without considering the negative data. The shaded areas represent the portions of the models below the DOI.

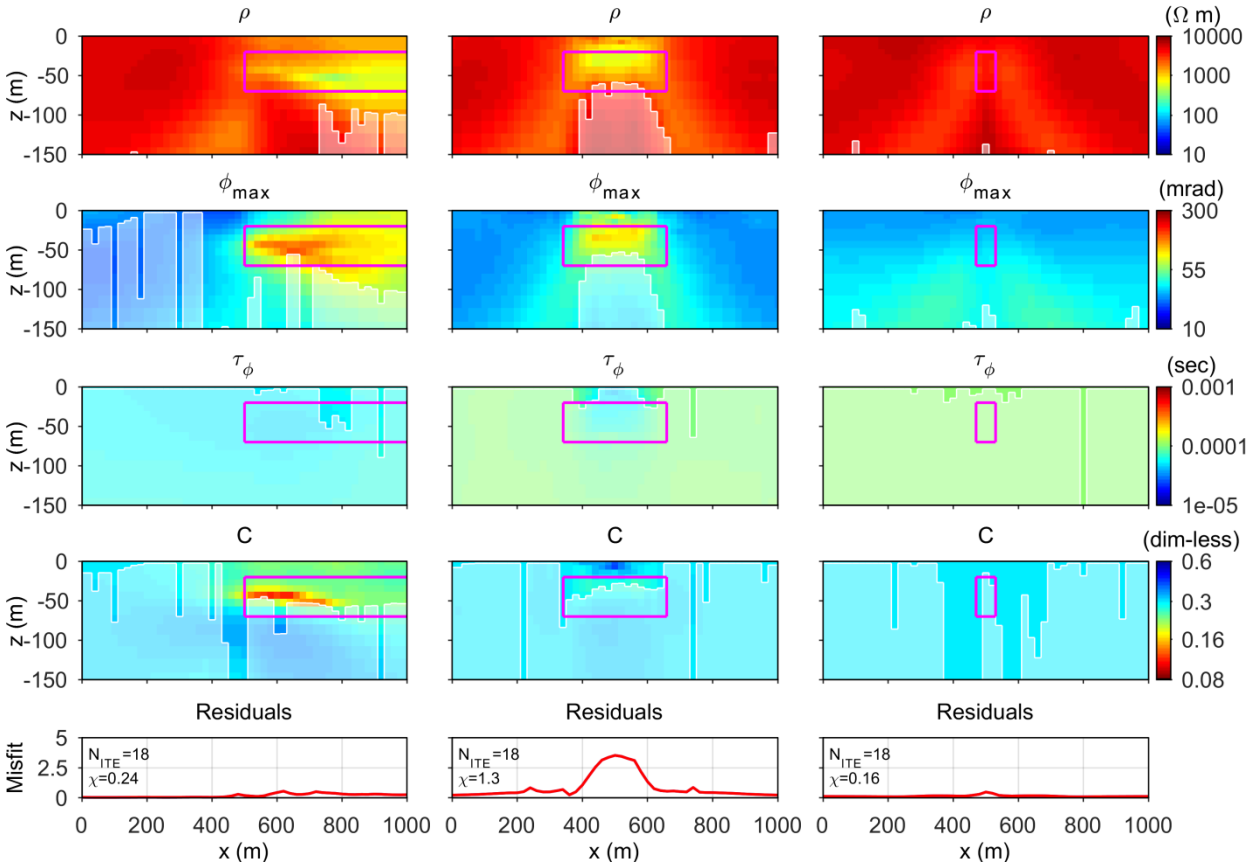

Figure 2.12. Inversion results from 1D LCI of the synthetic data for Models 2 (left column), 4 (middle column) and 6 (right column) using the robust scheme. The shaded areas represent the portions of the models below the DOI.

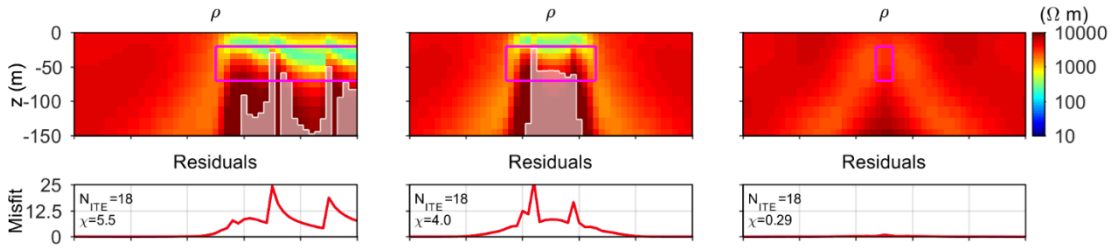

Figure 2.13. Inversion results from 1D LCI of the synthetic data for Models 2 (left column), 4 (middle column) and 6 (right column) inverting resistivity only and without considering the negative data. The shaded areas represent the portions of the models below the DOI.

To highlight the role of the robust inversion scheme in the results, we have carried out separate inversions with the elements of the robust scheme taken out one by one. The results are shown in Figure 2.14. These inversions are presented against the data misfits of the MPA inversions with the full robust scheme (black lines) for all six experimental models. In Figure 2.14a, the red line shows the data misfits of the inversions without the robust starting model for resistivity, where a homogeneous starting value $\rho_0 = 700\ \Omega\,\mathrm{m}$ is used instead. The data misfits without robust starting ρ_0 are generally larger than those using the robust scheme (black line) except for model 4. In Figure 2.14b, the blue line shows the data misfits of the inversions without the robust STD values (a 30% STD at the four time gates at the sign reversal). The misfits without the robust noise are larger than the misfits of the inversion with the robust scheme, except for model 6, for which there is a small decrease. In Figure 2.14c, the green line shows the data misfits without locking τ_φ and C in the first seven iterations. Again, the misfits are generally bigger especially for the models 1–3. In Figure 2.14d, the magenta line shows the data misfits of the inversion without the parameter-type dependent damping scheme, with a significant misfit increase for models 1 and 2; whereas models 3 and 4 show a deceased misfit. For the few models where the robust scheme does not give an improved data residual, we evaluated the model results with the general conclusion that the inversion results with robust scheme are more accurate representations of the true model, but we are not showing these results for brevity. Moreover, the inversion results obtained without any of the implementations of the robust scheme are significantly worse than those presented in Figure 2.14.

Finally, to test the robust scheme against noise contaminated data, 100 data sets contaminated with different random noise distributions were inverted for each experimental model. Figure 2.15 shows the distribution of the data misfits from the 100 inversions for six models. A good data misfit, approximately 1, is obtained for the most part of the inversions. Furthermore, the inversion models are very similar to those shown in Figures 10 and 12.

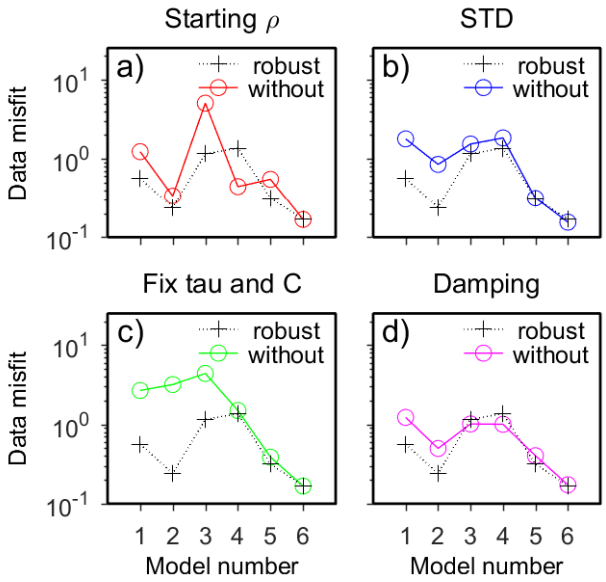

Figure 2.14. Comparison between the data misfits of the inversions for six experimental models (without noise contamination) with the robust scheme (black lines) and those without using it (colored lines). a) The red line shows the data misfits of the inversions without the robust starting ρ_0 (i.e. with starting $\rho_0 = 700$ Ωm for all inversions). b) The blue line shows data misfit of the inversion without robust STD values (i.e. without the increased STD around the sign reversal). c) The green line shows the data misfit of the inversion without fixing τ_φ and C in the first seven iterations. d) The magenta line shows the data misfit of the inversion without the parameter-type dependent damping scheme.

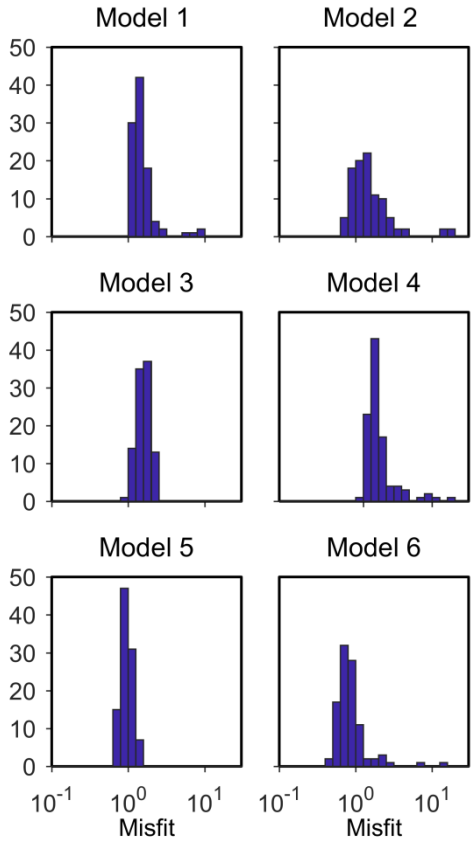

Figure 2.15. The distribution of the data misfits from the 100 inversions of the synthetic data with 100 different random noise contaminations for six models, using the robust scheme.

Field example

The survey

The field example is extracted from a SkyTEM survey over Hope Bay area, in the West Kitikmeot region of Nunavut Territory, Canada. The study area presents several world-class porphyry-type gold deposits in a greenstone belt environment, in particular, Doris, Madrid and Boston deposits, all TMAC Resources Inc. properties. The survey was requested by TMAC and covered 12,123 km in the Madrid deposit area. Its main purpose was to add relevant geological information to the understanding of gold deposits environment.

Due to the mineralization styles and as described in Kaminski et al. (2016), it is expected to have significant IP effect in this AEM survey. In fact, these authors demonstrated that this dataset needs to be inverted considering a multiparamer IP mode, in order to recover a reliable resistivity model and avoid distorted conductive anomalies when a resistivity-only parameterization is considered. Taking in account these characteristics, this dataset is ideal for the application of the proposed robust inversion scheme.

Kaminski et al. (2016) pointed out three conductive anomalies in the north portion of the SkyTEM survey which were significantly distorted when a resistivity-only model was applied, but better recovered using a multiparametric IP inversion (they used the RCC parameterization). In this work, we present the results for the proposed robust inversion scheme applied for a cut in a flight line profile with 3.2 km extension in the region of an anomaly given number three.

AEM system

The system used for the field example was the SkyTEM516, with dual magnetic dipole moments: low moment (LM) and high moment (HM). The key parameters for the transmitter and receiver systems are summarized in Table 3 (adapted from SkyTEM ApS survey report). The nominal terrain clearance for the transmitter/receiver system is 30 m, flight speed of 87 km/h and the nominal sampling rate is 10 Hz, after preliminary processing during the survey execution.

Table 3. SkyTEM516 system parameters used in the Hope Bay survey (adapted from SkyTEM ApS survey report).

	Parameter	Value	
		Low Moment (LM)	High Moment (HM)
Transmitter	Number of transmitter turns	2	16
	Transmitter area	536.36 m²	
	Peak current	5.3/5.3 A	113.8/117.9 A
	Peak moment	4,500 NIA	1,000,000 NIA
	Repetition frequency	210 Hz	30 Hz
	Turn-on time	-800.000 µs	-400.000 µs
	Ramp up to peak current time	0 ms	-0.3766 ms
	Turn-off time	1.776 µs	0 ms
	Ramp down to zero current time	29.050 µs	705.013 µs
	Duty cycle	33%	24%
	Waveform	Square	
Receiver	Sample rate	All decays were measured	
	Number of outuput gates	28	39
	Time gates interval (calibrated gatecenter referenced to the LM turn-off time)	From 54.115 µs to 1369.615 µs	From 172.615 µs to 10275.615 µs

	Receiver coil low pass filter	210 kHz	
	Receiver instrument low pass filter	300 kHz	
	Repetition frequency	210 Hz	30 Hz
	Front gate	0.0 µs	800 µs

Inversion results

In Figure 2.16a and 16b, the LM and HM AEM data of the field example are presented, respectively. The blue marks represent the positive data, the red marks represent the negative data, whereas the gray marks show the data removed during processing (with some portions of the profile in which all data are below the noise floor due to a very resistive ground). The chosen profile presents negative data in the LM and HM acquisitions, not only at late times (as in the synthetic examples) but also at early times, with full-negative AEM responses (above the noise floor) as well as responses starting negative, increasing to positive values, and finally decaying to zero.

The inversion results for the ρ_0; φ_{max}; τ_φ, and C parameters are presented in Figure 2.16c–16f, and the corresponding data misfit is presented in Figure 2.16g. The figure sections of the τ_φ and C parameters (Figure 2.16e and 16f) are plotted with a smaller depth range because the DOI is really shallow and no significant information is present in the deep part of the sections. Figure 2.17a shows a sounding example with data fit, with the corresponding 1D model used for generating the forward response presented in Figure 2.17b–17c.

The inversion results presented in Figures 16 and 17 were computed using the same robust setting of the synthetic examples, except for the starting resistivity value. Indeed, the resistivity-only inversion carried out on the positive data with tight lateral and vertical constraints give a too-resistive starting model, which prevents a good convergence of the inversion. Consequently, a homogeneous value equal to 250 Ωm was used as the starting value for the inversion.

The inversion model presents a shallow conductive and chargeable layer in a significant portion of the profile. This layer is responsible of the early-time negative data, and it makes an interpretation of the data in terms of a resistivity-only inversion impossible. Deeper conductive anomalies are present in the west portion of the profile, associated with moderate values in the φ_{max} section. The inversion in terms of the MPA model allows us to fit almost all the negative data present in the section, as evidenced by the example in Figure 2.17a.

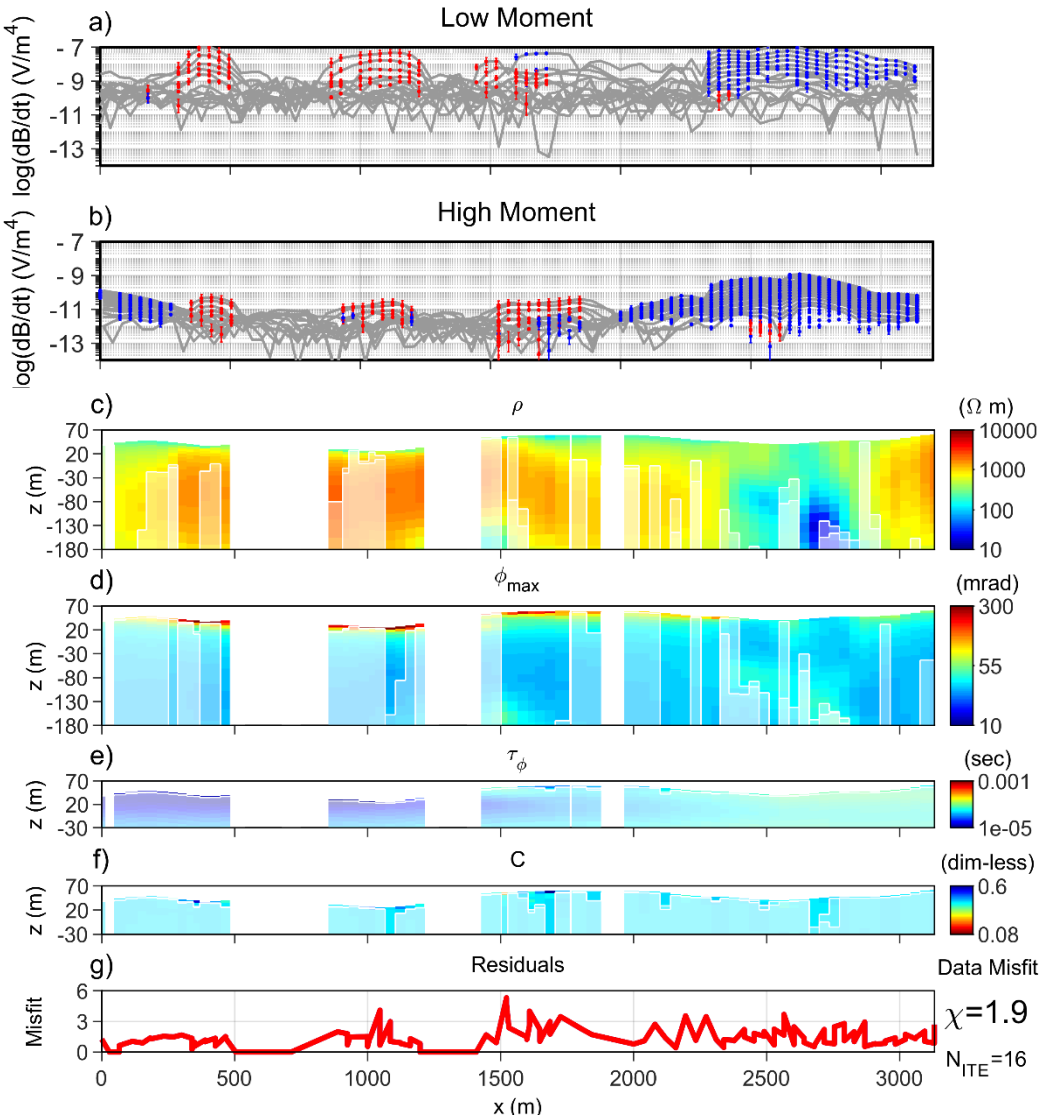

Figure 2.16. Data and inversion model of the field profile. a-b) LM and HM data. Blue and red marks indicate the positive and negative data (and error bars) used in the inversion. The grey lines represent all measured data, including the data points removed during processing because of no Earth signal. c-d-e-f) Inversion sections for the ρ_0, φ_{max}, τ_φ and C parameters. The shaded areas represent the portions of the models below the DOI. g) Misfit section.

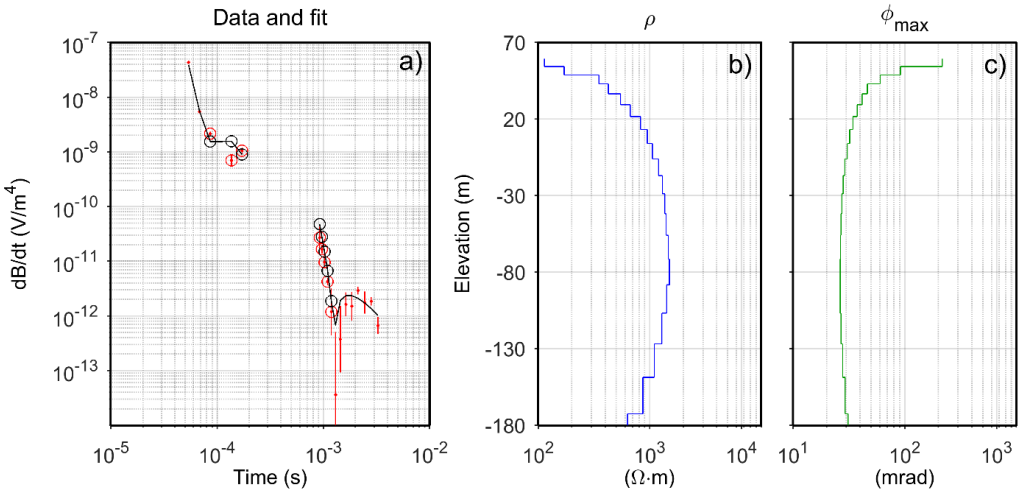

Figure 2.17. Example of data, fit and corresponding model. a) Data (red marks) and forward response (black line and marks); negative measured/forwarded data are circled. b) Resistivity model. c) Maximum phase angle model.

CONCLUSIONS

Based on the FE method and the Cole-Cole model, a 2D modeling algorithm has been developed to simulate ATEM IP data, and it is verified against the 1D AarhusInv solution. Using the modeling code, we generated 2D ATEM forward responses on six experimental models and studied the 2D IP effects on ATEM data. For inversion, a robust 1D LCI scheme for ATEM IP is presented, based on five new implementations: (1) using the MPA reparameterization of the Cole-Cole model, which decreases parameter correlations; (2) identification of a general robust starting model; (3) fixing of the τ and C parameters for the first few iterations; (4) definition of data standard deviations that facilitate convergence, especially around possible sign changes; and (5) a new parametertype dependent damping scheme.

From the comparison of the 2D IP responses, 1D IP responses, and 2D responses without IP, it is concluded that 2D IP edge effects are clearly present in the forward data. The magnitude of the 2D IP edge effects depends on the horizontal length of the 2D target and the distance between the receiver and the target, as well as on the four MPA Cole-Cole parameters, with stronger edge effects on models with more resistive backgrounds. Furthermore, 2D responses with no sign change or negative data below the noise level

are generated by the short target in the horizontal direction, and they would be hard to interpret as IP effects.

Two-dimensional synthetic data on six models were inverted. The inversion results show that it is possible to recover the 2D IP parameters using a 1D scheme, but pants-leg edge effects are present in the inversion models when large parameter contrasts exist. However, the 2D IP edge effects are less pronounced than the resistivity edge effects on models with more conductive backgrounds. Overall, the anomalies of the models that generate strong IP signals are wellresolved. Equally important, inverting with IP parameters, contrary to resistivity-only inversion, results in better defined resistivity sections. In other words — if data exhibiting IP effects are inverted ignoring the IP parameters, one will get erroneous resistivity models as a result. These considerations are corroborated by the inversion of a field example in which full-negative decays are present in many areas of the profile, making resistivity-only inversion impossible. However, incorporating IP parameters in the model description makes inversion possible with realistic resistivity structures of the subsurface and well-fitted data.

ACKNOWLEDGMENTS

This study has been jointly supported by the National Natural Science Foundation of China (grant nos. 41674134 and 41874159), National Key Research and Development Program of China (grant nos. 2016YFC0601104 and 2017YFC0602204), State Scholarship Fund of China, and the Special Fund for Basic Scientific Research of Central Colleges. The paper is also a part of the water center and the AirTech4water Innovation Fund Denmark project. Constructive comments by P. Leroy, two anonymous referees, the associate editor X. Garcia, and the assistant editor J. Shragge significantly improved this manuscript and are greatly appreciated. Also, the authors would like to thank SkyTEMApS and TMAC Resources Inc. to provide and allow access to the SkyTEM data set used in the field example in this work.

DATA AND MATERIALS AVAILABILITY

Data associated with this research are available and can be obtained by contacting the corresponding author.

REFERENCES

Auken, E. and A. Christiansen, 2004, Layered and laterally constrained 2D inversion of resistivity data: Geophysics, 69, no.3, 752-761.

Auken, E., A. Christiansen, C. Kirkegaard, G. Fiandaca, C. Schamper, A. Behroozmand, A. Binley, E. Nielsen, F. Effersø, N. Christensen, K. Sørensen, N. Foged and G. Vignoli, 2015, An overview of a highly versatile forward and stable inverse algorithm for airborne, ground-based and borehole electromagnetic and electric data: Exploration Geophysics, 46, no.3, 223-235.

Auken, E., A.V. Christiansen, L.H. Jacobsen and K.I. Sørensen, 2008, A resolution study of buried valleys using laterally constrained inversion of TEM data: Journal of Applied Geophysics, 65, no.1, 10-20.

Bérubé, C.L., M. Chouteau, P. Shamsipour, R.J. Enkin and G.R. Olivo, 2017, Bayesian inference of spectral induced polarization parameters for laboratory complex resistivity measurements of rocks and soils: Computers and Geosciences, 105, 51-64.

Cole, K. S. and R. H. Cole, 1941, Dispersion and Absorption in Dielectrics I. Alternating Current Characteristics: The Journal of Chemical Physics, 9, no.4, 341-351.

Fiandaca, G., E. Auken, A. Christiansen and A. Gazoty, 2012, Time-domain-induced polarization: Full-decay forward modeling and 1D laterally constrained inversion of Cole-Cole parameters: Geophysics, 77, no.3, E213-E225.

Fiandaca, G., A. Christiansen and E. Auken, 2015, Depth of Investigation for Multi-parameters Inversions: Near Surface Geoscience 2015-21st European Meeting of

Environmental and Engineering Geophysics.

Fiandaca, G., L.M. Madsen, and P.K. Maurya, 2018, Re-parameterization of the Cole-Cole model for improved spectral inversion of induced polarization data: Near Surface Geophysics, DOI 10.3997/1873-0604.2017065.

Kaminski, V. and A. Viezzoli, 2017, Modeling induced polarization effects in helicopter time-domain electromagnetic data: Field case studies: Geophysics, 82, no.2, B49-B61.

Kaminski, V., A. Viezzoli, and A. Menguini, 2016, Case studies: Hope Bay gold deposits: Aarhus Geophysics (http://www.aarhusgeo.com).

Kang, S., D. Fournier and D. Oldenburg, 2017, Inversion of airborne geophysics over the DO-27/DO-18 kimberlites - Part 3: Induced polarization: Interpretation, 5, no.3, T327-T340.

Kang, S. and D.W. Oldenburg, 2016, On recovering distributed IP information from inductive source time domain electromagnetic data: Geophysical Journal International, 207, no.1, 174-196.

Kozhevnikov, N. O. and E. Y. Antonov, 2008, Inversion of TEM data affected by fast-decaying induced polarization: Numerical simulation experiment with homogeneous half-space: Journal of Applied Geophysics, 66, 31-43.

Kozhevnikov, N. O. and E. Y. Antonov, 2010, Inversion of IP-affected TEM responses of a two-layer earth: Russian Geology and Geophysics, 51, 708-718.

Kratzer, T. and J. Macnae, 2012, Induced polarization in airborne EM: Geophysics, 77, no.5, E317-E327.

Lin, C., H. Tan, W. Wang, T. Tong, M. Peng, M. Wang, and W. Zeng, 2018, Three-dimensional inversion of CSAMT data in the presence of topography: Exploration Geophysics, 49, no.3, 253-267.

MacLennan, K., M. Karaoulis and A. Revil, 2014, Complex conductivity tomography using low-frequency crosswell electromagnetic data: Geophysics, 79, no.1, E23-E38.

Macnae, J., 2016, Quantifying Airborne Induced Polarization effects in helicopter time domain electromagnetics: Journal of Applied Geophysics, 135, 495-502.

Marchant, D., E. Haber and D. Oldenburg, 2014, Three-dimensional modeling of IP effects in time-domain electromagnetic data: Geophysics, 79, no.6, E303-E314.

Marquardt, D., 1963, An Algorithm for Least-Squares Estimation of Nonlinear Parameters: Journal of the Society for Industrial and Applied Mathematics, 11, no.2, 431-441.

Mitsuhata, Y., 2000, 2-D electromagnetic modeling by finite‐element method with a dipole source and topography: Geophysics, 65, no.2, 465-475.

Newman, G.A. and D.L. Alumbaugh, 1995, Frequency-domain modelling of airborne electromagnetic responses using staggered finite differences: Geophysical Prospecting, 43, no.8, 1021-1042.

Pelton, W., S. Ward, P. Hallof, W. Sill and P. Nelson, 1978, Mineral discrimination and removal of inductive coupling with multifrequency IP: Geophysics, 43, no.3, 588-609.

Smith, J., 1996, Conservative modeling of 3-D electromagnetic fields, Part II:

Biconjugate gradient solution and an accelerator: Geophysics, 61, no.5, 1319-1324.

Smith, R. and J. Klein, 1996, A special circumstance of airborne induced‐polarization measurements: Geophysics, 61, no.1, 66-73.

Unsworth, M., B. Travis and A. Chave, 1993, Electromagnetic induction by a finite electric dipole source over a 2-D earth: GEOPHYSICS, 58, no.2, 198-214.

Viezzoli, A., V. Kaminski and G. Fiandaca, 2017, Modeling induced polarization effects in helicopter time domain electromagnetic data: Synthetic case studies: Geophysics, 82, no.2, E31-E50.

Wannamaker, P., J. Stodt and L. Rijo, 1986, Two‐dimensional topographic responses in magnetotellurics modeled using finite elements: Geophysics, 51, no.11, 2131-2144.

Ward, S.H. and G.W. Hohmann, 1987, 4. Electromagnetic Theory for Geophysical Applications. in Electromagnetic Methods in Applied Geophysics - Theory: pp. 131-312, ed. Nabighian, M. N. and Corbett, J. D. Society of Exploration Geophysicists.

Zienkiewicz, O.C., 1977, The Finite Element Method: third edition, McGraw-Hill.

Appendix 2: Paper 2

AEMIP Robust Inversion Using Maximum Phase Angle Cole-Cole Model Re-parameterization Applied for HTEM Survey Over Lamego Gold Mine, Quadrilátero Ferrífero, MG, Brazil

Marco Antonio Couto Junior, Gianluca Fiandaca, Pradip Kumar Maurya, Anders Vest Christiansen, Jorge Luís Porsani, Esben Auken

EXPLORATION GEOPHYSICS, 2020, VOL. 51, NO. 1, 170–183 https://doi.org/10.1080/08123985.2019.1682458

ABSTRACT

This paper presents the results of airborne electromagnetic induced polarization inversions using the Maximum Phase Angle (MPA) model for a helicopter time domain survey in the Quadrilátero Ferrífero area, Minas Gerais State (MG), Brazil. The inversions were conducted using a laterally constrained robust scheme, in order to decrease the difficulties to recover the multi-parametric model in a very ill-posed inverse problem, often found in induced polarization studies. A set of six flight lines over the Lamego gold mine mineralized structure were inverted using the MPA re-parameterization of the Cole-Cole model and also the classical resistivity-only parameterization, in order to understand the implications of the induced polarization effect in the data and, consequently, in the resistivity model. A synthetic study was also conducted, seeking to understand what to expect from the resistivity-only inversions in the real data. According to borehole lithological data and previous structural knowledge from the literature, the results from the Maximum Phase Angle approach indicate an important chargeable body that seems to be in good agreement with a sulfide enriched carbonaceous/graphite and altered mafic unities, which are important markers for the gold mineralization.

Key Words: Airborne electromagnetics, Induced polarization

INTRODUCTION

During the last decade, the interest to model airborne electromagnetic induced polarization (AEMIP) phenomena has significantly increased (Kang and Oldenburg 2016; Kratzer and Macnae 2012; Macnae 2015; Marchant et al., 2014; Viezzoli et al., 2013). Due to the improvements of the helicopter transient electromagnetic (HTEM) systems in power and resolution, like the newest SkyTEM312HP (Gisselø and Nyboe 2018) and VTEM^{TM} *super max* (http://geotech.ca/) systems, these studies were mainly motivated by applications in mineral exploration, groundwater and environmental studies (Kaminski and Viezzoli 2017; Kang et al., 2017; Viezzoli et al., 2017; Viezzoli et al., 2016). In particular, for mineral exploration, it has potential to survey and characterize economic mineralizations related to disseminated sulfide zones, especially within deposits associated with hydrothermal and igneous processes. The use of AEMIP can help to decrease ambiguities between mineralizations and their host rocks, to understand the structural control and their association with chemical traps, like reactive carbonaceous units in highly hydrothermal altered terrains. In addition, AEMIP may be useful in some circumstances to map large areas with chargeability information in a very short time compared to ground-based induced polarization (IP) surveys. Covering large areas with ground-based IP methods usually present difficulties in accessibility, logistics and costs.

Although the newest powerful HTEM systems are superior in observing the AEMIP phenomenon, there are many existing airborne electromagnetic (AEM) surveys carried out with less powerful systems, which also contain IP effects. These data should be investigated for IP information, in order to provide preliminary information for new IP studies to be carried out in the same area and/or improve the resistivity and chargeability models. With this philosophy in mind, we present an AEMIP modeling study in the Lamego gold mine (AngloGold Ashanti property), in the Greenstone Belt Rio das Velhas, Quadrilátero Ferrífero (QF) area, Minas Gerais State (MG), Brazil, using data acquired with an AeroTEM^{HD} system. The survey was flown with N45W orientation, 250 m flight-line spacing and with total 3560 line-km. This HTEM system has a triangular pulse current waveform, with a peak moment of 711000 NIA and 17 off-time channels for the vertical component.

Due to the high resistive terrain of the greenstone belt, a very urbanized environment associated with mines and cities in the surroundings and a system with a low magnetic moment, the AEM data display several couplings to man-made structures and low signal-to-noise ratios in many parts of the survey. For these reasons it was challenging to find clear AEMIP anomalies. Nevertheless, some sign reversals (negative late time gates) and rapidly decaying dB/dt signals were recorded over the mineralized structure in Lamego mine area. Carbonaceous and graphite schists, associated with gold mineralization within disseminated metallic sulfides, occur in the mine area, which might be responsible for the IP effects in the AEM data. Indeed, the frequency-domain IP measurements conducted in the laboratory by Smith et al., (1983) on similar lithologies (from a greenstone belt environment in Saudi Arabia) show significant IP effects over the whole measurement range from 0.06 to 1024 Hz.

The AEMIP modelling was conducted on six flight lines over Lamego structure using the 1D laterally constrained robust inversion scheme proposed by Fiandaca et al., (2018a) and Lin et al., (2019), using the Maximum Phase Angle (MPA) re-parameterization of the Cole-Cole model (Fiandaca et al., 2018b) in order to reduce the correlation of the inversion parameters. In addition, the electrical resistivity models obtained through this approach were compared with the ordinary resistivity-only (RO) inversion, in order to understand the differences in the models, with and without IP modeling. All the results were integrated with borehole lithological data. The final result is an integration of all inverted sections in a 3D visualization of the polarizable body.

AREA OF STUDY

Lamego is one the most important gold mines in the Quadrilátero Ferrífero (QF) area, MG, Brazil, which is property of AngloGold Ashanti. It is characterized by an Archean orogenic gold deposit, within the rocks of the Rio das Velhas greenstone belt, in the North portion of the QF area. Structurally, the mine is characterized by a reclined, isoclinal and cylindrical fold (Martins et al., 2016)– Figure 2.1. Lithologically, it is characterized by a metamorphosed volcano-sedimentary sequence composed by mafic units, banded iron formation (BIF)/chert units and carbonaceous/micaceous schists.

According to Martins et al., (2016) and based on borehole data, the gold mineralization is associated with disseminated sulfides (mainly pyrite, arsenopyrite, chalcopyrite and sphalerite) that are classified in three groups: i) The quartz-carbonate/sulfides veins crosscut all lithologies, but with a better development within the BIF layers, with locally stockwork structure; ii) The Fe-carbonate replacement for sulfides within the BIF layers, which confines the sulfides in this lithology; and iii) Dissemination within the mafic units and carbonaceous metapelites/schists. The gold grade for each of these mineralization groups vary between 1.6-15.8 ppm, 0.03-6.63 ppm and 0.03-3.8 ppm, respectively.

Laboratory petrophysical data from lithological borehole samples were used as guidance to define the initial values for the input parameters in the inversion process. These data indicated a very resistive environment (> 1000 Ω·m for the mafic unities, reaching values greater than 5000 Ω·m in the micaceous metapelite zones) associated with the micaceous metapelite and mafic-ultramafic unities, but with conductive and chargeable zones that could be associated with the carbonaceous/graphite metapelites/schists and disseminated sulfides within both carbonaceous and mafic layers, which are an important guide to map the gold mineralization. It is expected that the IP effect might be generated mainly from these carbonaceous/graphite units, according to petrophysical data from Anglo Gold Ashanti, which presents average values for resistivity and chargeability for the lithological units in Lamego area. In fact, we observed very steep decays often associated with negative transients over Lamego structure. Furthermore, in this work, the IP methodology is used in order to try to define these carbonaceous units, that could be associated as a structural guidance for the gold mineralization.

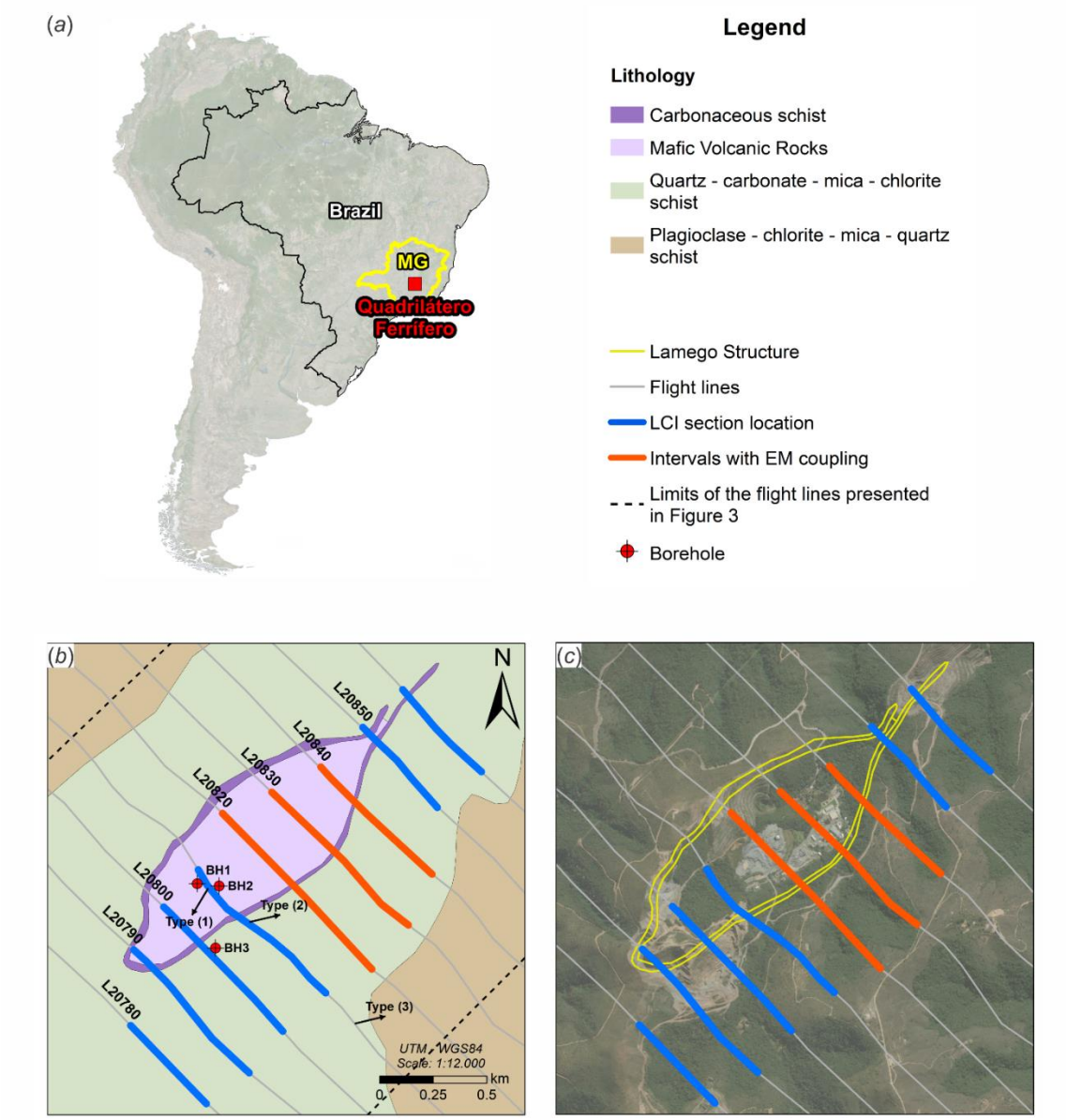

Fig. 1: Area of study location. (a) Quadrilátero Ferrífero (QF) location in Brazil and Lamego gold mine. (b) Detailed geological map of Lamego gold mine structure with flight line positions (grey lines, with their number indicated) – the borehole lithological data are indicated by the red points and the LCI sections used in this work are indicated by the blue lines along the flight lines, the orange lines indicate intervals with low signal amplitude and couplings, which are disabled in the inversion analysis. Types (1), (2) and (3) position indicate the types of soundings presented in the Fig. 2. The dashed lines indicate the spatial limits of all flight lines presented in this Fig. 2. (c) Satellite image over Lamego Mine area, with the indication of the flight lines and the mine infracture buildings which caused the coupling in the orange lines intervals.

HTEM Survey and System Description

The HTEM system used in the survey in QF region was the Aeroquest AeroTEM^{HD}, with 30 Hz base frequency triangular pulse waveform. The survey flight lines were oriented to NW-SE (azimuth 135) and the spacing between the lines was 250 m. The nominal terrain clearance was 30 m for the EM transmitter/receiver system, it covered 3560 line-km and had a nominal flight speed of 75 km/h with a data reading every 1.5 - 2.5 m (10 samples/s) along the flight line.

Although the AeroTEM^{HD} system is able to conduct measurements with X (flight line direction) and Z (vertical direction) components receiver coils, only the Z component was used in this work, due the high noise level of the X component. The EM system characteristics are summarized in Table 1, which is based on the information of the survey report and from the data files provided by the contractor.

Table 1: AeroTEM^{HD} system description summary for QF area (based on survey report and data files provided by Aeroquest).

	Parameter	Value
Transmitter	Loop diameter	20 m
	Peak current	323 A
	Peak moment	711,000 NIA
	Repetition frequency	30 Hz
	Turn-on time	- 4,476 µs
	Peak current time	- 2,133 µs
	Turn-off time (when 0 current is reached) *	0
	Waveform	Triangular
Receiver	Sample rate*	10 Hz
	Number of gates (only off-time used)	17
	Time gates interval (off-times) **	8.75 µs to 9,532 µs

* After on-survey processing.
** Time values related with the opening of the gates and referenced to the turn-off time.

METHODOLOGY

Cole-Cole Maximum Phase Angle model

In this work, the methodology used for the forward calculations of the AEMIP effect is based on the MPA re-parameterization of the Cole-Cole Model, introduced by and implemented in AarhusInv. The MPA is a re-parameterization of the frequency dependent complex resistivity for the Cole-Cole model (CC), as defined by (Pelton et al., 1978):

$$\tilde{\rho}(\omega) = \rho_0 \left[1 - m_0 \left(1 - \frac{1}{1 + \left(i\omega\tau_\rho\right)^C}\right)\right] \quad (1)$$

where $\rho_0 = \tilde{\rho}(\omega = 0)$ is the direct current resistivity, m_0 is the intrinsic chargeability as described in (Seigel 1959), τ_ρ is the relaxation time, C is the frequency dependency parameter, $\omega = 2\pi f$ is the angular frequency for the frequency f, and $i = \sqrt{-1}$ is the imaginary unit.

As demonstrated by Fiandaca et al., (2018b) and Lin et al., (2019), the MPA re-parameterization reduces the correlations between the model parameters and provides models with better resolution in comparison with the classical CC model, especially for low C values. The MPA uses the following model parameters:

$$\boldsymbol{m}_{MPA} = \{\rho_0, \phi_{max}, \tau_\phi, C\} \quad (2)$$

where ρ_0 and C are the same parameters of the CC model in equation (1), ϕ_{max} is the maximum phase angle of the CC complex conductivity (i.e. the minimum of the complex resistivity phase) and τ_ϕ is the relaxation time associated with the frequency ($f = 1/2\pi\tau_\phi$) where $\phi_{max}$is reached. The relation between $\tau_\rho$and τ_ϕ is given by (Fiandaca et al., 2018b):

$$\tau_\phi = \tau_\rho (1 - m_0)^{1/2C} \quad (3)$$

The use of the maximum phase of the complex conductivity in the inversion model, instead of the m_0 parameter of the classic Cole-Cole model, simplify the comparison with ancillary IP data, which are often phase spectra measured in the frequency domain in the laboratory on rock samples.

1D Laterally Constrained Robust Inversion Scheme for Induced Polarization Data

In this work, all AEMIP inversions were conducted using the 1D laterally constrained inversion (LCI) robust scheme proposed by Lin et al., (2019). This approach helps addressing the significant ill-posedness of a multi-parametric AEMIP inversion and recovers the MPA parameters in equation (2) properly. The LCI scheme minimizes an objective function with 2D lateral constraints on the model parameter space, given by:

$$Q = \left(\frac{\delta \boldsymbol{d}^T \boldsymbol{C}_{obs}^{-1} \delta \boldsymbol{d} + \delta \boldsymbol{r}^T \boldsymbol{C}_R^{-1} \delta \boldsymbol{r}}{N_d + N_R} \right) \quad (4)$$

where $\delta \boldsymbol{d} = \boldsymbol{d} - \boldsymbol{d}_{obs}$ is the difference between the forward response $\boldsymbol{d}$ and the onserved data $\boldsymbol{d}_{obs}$; $\delta \boldsymbol{r} = -\boldsymbol{R}\boldsymbol{m}$ is the roughness of the model vector parameter $\boldsymbol{m}$, and $\boldsymbol{R}$ is the roughness matrix; $\boldsymbol{C}_{obs}$ and $\boldsymbol{C}_R$ are the covariance matrices related to the data and constraints, respectively; and N_d and N_R are the numbers of data points and roughness constraints, respectively.

Using the LCI technique, the key points of the robust inversion scheme is summarized by the following steps (for a detailed description of this technique, we address the work of Lin et al., 2019):

1. Model re-parameterization using the Cole-Cole MPA approach;
2. Definition of a robust initial resistivity model through inversions of positive-only data using very tight spatial constraints. The initial models for the other parameters were defined manually. In this work, the initial values for ϕ_{max} was 300 mrad, similar to the phase range based on the analogous lithologies presented in Smith et al., (1983), and τ_ϕ and C started from 0.001 s and 0.5, respectively.
3. Locking of τ_ϕ and C for the first few (here five) iterations, to build structure in the resistivity and chargeability domains first.

4. Increasing the data standard deviation around the sign change in the dB/dt decay curve.
5. Modification of the damping scheme allowing for individual damping of the different parameters, which improves the balance of the multi-parameter model space.

DATA PROCESSING AND ANOMALY SELECTION

The preliminary data processing includes the standard automatic processing of voltage and altitude data, followed by manual processing, as described in (Auken et al., 2009). The automatic data processing was done in Aarhus Workbench (http://www.aarhusgeosoftware.dk) seeking the best preservation (compared to raw data) of the negative transients in the late times for AeroTEM^{HD} system by having limited lateral averaging and no slope filtering. The slope filtering was disabled to keep fast decaying signals arising from the IP effects. A manual processing step followed the automatic step as the signal-to-noise ratio was very low and many subtle details were close to the noise level. This manual processing was conducted similarly to the workflow described in Kaminski and Viezzoli (2017), in which we conducted a visual inspection of the data throughout the flight lines, in order to identify the very steep dB/dt decays and negative transients associated with the IP effect that may occur over the carbonaceous units, removing the data bellow the noise level.

Due the poor signal-to-noise ratio at the Lamego mine area, and some flight-line intervals were affected by couplings due to the proximity to the mine infrastructure (indicated in Figure 2.1-c). The flight lines that were not used due the poor signal-to-noise ratios and the intervals that present significant couplings are represented as grey and orange line intervals in Figures 1-b and 1-c. The poor signal-to-noise ratio in the grey marked might be explained by a highly resistive micaceous metapelite associated with a mafic-ultramafic environment, indicated by the dark and light brown in Figure 2.1-b, and also due to couplings caused by the highly urbanized surroundings. Despite the generally low signal-to-noise ratio of the dataset, it is still possible to distinguish a clear electromagnetic (EM) anomaly over the Lamego structure, indicating lithological changes in association

with the carbonaceous metapelites, BIFs and sulfide layers, as indicated in Figures 2-a and 2-b. Figure 2-c presents the three types of decay curves (raw data) that occur in the area: (1) the ones that could be associated with a typical IP response, (2) not very significant or less evident IP effect, and (3) the noisy data outside the Lamego structure. Type 3 soundings are in the grey flight line intervals refers to resistive lithological units and/or coupled data, which were not used in this work.

In Figure 2-b it is also noted that even inside the Lamego structure (Figure 2.1-b), it is possible to distinguish a contrast in the EM anomaly along the axial plane direction of the fold structure. The characteristic anomaly starts to appear close to the hinge zone in the NW portion of the structure (flight lines L20790, L20800 and L20810, blue and green lines in Figure 2-b), the amplitude decreases in the central part (flight lines L20820, L20830, orange and red lines in Figure 2-b) and increases again in the limb junction in the NE portion of the structure. A very small signal level is observed over the Lamego structure in flight lines L20820, L20830 and L20840 (orange lines intervals in Figures 1-b and 1-c) and these data are not used. In summary, six flight-line intervals with either distinguishable negative transients and/or over-steep slopes of the transient decays were selected for the MPA and RO inversions analysis and geological interpretation (blue lines in Figures 1-b and 1-c), which is presented in the next section.

Finally, Figure 3-a presents the detailed interval indicated by the vertical dashed lines in Figure 2-a, with a presentation of the typical dB/dt decay affected by IP effects, for both processed (Figure 3-b) and raw data (Figure 3c). When IP effects are present and trigger negative data the absolute signal level will be higher and often above the noise floor where data without sign changes are below the noise level at late times. Though, the noise level is often very hard to detect in the data sections as the data has been pre-processed by the contractor with a lateral smoothing filter to produce the “raw” data presented in Figure 3-a, bottom. Any decays that are only positive, but increase at late times have been culled.

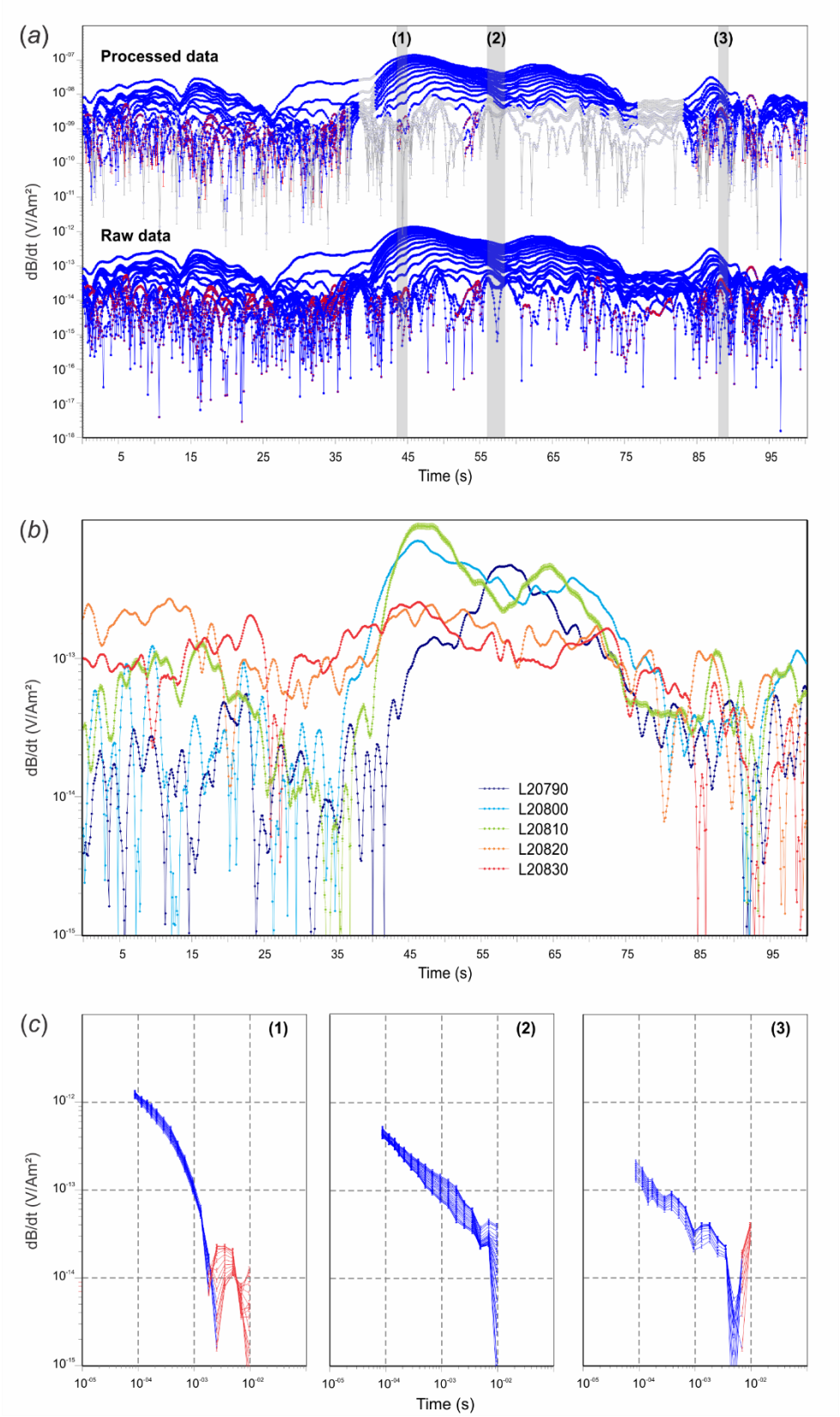

Fig. 2: (a) Comparison between raw and processed data for the anomaly over the Lamego structure with indication of anomaly types (1) with IP effect, (2) with not so

evident or not presented IP effect and (3) within the very low signal-to-noise ratio area and possibly coupled (not used). The sounding positions along the flight line are also indicated in Figure 2.1-b – the processed data are shifted from the raw data by a factor of $\times 10^5$ for clarity and the vertical black dashed lines indicate the interval presented in Figure 3. (b) Comparison between transient anomalies over the Lamego structure along the axial plane direction (NE-SW) showing the decrease in amplitude of the fifth time-channel window at 2.125×10^{-4} s (vertical component in the off-times) in the central part of the structure (L20820 and L20830). (c) Types (1), (2) and (3) dB/dt decays for raw data, as indicated in Figure 2.1-b and Figure 2-a.

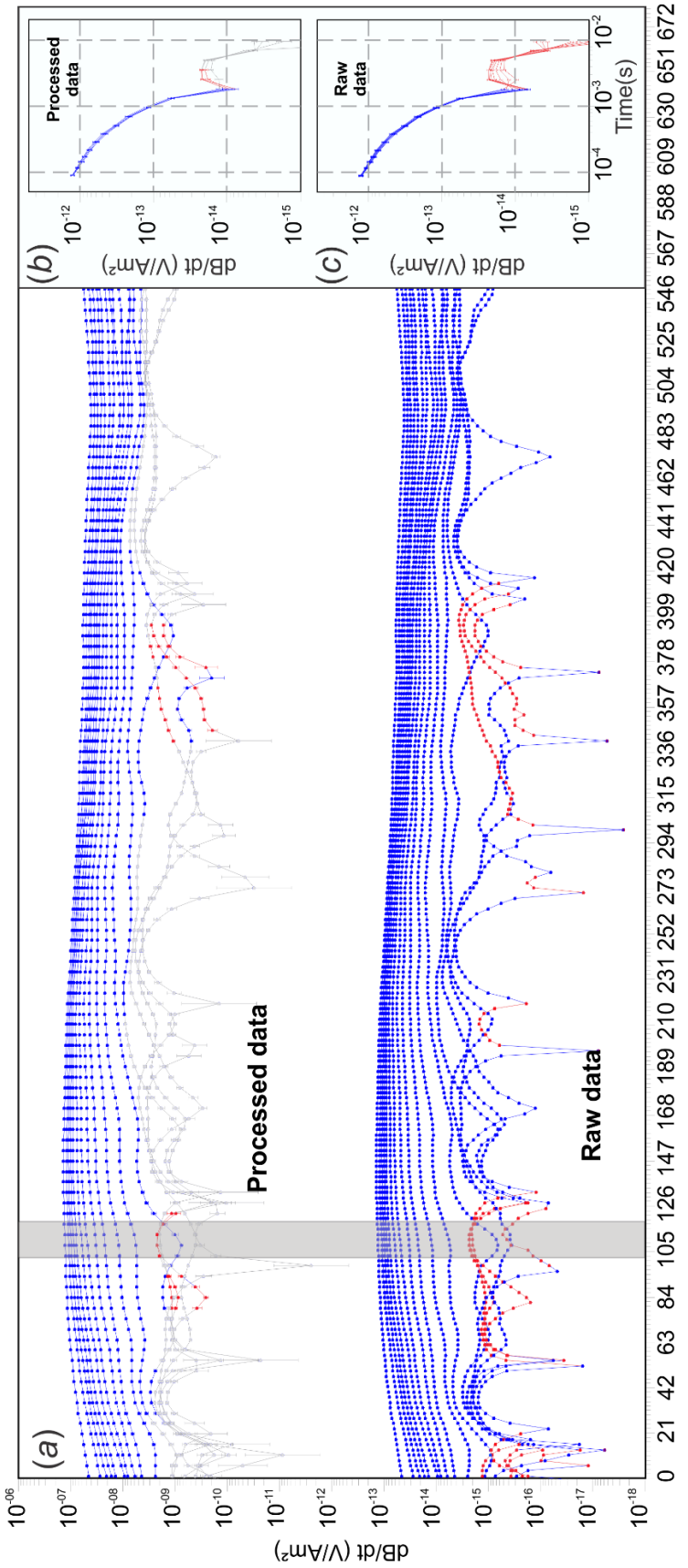

Fig. 3: Interval detailed indicated by the vertical black dashed line in Figure 2-a. (a) Processed and raw data for this interval. The vertical grey rectangle indicates the set of soundings showing the typical dB/dt decay with IP effect in Lamego Mine for the (b) processed data and for the (c) raw data.

RESULTS

MPA and RO Synthetic Modelling for a Polarizable Subsurface

Based on borehole lithological description and borehole petrophysical data (mean values for the lithological units) we generated synthetic MPA models and the corresponding transient electromagnetic (TEM) data for the AeroTEM^{HD} system. The synthetic data were inverted using the resistivity-only (RO) and MPA parameterizations, for a 3-layer model representing the typical lithological environment in the study area. The reference model used for the synthetic data is summarized in Table 2. It consists of a resistive and non-polarizable upper layer, a conductive and polarizable intermediate layer, and the third resistive non-polarizable layer. The layers lithological relevance is stated in the table as well.

Table 2: 3-layer model physical parameters for synthetic modelling. The thicknesses and resistivity values were based on borehole lithological and petrophysical average values data from AngloGold Ashanti and the IP parameters were based in the preliminary inversions of the AeroTEM^{HD} and reference values from Smith et al. (1983).

Layer	ρ_0 (Ω·m)	ϕ_{max} (mrad|)	τ_ϕ (ms)	C	Thickness (m)	Lythological Interpretation
1	1000	10	0.1	0.5	70	Metamafic rocks and/or sericitization alteration zones over mafic or felsic rocks (micaceous pelite)
2	300	10 to 500	10	0.5	300	Carbonaceous/graphite schists and/or carbonatic metapelite with graphite (Carbonate-quartz-sericite schists with carbonaceous material), which could present disseminated sulfides
3	1800	10	0.1	0.5	-	Metamafic volcanic rocks

Using the AarhusInv code (Auken et al., 2015) and with the configuration for the AeroTEM^{HD} system described in Table 1, also using the parameters presented in Table 2, we simulated four scenarios considering the increment in the ϕ_{max} value of the second layer from 10 to 500 mrad, i.e., gradually making the intermediate conductive layer more

polarizable and analyzing how well the RO and MPA inversions recover the true model by 1D smooth inversions. The parameters values for each parameter presented in Table 2 were decided based on the values achieved in the preliminary inversion results for the AeroTEM^{HD} data, based on the laboratory petrophysical frequency-domain IP measurements presented in Smith et al., (1983) for similar lithologies in a greenstone belt environment in Saudi Arabia and also data from borehole information for the resistivities values. In particular, in Smith et al., (1983) phase values between 100 and 350 mrad were measured in the frequency interval between 100 and 1000 Hz. A standard deviation of 5% was assigned to each gate of the forward response, but no perturbation was introduced, to focus only in the understanding of the differences responses between RO and MPA models, not considering any other effect in the synthetic data, like noise level and couplings. The 1D inversions were carried out using a 30-layer smooth model, using the L2 norm for the vertical constraints for both MPA and RO inversions. All RO inversions were conducted removing the negative gates and the last gate before the first negative gate. The MPA inversions were conducted considering all the 17 gates in the off-times for the AeroTEM^{HD} system.

Figure 4 presents the comparison between the inverted resistivity models for RO and the MPA parameterizations for the model described in Table 2. It is noticed that all the RO and MPA inverted models, in all scenarios, fit the data very well and recover a middle conductive layer. However, even though all inverted models fit the data well, there are significant discrepancies between the results of the two inversion approaches. All MPA results recovered the resistivity model with better agreement with the true model, while the RO inversions generally fail to accurately reproduce the true models.

In the first scenario ($\phi_{max} = 10$ mrad, Figure 4-a), the resistivity model is recovered for both MPA and RO smooth models decently. As ϕ_{max} increases, the conductive layer becomes more conductive and thinner in comparison to the true model and the top boundary of this layer appears deeper (values until 200 mrad, Figures 4-a, 4-b and 4-c) or shallower (for 500 mrad, Figure 4-d); the bottom of the layer remains always shallower than the true model. For all inverted models, the depth of investigation (DOI) was estimated following Fiandaca et al., (2015). The DOI values for RO inversion models suggest that there is very limited sensitivity to distinguish the bottom of the conductive

layer. On the other hand, the MPA resistivity models have a good agreement with the true model, underlining that this parameterization approach recovers a more reliable resistivity model. Also, the other MPA parameters are well recovered in the inversions (results not shown in figures for brevity).

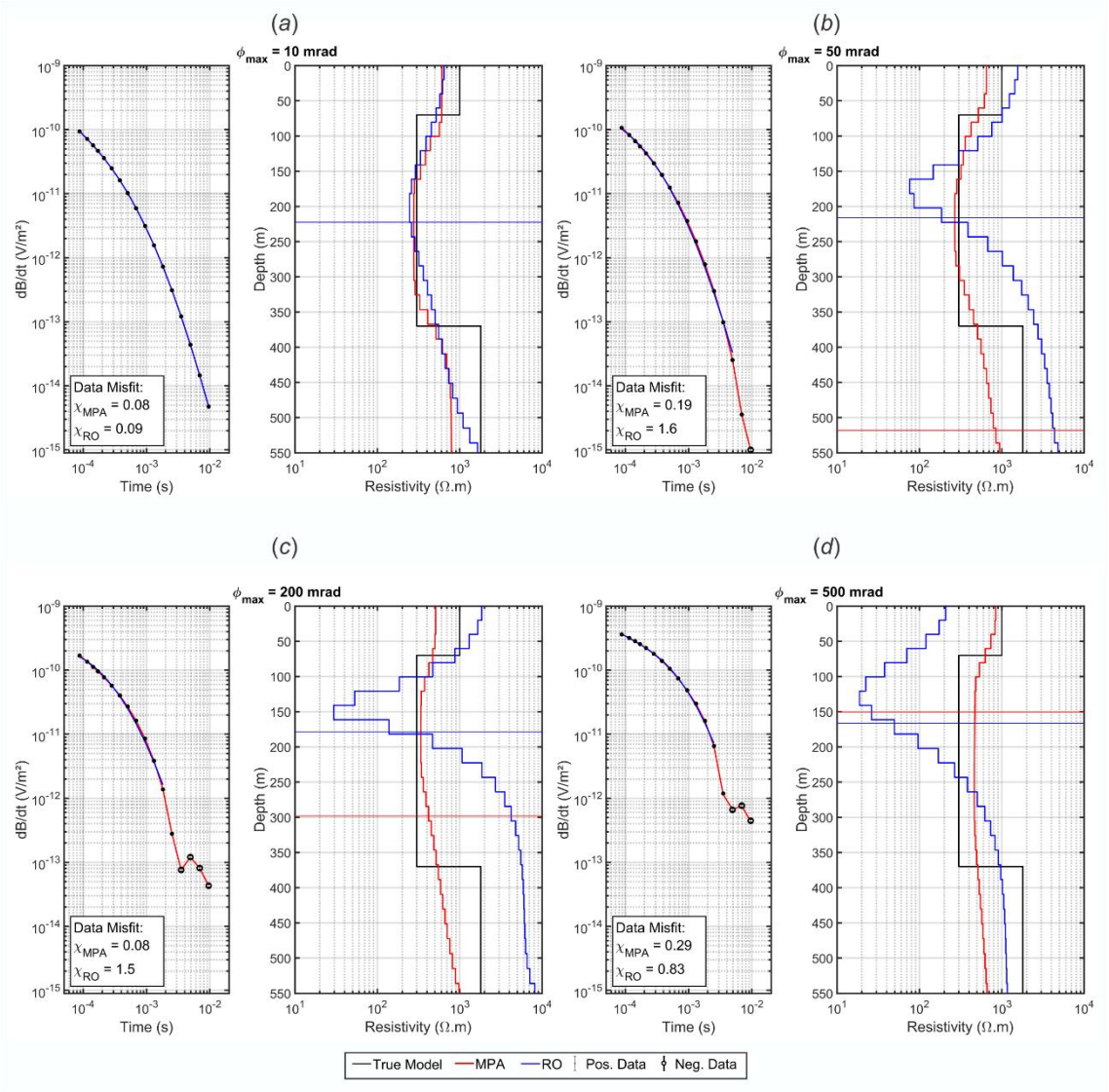

Fig. 4: MPA and RO inversion of synthetic 1D TEM data with IP. (a) $\phi_{max} = 10\,mrad$, (b) $\phi_{max} = 50\,mrad$, (c) $\phi_{max} = 200\,mrad$ and (d) $\phi_{max} = 500\,mrad$. DOIs are represented by the horizontal continuous lines, according to the models colors.

In the results presented in Figure 4, the increment in ϕ_{max} values also causes changes in the amplitude and slope of the transient decay curves before the negative part. In general, the amplitude of the dB/dt curve is increased and the slope is flatter in the early times and

steeper in the time values closer to the sign change. This decay curve behavior also explains the distortion in the resistivity model for the RO parameterization. Due to the RO limitations to fit the steep slope of the decay close to the sign change (which is not the case for MPA), the resulting model is made more extreme with a shallower top boundary for the bottom resistor layer and a more conductive and shallower intermediary conductor.

The next section presents the results for the AeroTEM^{HD} real data over the Lamego structure, which presents similar decay behavior and results as seen in the synthetic tests.

Inversion Results of the field data

The 1D laterally constrained inversions (LCI) using RO and MPA models were conducted for all the blue flight-line intervals shown in Figures 1-b and 1-c. Figure 5 and 6 show RO and robust MPA inversion results of a representative section for flight line L20810. For all robust MPA inversions, the starting values for the IP parameters were $\phi_{max} = 300\ mrad$, $\tau_{\phi} = 1\ ms$ and $C = 0.5$.

In Figure 5-a, for the North-West portion of the section, the RO inversion shows in general a three-layer model above DOI that consists of a shallow resistive (>200 Ω·m) layer, a conductive intermediate layer (< 30 Ω·m), and a deep resistor (>150 Ω·m). The South-East portion of the section show only a two-layer model with a thick and very resistive (> 1000 Ω·m) layer down to ~400 m underlain by the intermediate conductive layer, which can be seen throughout the section.

The resistivity model of the MPA inversion (Figure 6-a) presents a similar resistivity model, but overall with higher resistivity values and with the absence of the deep resistor bellow the conductive layer in the Northwestern portion of the profile. Furthermore, the vertical boundaries in top ~100 m of the MPA model agree better with the depth intervals for the micaceous schist in the borehole lithological data (BH1, BH2 and BH3, also indicated in Figures 1-b and 1-c), when compared to the RO inversion result. This is especially evident in the NW portion of the profile, which becomes shallower and more conductive in the RO inversion. The differences between the resistivity sections in

Figures 5-a and 6-a indicate that the IP effect cause an important influence in the dataset, and, consequently, in the way the RO inversions respond to it.

Concerning about the possibility to avoid the IP effect in RO inversions, it might be argued that if more late gates are removed in data processing, seeking to avoid the very steep decays of the dB/dt curves, the IP effect might be removed from the data and, consequently, a more reliable resistivity model might be retrieved by the RO inversion (at least for the shallower layers). However, this is not the case, as shown in Figures 7, in which two RO inversions are compared: the one with all positive-only data (Figure 7-a, as in Figure 5-a), and the inversion obtained only with the first nine gates (Figure 7-b). The two RO resistivity models are similar both in terms of resistivity ranges and patterns, and they both differ from MPA resistivity model (Figure 7-c, as in Figure 6-b). These results indicate that the IP effect is present in the early/intermediate times, which hinders its removal from the data by culling out the late times.

Another concern regarding the comparison of RO and MPA resistivity sections presented so far is that the ρ_0 MPA section represents the DC resistivity, but a significant change in resistivity occurs over frequencies in the Cole-Cole model when high chargeability values are present. Figure 7-d presents the ρ_∞ section in comparison with the ρ_0 section (Figure 7-c). As expected, it can be noted that the background value for ρ_∞ is smaller than the one for ρ_0. However, both models present similar structural behavior for the shallower and the deeper depth values, in better agreement with the borehole shallower data (the micaceous metapelite – X2/X2CL in the resistivity model sections) than the RO inversions, with no resistive bottom layers coming up as in the RO models, suggesting again that the IP effect plays an important role in the dataset and should be considered in order to recover a more reliable resistivity model.

The discrepancies between the MPA and RO inversion models can be further investigated by focusing on the 1D resistivity model plots for two sounding positions (soundings 19 and 74, position indicated in Figures 5 and 6) on flight line L20810, presented in Figure 8. These soundings show negative values in the late times of the dB/dt curve, similar to the synthetic tests for ϕ_{max} greater than 200 mrad (Figures 4-c and 4-d). The sounding positions along the profile are indicated by the vertical dashed lines in Figures 5 and 6. In

these plots, the inversion results of three-layer models are also shown together with smooth layer inversions.

LCI inversions for the RO parameterization resulted in resistivity models with thinner and more conductive intermediate layer, compared to all MPA results. In addition, the bottom of the conductive layer and the DOI for the RO models are shallower than for all MPA results, as predicted in the synthetic study. The presence of the negative transients above the noise level and the change in the slope of the dB/dt curve along the anomaly over the Lamego structure and the discrepancies of the resistivity models are all strong indications that a significant IP effect occurs in this region.

This effect maps into the strong chargeable body imaged by the MPA inversion (Figure 6-b), with ϕ_{max} values between ~ 300 mrad and ~ 450 mrad, and an apparent dip angle of ~ 25° towards SE. This polarizable anomaly is in good agreement with the occurrence of carbonaceous and carbonite schists enriched by carbonaceous material and/or graphite (XC and X1 in borehole legend in Figure 5, respectively) and also with the mafic metapelites that could present sulfides zones (XS in the borehole legend in Figure 5). The structural information recovered from the chargeable body is also in good agreement with the structural control of the the Lamego carbonaceous schist, according to Martins et al., (2016) who indicated abundant carbonaceous schists in the limbs zones. The limb zones present general dip angle between 20°-30° to SE and the carbonaceous metapelites layers are associated with $S_{1\text{-}2}$ foliation, which presents dip angles between 28°-42° towards 124°-134° directions.

In this area, there are no public available ground Spectral IP (SIP) measurements to be compared with these results. For comparison, we briefly discuss Smith et al., (1983) work, which presents laboratory petrophysical measurements for similar carbonaceous schists enriched by graphite and sulfide zones in mafic greenstone belt environment in the Wadi Bidah District, Saudi Arabia. Their carbonaceous samples presented mean resistivity-values around 300 Ω·m (range from 17 to 100000 Ω·m), phase values that could reach more than 200 mrad in the range of 100-1000 Hz (the operation range of the AeroTEM^{HD} survey presented in this paper), but with ϕ_{max} values of the order 400-450 mrad around 2.0 Hz and associated τ_{ϕ} around 8 ms for the most resistive samples. However, even

though the frequency range for the IP effect in the AeroTEM^{HD} system is different from the one used in Smith et al. (1983) measurements (Zonge Engineering GDP-12, which results were presented in the frequency range 0.06 – 1024 Hz), one of the advantages of using the MPA parameterization is that the inversion looks for the maximum phase value, which makes the comparison easier. The ϕ_{max} and τ_ϕ distributions recovered in this work (Figures 6-b and 6-c, respectively) present maximum values up to 450 mrad in the inner portions of the polarizable body and τ_ϕ up to 8 ms over the top this polarizable body. These values are compatible with the ones presented in Smith et al. (1983) for the carbonaceous lithologies, including their most resistive samples.

These results suggest that the MPA inversion approach was capable to map the zones of the top of the carbonaceous schist layer, which play an important role in the structural control of the gold mineralization in the Lamego mine (Martins et al., 2016).

Figures 6-c and 6-d present the MPA LCI sections for τ_ϕ and C, respectively. For the τ_ϕ section, the DOI is mainly close to the surface except at a few sounding positions at which more (negative) data are present, which implies that the parameter is not well resolved in the inversion, especially when positive-only data exist. On the other hand, the C coefficient is well resolved with values around 0.5, indicating that a Cole-Cole like spectral behavior is preferred by the inversion (and not a constant spectrum, which would correspond to C values around or below 0.1).

Figure 9 presents the general view of the spatial distribution of the polarizable body for all inverted flight-line intervals over the Lamego structure (blue lines in Figure 2.1), integrated with the geological map. The 3D volume of ϕ_{max} was created by inverse distance interpolation of the 2D MPA models. The high chargeability body is defined by a 400 mrad threshold. Figure 9 show two 3D views from different orientations: looking to SW upper view (Figure 9-a), to SW lateral view (Figure 9-b) and to NE upper view (Figure 9-c). In the view to NE, the polarizable body becomes thicker nearby the hinge zone of the structure, suggesting that the carbonaceous schist and graphite enriched layers

is thickened, as discussed in Martins et al., (2016). The view to NW presents a steeper dip of the polarizable body mapped in the NE portion, the limbs junction zone, estimated around 45° - 50° towards SE along the flight line direction (N45W), which is also in good agreement with the values presented Martins et al., (2016).

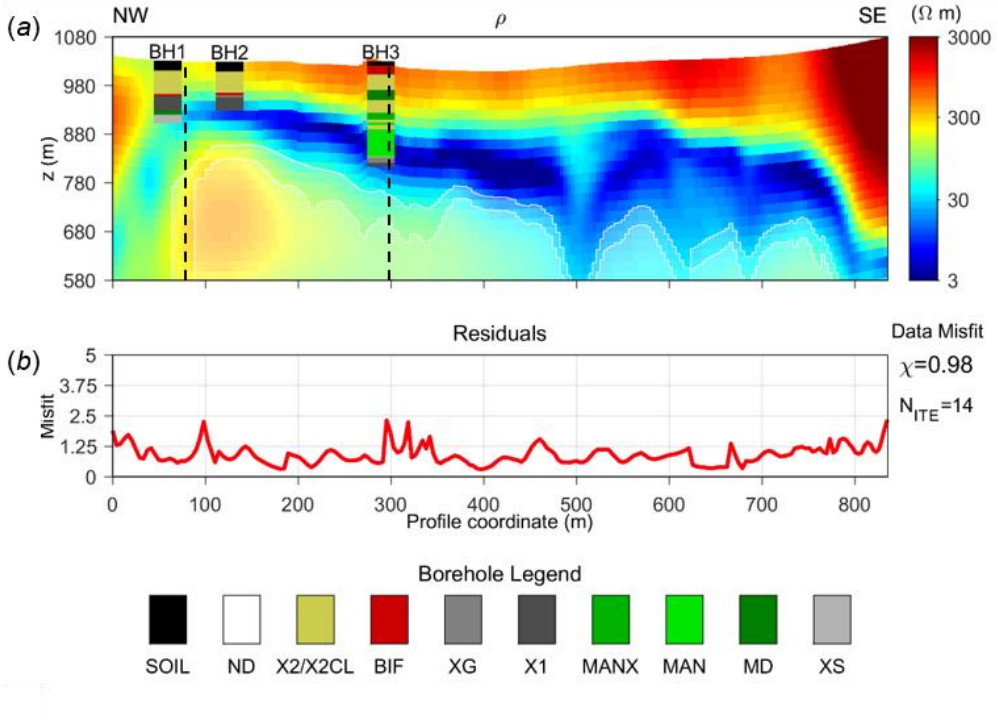

Fig. 5: Resistivity-only LCI for flight line L20810 interval over the Lamego structure. (a) Resistivity section. (b) Data misfit. In the borehole lithological legend: SOIL is the soil layer, ND is the non-descripted interval, X2/X2CL is the micaceous metapelite, BIF represents the banded iron formation layers, XG is the carbonaceous-graphite schists, X1 is the metapelite enriched with carbonaceous material, MAN is the metabasalt/metandesite, MANX is the MAN interval with chloritization alteration, MD is the metadiabase layer and XS is the altered felsic metavulcanoclastic layer. The vertical dashed lines represent the positions of the sounding 19 and 74.

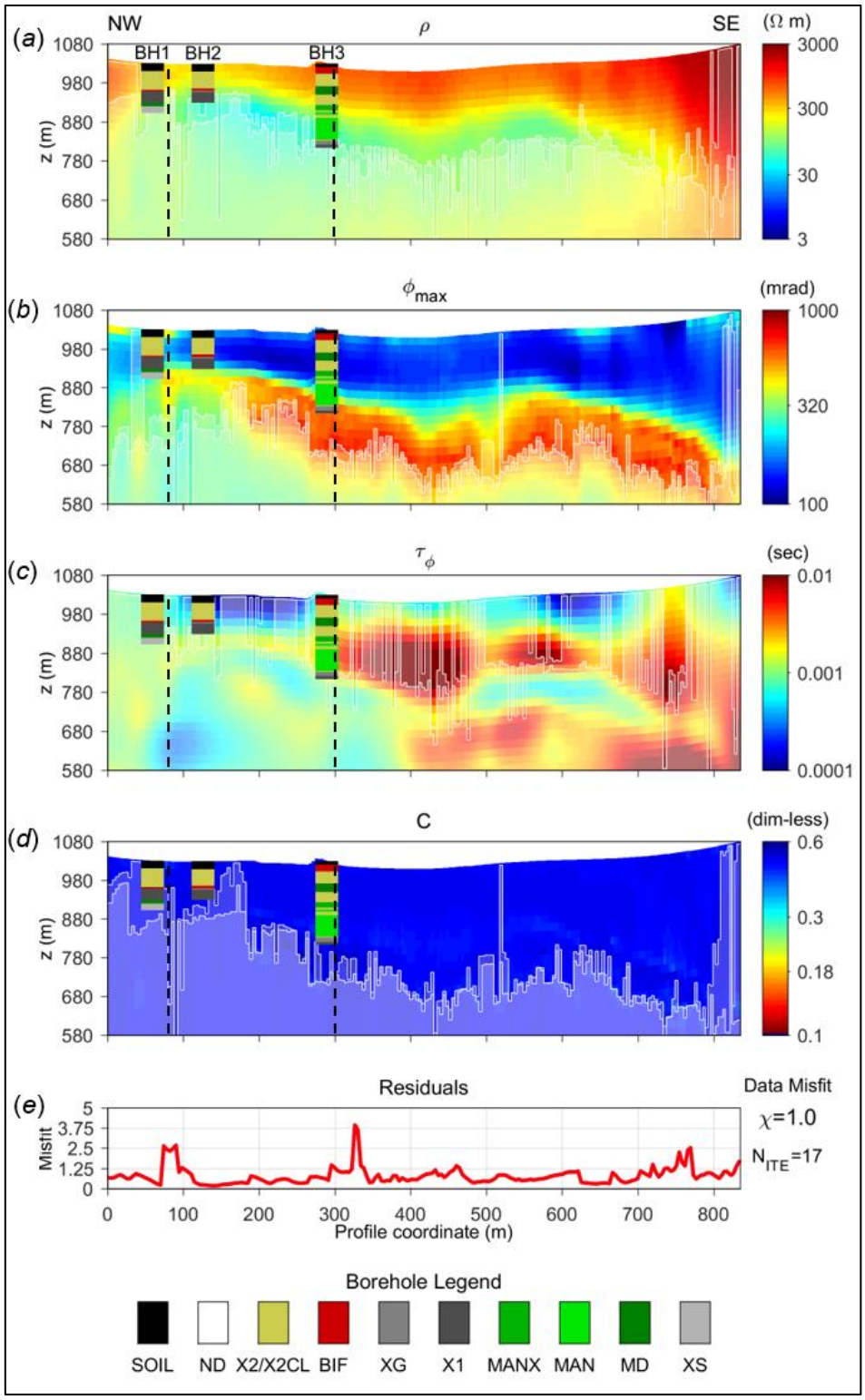

Fig. 6: MPA LCI for flight line L20810 interval over the Lamego structure. (a) Resistivity section. (b) ϕ_{max} section. (c) τ_φ section. (d) C section. (e) Residuals. The borehole description is associated with the borehole legend presented in Figure 4. The vertical dashed lines represent the positions of the sounding 19 and 74.

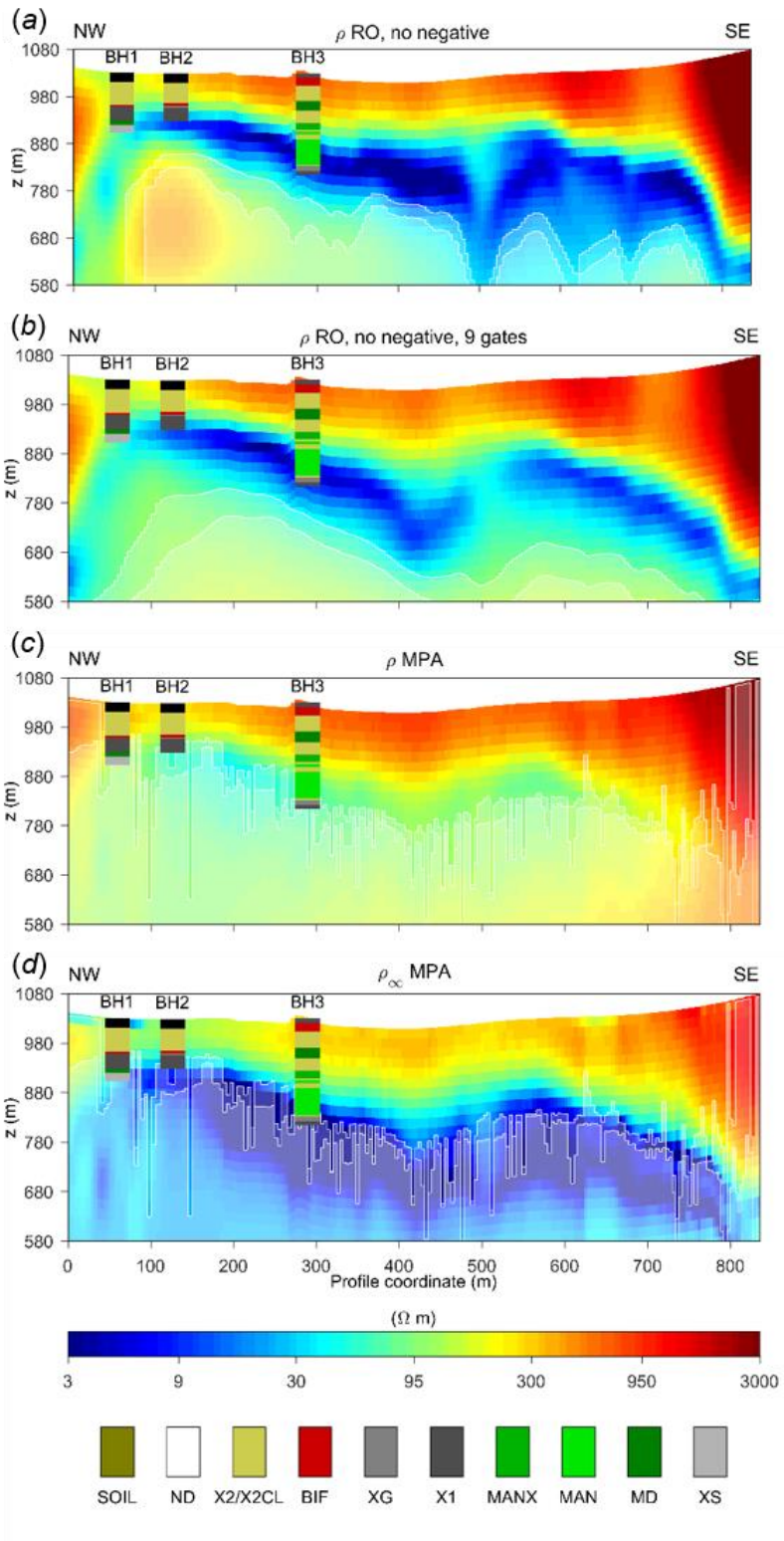

Fig. 7: Comparison between the RO and MPA resistivity sections for flight line L20810 with (a) all positive data RO model, (b) the first nine positive gates RO model, (c) ρ_0 MPA model and (d) ρ_∞ MPA model.

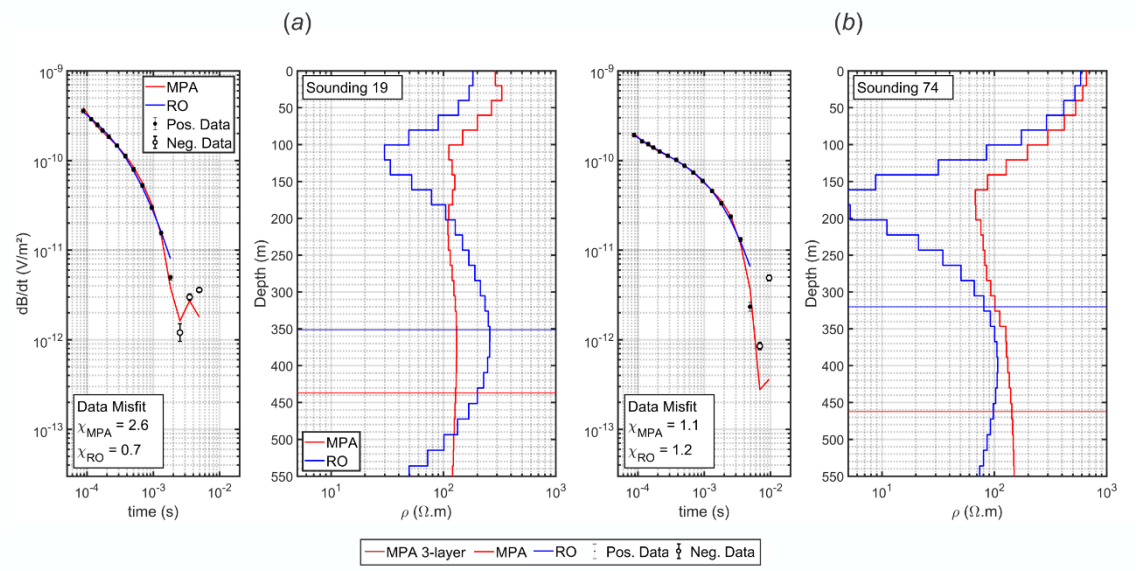

Fig. 8: dB/dt curves and 1D resistivity model for RO (blue curves) and MPA (red curves) for (a) Sounding 19 and (b) Sounding 74, which positions along flight line L20810 are indicated in Figures 4 and 5. DOIs are represented by the horizontal continuous lines, according to the models colors.

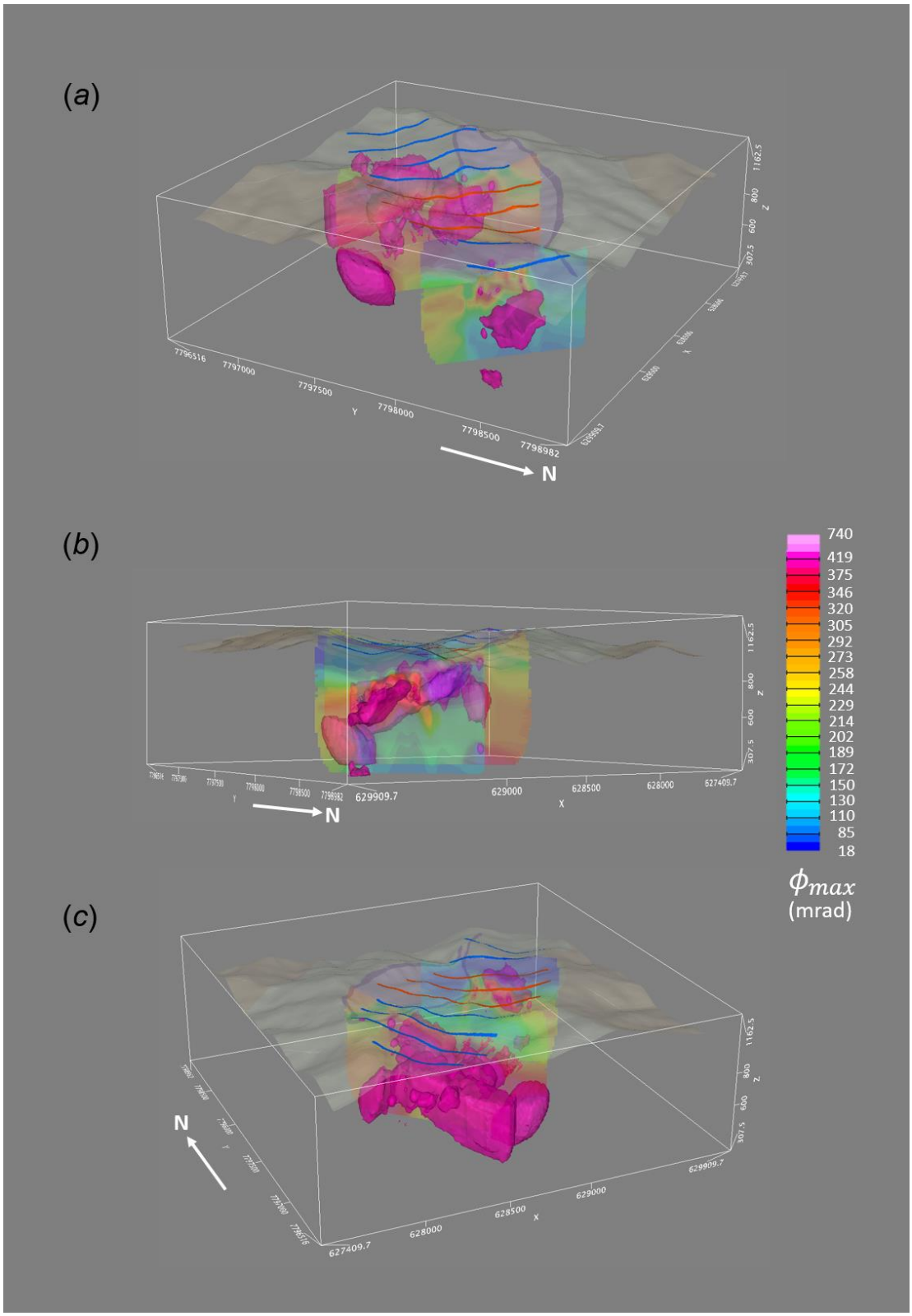

Fig. 9: 3D view of the polarizable body through the interpolation of all inverted flight-line intervals (blue lines). (a) Looking to SW upper view. (b) Looking to SW lateral view. (c) Looking to NE upper view. The white arrow indicates the North.

The surface represents the geological map as presented in Fig. 1 with the digital terrain model relief.

DISCUSSION

The results from MPA and RO inversions present several differences, indicating that the presence of the IP phenomenon in this AeroTEM^{HD} survey is significant over the Lamego mine area. These results are in good agreement with the synthetic study which demonstrated that the sensitivity to the IP parameters is significant not only for time values around the sign change and in the negative transients, but also in the positive part of the decay. Consequently, removing the negative data and carrying out a RO inversion could not be the best approach when dealing with IP-affected responses. In our example this would lead to a non-realistic resistivity model and to wrong interpretation of the conductor associated with the host rocks, like the carbonaceous/graphite. On the other hand, the MPA models had the capability of fitting negative data and a much better agreement with the borehole data. The depths of the top of the shallow resistive and non-polarizable layer associated with the micaceous schist and the top of the conductive and polarizable layer associated with the carbonaceous schist are in better agreement with the borehole profiles for the MPA model (Figures 6-a and 6-b), than for the RO results (Figures 5-a). However, the MPA modelling increases significantly the size of the model space, and it is significantly more sensitive than the RO inversion to the starting model. In this study, this limitation was addressed using ancillary information, as the laboratory spectra measured on similar lithologies, for guessing the starting values of the IP parameters.

In addition, it is worth mentioning that the classical Cole-Cole model inversions using the same 1D laterally constrained robust inversion scheme were tried, but not presented in this work. The resistivity and chargeability models of the classic Cole-Cole inversions still presented better agreement with the geological data than the RO parameterization, but the MPA results presented even better agreement and data misfit and are easier to compare to laboratory spectra.

In other areas of the QF region and also in other surveys conducted with AeroTEM^{HD} or other low moment systems, it is possible to have zones where the AEMIP phenomenon

is not very clear or only present few negative transients. However, the results presented in this paper indicate that in areas with expected polarizable anomalies, significant changes in the slope of the dB/dt curve could indicate the occurrence of IP effects. Finally, a remark about the ϕ_{max} range that gives significant IP effects in the data in the synthetic and field examples presented in this study. The low limit of ϕ_{max} values that affected the data significantly, down to a few tens of mrad, depends on the high resistivity of the background model. In more conductive environments, higher ϕ_{max} values are needed for a significant IP affect in the TEM responses.

CONCLUSIONS

An AeroTEM^{HD} survey was conducted over the Lamego mine area and the data were inverted with RO and MPA robust inversion scheme using the AarhusInv code. The MPA inversion approach with the robust scheme agreed better with the borehole data, and gave more reliable resistivity models than the RO inversion. In particular, the MPA inversions were able to provide a more reliable image of the carbonaceous schists/graphite enriched metapelites layers and/or the sulfide mafic units.

In addition, the ϕ_{max} model resulting from MPA inversion, allowed to distinguish the chargeable units that could be associated with the carbonaceous layers. The structural behavior of the polarizable body presents good agreement with the known dip and direction angles for the Lamego structure, and the ϕ_{max} values present good agreement with petrophysical measurements for similar lithologies in a greenstone belt environment. These results indicate that the MPA robust inversion scheme is reliable inversion procedure for inverting the IP-affected airborne TEM data in case of mineralizations associated with metallic sulfides and chargeable unities with carbonaceous content.

CONFLICTS OF INTEREST

The authors declare no conflicts of interest.

ACKNOWLEDGMENTS

This study was financed in part by the Coordenação de Aperfeiçoamento de Pessoal de Nível Superior - Brasil (CAPES) - Finance Code 001. The authors also would like to thank CPRM – Geological Survey of Brazil, who provided the AeroTEM^{HD} and geological data, AngloGold Ashanti, who provided the borehole and petrophysical data. In particular, Marco Antonio Couto Junior also would like to thank CPRM researcher Rayanni Caroline Ramos Ferreira for the discussions about Lamego geology, which was essential for the interpretation of these results. Jorge Luis Porsani would also like to thank CNPq-Conselho Nacional de Desenvolvimento Científico e Tecnológico for fellowship (grants: 303731/ 2017-6).

REFERENCES

Auken, E., Christiansen, A.V., Fiandaca, G., Schamper, C., Behroozmand, A.A., Binley, A., Nielsen, E., Effersø, F., Christensen, N.B., Sørensen, K.I., Foged, N., and Vignoli, G., 2015, An Overview of a Highly Versatile Forward and Stable Inverse Algorithm for Airborne, Ground-Based and Borehole Electromagnetic and Electric Data. *Exploration Geophysics* **2015**, 223-35.

Auken, E., Christiansen, A.V., Westergaard, J.A., Kirkegaard, C., Foged, N., and Viezzoli, A., 2009, An Integrated Processing Scheme for High-Resolution Airborne Electromagnetic Surveys, the Skytem System. *Exploration Geophysics* **40**, 184-92.

Fiandaca, G., Christiansen, A., and Auken, E., Depth of Investigation for Multi-Parameters Inversions. *Near Surface Geoscience 2015-21st European Meeting of Environmental and Engineering Geophysics*.

Fiandaca, G., Lin, C., Auken , E., and Christiansen, A., 2018a, Robust Inversion of Induced Polarization Effects in Airborne Transient Electromagnetic. *AEM2018 – 7th International Workshop on Airborne Electromagnetics – Extended Abstracts.*

Fiandaca, G., Madsen, L.M., and Maurya, P.K., 2018b, Re-Parameterizations of the Cole-Cole Model for Improved Spectral Inversion of Induced Polarization Data. *Near Surface Geophysics* **16**, 385-99.

Gisselø, P.G. and Nyboe, N.S., 2018, Optimized for Depth of Investigation. Aem2018 – 7th International Workshop on Airborne Electromagnetics. *AEM2018 – 7th International Workshop on Airborne Electromagnetics – Extended Abstracts.*

Kaminski, V. and Viezzoli, A., 2017, Modeling Induced Polarization Effects in Helicopter Time-Domain Electromagnetic Data: Field Case Studies. *GEOPHYSICS* **82**, B49-B61.

Kang, S., Fournier, D., and Oldenburg, D.W., 2017, Inversion of Airborne Geophysics over the Do-27/Do-18 Kimberlites — Part 3: Induced Polarization. *Interpretation* **5**, T327-T40.

Kang, S. and Oldenburg, D.W., 2016, On Recovering Distributed Ip Information from Inductive Source Time Domain Electromagnetic Data. *Geophysical Journal International* **207**, 174-96.

Kratzer, T. and Macnae, J., 2012, Induced Polarization in Airborne Em. *Geophysics* **77**, 10.

Lin, C., Fiandaca, G., Auken , E., Couto, M.A., and Christiansen, A., 2019, A Discussion of 2d Induced Polarization Effects in Airborne Electromagnetic and Inversion with a Robust 1d Laterally Constrained Inversion Scheme. *Submitted to Geophysics*.

Macnae, J., 2015, Quantifying Airborne Induced Polarization Effects in Helicopter Time Domain Electromagnetics. *Journal of applied geophysics*, 8.

Marchant, D., Haber, E., and Oldenburg, D., 2014, Three-Dimensional Modeling of Ip Effects in Time-Domain Electromagnetic Data. *Geophysics* **79**, E303-E14.

Martins, B.d.S., Lobato, L.M., Rosière, C.A., Hagemann, S.G., Santos, J.O.S., Villanova, F.L.d.S.P., Figueiredo e Silva, R.C., and de Ávila Lemos, L.H., 2016, The Archean Bif-Hosted Lamego Gold Deposit, Rio Das Velhas Greenstone Belt, Quadrilátero Ferrífero: Evidence for Cambrian Structural Modification of an Archean Orogenic Gold Deposit. *Ore Geology Reviews* **72**, 963-88.

Pelton, W.H., Ward, S.H., Hallof, P.G., Sill, W.R., and Nelson, P.H., 1978, Mineral Discrimination and Removal of Inductive Coupling with Multifrequency Ip. *Geophysics* **43**, 588-609.

Seigel, H.O., 1959, Mathematical Formulation and Type Curves for Induced Polarization. *Geophysics* **24**, 547-65.

Smith, B.D., Tippens, C., Flanigan, V., and Sadek, H., 1983, Preliminary Results of Spectral Induced Polarization Measurements, Wadi Bidah District, Kingdom of Saudi Arabia. *US Geological Survey, Open-File Report*, **83-612**.

Viezzoli, A., Fiandaca, G., and Sergio, S., Study on the Potential of Recovering Ip Parameters from Airborne Tem Data in Layered Geology. *6th International AEM Conference and Exhibition*.

Viezzoli, A., Kaminski, V., and Fiandaca, G., 2017, Modeling Induced Polarization Effects in Helicopter Time Domain Electromagnetic Data: Synthetic Case Studies. *GEOPHYSICS* **82**, E31-E50.

Viezzoli, A., Kaminskiy, V., Ebner, N., and Menghini, A., Extracting Ip Information from Aem Data to Improve the Hydrogeological Interpretation. *ASEG-PESA-AIG 2016*.

Annex 1: Workbench Geometric File (.gex) Used For The AeroTEM^{HD} Data

```
[General]
Description=AEROTEM setup
GPSPosition1=0.00 0.00 0.00
AltimeterPosition1=0.00 0.00 0.00
InclinometerPosition1=0.00 0.00 0.00
RxCoilPosition1=-4.80 0.00 0.00
TxCoilPosition1=0.00 0.00 0.00
FrontGateDelay=0.00
RxCoilLPFilter1=1.00 6.000E+04
LoopType=7
TxLoopSides=17.72 17.72
CalculateRawDataSTD=0
WaveformPoint01=-4.476E-03 0.000E+00
WaveformPoint02=-2.134E-03 1.000E+00
WaveformPoint03=0.000E+00 0.000E+00
NumberOfTurns=5
GateTime01=8.750E-05 7.360E-05 1.014E-04
GateTime02=1.153E-04 1.014E-04 1.292E-04
GateTime03=1.431E-04 1.290E-04 1.568E-04
GateTime04=1.709E-04 1.570E-04 1.848E-04
GateTime05=2.125E-04 1.847E-04 2.403E-04
GateTime06=2.820E-04 2.403E-04 3.236E-04
GateTime07=3.792E-04 3.236E-04 4.347E-04
GateTime08=5.042E-04 4.347E-04 5.736E-04
GateTime09=6.848E-04 5.737E-04 7.959E-04
GateTime10=9.487E-04 7.959E-04 1.102E-03
GateTime11=1.310E-03 1.101E-03 1.518E-03
GateTime12=1.810E-03 1.518E-03 2.101E-03
GateTime13=2.518E-03 2.101E-03 2.935E-03
GateTime14=3.518E-03 2.935E-03 4.101E-03
GateTime15=4.921E-03 4.101E-03 5.740E-03
GateTime16=6.893E-03 5.740E-03 8.046E-03
GateTime17=9.532E-03 8.046E-03 1.102E-02
[Channel1]
RxCoilNumber=1
GateTimeShift=0.000E+00
GateFactor=1.000E+00
RemoveInitialGates=0
PrimaryFieldDampingFactor=0.10
UniformDataSTD=0.05
NoGates=17
RepFreq=30.00
TxApproximateCurrent=300.00
ReceiverPolarizationXYZ=Z
FrontGateTime=-1
TiBLowPassFilter=-1.00 1.000E+00
```

Annex 2: Workbench Processing Parameters File (.gpr) For Roça Grande and Lamego Areas

Roça Grande

```
//[GPS]
2000, Device GPS=All GPS (GP)
2001, Beat Time [s]=0.5
2002, Filter Length [s]=7.0
2003, Polynomial Order=3
2004, Move GPS in x-direction from frame center [m]=0
5000, Keep Raw Sounding Distance=OFF
//[Tilt]
2200, Device AN=All
2201, Median Filter=ON
2202, Median Filter Length [s]=3.0
2203, Average Filter Length [s]=2.0
5000, Keep Raw Sounding Distance=OFF
//[Alt]
2100, Device ALT=All
2101, Tilt Correction Threshold [s]=5
2102, First Filter Poly Order=5
2103, First Filter Number of Passes=9
2104, First Filter Shift Length [s]=6
2105, First Filter Length [s]=40
2106, First Filter Lower Threshold [m]=1
2107, First Filter Upper Threshold [m]=30
2108, Second Filter Poly Order=9
2109, Second Filter Length [s]=40
5000, Keep Raw Sounding Distance=OFF
//[Channel 1]
900, Noise Channel=OFF
910, Use 2nd order slope filters =ON
1000, Sounding Bin Spacing [s]=2
1001, Current Time Distance [s]=0.5
1100, Cap Sign Filter=OFF
1101, Cap Sign from time [s]=1e-3
1102, Cap Sign noise level (ms)[v/m2]=1e-15
1103, Cap Sign noise slope=-0.8
1104, Cap Sign back step=3
1200, Cap Slope Filter=ON
1201, Cap Slope from time [s]=8e-4
1202, Cap Slope noise level (ms)[v/m2]=2e-15
1203, Cap Slope noise slope=-0.4
1204, Cap Slope min slope=-0.8
1205, Cap Slope max slope=0.8
1206, Cap Slope back step=3
1500, Ave Sign Filter=OFF
1501, Ave Sign from time [s]=4e-4
1502, Ave Sign back step=1
1600, Ave Slope Filter - Late Times=ON
1601, Ave Slope from time [s]=8e-4
1602, Ave Slope min slope=-0.6
1603, Ave Slope max slope=0.6
1604, Ave Slope back step=0
1620, Ave Slope Filter - Early Times (ET)=OFF
1621, Ave Slope from time (ET) [s]=20e-6
1622, Ave Slope (ET) (+/-)=0.7
1623, Ave Slope back step (ET)=0
1640, Ave STD Filter=ON
1641, Ave STD from time [s]=8e-4
1642, Ave STD max=3
1700, Trapez Filter=ON
```

```
1701, Trapez Sounding Distance [s]=0.1
1702, Trapez Gate Time 1 [s]=1e-5
1703, Trapez Gate Time 2 [s]=1e-4
1704, Trapez Gate Time 3 [s]=1e-3
1705, Trapez Width 1 [s]=0.25
1706, Trapez Width 2 [s]=0.5
1707, Trapez Width 3 [s]=1
1720, Trapez 2nd Tx min. Altitude [m]=999
1721, Trapez 2nd Width 1 [s]=6
1722, Trapez 2nd Width 2 [s]=12
1723, Trapez 2nd Width 3 [s]=36
1708, Trapez Spike Factor=20
1709, Trapez Min. No. Gates [%]=20
1710, Trapez Min. No. Gates per sound.=6
1711, Trapez Sync. location of sound.=ON
1712, Trapez Require left/right sound.=OFF
1713, Minimum allowed Tx altitude [m].=5.0
1714, Maximum allowed Tx altitude [m].=999.0
1800, Use Neural Network=OFF
1801, Neural Network=Please select a neural network
1802, Neural Network Bias=0
//[DEM]
DEM=0
DEMGrid=DEM_SRTM_1ArcSec
//[Processors]
GPS=-1
Tilt=-1
Altitude=-1
Transmitter=-1
Data=-1
Channel 1=-1
KeepRaw=-1
KeepRawDistance=0
```

Lamego Mine

```
//[GPS]
2000, Device GPS=All GPS (GP)
2001, Beat Time [s]=0.5
2002, Filter Length [s]=7.0
2003, Polynomial Order=3
2004, Move GPS in x-direction from frame center [m]=0
//[Tilt]
2200, Device AN=All
2201, Median Filter=ON
2202, Median Filter Length [s]=3.0
2203, Average Filter Length [s]=2.0
//[Alt]
2100, Device ALT=All
2101, Tilt Correction Threshold [s]=5
2102, First Filter Poly Order=5
2103, First Filter Number of Passes=9
2104, First Filter Shift Length [s]=6
2105, First Filter Length [s]=40
2106, First Filter Lower Threshold [m]=1
2107, First Filter Upper Threshold [m]=30
2108, Second Filter Poly Order=9
2109, Second Filter Length [s]=40
//[Channel 1]
900, Noise Channel=OFF
910, Use 2nd order slope filters =ON
1000, Sounding Bin Spacing [s]=2
1001, Current Time Distance [s]=0.5
1800, Use Neural Network=OFF
1801, Neural Network=Please select a neural network
1802, Neural Network Bias=0
1100, Cap Sign Filter=OFF
1101, Cap Sign from time [s]=20e-6
1102, Cap Sign noise level (ms)[v/m2]=5e-8
1103, Cap Sign noise slope=-0.8
1104, Cap Sign back step=3
1200, Cap Slope Filter=OFF
1201, Cap Slope from time [s]=20e-6
1202, Cap Slope noise level (ms)[v/m2]=5e-7
1203, Cap Slope noise slope=-0.6
1204, Cap Slope min slope=-1.5
1205, Cap Slope max slope=1.5
1206, Cap Slope back step=3
1500, Ave Sign Filter=OFF
1501, Ave Sign from time [s]=20e-6
1502, Ave Sign back step=1
1600, Ave Slope Filter - Late Times=OFF
1601, Ave Slope from time [s]=1.5e-5
1602, Ave Slope min slope=-1.6
1603, Ave Slope max slope=1.6
1604, Ave Slope back step=0
1620, Ave Slope Filter - Early Times (ET)=OFF
1621, Ave Slope from time (ET) [s]=20e-6
1622, Ave Slope (ET) (+/-)=0.7
1623, Ave Slope back step (ET)=0
1640, Ave STD Filter=ON
1641, Ave STD from time [s]=30e-6
1642, Ave STD max=5
1700, Trapez Filter=ON
1701, Trapez Sounding Distance [s]=0.2
1702, Trapez Gate Time 1 [s]=1e-5
1703, Trapez Gate Time 2 [s]=1e-4
1704, Trapez Gate Time 3 [s]=1e-3
1705, Trapez Width 1 [s]=0.1
1706, Trapez Width 2 [s]=0.2
1707, Trapez Width 3 [s]=0.5
1720, Trapez 2nd Tx min. Altitude [m]=999
1721, Trapez 2nd Width 1 [s]=6
```

```
1722, Trapez 2nd Width 2 [s]=12
1723, Trapez 2nd Width 3 [s]=36
1708, Trapez Spike Factor=20
1709, Trapez Min. No. Gates [%]=20
1710, Trapez Min. No. Gates per sound.=6
1711, Trapez Sync. location of sound.=ON
1712, Trapez Require left/right sound.=OFF
1713, Minimum allowed Tx altitude [m].=5.0
1714, Maximum allowed Tx altitude [m].=999.0
//[DEM]
DEM=0
DEMGrid=<No DEM nodes>
//[Processors]
GPS=-1
Tilt=-1
Altitude=-1
Transmitter=-1
Data=-1
Channel 1=-1
KeepRaw=-1
```